A STUDY OF GENERAL CHARACTERISTICS OF Si-EMULSION COLLISIONS AT 14.6 AGeV

ABSTRACT
THESIS

SUBMITTED FOR THE AWARD OF THE DEGREE OF

Doctor of Philosophy

IN

PHYSICS

By

SAIFUL ISLAM

Under the Supervision of

Dr. RASHID HASAN

DEPARTMENT OF PHYSICS
ALIGARH MUSLIM UNIVERSITY
ALIGARH (INDIA)

2005

Fed [illegible] mputer

Relativistic nucleus-nucleus collisions provide an opportunity to probe the high energy density region in the laboratory. It is expected that at extreme energy densities, there will be a phase transition of ordinary nuclear matter to a new state of matter – the quark-gluon plasma (Q.G.P.). The experimental challenge is to confirm Q.G.P. formation and study the properties of the new state of matter. The study of relativistic nuclear collisions will also provide the knowledge of the equation state of nuclear matter at densities relevant to the interior of neutron stars and for our understanding of the creation of the universe. But the relativistic nucleus-nucleus collision is a very complex process and in order to know and detect the signatures of Q.G.P. formation one must have a thorough understanding of the mechanism of the multiparticle production and fragmentation processes. Thus it is important to study different aspects of nucleus-nucleus collisions at relativistic energies. The availability of heavy ions with relativistic energies at CERN, Dubna and BNL made it possible to study nucleus-nucleus collisions in a systematic manner.

After giving a brief introduction to the subject in chapter I, the experimental technique has been described in chapter II. An emulsion stack exposed horizontally to 14.6*A GeV* silicon beam from Alternating Gradient Synchrotron at Brookhaven National Laboratory has been used for the present work. Nuclear emulsion having the highest special resolution among all particle detectors is an ideal detector. The dimensions of emulsion pellicles are $16.0 \times 10.0 \times 0.06$ cm^3. The sensitivity of emulsion is about 24 grains per 100 μm for singly charged particles with minimum ionizations.

Primary collisions are picked up by along the track scanning. Each primary track is followed until it collided or left the pellicle. Collisions lying within 3mm of the leading edge are not recorded. Each emulsion stack is doubly scanned along the tracks, fast in the forward directions and slowly in the backward one. 1107 collisions of ^{28}Si are picked up by following 12258.8 *cm* of primary beams, leading to the collision mean free path of ^{28}Si in emulsion λ = 11.07±0.48 *cm*. Scanning is carried out with almost 100% efficiency. Collisions that are within 20 μm from the top or bottom surface of the emulsion stack and caused by primaries making an angle greater than 2^0 with the mean beam direction are not recorded. In this way 784 inelastic collisions (events) of 14.6*A GeV* silicon ions in nuclear emulsion are recorded.

In each event polar and azimuthal angles of all secondary particles are measured under high magnification. The accuracy in the measurement of polar angle is 1mrad and

in the measurement of azimuthal angle it is about 5^{o} Depending on ionization, all secondary tracks emitted from the collision vertices are classified as shower, grey, black particles and projectile fragments using the commonly accepted emulsion terminology described in chapter II

Events are classified into different target groups using the following standard emulsion criteria

- *AgBr* events: (i) $N_h \geq 8$ or (ii) $N_h < 8$ and at least one track with $R \leq 10\mu m$ and no track with $10 < R \leq 50\mu m$
- *CNO* events· $2 \leq N_h < 8$ and no track with $R < 10\mu m$
- *H* events: (i) $N_h = 0$ or (ii) $N_h = 1$ but falling in none of the above categories.

In this way out of 784 inelastic collisions in *Emulsion*, we have separated 360 collisions with *AgBr* target group, 287 collisions with *CNO* target group and 137 collisions with *H* target.

In chapter III we have studied the general characteristics of these collisions. The dependence of the percentage of collisions with nuclei of different target groups in emulsion on the mass of the projectile is studied. The mean multiplicities of all the secondary charged particles are calculated and are observed to depend on the mass of the target nucleus whereas the average multiplicity ot shower particles depends on the energy of the projectile also. These dependences are well described by the relation $\langle N_i \rangle = a_i \langle A_T \rangle^{bi}$.

The pseudorapidity distributions of shower particles produced in ^{28}Si-*Emulsion* collisions at 4.5*A GeV* and 14.6*A GeV* are plotted It is observed that with increase in the energy of the projectiles, the peak of the pseudorapidity distribution shifts towards the higher value of η, which corresponds to small angle of emission. The pseudorapidity distributions of shower particles are fitted well with Gaussian distribution for ^{28}Si-*AgBr*, ^{28}Si-*CNO* and ^{28}Si-*H* collisions It is observed that the distributions are almost the same at higher values of pseudorapidity and the centroids of the distribution grow and shift towards smaller values of pseudorapidity as the target mass increases from *H* to *AgBr* group

Further, pseudorapidity distributions of shower particles are used to describe the target fragmentation region, the central region and the projectile fragmentation region

The target fragmentation region corresponds to the lower η values, that is, larger values of emission angle, which is characterized by the target nuclei. The projectile fragmentation region is assumed to be populated by fragments of projectile nucleus corresponding to larger values of η, that is, small angles of emission. The central region is believed to be enriched by the particles produced in collisions of the participants of colliding nuclei and is independent of either of the fragmentation regions.

The charged particle multiplicity correlations in ^{28}Si-*Emulsion* collisions at 14.6*A GeV* are studied. It is found that these correlations have a linear dependence with positive slope. The strongest correlation is observed between $<N_s>$ and N_g with a slope 2.67 ± 0.13 for ^{28}Si-*Emulsion* collisions at 14.6*A GeV*. The angular distributions of relativistic charged particles are independent of target mass and prominent peaks are observed at smaller angles. However, the angular distributions of grey and black particles (target fragments) show no significant peaks.

The study of multiplicity moments shows that the values of the ratio $<N_s>/D$ for various projectiles are almost the same that indicates a similar mechanism of shower particle production. The values of dispersion increase linearly with increase in the mean multiplicity of shower particles and the values of multiplicity moments C_q increase with increasing value of q. The same trend is followed by the data on different projectiles as well. The shape of the multiplicity distribution of shower particles strongly depends on target mass. The multiplicity distributions of grey and black particles show that the distributions for ^{28}Si-*AgBr* collisions are broader than those for ^{28}Si-*CNO*. The tail of the multiplicity distribution of shower particles extends to much higher values of N_s with the increase in projectile energy. This is due to the production of more relativistic charged particles with increasing energy.

The negative binomial distribution is found to describe well the shower particle multiplicity distributions for ^{28}Si-*Emulsion*, ^{28}Si-*AgBr* and ^{28}Si-*CNO* collisions for windows of different sizes in both the pseudorapidity (η) and azimuthal angle (φ) phase spaces. In both the phase spaces, increasing values of clan size $\overline{n}_c$ are observed corresponding to each window size for ^{28}Si-*CNO*, ^{28}Si-*Emulsion* and ^{28}Si-*AgBr* collisions. This is an evidence of the increase in the size of clusters with increase in the target mass.

From the results obtained from the analysis of the charged particles in the forward and backward hemispheres, it is clear that the backward particle production may be a consequence of the isotropic decay of a highly excited target nucleus in its rest frame

after the forward particle production. The average multiplicities of shower and grey particles in both the hemispheres increase with increasing target size. These dependences on the target size are well parameterized by the power law form $\left\langle N_i^k \right\rangle = \beta_i^k \left\langle A_T \right\rangle^{\alpha_i^k}$. A mild dependence of the forward backward ratio on the size of the projectile is observed for target fragments, whereas in the case of relativistic charged particles, a strong dependence is observed. The results obtained from the analysis of multiplicity distributions of the shower and grey particles emitted in the backward hemisphere confirm the limiting fragmentation hypothesis. Further, the results of the forward-backward multiplicity correlations show that the dependences of $<N_s^F(N_s^B)>$ on N_s^B and $<N_s^B(N_s^F)>$ on N_s^F are linear. The average number of shower and grey particles in the forward hemisphere depend strongly on the total number of shower and grey particles emitted in the backward hemisphere, whereas the average number of grey and shower particles in the backward hemisphere depends weakly on the total number of shower and grey particles emitted in the backward hemisphere. This shows that pions and protons emitted in the backward hemisphere are somewhat different from those emitted in the forward hemisphere.

In chapter IV, the modified moments G_q and the scaled factorial moments F_q are used to study of multifractality in $^{28}Si\text{-}AgBr$ collisions at $14.6A\ GeV$ in both the η and φ spaces. The connection between the G_q moments and the scaled factorial moments F_q has also been investigated. Presence of dynamical fluctuations and multifractality in our data in both the η and φ spaces are observed. Further, experimental results are compared with the string hadronic *UrQMD* model. It is observed that *UrQMD* model fails to explain the observed dynamical fluctuations and multifractality in our data in both the η and φ spaces. It also fails to explain the observed power law growth of the scaled factorial moment with decreasing bin size in both the spaces.

We have also used Takagi method to study multifractality in our data and observed that the results for the random and *UrQMD* events are about the same as those obtained for the experimental events in both the spaces. Thus no meaningful conclusion regarding multifractality in the data could be drawn from the analysis done using the Takagi method. We therefore suggest that only F_q-moment or G_q-moment method should be used for the study of multifractality in multiparticle production as the multiplicity moments calculated using the Takagi method are dominated by statistical fluctuations.

The generalized dimension D_q are determined from G_q-moment and F_q-moment analyses for experimental and *UrQMD* events in both the spaces. D_q values for our experimental events are found to decrease with increasing q. This shows the presence of multifractality in our data. However, for *UrQMD* events, D_q values for different q values are equal within the errors. Thus, the model again fails to explain the observed dynamical fluctuations and multifractality in our data. Therefore, we conclude that the string hadronic *UrQMD* model could not explain the experimental results on the generalized dimensions. The multifractal specific heat c is also determined from G_q-moment and F_q-moment analyses. Differences in the values of D_q and c from the two methods are mainly due to the difference in the definitions of G_q-moments and F_q-moments.

In chapter V, we have studied the scaled factorial cumulant moments for shower particles produced in ^{28}Si-*AgBr* collisions at 14.6*A GeV*. We observed that both the second and third order scaled factorial cumulant moments K_2 and K_3 have non-zero values that is an evidence of the presence of dynamical two particle and three particle correlations. To compare our results with the string hadronic model *UrQMD,* we have simulated 1400 *UrQMD* events. The scaled factorial cumulant moments K_2 and K_3 for *UrQMD* events are also studied. It is observed that the values of K_3 for *UrQMD* events for different M are almost zero, indicating the absence of three particle correlations in these events. However, K_2 values for different M deviate significantly from zero, indicating that significant two particle correlations are present in *UrQMD* events. Further, to extract more information from the scaled factorial cumulant moment analysis we have investigated the slopes of K_q versus ln$M$ plots (cumulant indices). The cumulant indices for experimental events are $\pi_2 = 0.018 \pm 0.004$, $\pi_3 = 0.012 \pm 0.003$, whereas for *UrQMD* events they are $\pi_2 = 0.002 \pm 0.001$, $\pi_3 = -0.000 \pm 0.000$. The cumulant indices for *UrQMD* events are consistent with being zero. However, not only two particle correlations but also significant three particle correlations are present in our data. Moreover, the values of cumulant indices for our data are also not zero. Thus the model *UrQMD* fails to explain the observed correlations in our data.

We have observed that the cumulant indices show an inverse dependence upon the pseudorapidity density. This indicates that all types of interactions involve similar physics in terms of the types of particle sources created. We have calculated the number of independent sources for ^{28}Si-*AgBr* collisions at 14.6*A GeV*. The value of the average number of independent sources ($\overline{N}$) obtained using independent source model deviates

significantly the value obtained using the negative binomial distribution. One of the reasons for different values of $\overline{N}$ obtained from two methods could be the assumption used in arriving at $\overline{N} = \frac{3a\langle\rho\rangle}{b}$ that is used to find $\overline{N}$. It has been assumed that the second order scaled factorial cumulant of the number of sources is zero. This assumption is not valid because the multiplicity distribution is not Poissonian as $K_2 \neq 0$. The other assumption that three particle correlations are negligible compared to two particle correlations is also not valid as significant three particle correlations are present in our data.

Additional information about the dynamics of multiparticle production can be obtained by investigating bin-bin correlations through the study of factorial correlators. The correlators measure not only the non-statistical local density fluctuations but also give important information about the correlations between the local density fluctuations in different regions of phase space. We have studied factorial correlators for ^{28}Si-$AgBr$ collisions at 14.6A GeV and for $UrQMD$ events in the full range of correlation length (D) and observed power law behaviour in the region $D < 0.5$. The slopes (ϕ_{ij}) obtained for $UrQMD$ events are very nearly equal to zero. In the experimental events we observed that the slopes (ϕ_{ij}) increase with increase in the order of correlations but for $UrQMD$ events for $\delta X = 0.125$ and 0.036, we observed no such pattern. Thus $UrQMD$ model fails to explain our experimental results on factorial correlators also. Further, we have observed results in favour of δX independence of C_{ij} for small values of D, but the scaling seems to fail at large values of D ($D > 0.5$). The results obtained for our data are in agreement with the α-model, which predicts that the factorial correlators have a power law increase with decreasing distance between intervals and have no dependence on the size of the intervals (δX). But this does not guarantee the success of α-model, as other models with short-range order have similar predictions.

Further, the scaled factorial moments F_q are studied for ^{28}Si-$AgBr$ collisions at 14.6A GeV. These moments follow the generalized power law $\langle F_q(M)\rangle \propto [g(M)]^{\phi_q}$. The values of ϕ_q/ϕ_2 obtained from the linear fits of $\ln\langle F_q\rangle$ versus $\ln\langle F_2\rangle$ graphs are found to obey the Brax-Peschanski formula for intermittency indices with Levy index $\mu = 1.635 \pm 0.012$ for η space and $\mu = 1.801 \pm 0.003$ for φ space. These values lie within the Levy stable region 0 μ 2. The generalized dimensions D_q decreases with increasing q, which

indicates that the multiparticle production in ^{28}Si-$AgBr$ collisions at $14.6A\ GeV$ is a self-similar cascade process. The multifractal spectra $f(\alpha_q)$ in η and φ spaces are obtained. $f(\alpha_q)$ spectra are smooth and concave downward, indicating the presence of dynamical fluctuations in our data.

We have collected very useful information about the dynamics of multiparticle production in nucleus-nucleus collisions at relativistic energy. Significant dynamical fluctuations have been observed in our data. It is believed that the fluctuations could be due to the formation of quark-gluon plasma (Q.G.P.) in these collisions. But evidence of dynamical fluctuations has also been obtained in low energy nucleus-nucleus collisions where the formation of Q.G.P. is not expected. Even in target fragmentation process, where the Q.G.P. phase transition is most unlikely, evidence of dynamical fluctuations has been reported by some investigators. So Q.G.P. phase transition cannot be the only reason for the fluctuations observed in our data. It may be possible that the observed fluctuations may have a more conventional explanation. The presence of random cascade mechanism or short-range correlations or some collective phenomena may be responsible for the observed dynamical correlations in relativistic nucleus-nucleus collisions.

A STUDY OF GENERAL CHARACTERISTICS OF Si-EMULSION COLLISIONS AT 14.6 AGeV

THESIS

SUBMITTED FOR THE AWARD OF THE DEGREE OF

Doctor of Philosophy

IN

PHYSICS

By

SAIFUL ISLAM

Under the Supervision of

Dr. RASHID HASAN

DEPARTMENT OF PHYSICS
ALIGARH MUSLIM UNIVERSITY
ALIGARH (INDIA)

2005

CERTIFICATE

This is to certify that the thesis entitled "A Study of General Characteristics of Si-Emulsion Collisions at 14.6 AGeV" which is being submitted by Mr. Saiful Islam is a record of the research work carried out by him under my supervision. The research work presented in the thesis has not been submitted for the award of any other degree by him or by anyone else.

Dated: 4 July, 2005

(Dr. Rashid Hasan)
Reader,
Department of Physics,
Aligarh Muslim University,
Aligarh 202 002
INDIA

Acknowledgements

It is a matter of great pleasure for me to express my deepest sense of thankfulness and indebtedness to my supervisor Dr. Rashid Hasan, whose precious guidance, encouragement and sympathetic attitude were immensely helpful and invaluable throughout the present work. These mere words are not sufficient to applaud his guidance. I will cherish throughout my life the valuable suggestions, constructive criticism and unending support that I received from him. His erudite presence has been a constant source of inspiration and motivation during the course of this work.

I am highly indebted to Prof. Mohammad Irfan, Chairman, Department of Physics, A.M.U. Aligarh, for moral support and providing me the necessary facilities in carrying out my research.

I am highly thankful to Prof. P. L. Jain, Department of Physics, State University of New York at Buffalo, for sending us the processed emulsion plates used in the present investigation.

I express my sincere thanks to Prof. Mohammad Zafar for his encouragement and healthy suggestions on different aspects of this work.

I would like to thank to Dr. A. R. Khan, Dr. Shakeel Ahmad, Dr. M. S. Ahmad and Dr. Shahid Hussian for their useful suggestions and advices.

My sincere thanks are due to my co-worker Dr. M. Mohib-ul Haq for his valuable suggestions and encouragement.

Thanks are due to Mr. Habibur Rehman for his skillful scanning of emulsion plates and for his generous advices.

Thanks are also due to Dr. N. Ahmad, Dr. A. Agarawal, Mr. Wasi Khan, Mr. M. Ayaz, Mr. Shafiqullah and Mr. S. Soni and other friends for their cooperation and moral support.

I express my deep sense of gratitude to respected Mr. M. Tariq Khan and Mr. M. Saeed for their moral support and keen interest in my academic achievements.

Last but not least, I would like to acknowledge the blessings and love of my parents, sisters and my wife.

Finally, the financial assistance from the Aligarh Muslim University, Aligarh is acknowledged with thanks.

Saiful Islam

Dedicated

To

My Parents

CONTENTS

CHAPTER III

General Characteristics for ^{28}Si-*Emulsion* Collisions at 14.6*A GeV*

CHAPTER IV

Multifractal Analysis of Multiplicity Fluctuations in ^{28}Si-$AgBr$ Collisions at 14.6A GeV

CHAPTER V

Scaled Factorial Cumulant Moments and Factorial Correlators for ^{28}Si-$AgBr$ Collisions at 14.6A GeV

CHAPTER VI

Levy Stable Law of Intermittency and Multifractal Spectrum for ^{28}Si-$AgBr$ Collisions at 14.6A GeV

CHAPTER VII

List of Figures

List of Tables

CHAPTER I

Introduction

1.1 Introduction

The main aim of heavy ion physics is the study of strongly interacting nuclear matter at extreme energy densities. Quantum chromodynamics (Q.C.D.), the theory of strong interactions, predicts that at such extreme densities, there will be a phase transition of ordinary nuclear matter to a new state of matter - the quark-gluon plasma (Q.G.P.). This sate of matter might have existed during the first fraction of a second after the big bang and may also exist in the core of neutron stars.

Conditions of extreme energy densities could be achieved in the laboratory during nucleus-nucleus collisions at relativistic energies. Thus the study of relativistic nuclear collisions is very important not only because it provides an opportunity to test quantum chromodynamics on a new natural scale but it will also provide the knowledge of the equation state of nuclear matter at densities relevant to the interior of neutron stars and for our understanding of the creation of the universe.

The quark-gluon plasma (Q.G.P.), if produced during nucleus-nucleus collisions at relativistic energies, will be very short lived. Upon expansion and cooling, it will hadronize into variety of baryons, anti-baryons and mesons. The experimental challenge is to confirm Q.G.P. formation from the study of these final state particles and subsequently study the properties of the new state of matter. But the nucleus-nucleus collision is a very complex process and in order to disentangle the signature of Q.G.P. formation one must have a thorough understanding of multiparticle production in high energy collisions and fragmentation processes.

Historically, the study of nucleus-nucleus collisions became possible after the discovery of heavy nuclei in the cosmic rays in 1948 by Frier et al. [1]. At that time it was the only available source of energetic particles. The nature and energy of these incident particles were not accurately known and statistics (intensity/flux) were small. Due to lack of complete knowledge of the incident particles, it was difficult to get information regarding the mechanism of multiparticle production in high-energy nuclear collisions.

With the availability of variety of heavy ions with controlled energies and fluxes at CERN, LBL and Dubna, it has become possible to study in a systematic manner, different aspects of nucleus-nucleus collisions at relativistic energies. Nucleus-nucleus collisions at relativistic energies provide very high energy densities in a small volume, revealing many new phenomena. Many signals for Q.G.P. formation have been

suggested, but it is difficult to conclude whether these signals are really an outcome of Q.G.P. or some collective phenomena. Collecting detailed experimental information covering all aspects of particle production in high energy nuclear collisions using different projectiles of varying energy is essential in this context.

1.2 Geometry and Space-Time Evolution of Nucleus-Nucleus Collisions

The dynamics of nucleus-nucleus collisions can be viewed from the space-time diagram with the longitudinal coordinate z and the time coordinate t as shown in Figure1.1. As the nuclei are extended objects, their geometry plays an important role in nucleus-nucleus collisions. Figure 1.2 shows a sketch of the collision between two nuclei A and B. They appear in the centre of mass frame as two Lorentz contracted pancakes with limited thickness $\sim 1fm$ [2,3]. The impact parameter, b, represents the transverse distance between the centers of the two colliding nuclei and it separates the nucleons into participants and spectators. Spectators proceed with little perturbation along the original direction. In the first instance of reaction, the energy lost by the participant baryons is deposited in the collision region. As a result a large amount of energy is deposited in that small region of space in a short interval of time. The matter created in the collision region has a very high energy density, but has a small net baryon content. The energy deposited in the collision region is carried out in the form of quarks, gluons or hadrons. Figure 1.1 represents space-time scenario suggested by Bjorken [4] for a high-energy nucleus-nucleus collision. As the energy density is very high in the region around $z = 0$, the quark-gluon plasma may be formed in the central rapidity region. At this high energy density the hadrons cannot exist. From the very energetic or 'hard' collisions among the quarks and gluons, additional gluons and light and heavy quarks are produced. These new quarks and gluons, along with those present initially, undergo a cascade of further collisions. The gluons produced thermalize in less than the time required for the nuclei to interpenetrate, sharing their energy equally among themselves. As a result the quark-gluon plasma may go in local thermal equilibrium that lives long enough to generate detectable signals. The hot and dense stage of the collision, where the plasma is expected to exist, lasts only about three times as long as the interpenetration stage. Experiments will have to sample this stage for the evidence of the existence and

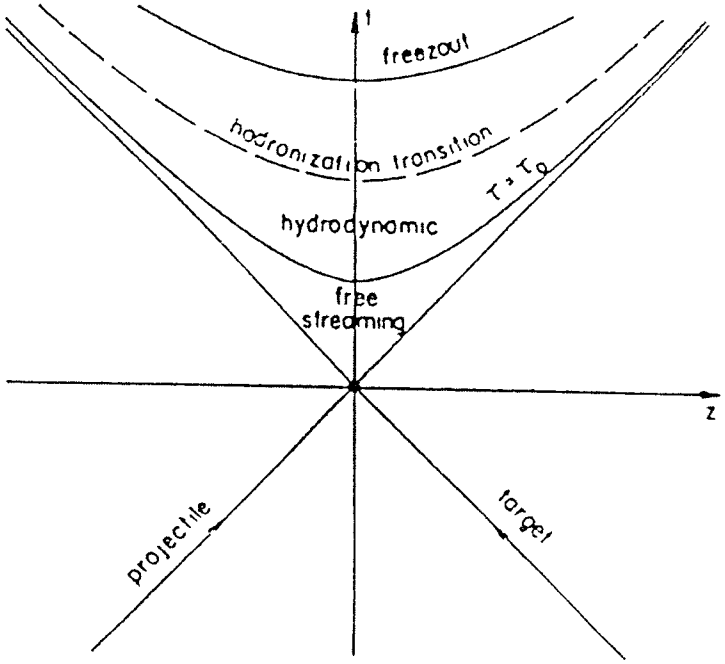

Figure 1.1: Space time diagram of a central relativistic nucleus – nucleus collision.

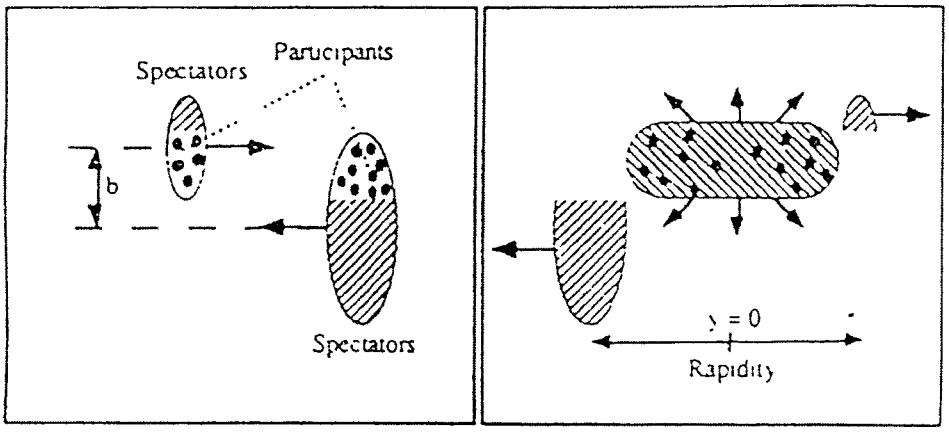

Figure 1.2: Schematic representation of a nucleus – nucleus collision at impact parameter b, assuming straight – line geometry.

properties of the quark-gluon plasma [5]. As the plasma expands, mainly along the longitudinal direction, its temperature falls and reaches a critical temperature T_c after a few *fm/c*. The matter then spends a long time in the mixed phase and the quarks and gluons condense into a gas of hadrons with release of large amount of latent heat. As a result, hadronic phase appears with highly excited and large density of hadrons. The hadrons scatter from one another, maintaining the pressure and causing further expansion and cooling. The multiple scatterings of the particles tend to distribute the available energy equally among them. Eventually, the system may expand to very large dimensions ($V \sim 10^4$-10^5 fm^3) till freeze-out, that is, the interactions cease and the particles stream out freely without further disturbance [2]. The number of particles at the end reflects the energy deposited in the collision. This energy rises with the beam energy.

1.3 Signals of Q.G.P.

The ultimate aim of high-energy physicists is to detect the quark-gluon plasma that is expected to be formed in the relativistic nucleus-nucleus collisions. The Q.G.P. formed exists only for a fraction of the evolution time and cannot be detected directly. Experiments must identify some features of the data that cannot be present in the absence of the quark-gluon plasma. Hence it is very important to know as to what observables must be looked at experimentally to see the quark-gluon plasma. These are called the signals of the quark-gluon plasma. Some of the probable signals are described below in brief.

1.3.1 Lepton Pair Production

In the quark-gluon plasma, a quark can interact with an antiquark to form a virtual photon, which subsequently converts into a lepton and an anti-lepton. The system of the produced lepton-antilepton pair is called a dilepton or simply lepton pair. The mean free paths of the leptons are expected to be quite large and the leptons are not likely to suffer further collisions after they are produced. They exist in the colliding system virtually unaffected by the surrounding hadronic matter. The production rate and momentum distribution of the produced lepton pairs depend on the momentum distributions of quarks and antiquarks in the plasma, which are governed by the thermodynamic condition of the

plasma. Therefore, lepton pairs carry information on the thermodynamical state of the medium at the moment of their production [6-16].

The lepton pairs can also be produced from the interactions of charged hadrons and their antiparticles. Thus in order to identify separately the dileptons produced from the Q.G.P., the yield of dilepton from the Q.G.P. must be greater than or comparable to their yield from a non-Q.G.P. source.

1.3.2 J/ψ Suppression

J/ψ particle is the meson consisting of bound state of a charm-anticharm quark pair. J/ψ particles are produced by the hard scattering process in nucleus-nucleus collisions [17]. The interactions between quarks are screened by the other quarks in the deconfined state. Therefore, if the Q.G.P. is formed in the region of J/ψ production, J/ψ particles cannot survive in the plasma and the final yield of J/ψ particles will be suppressed as compared to the case when there is no Q.G.P. Bound states with larger radii are dissociated first, while the ones with smaller radii are dissociated later. Therefore the suppression of J/ψ provides a striking signature of the existence of quark-gluon plasma [18-20]. The observed J/ψ production is currently under intense theoretical and experimental investigation Another test of this signature would be to observe that the upsilon ($b\bar{b}$) production probability is little changed. The production cross section of upsilon is very small, hence high energy beam is required to create a significant number of upsilons [21]. However data on upsilon production in ultrarelativistic nucleus-nucleus collisions will not be available until *LHC* becomes operational.

1.3.3 Strangeness Enhancement

Strangeness enhancement is another signal for the Q.G.P. This is due to the production of additional strange quarks in the quark-gluon plasma. The enhancement of the number of strange quarks and antiquarks leads to an enhancement of strange particles. Thus the increased number of mesons and baryons containing strange quarks observed will be an evidence for the formation of Q.G.P. A significant increase in the number of strange particles in nucleus-nucleus collisions in comparison to hadron-hadron collisions [22,23] have been observed at *SPS* and *AGS* energies.

1.3.4 Fluctuations

The fluctuations in the densities of charged particles in phase space caused by some real underlying dynamics are known as dynamical fluctuations. The dynamical fluctuations provide an important signal for the formation of quark-gluon plasma. However, these fluctuations may also be due to the collective phenomena like formation of minijets, or due to the random cascading effects. The fluctuations due to the low multiplicity of the particles in an event are known as statistical fluctuations. Different methods like the scaled factorial moment, scaled factorial cumulant moment, modified G_q-moment are proposed to study the dynamical fluctuations. The scaled factorial moment method is able to suppress the statistical fluctuations due to low multiplicity. However, the statistical fluctuations due to low multiplicity are minimized in the modified G_q-moment but not completely suppressed. For the confirmation of the dynamical fluctuation observed, the results obtained from experimental data are compared with the corresponding results obtained for randomly generated events.

1.4 Impact Parameter and Classification of Nucleus-Nucleus Collisions

The transverse distance between the centres of mass of the projectile and the target nuclei is known as impact parameter. It plays an important role in the classification of nucleus-nucleus collisions at relativistic energies. The characteristics of these collisions depend on the geometrical configuration of the system (i.e. target and projectile). From the geometrical point of view, relativistic nucleus-nucleus collisions are classified into three different categories, namely: (i) Peripheral, (ii) quasi-central and (iii) central collisions. Figure 1.3 shows three types of collisions quite clearly. The following criteria are used to classify the nucleus-nucleus collisions:

(i) $b \approx R_P+R_T$ for peripheral collisions

(ii) $R_P+R_T > b > |R_P-R_T|$ for quasi-central collisions

(iii) $0 \leq b \leq |R_P-R_T|$ for central collisions

where R_P and R_T are the radii of the projectile and target nuclei and b is the impact parameter.

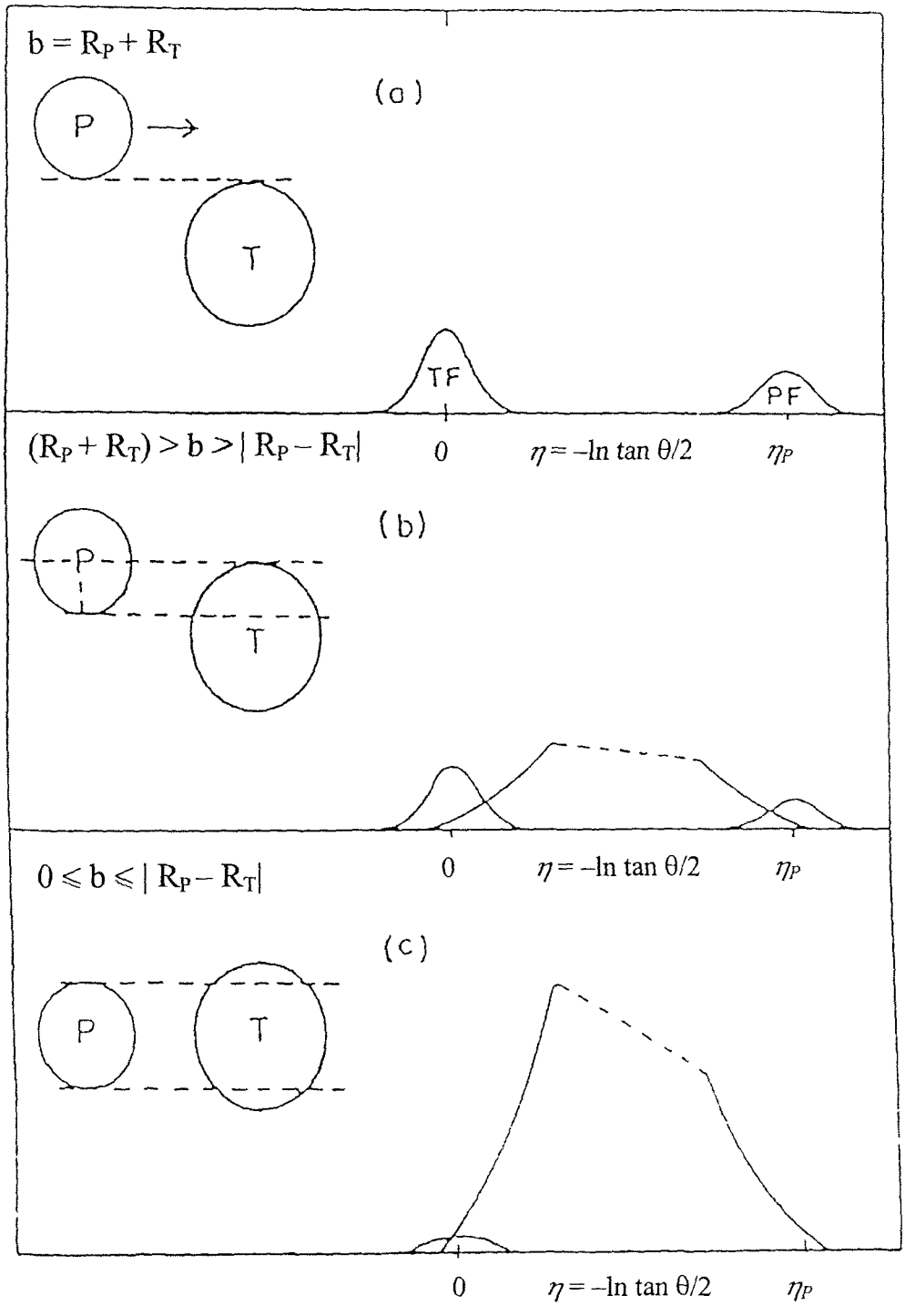

Figure 1.3: A schematic outline of pseudorapidity distributions in relativistic nucleus-nucleus collisions.

According to the criteria used for the peripheral collisions, it is clear that two centres of the colliding nuclei are well separated which allow only a small momentum or energy transfer between the nuclei during collision, leading to the breakup of one or both the nuclei into fragments. The projectile fragments are emitted within a narrow cone around the beam direction while the target fragments are nearly isotropically distributed in the laboratory frame. The characteristics of the emitted fragments are determined by the intrinsic fermi momentum distribution of nucleons within the fragmenting nuclei [24]. The pseudorapidity distribution of projectile fragments and target fragments are well separated at relativistic energies as shown in Figure 1.3.

From the criteria used for the quasi-central and central collisions, it is clear that the projectile and target nuclei are closer to each other. In these types of collisions the nuclei may no longer be spectators, but take part in the reaction and are scattered in the rapidity space between the projectile fragmentation region and target fragmentation region. The difference between the two types could be understood on the basis of number of nucleons taking part in the reaction. The whole of the kinamatically allowed rapidity space is available for the produced particles, the difference being in the degree of population in the central region. In the central collisions where the impact parameter is less than the absolute value of the difference between the radii of projectile nucleus and target nucleus, the collisions are more violent and complex. We expect almost complete extinction of projectile fragment with the emission of large number of produced particles and the emitted target fragments. The emissions of particles are symmetric with respect to the direction of the incident beam. When projectile radius (R_P) is less than target radius (R_T), the rapidity space available for the particles is almost limited to the region between projectile fragment and target fragment. If the interacting nuclei are of the same size (i.e. $R_P = R_T$), the probability for central collisions becomes almost zero [25]. This shows that a strict geometrical definition of the central collisions is not appropriate. In fact we don't have any strict definition of what we mean by a central collision.

1.5 Nuclear Fragmentation

The first experimental information about the fragmentation of nuclei was obtained in experiments with cosmic rays [26,27]. The geometrical aspects of a collision can be understood in terms of the participant- spectator model [28]. At relativistic energies, the projectile and target fragmentation regions are separated in the pseudorapidity plot.

Consequently, no correlation exists between projectile and target nucleus and the modes of fragmentation are independent of target mass [29]. Information on projectile fragmentation comes from single particle inclusive experiments. In single particle inclusive experiments, the reaction is

$$P + T = F + X \quad , \qquad 1.1$$

where P and T represent the projectile and target nuclei, F is the detected (single) fragment and X refers to all other undetected reaction products. In limiting fragmentation, the distribution of products with finite energies in the rest frame of target or projectile approaches a limiting form as incident energy increases. Experimental results on limiting fragmentation demonstrate that in a given range of incident energies, a particular distribution shows almost similar shape. Since the target and projectile regions are well separated, the fragmentation cross sections can be factorized into target and projectile related regions. The cross section for the production of a particular projectile fragment may be written as [30]

$$\sigma_{PT}^{F} = \gamma_{P}^{F} \gamma_{T} \qquad 1.2$$

where γ_P^F depends only on the projectile and the detected fragment, and γ_T depends only on the target material. Similarly. to describe the target fragmentation, the projectile and target may be interchanged.

In emulsion experiments, the angular distributions of the projectile fragments for events exhibiting either no or very small target excitation exhibit features of limiting fragmentation [30,31]. Exceptions to strict factorization have been observed for fragmentation cross sections in hydrogen [32], helium [33], and heavy targets, where single nucleon stripping is enhanced by Coulomb dissociation of projectile in the virtual photon field of target nucleus [32,34].

The study of projectile and target fragmentation processes gives a lot of information on nuclear structure. The projectile fragments may be useful in determining the momentum distribution of a nuclear cluster inside the projectile nucleus. Furthermore, the projectile fragmentation at high energies has proved to be a powerful tool for the production of new exotic nuclei. Fragmentation characteristics have much importance for

solutions of a number of problems of astrophysics, cosmic ray physics and radiation physics.

1.6 Nuclear Shock Waves

In nucleus-nucleus collisions at high energies, if the speed of the projectile exceeds the speed of sound in nuclear matter then due to the effect of strong perturbations in density and pressure, shock waves may be produced. These waves are characterized by the near discontinuities in the density, pressure and temperature. Regions of high nuclear density (2-4 times the normal density) and high temperature (T~30-200MeV) called the shock zones are expected to be created along the direction of propagation of shock waves.

Glassgold et al. [35] introduced the idea of formation of nuclear shock waves in the relativistic nucleus-nucleus collisions. Later, several theoretical models for nuclear shock waves were suggested. The predicted angular distributions of the nuclear matter are different in different shock wave models. Some models predict narrow peaks at a straight angle for conical shock front [35-39] whereas other models predict broad forward peaked distributions [40]. However, the common prediction of these models is the emission of target fragments in the direction perpendicular to the Mäch shock front. Therefore, the observed peaks in the angular distribution of the reaction products at forward and backward angles, which by following their positions and their shift with the energy of the projectile, will be interpreted as signature of shock waves.

A number of experiments have been performed to search the shock waves in nucleus-nucleus collisions. The experiments of Baumgardt et al. [41,42] show comparatively sharp peaks in the angular distribution of particles emitted in the collisions of $AgCl$ crystals with ^{4}He, ^{12}C and ^{16}O. The position of the peak shifts with the projectile energy. No narrow peaks were found by Poskanzer et al. [43] in the angular distributions of ^{3}He and ^{4}He emitted in the interaction of ^{16}O with Ag and U nuclei at 1.05A GeV. The experiment of Jakobsson et al. [44] shows broad angular distributions, which are in quantitative agreement with shock wave calculations. However, they did not observe any narrow peaks, neither in the angular nor in the energy distributions of the nuclei. Presence of some short range correlations among the target fragments have been observed by several groups [45,46] that may be due to the formation of shockwaves in nucleus-nucleus collisions.

1.7 Organization of Thesis

The ultimate aim of nucleus-nucleus collisions is to observe the signals from the quark-gluon plasma that is expected to be formed during the collisions. During the last decade many efforts have been made to observe these signals experimentally but it is not achieved till date. In order to observe the unambiguous signals of Q.G.P., it is essential to have a complete knowledge of multiparticle production and fragmentation process in the relativistic nucleus-nucleus collisions. In this thesis different features of the multiparticle production in ^{28}Si-*Emulsion* collisions at 14.6*A GeV* are studied. After giving a brief introduction to nucleus-nucleus collisions at relativistic energies in the present chapter, the thesis is organized in the following way.

The experimental technique used is described in chapter II. The mechanism of track formation, scanning procedure, various track parameters and their measurements are discussed. Also some models of multiparticle production in relativistic nucleus-nucleus collisions and event generators have been described.

In chapter III, general characteristic of ^{28}Si-*Emulsion* collisions at 14.6*A GeV* have been studied. The method of separating collisions with different target groups like *H*, light nuclei (*CNO*) and heavy nuclei (*AgBr*) has been discussed. The average multiplicities of the secondary charged particles emitted in these collisions are calculated and compared with the average multiplicities for ^{28}Si-*Emulsion* collisions at 4.5*A GeV* [47] and their dependence on the target mass is studied through the power law relation. One of the effective methods to understand the mechanism of particle production is the multiplicity correlations among the secondary charged particles. Multiplicity correlations have therefore been studied for the charged particles for our data. The angular distributions of grey, black and shower particles have been studied for different N_s intervals for different target groups. Multiplicity distributions of shower, grey, black and heavily ionizing particles have been studied for our data and compared with the distributions at energy 4.5*A GeV* of ^{28}Si-*Emulsion* collisions [48]. Multiplicity distributions of shower, grey and black particles for collisions with different target groups in emulsion are also studied.

To test the validity of negative binomial distribution (NBD), multiplicity distributions of the shower particles produced in ^{28}Si-*Emulsion* collisions at 14.6*A GeV* with varying window size in both the pseudorapidity and azimuthal angle phase spaces

are fitted with the NBD using the CERN MINUIT program (keeping $\bar{n}$ and k as free parameters).

To investigate the effect of mass and energy of the projectile, the average multiplicities of the charged particles produced in the forward and backward hemispheres and their ratios in the two hemispheres are calculated. Multiplicity distributions in the backward hemisphere have been studied and fitted with the exponential law formula $P\left(N_i^B\right) = P_i e^{-\lambda_i^B N_i^B}$ [49], where i stands for shower or grey particles. The above relation represents the fundamental equation of decay of an excited system. Finally, multiplicity correlations between the charged particles in the forward and backward hemispheres are studied.

In chapter IV, we study the fractal behavior of multiplicity fluctuations in $^{28}Si\text{-}AgBr$ collisions at $14.6A\ GeV$ using the modified G_q-moment, F_q-moment and Takagi method in both the pseudorapidity and azimuthal angle spaces. A fractal structure has the property that if one magnifies a small portion, it shows the entire complexity of the system. Different methods have been proposed for studying the fractal structures in multiparticle data [50-53]. Usually the term fractal is used to characterize systems with properties of self-similarity. The power law behaviour of the scaled factorial moments indicates the existence of self-similarity, which is closely related to multifractality. We have therefore studied the connection between F_q-moments and G_q-moments. A relation between the intermittency indices and the fractal indices has been derived. We have also calculated the values of the generalized fractal dimensions D_q^{dyn} and the multifractal specific heat (c) for our data. Further, we have simulated $^{28}Si\text{-}AgBr$ collisions using the string hadronic model *UrQMD*. The results obtained for the experimental data are compared with the corresponding results obtained for events simulated using the string hadronic model *UrQMD*.

In chapter V, the scaled factorial cumulant moment method [54] is used to study the presence of dynamical fluctuations in the pseudorapidity distributions of shower particles produced in $^{28}Si\text{-}AgBr$ collisions at $14.6A\ GeV$. This method is similar to the scaled factorial moment method. But the advantage of this method over to the scaled factorial moment method is that it is able to remove the effects of lower order correlations and thus can explicitly focus on the correlations of a given order. We compare our results on the scaled factorial cumulant moments with the corresponding results obtained for

^{28}Si-$AgBr$ collisions simulated using the string hadronic model *UrQMD* and the independent source model.

Further, factorial correlators are studied to get extra information about the local dynamical fluctuations in different domains of phase space for shower particles produced in ^{28}Si-$AgBr$ collisions at 14.6A *GeV*. Using this method, we study bin-bin correlations of shower particles that seem to reflect the presence of larger dynamical fluctuations in comparison to the dynamical fluctuations observed for a single bin using the scaled factorial moment method. The results obtained are compared with the corresponding results for ^{28}Si-$AgBr$ collisions simulated using the string hadronic model *UrQMD*. Finally, we also confront our results with the predictions of the α-model.

After having established in chapter V that multiparticle production in nucleus-nucleus collisions behaves like a fractal system, we study, in chapter VI, the fractal system in detail. As a fractal system, the multiparticle production can be characterized in terms of a very important parameter called Levy stability index μ [55], which tells us about the behaviour of fluctuations in the tail of the multiplicity distributions. Levy stability indices μ have been determined for ^{28}Si-$AgBr$ collisions at 14.6A *GeV* in both the pseudorapidity and azimuthal angle spaces. Further, using the theory of multifractals we have calculated the multifractal spectrum $f(\alpha_q)$ where α_q is the Lipschitz-Holder exponent.

Finally, in chapter VII the conclusions drawn from the results obtained in the present investigation are discussed.

References

1. P. Frier et al., *Phys. Rev.* **74** (1948) 213.
2. J. D. Bjorken, *Proc. Int. Summer Inst. on Theo. Phys. Hamburg* (1973) 93.
3. C.Y. Wong, *Intro. to High Energy Heavy Ion coll.* (1994) 271.
4. J. D. Bjorken, *Phys Rev.* **D 27** (1983) 140.
5. Nucl. Phys.: *The Core of Matter, The Fuel of Stars, National Acadamy Press,* India (1999) 87.
6. P. V. Ruuskanen, *Nucl. Phys.* **A 522** (1991) 255c; *Nucl. Phys.* **A 544** (1992) 169c.
7. K. Kajantie et al., *Phys. Rev.* **D 34** (1986) 2746.
8. E. L. Feinberg, *Nuovo Cim.* **A 34** (1976) 391; *Phys. Lett.* **B 78** (1978) 150.
9. G. Demokos and J. I. Goldman, *Phys. Rev.* **D 23** (1981) 203.
10. S. Chin, *Phys. Lett.* **B 119** (1982) 51.
11. R. C. Hwa and K. Kajantie, *Phys. Rev.* **D 32** (1985) 1109.
12. L.D. Mclerran and T. Tiomela, *Phys. Rev.* **D 31** (1985) 545.
13. J. Cleymans and J. Fingberg, *Phys. Lett.* **B 168** (1986) 405; J. Cleymans et al., *Phys. Rev.* **D 35** (1987) 2153.
14. S. Raha and B. Sinha, *I.J.M.P.* **A 6** (1991) 517.
15. L. H. Xia et al., *Phys. Rev.* **C 41** (1990) 572.
16. C. Y. Wong, *Phys. Rev.* **C 48** (1993) 902.
17. C. Y. Wong, *Int. to High-Energy Heavy-Ion Collisions* (1994) 354.
18. T. Matsui and H. Satz, *Phys. Lett.* **B178** (1986) 416.
19. P. Abreu et al., *Phys. Lett.* **B247** (1990) 137.
20. T. Matsui, *Z. Phys.* **C38** (1988) 245.
21. Nucl. Phys.: The Core of Matter, The fuel of Stars, *National Academy Press, Washington D.C.* (1999) 94.
22. T. Abott et al., *Phys. Rev. Lett.* **64** (1990) 847; *Phys. Rev. Lett.* **66** (1991) 1567.
23. T. Van Hecke et al., *Nucl. Phys.* **A 525** (1991) 227c.
24. H. H. Heckman et al., *LBL – Report* (1977) 7509.
25. I. Otterlund, Lund Univ. *Report LUIP* (1979) 7904.
26. C. F. Powell, P. H. Folwer and D. M. Perkins, *Study of Elementary Particles by the Photographic Method* (Pergamon, London, 1959).

27. V. S. Barashenkov and V. D. Toneev, *Interactions of High Energy Particles and Atomic Nuclei with Nuclei* (Atonizdat, Moscow, 1959).
28. J. Hufner et al., *Phys. Rev.* **C 12** (1985) 1888.
29. M. S. Ahmad et al., *Nucl. Phys.* **A 499** (1989) 821.
30. H. H. Heckman et al., *Phys. Rev.* **C 17** (1978) 1735.
31. R. Bhanja et al.; *Nucl. Phys.* **A 438** (1985) 740
32. P.J. Lindstrom et al., *LBL- Report* (1975) 3650.
33. G. M. Raisbeck and F. Yion, *Phys. Rev. Lett.* **35** (1975) 155.
34. H. H. Heckman and P.J. Lindstrom, *Phys. Rev. Lett.* **37** (1976) 56.
35. A. E. Glassgold et al., *Ann. Phys. (N.Y)* **6** (1959) 1.
36. M. I. Sobel et al., *Nucl. Phys.* **A 251** (1975) 502.
37. W. Scheid et al., *Phys. Rev. Lett.* **32** (1974) 741.
38. G. F. Chapline et al., *Phys. Rev.* **D 8** (1973) 4302.
39. C. Y. Wong et al., *Phys. Lett.* **B 49** (1974) 243.
40. A. A. Andreson et al., *Phys. Rev. Lett.* **35** (1975) 905.
41. H. G. Baumgardt et al., *Z. Phys.* **A 273** (1975) 359.
42. H. G. Baumgardt et al., *Proc. Int. Workshop on Gross Properties of Nuclei and Nuclear Excitation IVth Hirschegg., Austria, AED Conf.* 76-015-000 (1976) 105.
43. A. M. Poskanzer et al., *Phys. Rev. Lett.* **35** (1975) 1701.
44. B. Jakobsson et al., *Nucl. Phys.* **A 276** (1977) 523.
45. D. Gosh et al.; *Can. J. Phys.* **64** (1984) 239.
46. R. Hasan et al.; *Can. J. Phys.* **62** (1984) 442.
47. M. Mohery & N.N. ABD Allah, *IJMP* **E 11** No.2 (2002) 161.
48. B.K. Singh et al., *Nucl. Phys.* **A 570** (1994) 819.
49. A Abdelsalam , *J. Phys. G: Nucl. Part. Phys.* **28** (2002) 1375.
50. R. C. Hwa and J. Pan, *Phys. Rev.* **D 45** (1992) 1476.
51. Ph. Brax and R.Peschanski, *Nucl. Phys.* **B 346** (1990) 65.
52. R. C. Hwa, *Phys. Rev.* **D 41** (1990) 1456.
53. C. B. Chiu, R. C. Hwa, *Phys. Rev.* **D 43** (1991) 100.
54. P. Carruthers et al., *Phys. Lett.* **B 254** (1991) 258.
55. Ph. Brax and R.Peschanski, *Phys. Lett.* **B 253** (1991) 226.

CHAPTER II

Experimental Technique

2.1 Introduction

To study the hadron-nucleus and nucleus-nucleus collisions at relativistic energies, nuclear emulsion is preferred due to its higher capabilities in comparison to bubble chamber and counters. Nuclear emulsion serves as detector as well as target. It is a versatile instrument to detect charged particles and is capable of giving information about their masses, energies, modes of interaction and decay. Information recorded in the form of photograph of the collisions after developing the emulsion stack can be stored for many years by keeping the stack under specified conditions. It is a 4π detector having good spatial resolution and is quite suitable to measure particles' multiplicities and their space angles, azimuthal angles etc.

The composition of nuclear emulsion is heterogeneous. It consists of three basic components: (a) crystals of silver halide, mostly bromide with small admixture of iodine, (b) gelatin and glycerin and (c) water. Glycerin is used as plasticizer, to reduce the brittleness of the emulsion. The compositions of different groups of nuclei in emulsion are such that for *p-Emulsion* collisions about 71% of the collisions occur with heavy nuclei group, AgBr, 25% with light nuclei group (*CNO*) and 4% with hydrogen nuclei [1]. However, for nucleus-nucleus collisions, these number change with the mass of the projectile. The average mass number $<A>$ of nuclei of different groups may be obtained from the equation

$$< A >= \frac{\Sigma N_i A_i}{\Sigma N_i} \qquad 2.1$$

where A_i and N_i represent mass number and the number of atoms of ith element respectively present in a particular group. The average mass numbers $<A>$ of *H*, *CNO* and *AgBr* group of nuclei are 1, 14 and 94 respectively.

When a charged particle traverses through a medium, it excites and ionizes the atoms of the medium due to the coulomb interactions. This results in the loss of energy of the charged particle. If a particle of charge Ze and mass M traverses with velocity v in a medium of atomic number z and mass number A, then the rate of energy loss dE per unit length dx traversed is given by the Bethe's formula:

$$\frac{-dE}{dx} = \frac{4\pi^2 Z^2 e^4}{m_e v^2 A} N \left[z \left\{ \ln\left(\frac{2 m_e v^2}{I(1-\beta^2)} \right) - \beta^2 \right\} - C_k \right], \qquad 2.2$$

where minus sign indicates loss of energy, $\beta = v/c$, N is the number density of the medium, I is the mean ionization potential and m_e is the mass of the electron. C_k denotes the correction factor in case the velocity of the incident particle is comparable with that of the k-shell electron. For a heterogeneous medium like emulsion, the above relation is modified to

$$\frac{-dE}{dx} = \frac{4\pi^2 Z^2 e^4}{m_e v^2 A} \sum_i N_i \left[z_i \left\{ \ln\left(\frac{2m_e v^2}{I_i(1-\beta^2)} \right) - \beta^2 \right\} - C_k \right], \qquad 2.3$$

where i refers to different elements present in the emulsion. It is clear from Equation 2.3 that energy loss does not depend on mass M of the charged particle. Since the logarithmic term varies only slightly with v, the rate of energy loss is directly proportional to the square of the charge (Ze) of the particle and is inversely proportional to the square of its velocity.

Energy lost by the charged particle while passing through emulsion is transferred to the atomic electrons. As a result, the atom goes to an exited state. If the energy gained by the electron is greater than its ionization potential energy then electron becomes free and is librated from the atom. The atom is ionized and the formation of latent image along the path of particle takes place due to the ionization of silver atoms by interactions of the charged particle with silver halide grains. The mechanism of formation of latent image was first explained by Gurney & Mott [2,3]. On immersing the emulsion in a reducing bath, called developer, electrons are transferred from the molecules of developer to the latent images. The interstitial silver ions are then attracted from the body of the crystal and deposited on the latent image specks. In other words, the ionization of the atom changes some of the halide grains in such a way that they, when immersed in a developer, get converted into silver grains, which may easily be distinguished because of their black colour. After the development, the emulsion is put in a fixer, which dissolves all the undeveloped grains while leaving the developed grains unaffected. Due to removal of undeveloped grains a reduction in the thickness of the emulsion take place, which is known as shrinkage. This has to be taken into account while doing the calculations. After fixing, the emulsion is washed and then dried. A series of black grains is formed which is the track of the particle. The number density of the grains forming the track of a charged particle depends on the nature, charge and velocity of the particle. From Equation 2.3 it is

clear that the rate of energy loss is inversely proportional to the square of velocity. As a result, at high velocity small number of grains is formed and vice versa. If the charge of the particle is large, the rate of loss of energy is large, as a result the number density of grains is also large and vice versa. Particles of different ionizing powers produce tracks with different grain densities and thus they appear quite different. The nuclear emulsion has high density and stopping power, about 1700 times the stopping power of standard air. Thus many short-lived particles can be brought to rest in emulsion before they decay.

There are some drawbacks with nuclear emulsion also. As the number of grains developed depends on the charge of the particle passing through the medium, no grain is formed when a neutral particle passes through the emulsion and thus neutral particles cannot be detected in emulsion. Further, the emulsion technique is very slow and it requires a special dark room processing and very careful handling before development. Shielding from the background radiation is necessary. To maintain the shape and rigidity of the stack, it should be kept at low temperature that is below the melting point of gelatin, which is about 45^0. The other drawback of emulsion is that the identification of the target nucleus is not precise.

2.2 Scanning

The process of searching the positions of collisions in the emulsion pellicles is called scanning. The scanning can be performed in two ways: (i) area scanning and (ii) line scanning. In the following sections we discuss these two types of scanning in detail.

2.2.1 Area Scanning

In this type of scanning the upper or lower surface of emulsion pellicle is set in the field of view of the microscope and the positions of collisions in this field of view are recorded. After that next layer of the pellicle is focused in the field of view by rolling the fine focus of the controlled z-motion of the microscope and positions of collisions are recorded. This process is repeated again and again till the full depth of the pellicle is scanned. The field of view is then shifted along the X (or Y) motion of the microscope until the whole X (or Y) –strip of the pellicle is scanned. After that, the field of view is then shifted to the next X (or Y) –strip. In this way the whole emulsion pellicle is scanned.

This method is considerably faster than the line scanning, but there is a chance to miss the collisions having small number of tracks.

2.2.2 Line Scanning

This method of scanning is preferred when a parallel beam of particles is incident perpendicular to the surface of one edge of emulsion stack that is called leading edge and pass parallel to the surface of emulsion pellicle and may leave the opposite side of the stack. In this method, first a primary track is picked up at the leading edge of the emulsion pellicle and is followed until it interacts in emulsion or leaves the pellicle. Similarly all the primary tracks are picked up one by one and followed until they interact or leave the pellicle. Locations of all the primary collisions are recorded. The line scanning is effective in the following conditions of exposure:

- The flux of the beam is not dense and is spread out through out the leading edge.
- The available length for the traversal of beam is large, that is, the beam does not dip much.

2.3 Track Parameters and their Measurements

There are some parameters like range, ionization, grain density, blob density, blob and gap densities and delta ray density, which are used for the identification of a particle and estimation of its energy.

2.3.1 Range

The distance traversed by a charged particle in the unprocessed emulsion before its kinetic energy reduces to zero is called the range of the particle R and is given as

$$R = \int_0^{E_0} \frac{dE}{(-dE/dx)} \qquad 2.4$$

where E_0 is the initial kinetic energy of the particle and $-dE/dx$ represents the rate of energy loss of the particle. But during the development of emulsion stack, the shrinkage and distortion affect the particle range. Therefore these effects must be taken into consideration while computing the true range.

2.3.2 Grain Density

The track of a particle in emulsion appears as minute trails of black grains. The number of grains per unit length is known as grain density. Grain density is found to be a reliable parameter for estimating the ionization caused by a particle. However, the grain density of a track corresponding to the particular value of ionization depends on the degree of development of emulsion. For accurate results the relative grain density g^* of the track of the particle is determined by the relation

$$g^* = \frac{g}{g_0} \qquad 2.5$$

where g is the grain density of the track of the particle and g_0 is the grain density of singly charged relativistic particles in the same emulsion. The grain density is proportional to the ionization loss per unit length, that is,

$$g \propto -\frac{dE}{dx} \propto \frac{Z^2}{\beta^2} f(\beta) \qquad 2.6$$

For singly charged relativistic particles, Z=1, therefore

$$g_0 \propto \frac{1}{\beta^2} f(\beta). \qquad 2.7$$

The value of the parameter g_0 has been determined by measuring the grain density of a number of tracks of singly charged relativistic particles.

2.3.3 Blob Density

If the velocity of the particle is not very large, the grain density of the track of the particle is large. As a result some of the grains in the track are clogged together. A group of unresolvable grains is called blob. The counting of the number of grains in a blob is very difficult. Therefore, the number of individually resolved blobs is counted without estimating the number of grains in the blobs.

Fowler and Perkins [4] suggested the following empirical relation between the blob density B and the grain density g

$$B = g \exp.(-\alpha\, g), \qquad 2.8$$

where α is a parameter which depends on the average grain size and optical resolution of the microscope.

2.3.4 Blob and Gap Density Method

The blob and gap density method is used for estimating the ionization of charged particles having small velocities. A blob is defined as a cluster of grains with no gap visible between them and the length of the gap (L) is defined as the distance between inside edges of two neighbouring blobs.

This method was first introduced by Ceallaigh [5] and latter on extended by Fowler and Perkins [4]. It is based on the fact that gap lengths have an exponential frequency distribution for widely different values of specific ionization that can be written as

$$H(L) = B \exp.(-g\,L), \tag{2.9}$$

where $H(L)$ denotes the density of gaps of length greater than L and B is the blob density. It was shown by Fowler and Perkins [4] that the coefficient g of the exponential is a good measure of the ionization of the track. If H_1 and H_2 denote densities of gaps having length greater than gaps L_1 and L_2 respectively, then the coefficient g can be determined from the following relation,

$$g = \frac{1}{L_2 - L_1} \ln\left(\frac{H_1}{H_2}\right) . \tag{2.10}$$

2.3.5 Delta Ray Density Method

In general, the energies of the ejected electrons from the atoms due to the coulomb interactions with the charged particle passing through the emulsion are very low, but sometimes the energy gained by the ejected electron is greater than the critical value ($\approx 5KeV$). These electrons are able to travel through several crystals and ionize them. As a result, small tracks of these electrons are formed, which are known as δ-rays. Information regarding the charge of a particle can be obtained by measuring δ-ray density along its trajectory. The δ-ray density depends on the resolution of the emulsion, its sensitivity, convention used, charge and velocity of the moving particle. Certain conventions are adopted for counting the number of δ-rays associated with the track of a charged particle.

Dainton et al [6] defined a track as a δ-ray if it contained at least four grains, while Tidman et al [7] defined a grain configuration as a δ-ray if it had a projected range of at least $1.58\mu m$ on the plane of the emulsion from the axis of the track. The number of collisions per unit length in which the energy transfer exceeds the critical value, that is δ-ray density, is given by

$$n_\delta = \text{constt.}\ Z^2 \qquad 2.11$$

where Z is the charge of the particle. If Z=1

$$n_\delta = \text{constant} \qquad . \qquad 2.12$$

Thus the value of the constant can be obtained empirically by counting δ-rays per unit length along the track of a singly charged relativistic particle. The charge of other relativistic particles can be obtained using Equation 2.11.

2.4 Classification of Secondary Particles

Secondary particles produced in each collision are classified by determining their energy loss in emulsion. This is done by counting the number of grains over a certain length ($\sim 100\mu m$). The normalized grain density is defined as $g^* = g/g_o$, where g is the observed grain density of the track of the particle and g_o is the grain density of a track caused by a relativistic singly charged particle such as electron or proton. Therefore, the secondary particles produced in the collision are classified as shower, grey, black particles and projectile fragments according to the following standard emulsion criteria:

- Shower particles: These are singly charged relativistic particles with relative ionization $g^*<1.4$. The ionization cut corresponds to the particles' velocities $\geq$ 0.7c. These are produced particles (mainly pions) with energies greater than 400 MeV. Their number is denoted as N_s.
- Grey particles: These are the particles with relative ionization $1.4 \leq g^* < 10$ and range in emulsion $L > 3$ mm. This corresponds to the particles' velocities in the interval 0.23c to 0.7c. They are singly charged particles. These particles are mainly protons from the target having energies in the range 26 MeV – 400 MeV. Their number is denoted as N_g.
- Black particles: These are the particles with relative ionization $g^* \geq 10$ and the range $L \leq 3$ mm. These are the spectator target protons with energies less than 26 MeV and multi-charged target fragments. Their number is denoted as N_b.

- Projectile Fragments: These are fragments of projectile nucleus with range $Z \geq 2$ and have the same momentum per nucleon as the projectile nucleus. The ionization of the fragments remains constant over a wide range but changes with their charges. They are collimated in a narrow cone in the forward direction and can be very easily separated from the target fragments. Their number is denoted as N_f.

2.5 Angle Measurement of Secondary Particles

Except some shower particles and projectile fragments, the tracks of secondary particles are generally well separated and projected and dip angles are measured directly with the help of the goneometer and by Z-motion of the microscope. The coordinate method is used for angle measurement of the tracks which are not well separated or are collimated in a narrow cone in the forward direction.

2.5.1 Projected Angle

To measure the projected angle θ_P, the primary track of the collision (star) is aligned parallel to the X-motion of the microscope. The vertex of the collision is focussed at the center of the graticule of the goneometer. Now the primary beam track is aligned with one of the reference line of the goneometer. After that by rotating the goneometer, the secondary tracks are aligned one by one and goneometer reading are taken for the projected angle with respect to the reference line.

In the coordinate method, the vertex of the collision is focussed at the center of the graticule of the goneometer and readings of X-motion, Y-motion and Z-motion of the scale (say X_0, Y_0, Z_0) are taken. The stage is then moved forward to at least ten fields of view following the track very carefully. A point on the track is focussed and readings of X, Y and Z motion (say X_1, Y_1, Z_1) are taken. Then the projected angle θ_P is calculated using the following relation

$$\theta_P = \tan^{-1}\left(\frac{\Delta Y}{\Delta X}\right) \qquad 2.13$$

where $\Delta X = X_1 - X_0$ and $\Delta Y = Y_1 - Y_0$.

2.5.2 Dip Angle

In this method the track, for which the dip angle is to be measured, is aligned along the scale of eyepiece graticule. The dip is measured by moving the *Z*-motion of the microscope with respect to the dip of the star's vertex for a projected length *L* of the track in *X*-*Y* plane. Now the dip angle is calculated by using the relation

$$\theta_d = \tan^{-1}\left(S.\frac{dip}{L}\right) \qquad 2.14$$

where *S* is the shrinkage factor. In terms of the coordinates

$$\theta_d = \tan^{-1}\left(S.\frac{\Delta Z}{L}\right) \qquad 2.15$$

where $L = \sqrt{\Delta X^2 + \Delta Y^2}$.

2.5.3 Space Angle

It is the angle of the secondary track with respect to the forward direction of the primary track. It is calculated using the relation

$$\cos\theta = \cos\theta_p \times \cos\theta_d \qquad 2.16$$

where θ denotes the space angle.

2.5.4 Azimuthal Angle

This is the angle of projection of the secondary track in the *Y*-*Z* plane with respect to the *Y*-axis and can be calculated using the following relation

$$\cos\varphi = (\sin\theta_p \times \cos\theta_d)/\sin\theta \ . \qquad 2.17$$

2.6 Rapidity Variable

Rapidity (*Y*) is a useful parameter in the study of relativistic nucleus-nucleus collisions. It is defined as

$$Y = \tanh^{-1}(\beta_L) \qquad 2.18$$

$$Y = -\frac{1}{2}\ln\frac{1+\beta_L}{1-\beta_L} \qquad 2.19$$

where β_L is the velocity of the particle along the incident beam. For relativistic particles (like pions) emitted after the collision, the rapidity is approximated by a parameter, which

is known as pseudorapidity (η) variable. Using Equation 2.19 and taking approximations for relativistic particles, we get

$$Y \to \eta = -\ln \tan \theta/2 \qquad 2.20$$

where θ is the space angle. The advantage of transforming the rapidity into pseudorapidity is that it is a measurable quantity. But the rapidity cannot be measured in emulsion experiments.

2.7 Theoretical Models of Nucleus-Nucleus Collisions

Various models have been proposed [8-21] to describe the mechanism of particle production and to find as to how various parameters of the system behave during the multiparticle production in high energy nucleus-nucleus collisions. Different models describe different aspects of the collision and are used to explain the experimental results. To find the signals of phase transition that is expected in relativistic nucleus-nucleus collisions, some event generators like *FRITIOF*, *UrQMD* etc. have also been developed to simulate nucleus-nucleus collisions. All these event generators assume no Q.G.P. formation and help in understanding the background signals. In the following sections, some of these models and event generators are briefly described.

2.7.1 Participant - Spectator Model

This model is very simple and shows good agreement with experimental data. According to this model, during a nucleus-nucleus collision some nucleon groups, which are located in the overlapped regions of the projectile and target, will just pass through keeping their initial velocities. These nucleon groups are called spectators. On the other hand, in the overlapped region, nucleons interact violently with each other and it is assumed that projectile participants transfer all of their momentum to the effective centre of mass system of all the participant nucleons forming a fireball, which moves forward in the laboratory frame at a velocity intermediate between those of the target and the projectile. This picture is called the participant spectator or fireball model [22] and the three regions produced are known as the participant region, the projectile spectator region and the target spectator region. The energy density in the fireball is extremely high and consequently, it may be treated as an ideal gas, whose properties may be determined by

the laws of thermodynamics. If A_T and A_P represent the number of nucleons in the target and projectile nucleus respectively, the geometrical cross section is given by

$$\sigma_g = \pi r_o^2 (A_T^{1/3} + A_P^{1/3})^2 \qquad 2.21$$

where r_o = 1.0 – 1.2 *fm*. If a proton inside the projectile hits the target, it falls in the participant group, otherwise remains as a spectator. Therefore, the average number of participant protons from the projectile nucleus is approximately given by Z_{proj} (number of protons in the projectile nucleus) times the ratio of the target cross section to the geometrical cross section (σ_g), given as [23,24]

$$\left\langle Z_{proj}^{part} \right\rangle = Z_{proj} \frac{\pi r_0^2 A_T^{2/3}}{\sigma_g} \qquad 2.22$$

$$= Z_{proj} \frac{A_T^{2/3}}{\left(A_P^{1/3} + A_T^{1/3} \right)^2} \qquad 2.23$$

Similarly, the average number of participants from the target nucleus is

$$\left\langle Z_{tar}^{part} \right\rangle = Z_{tar} \frac{A_P^{2/3}}{\left(A_P^{1/3} + A_T^{1/3} \right)^2} \qquad 2.24$$

where Z_{tar} represents number of protons in the target nucleus.

Thus the total number of participant protons Z_{eff}^{part} is given by

$$Z_{eff}^{part} = \left\langle Z_{proj}^{part} \right\rangle + \left\langle Z_{tar}^{part} \right\rangle \qquad 2.25$$

$$= \frac{Z_{proj} A_T^{2/3} + Z_{tar} A_P^{2/3}}{\left(A_P^{1/3} + A_T^{1/3} \right)^2} \qquad 2.26$$

Similarly, the total number of protons of target and projectile spectators are respectively given as

$$Z_{eff}^{proj.spectator} = Z_{proj} - \left\langle Z_{proj}^{part} \right\rangle \qquad 2.27$$

$$= \frac{Z_{proj}\left(A_P^{2/3} + 2A_P^{1/3}A_T^{1/3}\right)}{\left(A_P^{1/3} + A_T^{1/3}\right)^2} \qquad 2.28$$

$$Z_{eff}^{tar.spectator} = Z_{tar} - \left\langle Z_{tar}^{part} \right\rangle \qquad 2.29$$

$$= \frac{Z_{tar}\left(A_T^{2/3} + 2A_P^{1/3}A_T^{1/3}\right)}{\left(A_P^{1/3} + A_T^{1/3}\right)^2} \qquad 2.30$$

The merits of this model are its simplicity and non-involvement of the adjustable parameters.

2.7.2 Firestreak Model

The nuclear firestreak model was proposed by Myers [25]. It is a generalization of the fireball model. It explicitly includes chemical equilibrium among the hadronic species as well as thermal equilibrium. In this model, the overlapping volume of the colliding nuclei is divided into a series of tubes parallel to the direction of projectile beam. According to this model, each projectile tube interacts only with that target tube which lies directly in its path and forms a fire streak. Tube-tube collisions are treated as in the fireball model assuming thermalization to occur in each of the tube-tube collisions separately. At every impact parameter the energy available for thermalization in each tube individually is to be calculated. Production of protons can be described by this model.

The nuclear matter in each case can be treated as a thermodynamic system in chemical equilibrium. As a natural consequence of the fire streak geometry, there exists a temperature gradient across the fireball. Furthermore in the model, the angular momentum is conserved, whereas in the case of nuclear fireball model it is not. The energy range of this model is limited. It is not expected to work at very low energies, where the whole target and projectile may combine and subsequently decay. At extremely high energies the target may become partially transparent to the projectile due to fall of the nucleon-nucleon cross section. The only free parameter in this model is the freeze out density below which the hadrons stop interacting.

2.7.3 Hydrodynamical Model

The first hydrodynamic model for relativistic collisions was the Fermi-Landau model [26] describing *p-p* collisions at very high energies. Later Hydrodynamical models [27-29] have been developed for nucleus-nucleus collisions also. According to these models, the target and projectile nuclei instantaneously merge just after the collision and attain equilibrium by forming a drop of nuclear fluid whose subsequent evolution in time is governed by standard laws of thermodynamics. The outward flow of fluid is primarily along the axis of the beam of nuclei and most of the particle production takes place during the initial collision when the projectile and target nuclei merge together. And after that the matter may undergo hydrodynamical expansion. The two nuclear fluids, projectile fluid and target fluid are considered in these models. The behaviour of each of these fluids is determined by the fluid dynamics, conservation equation for nucleon number, momentum and energy. Additional terms are introduced into these equations to allow for a coupling of two fluids by means of energy and momentum transfer. There are some constraints for the validity of fluid dynamics. They are: (i) the system comprising of the two colliding nuclei must contain a large number of degrees of freedom, (ii) the collision must last a sufficiently long time for local equilibrium to occur and (iii) either the bombarding energy must low or the interaction strength between the two nuclei must be large. Constraint (iii) ensures that the two nuclei merge instantaneously to form a single fluid.

2.7.4 Wounded Nucleon Model

Wounded nucleon model is the simplest and historically the first predictor of multiparticle production in nucleus-nucleus collisions. If n_{AA} represents particle multiplicity in nucleus-nucleus collisions at a given energy then according to this model

$$n_{AA} = \frac{1}{2} W \times n_{PP}, \qquad 2.31$$

where W is the average number of participating or wounded nucleons and n_{PP} represents the average proton multiplicity at an equivalent energy per nucleon. The number of wounded nucleons contains all the geometrical effects, i.e. the effects of nuclear radii, density and impact parameter and it can be given in terms of interaction cross sections σ [30,31] as

$$W = A_T \frac{\sigma_{NP}}{\sigma_{PT}} + A_P \frac{\sigma_{NT}}{\sigma_{PT}}, \qquad 2.32$$

$$= W_T + W_P \qquad 2.33$$

where subscript P and T denote projectile and target respectively, N denotes an individual nucleon. σ_{PT} is the total inelastic hadronic cross-section for the projectile nucleus interacting with the target [32], and σ_{NP} and σ_{NT} are the corresponding nucleon-nucleus cross-sections. A_P and A_T denote the mass numbers of projectile and target nuclei respectively. In Equation 2.33 the terms W_T represents the number of wounded target nucleons where

$$W_T = A_T \frac{\sigma_{NP}}{\sigma_{PT}} \qquad 2.34$$

and W_P represents the number of wounded projectile nucleons where

$$W_P = A_P \frac{\sigma_{NT}}{\sigma_{PT}} \qquad 2.35$$

In the central nucleus-nucleus collisions, the number of total wounded nucleons W, which depends on the cross sections that are functions of the maximum impact parameter b_{max}, is determined with the help of the maximum impact parameter. The value of b_{max} for the central nucleus-nucleus collisions can be determined from the partial cross section as given by

$$\sigma_{par} = \pi b_{\max}^2 = \sigma_{PT} \frac{N_{central}}{N_{total}}, \qquad 2.36$$

where $N_{central}$ is the number of central collisions in the data sample and N_{total} is the total number of nucleus-nucleus collisions obtained from a minimum bias scan of emulsions. The wounded nucleon model predicts that the cross-section for the excited nucleons due to various interactions is assumed to be the same as that for the unexcited nucleons. Using above assumptions, the number of target and projectile collisions may be obtained by the relations

$$\upsilon_T = A_T \frac{\sigma_{NN}}{\sigma_{NT}} \qquad 2.37$$

and $$\upsilon_P = A_P \frac{\sigma_{NN}}{\sigma_{NP}} \qquad 2.38$$

where ν_T and ν_P denote the average number of target and projectile collisions respectively, σ_{NN} is the nucleon-nucleon production cross section. Further the total number of collisions caused by the projectile nucleons with the target nucleons may be obtained from the relation

$$\upsilon = W_P \upsilon_T = W_T \upsilon_P \qquad 2.39$$

It has been reported [31-33] that the predictions of the wounded nucleon model are quite compatible with results obtained for experimental as well as *FRITIOF* data at *SPS* energies.

2.7.5 Inside-Outside Cascade Model

During a head on collision of two equal nuclei in the center of mass frame, a substantial Lorentz contraction occurs in the longitudinal direction. We can represent the two colliding nuclei by two thin disks. For simplicity, consider the collision at extremely high energy so that the longitudinal thickness of the nuclei can be neglected and the longitudinal coordinates of the nucleon of the same nucleus can be approximated to be the same.

Figure 2.1 shows the configuration of the two nuclei before collision in the center of mass system. The projectile nucleus P comes from Z=-∝ with a velocity close to the speed of light and meets the target nucleus T which comes from Z=+∝ also with the speed close to the speed of light. They meet at Z=0 and t = 0, where collisions of the nucleons of the projectile nucleus with the nucleons of the target nucleus take place. Then at some later time, t, the system can be seen as composed of separate projectile and target remnant regions, with a cylinder of hot material stretching between them. We can imagine a thin slice of this stretching cylinder, chosen so that the material within the slice is all moving at approximately the same velocity along the beam axis. In this model, Bjorken [34] assumed that shortly after the collision equal amounts of energy are deposited in each of these frames. This initial condition allows the evolution of the system to be described by simple hydrodynamic equations. With these assumptions he showed that the entropy S remains constant per unit rapidity, preserving a record of the early conditions in the collision [34,35].

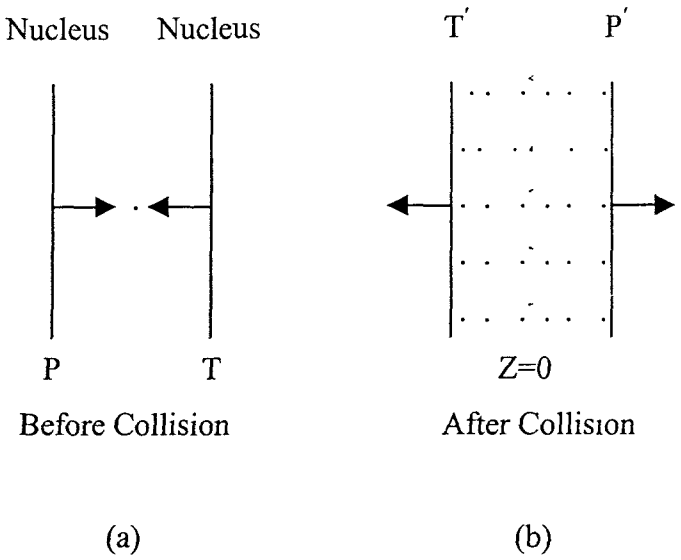

Figure 2.1: (a) The configuration of two colliding nuclei P and T before collision (b) The configuration after collision with energy deposited in the region around Z ~ 0.

2.8 Event Generators

2.8.1 *FRITIOF*

To observe the signals from *QGP* we need non-*QGP* background. For this purpose some event generators are built according to non-*QGP* models based on known physics. *FRITIOF* is such a non-*QGP* model, which has succeeded in describing many experimental data on hadron-hadron collisions from low energies at *ISR* up to top of *SPS* energy [36] by careful treatment of gluon radiation and hard parton scattering. In this model, during the collision, two hadrons are excited due to momentum transfer and the highly excited string like objects (colour dipole) are allowed to emit gluons until transverse momentum of emission of gluon reaches a given minimal cut. Then the formed objects are fragmented into final hadrons. The *FRITIOF* model has also been developed to describe hadron-nucleus and nucleus-nucleus collisions by assuming that the reaction is a superposition of hadron-hadron collisions in which geometry of nucleus plays an important role. This picture is based on the fact that the global features in nucleus-nucleus collisions are satisfactorily explained by the collision geometry together with independent hadron-hadron collisions.

2.8.2 *UrQMD*

The Ultrarelativistic Quantum Molecular Dynamics (*UrQMD*) model is based on transport theory, which played an important role in the interpretation of experimental results and in predicting new interesting effects in relativistic nucleus-nucleus collisions. The *UrQMD* model is the first microscopic model, which attempts to include the colour coherent phenomena [37,38]. It is based on a colour string formation and resonance decay. It is designed to study multifragmentation, correlations, rapidity distributions etc. It can be used to simulate the data for nucleus-nucleus collisions in the energy range from *SIS* (Schwer Ionen Synchrotron) to *RHIC* (Relativistic Heavy Ion Collider). It runs on various *UNIX* based computing platforms. The program is written in *FORTRAN*.

References

1. B. Andersson et al., *Phys. Lett.* **B 73** (1978) 343.
2. R. W. Gurney and N. F. Mott, *Proc. Roy. Soc. (London)* **A 164** (1938) 151.
3. N. F. Mott and R. W. Gurney, *Elec. Proc. In Ionic Crys. 2nd ed., Clarendon Press, Oxford* (1948).
4. Fowler and Perkins, *Phil. Marg.* **46** (1955) 587.
5. C. O. Ceallaigh, *CERN Report,* **B. S.** (1954) 11.
6. A. D. Dainton, P. H. Fowler and D. W. Kent, *Phil. Marg. Sec.7* **43** (1952) 729.
7. D. A. Tidman, E. P. George and A. J. Herz, *Proc. Roy. Soc. (London)* **A 66** (1953) 1019.
8. A. Z Mekjian, *Phys. Rev.* **C 17** (1978) 1051.
9. A. Z Mekjian, *Phys. Lett.* **B 89** (1980) 177.
10. S. Das Gupta and A. Z Mekjian, *Phys. Report* **72** (1981) 131.
11. J. P Bondrof et al., *Nucl. Phys.* **A 296** (1978) 320.
12. P. J Siemens and J.O Rasmussen, *Phys. Rev. Lett.* **42** (1979) 844.
13. H. Stocker et al., *Phys. Rev. Lett.* **44** (1980) 725.
14. Y. Yariv and Z. Fraenkel, (i) *Phys. Rev.* **C 20** (1979) 2277.
    (ii) *Phys. Rev.* **C 24** (1981) 488.
15. J. Cugnon, *Phys. Rev.* **C 22** (1980) 1885.
16. J. Cugnon et al., *Nucl. Phys.* **A 360** (1981) 444.
17. I. Utterlund and E. Sterlund, *Lund Univ. Report LUIP-7806* (1978).
18. M. Sandel et al., *Phys. Rev.* **C 20** (1979) 744.
19. R. Hagedron and J. Rafelski, *Phys. Lett.* **B 97** (1980) 136.
20. A. Capetta et al., *LBL-Report 16281* (1983).
21. A. Bialas and W. Czyz, *Proc. Workshop on Future Relativistic Heavy Ion* Experiments, *Darmstadt* (1980).
22. J. Gosset et al., *Phys. Rev.* **C 18** (1978) 844.
23. R. J. Glauber and Matthial, *Nucl. Phys.* **B 21** (1970) 135.
24. S. Nagamiya, *Nucl. Phys.* **A 335** (1980) 517.
25. W. D. Myers, *LBL-Report 6569*; *Nucl. Phys.* **A 296** (1978) 177.
26. L. D. Landau, *Izv. Akad. Nauk. SSSR,* **17** (1953) 51.
27. A. A. Amsden et al., *Phys. Rev.* **C 15** (1977) 2509.

28. V. S Barashenkov et al., *UPS Fiz Nauk* **109** (1973) 93.
29. A. A. Amsden et al., *Phys. Rev. Lett.* **35** (1975) 905.
30. M. A. Nasr, *Ph. D. Thesis* submitted to *Aligarh Muslim University*, India (1995).
31. A. Bialas, M. Bleszynski and W. Czyz, *Nucl. Phys.* **B 111** (1976) 461.
32. H. Sumiyoshi, *Phys. Lett.* **131** (1983) 241.
33. A. Dabrowska et al., *Phys. Rev.* **D47** (1993) 1751.
34. J. D Bjorken, *Phys. Rev.* **D27** (1983) 140.
35. David H. Skelding, *Ph. D. Thesis submitted to University of Washington, USA* (1996)
36. Ding Linkai and Evert Stenlund, *Phys. Lett.* **B** (1988) 204.
37. M. Bleicher et al., *J. Phys.* **G 25** (1999) 1859.
38. S. A. Bass et al., *Prog. Part. Nucl. Phys.* **41** (1998) 225.

CHAPTER III

General Characteristics of ^{28}Si-Emulsion Collisions at 14.6A GeV

3.1 Introduction

One of the aims of the experimental high energy physicists is to observe the formation of a new state of matter, the quark-gluon plasma. Quantum chromodynamics predicts that at extremely high density the hadronic matter would undergo a phase transition to the quark-gluon plasma. Conditions of high density could be achieved in nucleus-nucleus collisions at relativistic energies. Therefore, nucleus-nucleus collisions at relativistic energies offer a unique environment for the creation and study of the quark-gluon plasma in the laboratory. A special feature of phase transition is that the system experiences large fluctuations in thermodynamical quantities such as temperature and entropy. In nucleus-nucleus collisions these thermodynamical quantities can be studied through the experimentally observed quantities such as the average transverse momentum and multiplicity of the produced particles. However, in order to observe these 'signals' for the formation of the quark-gluon plasma, we must have a thorough understanding of multiparticle production and nuclear fragmentation process. This is essential in order to have a clear picture of the background on which the signals regarding the formation of the quark-gluon plasma are expected to be found. Thus it is important to study different aspects of nucleus-nucleus collisions at relativistic energies. The availability of heavy ions with relativistic energies at CERN, Dubna and BNL made it possible to study nucleus-nucleus collisions in a systematic manner.

In this chapter, we report the results on the general characteristics of ^{28}*Si-Emulsion* collisions at 14.6*A GeV*. The multiplicities of shower, grey, black and heavily ionizing particles and their correlations have been studied. The angular distributions of shower, grey and black particles have been studied and compared with the corresponding results for projectiles of different energies. To study the dependence on projectile energy, the multiplicity distributions of shower, grey, black and heavily ionizing particles for our data have been plotted and compared with the distributions obtained for ^{28}*Si-Emulsion* collisions at 4.5*A GeV* [1]. Further, to observe the validity of the negative binomial distribution for our data, we fitted the multiplicity distributions of shower particles in different intervals of pseudorapidity and azimuthal angle spaces with the negative binomial distribution. We have also investigated the effect of mass and energy of the projectile on the forward-backward multiplicity ratios for different particles. Multiplicity distributions in the backward hemisphere have been studied and fitted with

exponential law formula $P(N_i^B) = P_i e^{-\lambda_i^B N_i^B}$ [2], where i stands for shower or grey particles. The above relation represents the fundamental equation of decay of an excited system. Finally, multiplicity correlations in the forward-backward hemispheres have been studied.

3.2 Detection of Events

In the present work an emulsion stack exposed to $14.6AGeV$ silicon beam from Alternating Gradient Synchrotron at Brookhaven National Laboratory has been used. The dimensions of emulsion pellicles were $16.0 \times 10.0 \times 0.06$ cm^3. The sensitivity of emulsion was about 24 grains per $100\,\mu m$ for singly charged particles with minimum ionizations.

Primary collisions were picked up by along the track scanning. Each primary track was followed until it collided or left the pellicle. Collisions lying within 3 *mm* of the leading edge were not recorded. Each emulsion stack was doubly scanned along the tracks, fast in the forward direction and slowly in the backward one. 1107 inelastic collisions of ^{28}Si were picked up by following 12258.8 cm of primary beams, leading to the collision mean free path of ^{28}Si ions in emulsion λ=11.07±0.48 *cm*. Scanning was carried out with almost 100% efficiency. Collisions that were within 20 μm from the top or bottom surface of the emulsion stack or caused by primaries making an angle greater than 2^0 with the mean beam direction were rejected. In this way 784 inelastic collisions (events) of 14.6*A GeV* silicon ions in nuclear emulsion were recorded.

In each event polar and azimuthal angles of all secondary particles were measured under high magnification as already mentioned in chapter II. The accuracy in the measurement of polar angle was 1 *mrad* and in the measurement of azimuthal angle it was about 5^o. Depending on ionization, all secondary tracks emitted from the collision vertices were classified as shower, grey, black and projectile fragments using the commonly accepted emulsion terminology described in chapter II.

3.3 Mean Free Path

Using the Bradt-Peters relation for nucleus-nucleus cross sections [3], the following relationship between the charge Z of a projectile and its mean free path λ_Z can be obtained

$$\lambda_Z = \wedge Z^{-b}, \qquad 3.1$$

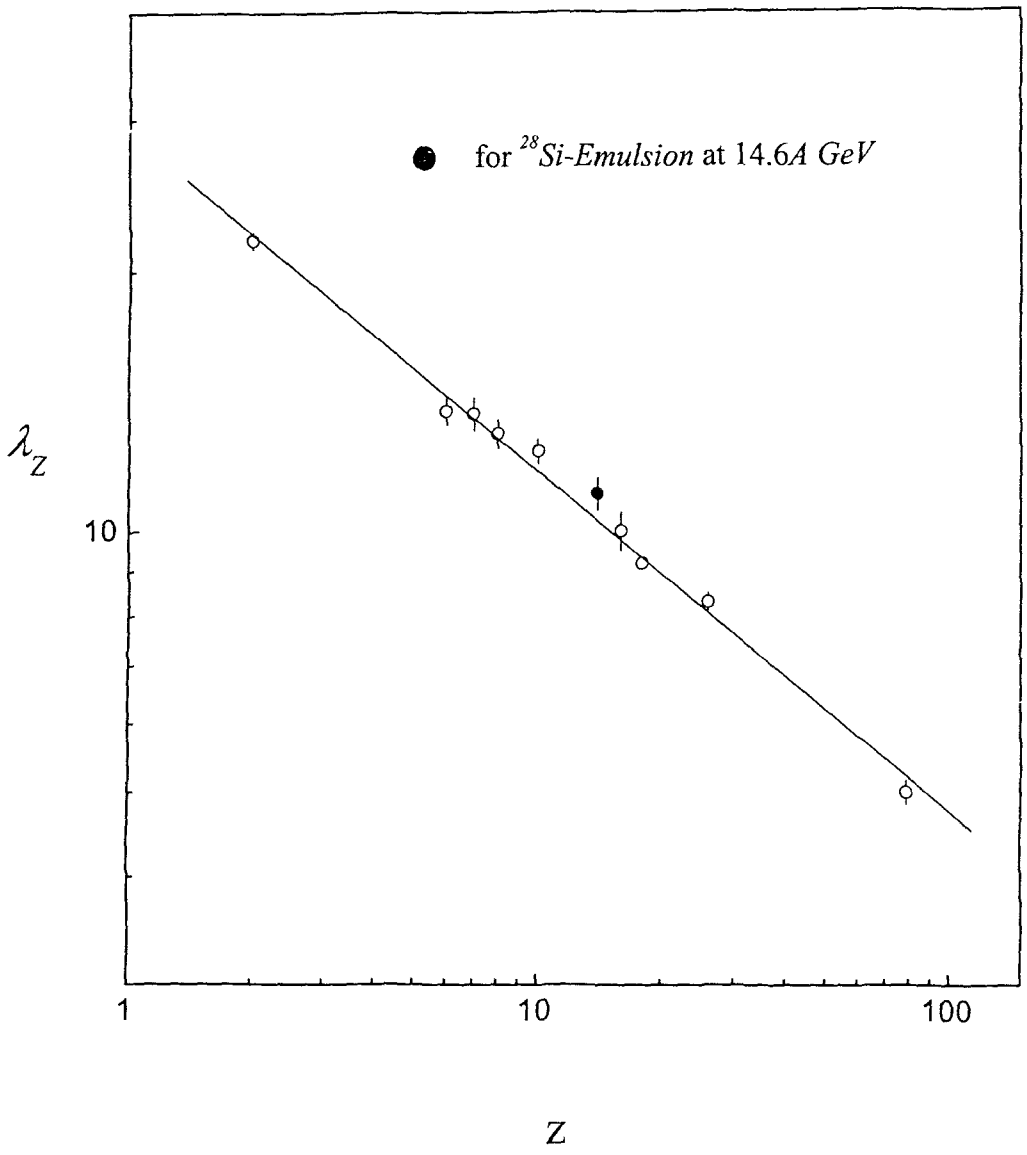

Figure 3.1: Mean free path λ_Z versus charge Z plot for different projectiles in nuclear emulsion on log-log scale.

where λ_Z is the mean free path of the projectile of charge Z and $\wedge$ is the charge independent mean free path. In Figure 3.1, open circles represent the experimental values of the mean free path of various projectiles in nuclear emulsion. The data points for different projectiles have been taken from references [2,4-9]. Solid circle represents our data point for silicon (Z=14). In the figure the solid straight line represents the fitting of the experimental points according to Equation 3.1 on log-log scale. The experimental data fit well with the above equation for $\wedge = 28.84 \pm 1.02$ and $b = 0.39 \pm 0.01$. These values are in agreement with the corresponding values reported by other workers [1,10,11].

3.4 Probability of Collisions with Different Target Groups

The exact identification of target in an emulsion experiment is difficult as the medium is composed of *H*, *C*, *N*, *O*, *Ag* and *Br* nuclei. Collisions were divided into three target groups as *H*, *CNO* and *AgBr*. Usually events with number of heavy particles $N_h \leq 1$ are classified as collisions with hydrogen (target mass $A_T = 1$), events with $2 \leq N_h < 8$ as collisions with light nuclei *CNO* ($\langle A_T \rangle = 14$) and events with $N_h \geq 8$ as collisions with heavy nuclei *AgBr* ($\langle A_T \rangle = 94$). In this method the separation of events ($N_h \geq 8$) for *AgBr* target events is quite accurate, but in events with $2 \leq N_h < 8$, there is an admixture of *CNO* target events and peripheral *AgBr* target events. To overcome this, events were classified into different target groups using the following criteria [12]:

AgBr events: (i) $N_h \geq 8$ or (ii) $N_h < 8$ and at least one track with $R \leq 10\,\mu m$ and no track with $10 < R \leq 50\,\mu m$

CNO events: $2 \leq N_h < 8$ and no track with $R < 10\,\mu m$

H events: (i) $N_h = 0$ or (ii) $N_h = 1$ but falling in none of the above categories.

In this way out of 784 inelastic collisions in *Emulsion*, 360 events belong to *AgBr* target group, 287 events belong to *CNO* target group and 137 events belong to *H* target. The percentages of occurrence of collisions with different target groups in emulsion have been calculated and are given in Table 3.1 along with the corresponding values obtained for collisions of various projectiles in emulsion at different energies taken from references

Table 3.1: Percentage of occurrence of collisions with various groups of nuclei in emulsion.

Projectiles	Energy *A GeV*	Target			Ref.
		H	*CNO*	*AgBr*	
^{1}p	3.0	18.00	49.50	32.50	13
^{4}He	4.5	21.03	40.02	38.55	14
^{6}Li	4.5	7.00	32.00	61.00	15
^{12}C	4.5	22.20	31.35	46.45	5
^{14}N	2.1	12.70	32.90	54.40	16
^{16}O	2.1	13.00	29.00	58.00	17
^{24}Mg	4.5	11.03	34.98	53.99	18
^{28}Si	4.5	18.12	28.35	53.52	19
^{28}Si	14.6	17.47	36.60	45.91	*
^{56}Fe	1.7	14.33	34.12	51.55	20

* Present work

[5,13-20]. The result shows that the reaction cross-section or the percentage of collisions with different target groups depends weakly on the mass of the projectile.

3.5 Multiplicities of Secondary Particles

When a high energy projectile hits a nucleus, a number of charged and uncharged particles are produced. The emergence of fast particles producing shower and grey tracks in nuclear emulsion occurs in a very short time after the instant of impact of the projectile. Thereafter, the nucleus remains in an excited state for a quite long time on nuclear time scale. Finally, the nucleus de-excites resulting in the emission of large number of nucleons and other heavy fragments. The particles emitted through this process generally appear as black tracks in emulsion. The total number of grey and black tracks is known as heavy tracks.

Table 3.2 presents the mean multiplicities of shower $<N_s>$, grey $<N_g>$ and black $<N_b>$ particles for ^{28}*Si-Emulsion* collisions at 14.6*A GeV* along with the corresponding results for collisions of various projectiles in emulsion [5,14,19,21-25]. It can be seen from the table that $<N_b>$ remains practically unchanged from proton to iron, indicating the approximate equality of residual nucleus excitations.

The average multiplicities of shower (N_s), grey (N_g), black (N_b), heavy (N_h) particles and total charged particles ($N_{ch} = N_h + N_s$) for collisions with different target groups in emulsion are given in Table 3.3 along with the corresponding results for ^{28}*Si-Emulsion* collisions at 4.5*A GeV* [19]. From the table one can see that the average multiplicity of all types of particles increases with increase in the mass of the target nucleus, whereas the average multiplicity of shower particles increases with increasing projectile energy also. The dependence on the target mass can be parameterized by the power law relation [19]

$$<N_i> = a_i <A_T>^{b_i} \qquad 3.2$$

where $i = s$, g or b (shower, grey or black particles) etc. In Figures 3.2 (a) - (e) solid circles represent the plots of $<N_s>$, $<N_g>$, $<N_b>$, $<N_h>$ and $<N_{ch}>$ versus $<A_T>$ respectively and smooth curves with solid line represent the fitting of the experimental points with Equation 3.2 for the corresponding plots. The values of fitting parameters a_i and b_i are given in Table 3.3. From the table it is clear that the values of b_i for ^{28}*Si-Emulsion* collisions at 14.6*A GeV* are almost comparable to those obtained by Mohery and Abd-Allah [19] for ^{28}*Si-Emulsion* collisions at 4.5*A GeV*. The values of b_s and b_g for our

Table 3.2: Average multiplicities of secondary particles in hadron-nucleus and nucleus-nucleus collisions.

Collisions	Energy *A GeV*	$<N_b>$	$<N_g>$	$<N_s>$	Ref.
^{1}*p-Emulsion*	4.5	3.77±0.08	2.81±0.06	1.63±0.02	21
^{4}*He-Emulsion*	4.5	4.70±0.20	4.70±0.20	3.90±0.10	14
^{12}*C-Emulsion*	4.5	4.51±0.10	5.96±0.13	7.77±0.17	5
^{14}*N-Emulsion*	2.1	4.57±0.21	5.29±0.31	8.85±0.28	22
^{16}*O-Emulsion*	4.5	4.88±0.29	7.60±0.60	10.50±0.60	23
^{24}*Mg-Emulsion*	4.5	7.74±0.14	12.29±0.20	12.37±0.22	24
^{28}*Si-Emulsion*	4.5	5.66±0.18	7.14±0.25	12.01±0.32	19
^{28}*Si-Emulsion*	14.6	5.49±0.19	3.85±0.17	18.72±0.73	*
^{56}Fe-*Emulsion*	1.7	4.45±0.14	8.71±0.34	13.30±0.40	25

* Present work

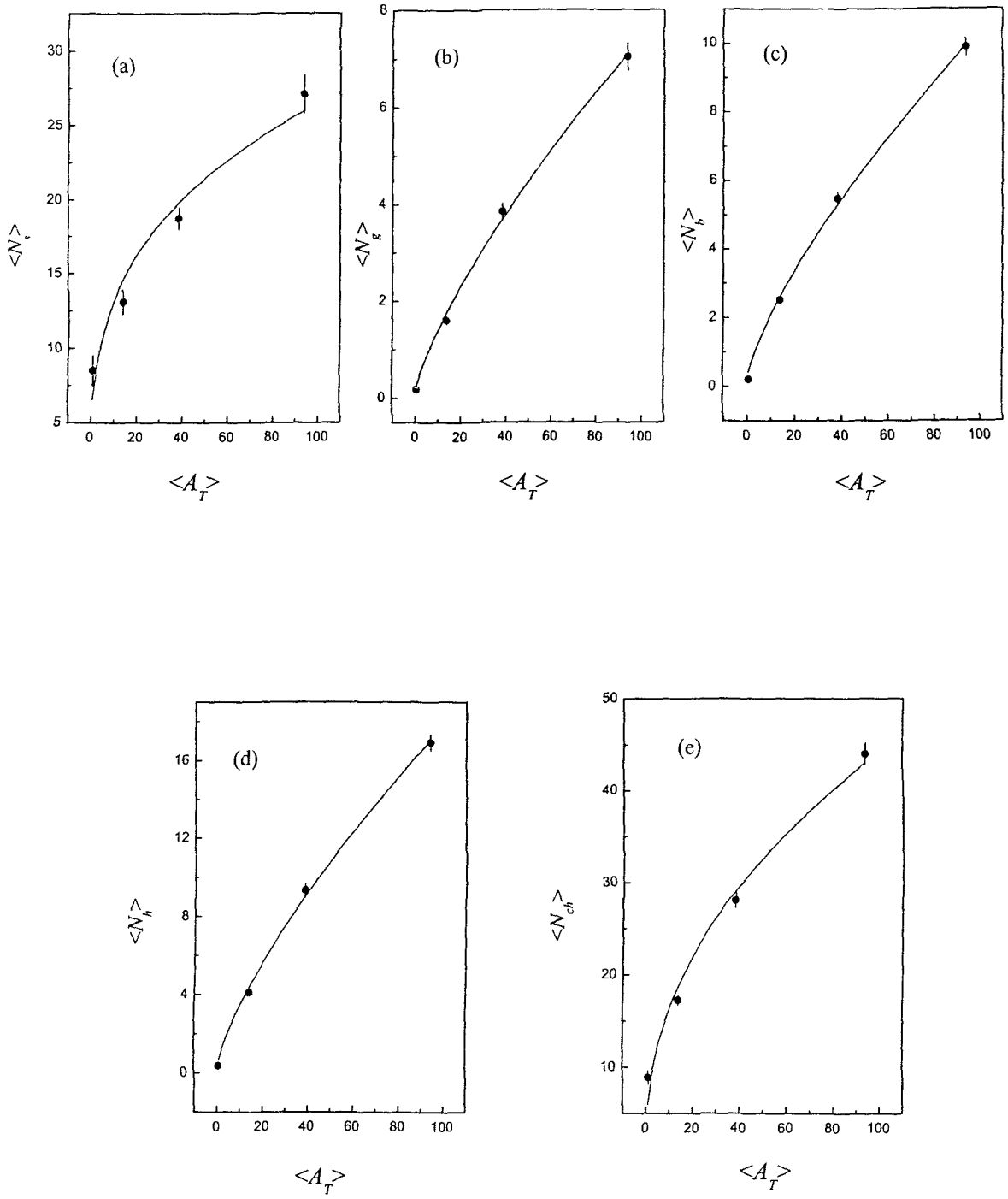

Figure 3.2: (a)-(e) represent $\langle N_i \rangle$ versus $\langle A_T \rangle$ plots, where i=s, g , b, h and ch respectively for ^{28}Si collisions with different target groups in emulsion at 14.6A GeV. Smooth curve in each plot represents fit to the data using Equation 3.2.

Table 3.3: The average multiplicities of charged secondary particles emitted in collisions of ^{28}Si nuclei with different target groups at 4.5*A GeV* and 14.6*A GeV*.

Energy *A GeV*	$<N_t>$	Target				$<N_t> = a_t <A_T>^{b_t}$		Ref.
		H	*CNO*	*AgBr*	*Emulsion*	a_t	b_t	
4.5	$<N_s>$	2.94±0.22	7.50±0.32	19.41±0.52	12.01±0.32	2.68±0.16	0.40±0.01	19
	$<N_g>$	0.49±0.04	2.09±0.09	13.91±0.30	7.14±0.25	0.31±0.02	0.80±0.02	
	$<N_b>$	--	2.09±0.08	10.42±0.25	5.66±0.18	0.24±0.02	0.81±0.02	
14.6	$<N_s>$	8.51±1.02	13.11±0.83	27.08±1.28	18.72±0.73	6.52±1.48	0.30±0.06	Present work
	$<N_g>$	0.18±0.03	1.61±0.09	7.03±0.29	3.85±0.17	0.25±0.04	0.73±0.04	
	$<N_b>$	0.20±0.03	2.51±0.08	9.89±0.26	5.49±0.19	0.41±0.06	0.70±0.03	
	$<N_h>$	0.37±0.04	4.11±0.09	16.92±0.41	9.34±0.32	0.66±0.10	0.72±0.03	
	$<N_{ch}>$	8.88±0.74	17.22±0.54	44.00±1.18	28.06±0.80	5.88±1.44	0.44±0.06	

data on nucleus-nucleus collisions are slightly higher than the corresponding values in the case of hadron-nucleus collisions [26-28]. This may be due to the fact that ^{28}Si projectile at a given impact parameter is an extended object rather than a point object as in the case of an incident hadron.

3.6 Pseudorapidity Distributions

Pseudorapidity of a particle is defined as η = - ln tan (θ/2) (see section 2.6), where θ is the angle of emission of the particle with respect to the direction of the projectile. The pseudorapidity (η) distribution of shower particles produced in ^{28}Si-*Emulsion* collisions at 14.6*A GeV* is shown in Figure 3.3. The distribution is normalized by total number of events. A gaussian distribution given by the relation

$$\rho_G(\eta) = \rho_{\max} \exp\left[-\frac{(\eta - \eta_{peak})^2}{2\sigma^2}\right] \qquad 3.3$$

was fitted to the experimental distribution. The fitted value of parameters are $\eta_{peak} = 2.38 \pm 0.03$, $\sigma = 1.09 \pm 0.03$ and $\rho_{\max} = 6.92 \pm 0.16$.

In Figure 3.4 we compare our pseudorapidity distribution with the distributions for ^{28}Si-*Emulsion* collisions at 4.5*A GeV* [29]. We observe that as the energy of the projectile increases the centroid of the distribution grows and the position of η_{peak} shifts towards higher values. However, the overall shape of the distribution remains the same.

In Figure 3.5 the pseudorapidity distributions for the collisions of Silicon beam with *H, CNO* and *AgBr* groups of nuclei are plotted to detect any possible target mass dependence. In the figure smooth curves represent the gaussian fits to the distributions. From the plots one may observe that the distributions are almost the same at higher values of pseudorapidity and the centroids of the distribution grow and shift towards smaller values of pseudorapidity as the target mass increases from *H* to *AgBr* group. Similar results were obtained by M. Tariq et al. [29] for ^{28}Si-*Emulsion* and ^{12}C-*Emulsion* collisions at 4.5*A GeV*. Thus we can conclude that the distributions corresponding to lower values of η are related to the target nuclei and those corresponding to higher η values to the projectile nuclei. Hence the pseudorapidity space can be divided into three regions as: (i) target fragmentation region, (ii) central region and (iii) projectile fragmentation region. The target fragmentation region corresponds to lower η values, that is, larger values of emission angle, which is characterized by target nuclei. The projectile

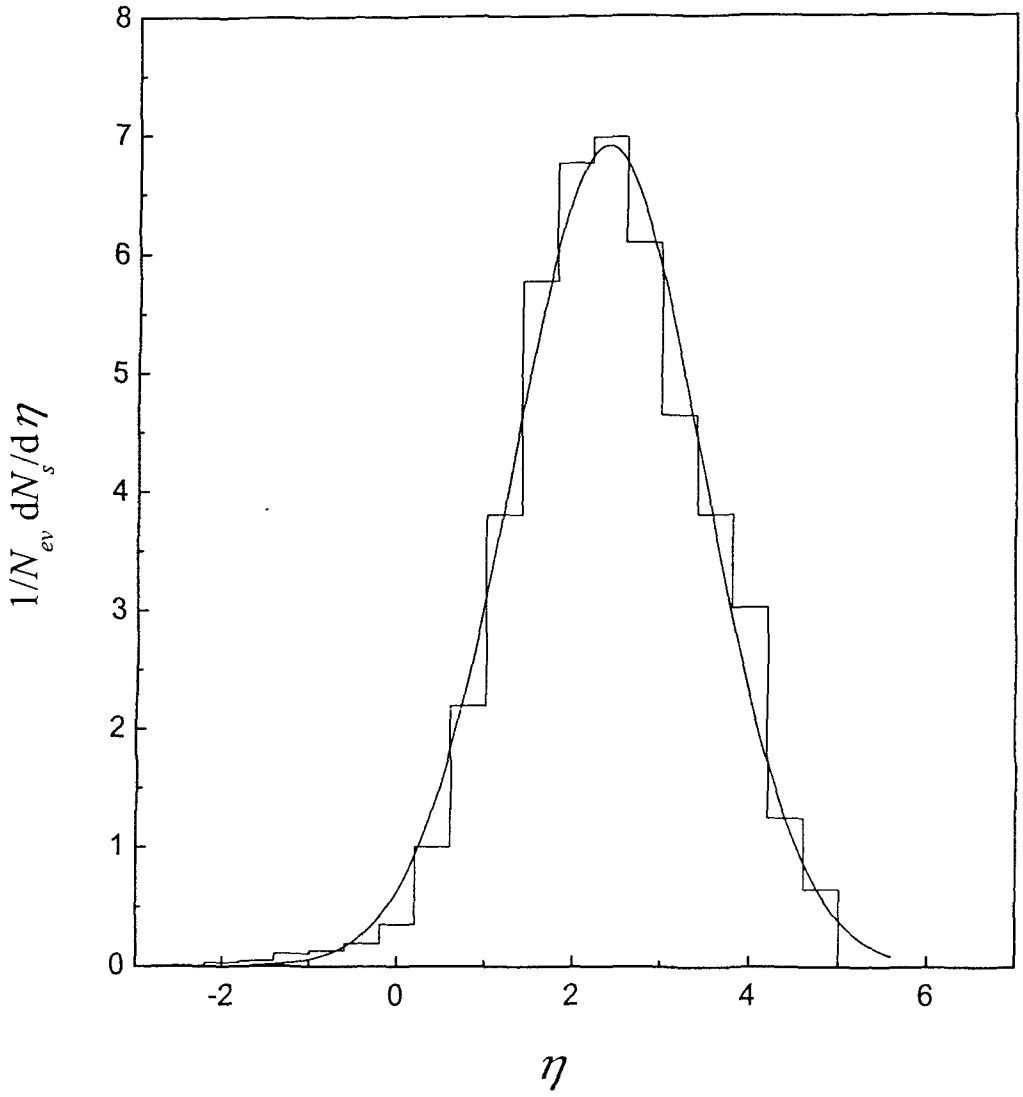

Figure 3.3: Histogram represents the pseudorapidity distribution for ^{28}*Si-Emulsion* collisions at 14.6*A GeV* and smooth curve represents the Gaussian fit of the distribution.

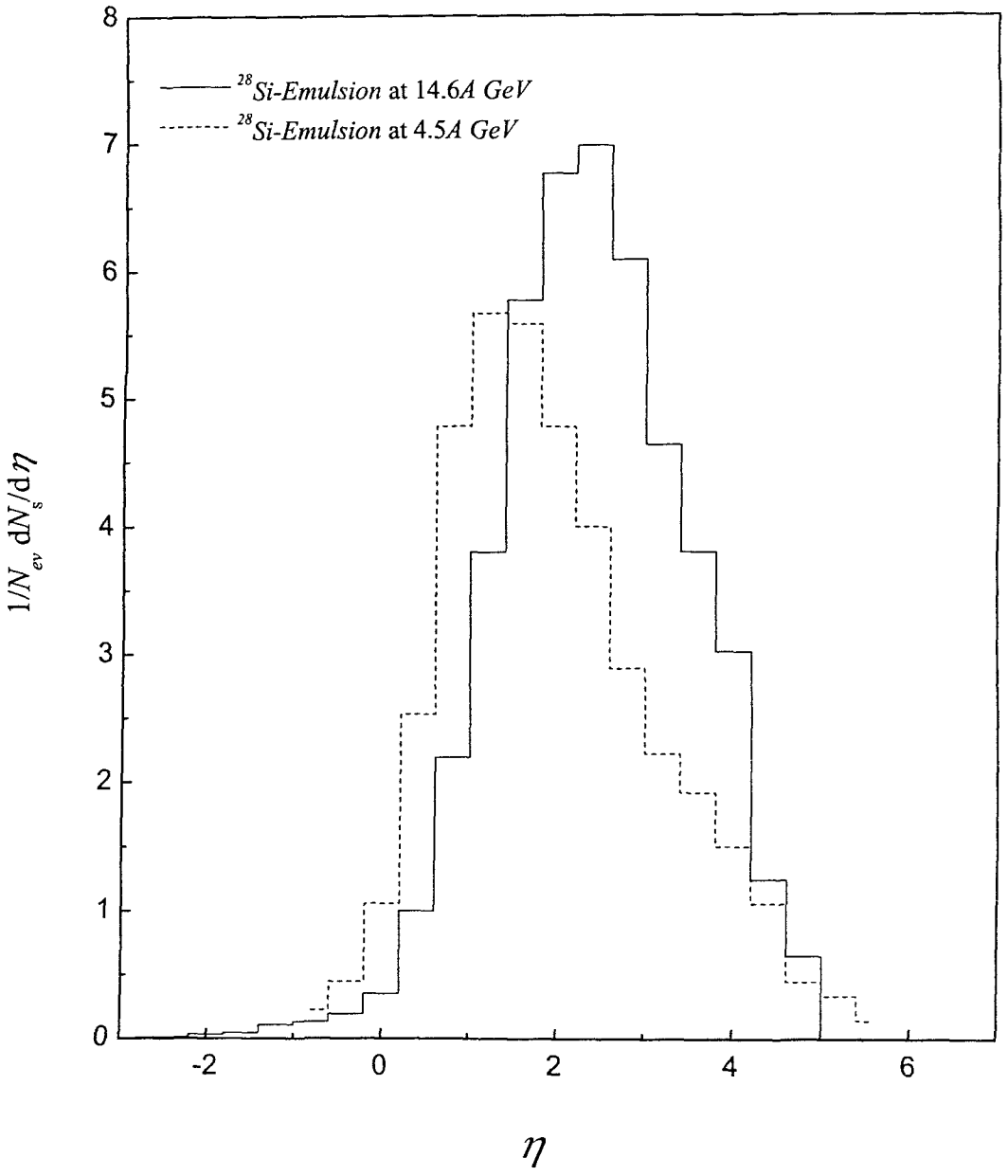

Figure 3.4: Plots of pseudorapidity distributions for ^{28}*Si-Emulsion* collisions at 4.5*A GeV* and 14.6*A GeV*.

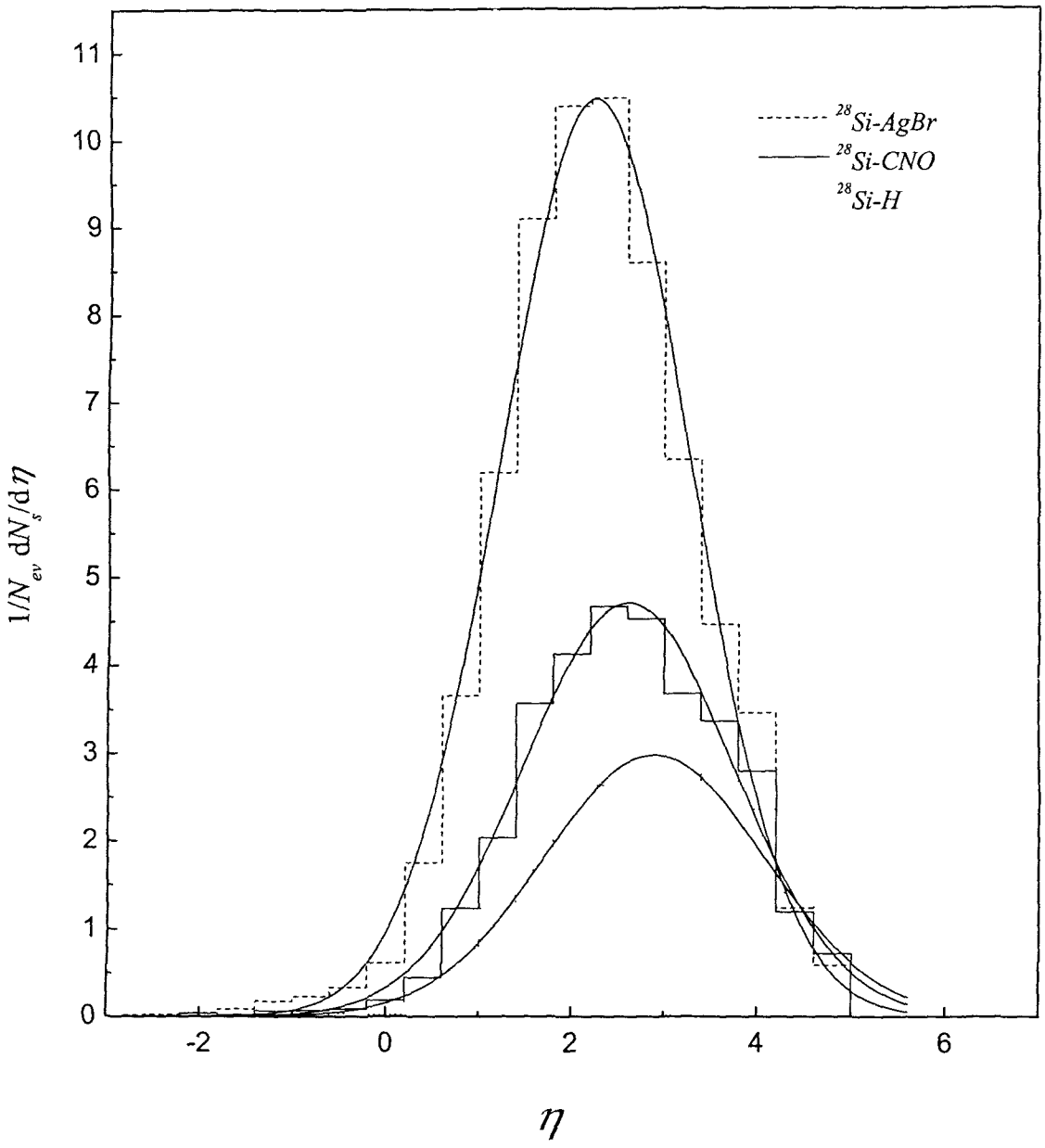

Figure 3.5: Histograms represent the pseudorapidity distributions for ^{28}*Si-AgBr*, ^{28}*Si-CNO* and ^{28}*Si-H* collisions at 14.6*A GeV* and smooth curves represent the Gaussian fit of the distributions.

fragmentation region is assumed to be populated by fragments of projectile nucleus corresponding to larger values of η, that is, small angles of emission. The central region is believed to be enriched by the particles produced in collisions and is independent of either of the fragmentation regions.

3.7 Multiplicity Correlations

One of the effective methods to understand the production mechanism for collisions induced by hadrons and nuclei at various energies is to obtain the correlations among the secondary particles emitted in these collisions. The correlations between the multiplicities of different charged secondaries $\langle N_i \rangle = f(N_j)$ have been studied extensively in the case of hadron-nucleus collisions [30,31] and it was found that the correlations could be approximated by a linear relationship of the type

$$\langle N_i \rangle = a + b\, N_j \qquad 3.4$$

where N_i and N_j stand for N_s, N_g, N_b, or N_h and $i \neq j$, and b is the slope of the linear fit. Here we extend this analysis to nucleus-nucleus collisions. In this section we study the multiplicity correlations for ^{28}*Si-Emulsion* collisions at 14.6*A GeV*. It has been observed that like hadron-nucleus collisions, multiplicity correlations in nucleus-nucleus collisions can also be approximated by a linear dependence with a positive slope.

In Figure 3.6 (a) we plot for our data $\langle N_i \rangle$ as a function of N_g, where $i = b$, s or h. In the figure the experimental correlations have been fitted to the straight line (Equation 3.4). We observe from the figure that both $\langle N_s \rangle$ and $\langle N_h \rangle$ increase linearly with N_g in the whole range of N_g. However, $\langle N_b \rangle$ increases linearly with N_g only upto $N_g \approx 10$, after that it levels off i.e. the value of $\langle N_b \rangle$ saturates. The other correlations, namely $\langle N_i \rangle$ versus N_b, $\langle N_i \rangle$ versus N_s and $\langle N_i \rangle$ versus N_h are presented in Figures 3.6 (b) - (d) respectively. All these correlations can also be approximated by linear relations with positive slopes. However, like $\langle N_b \rangle$ versus N_g correlation, $\langle N_g \rangle$ versus N_b correlation also levels off after $N_b \approx 12$. The saturation effect in $\langle N_b \rangle$ versus N_g and $\langle N_g \rangle$ versus N_b correlations have also been observed by Stenlund and Otterlund [32] for *p–Emulsion* (6.2-400 *GeV*) and π^-*-Emulsion* (200 *GeV*) collisions, by Ahmad and Irfan [33] for ^{12}*C-Emulsion* and ^{28}*Si-Emulsion* at 4.5*A GeV* and by A. Dabrowska et al. [34] for ^{16}*O-Emulsion* and ^{32}*S-Emulsion* collisions at 200*A GeV*. $\langle N_b \rangle$ versus N_g and $\langle N_g \rangle$ versus N_b correlations seem to be independent of the nature of the projectile and its energy. In Table 3.4 the

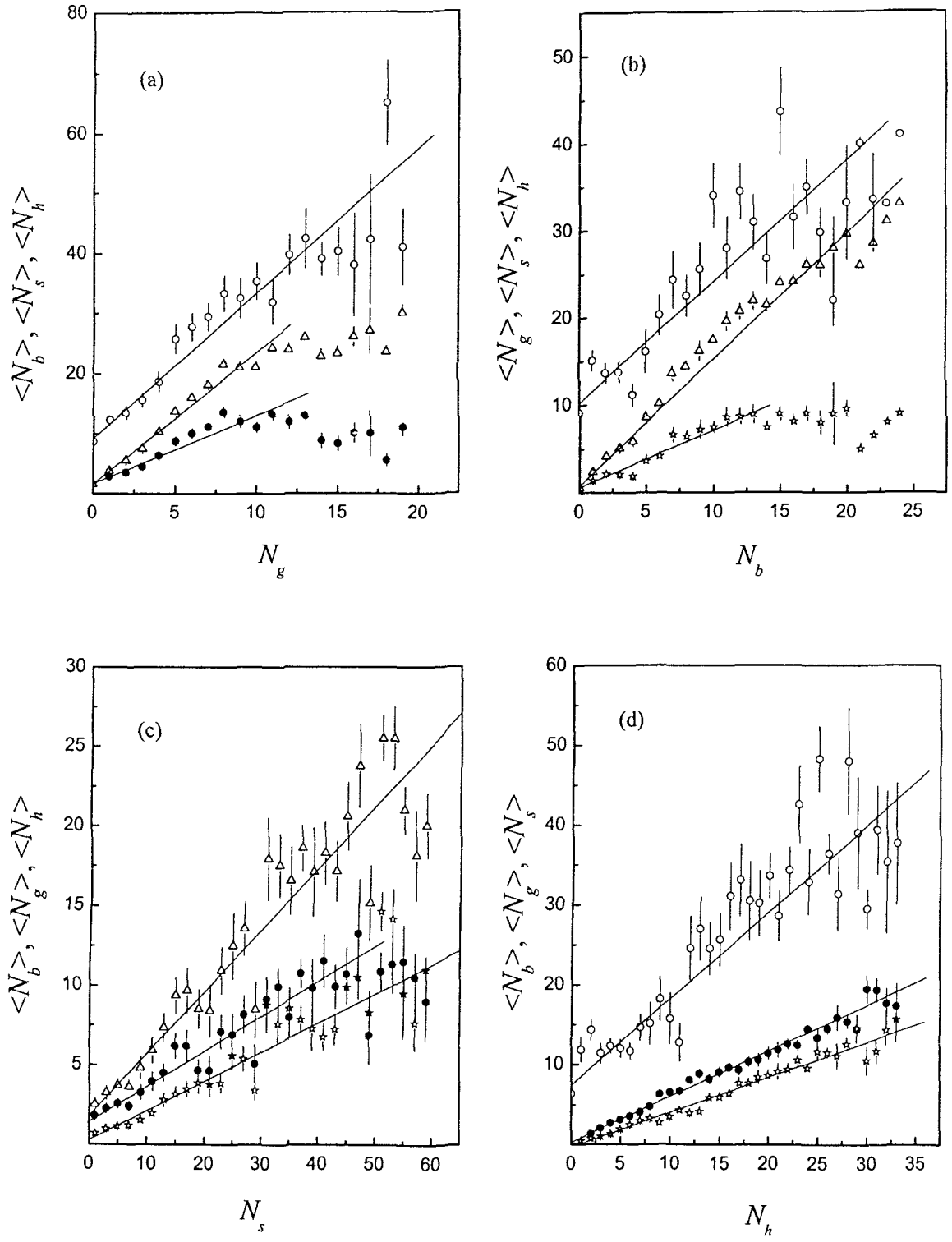

Figure 3.6: Multiplicity correlations $<N_i>=f(N_j)$ and their approximation by a linear dependence $<N_i> = a + bN_j$ for ^{28}*Si-Emulsion* collisions at 14.6*A GeV*. Symbols ● , ☆ , ○ and △ represent black, grey, shower and heavy particles respectively.

Table 3.4: Values of inclination coefficients (b) in the multiplicity correlations in the case of *p-Emulsion* and ^{12}C*-Emulsion* collisions at 4.5*A GeV* and ^{28}Si*-Emulsion* collision at 14.6*A GeV*.

Collisions	$<N_b>$	$<N_g>$	$<N_s>$	$<N_h>$	Reference
N_b p	--	0.51±0.01	-0.03±0.01	1.52±0.02	31
^{12}C	--	0.98±0.09	0.59±0.06	1.82±0.12	35
^{28}Si	--	0.66±0.04	1.39±0.08	1.45±0.04	present work
N_g p	1.09±0.02	--	-0.06±0.01	1.97±0.02	31
^{12}C	0.36±0.04	--	0.51±0.06	1.52±0.12	35
^{28}Si	1.13±0.07	--	2.67±0.13	2.18±0.07	present work
N_s p	0.01±0.04	-0.04±0.04	--	-0.03±0.06	31
^{12}C	0.50±0.06	0.82±0.07	--	1.30±0.09	35
^{28}Si	0.22±0.01	0.18±0.01	--	0.39±0.02	present work
N_h p	0.60±0.01	0.40±0.01	-0.02±0.01	--	31
^{12}C	0.47±0.07	0.65±0.10	0.30±0.05	--	35
^{28}Si	0.57±0.01	0.44±0.01	1.08±0.07	--	present work

slopes of the linear fits of experimental points for the multiplicity correlations for ^{28}*Si-Emulsion* collisions at 14.6*A GeV* are given along with the results obtained by B.P. Bannik et al. [31] for *p-Emulsion* at 4.5*A GeV* and by M. S. Ahmad et al. [35] for ^{12}*C-Emulsion* at 4.5*A GeV*. From the results given in Table 3.4, the following conclusions may be drawn.

- The multiplicity correlation between $<N_s>$ / $<N_h>$ and N_b is strong and is moderate between $<N_g>$ and N_b. However in the case of *p-Emulsion* [31] collisions at 4.5*A GeV*, the correlation between $<N_h>$ and N_b is very strong, between $<N_g>$ and N_b moderate and negative between $<N_s>$ and N_b.
- From the table one can see that the strongest correlation is observed between $<N_s>$ and N_g. The correlation between $<N_h>$ and N_g is also strong. But the correlation between $<N_b>$ and N_g is observed weak in comparison with the correlations for $<N_s>$ and $<N_h>$ with N_g. However in the case of ^{12}*C-Emulsion* collisions at 4.5*A GeV* [35], there is a strong correlation between $<N_h>$ and N_g and a moderate between $<N_b>$ / $<N_s>$ and N_g. Again there is a negative correlation between $<N_s>$ and N_g and a very strong correlation between $<N_h>$/ $<N_b>$ and N_g in the case of *p-Emulsion* collisions at 4.5*A GeV* [31].
- There is a moderate correlation for $<N_b>$, $<N_g>$ and $<N_h>$ with N_s. Also in the case of ^{12}*C-Emulsion* collisions at 4.5*A GeV* moderate correlations for $<N_b>$ and $<N_g>$ with N_s are observed but there is a strong correlation between $<N_h>$ and N_s.
- For ^{28}*Si-Emulsion* at 14.6*A GeV*, ^{12}*C-Emulsion* at 4.5*A GeV* and *p-Emulsion* at 4.5*A GeV* collisions moderate correlations are observed for $<N_b>$ and $<N_g>$ with N_h. Between $<N_s>$ and N_h negative correlation is observed for *p-Emulsion* collisions and moderate correlation is observed in the case of ^{28}*Si-Emulsion* collisions at 14.6*A GeV*.

3.8 Angular Distributions of Charged Particles

The angular distributions of shower particles produced during the collisions of ^{28}*Si* nuclei with *Emulsion* and with different target groups (*AgBr*, *CNO* and *H*) at 14.6*A GeV* for the four groups of N_s intervals $N_s \geq 0$, $N_s \leq 10$, $10 < N_s \leq 20$ and $N_s \geq 20$ are shown in Figure 3.7. From the figure, one can observe that the angular distributions of shower particles are almost similar and prominent peaks are observed at smaller angles.

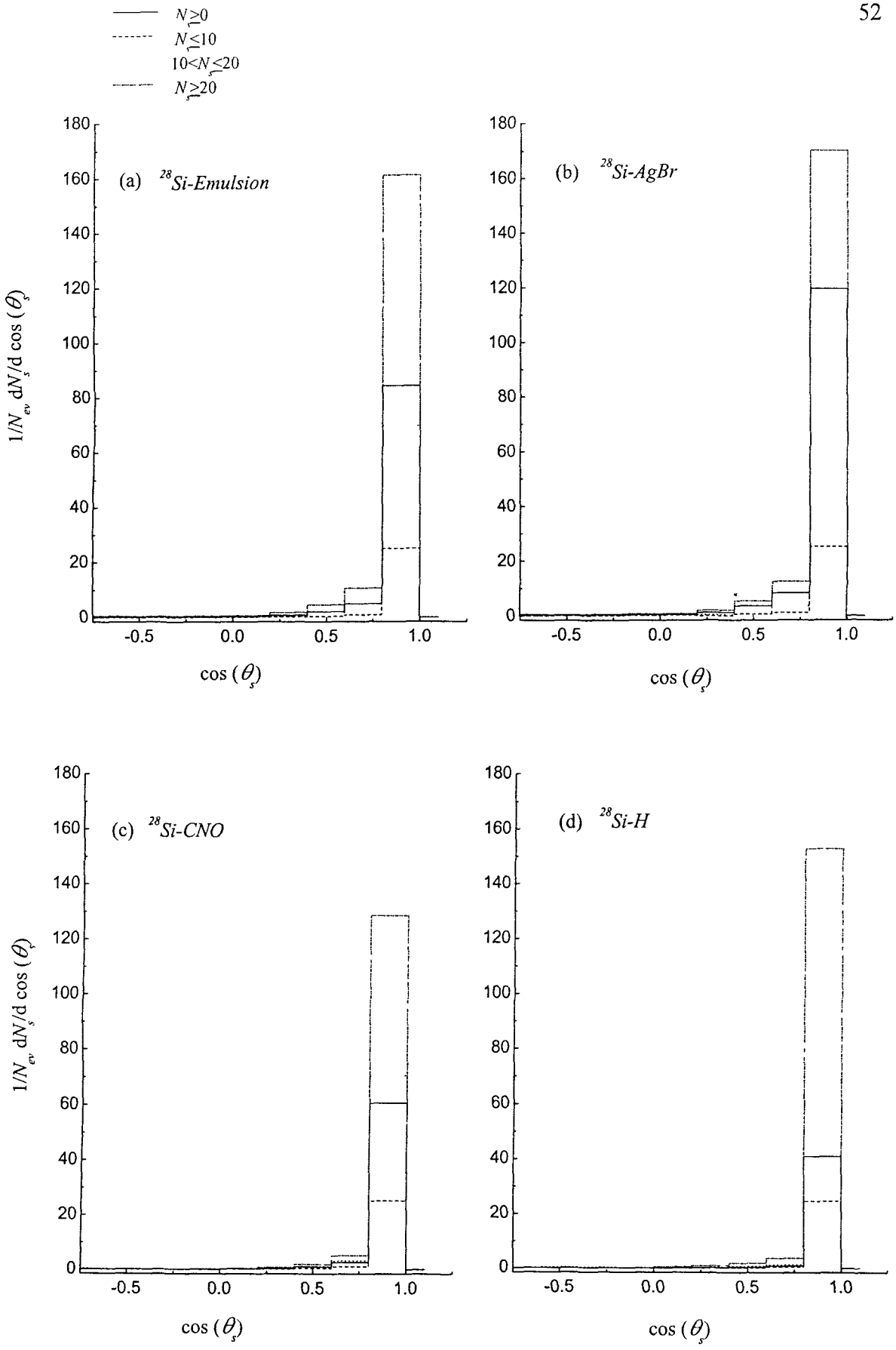

Figure 3.7 : (a)-(d) represent angular distributions of shower particles in different N_s intervals for ^{28}Si-*Emulsion*, ^{28}Si-*AgBr*, ^{28}Si-*CNO* and ^{28}Si-*H* collisions at 14.6*A GeV* respectively.

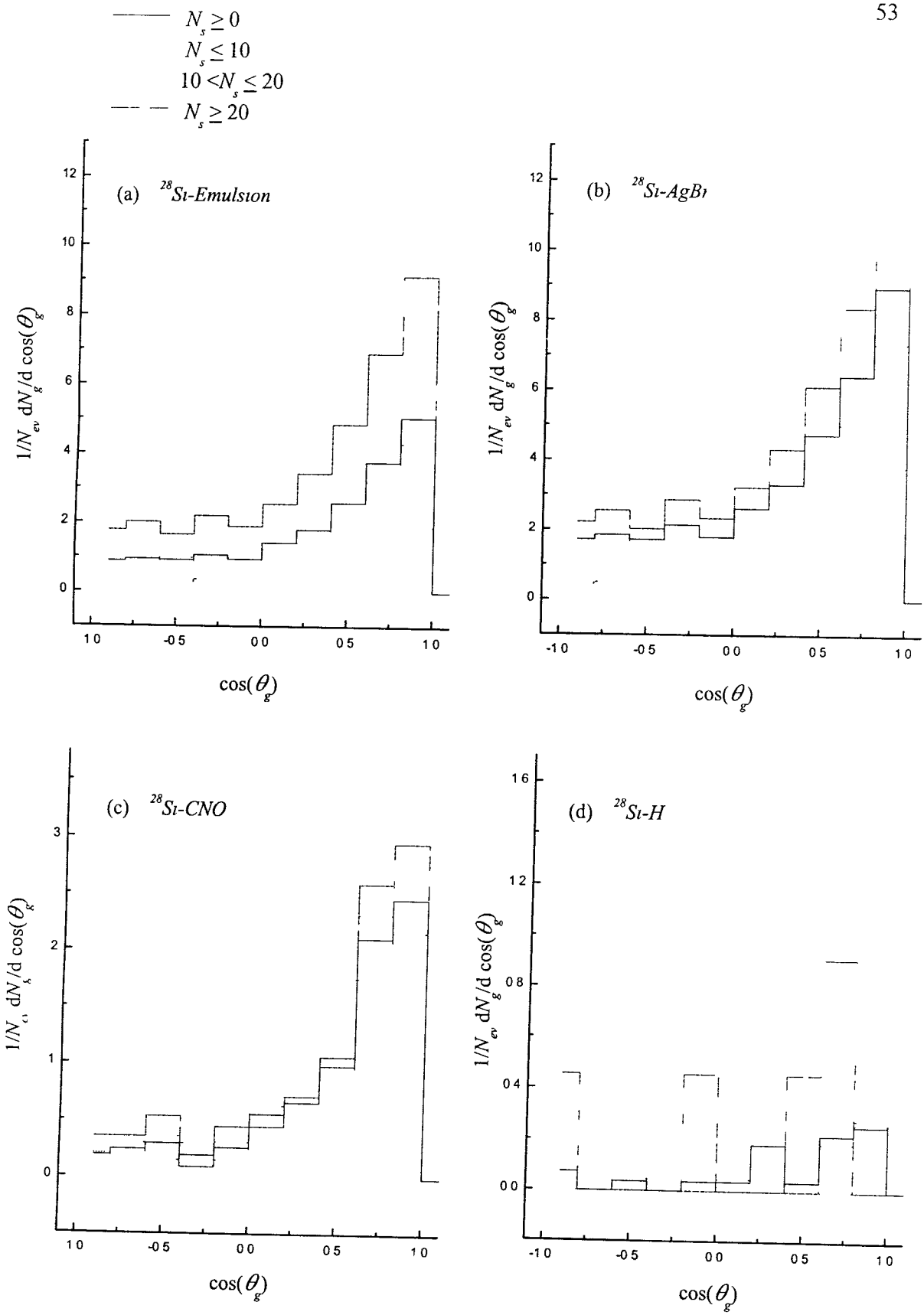

Figure 3.8: (a)-(d) represent angular distributions of grey particles in different N_s intervals for ^{28}Si-*Emulsion*, ^{28}Si-*AgBr*, ^{28}Si-*CNO* and ^{28}Si-*H* collisions at 14.6*A GeV* respectively.

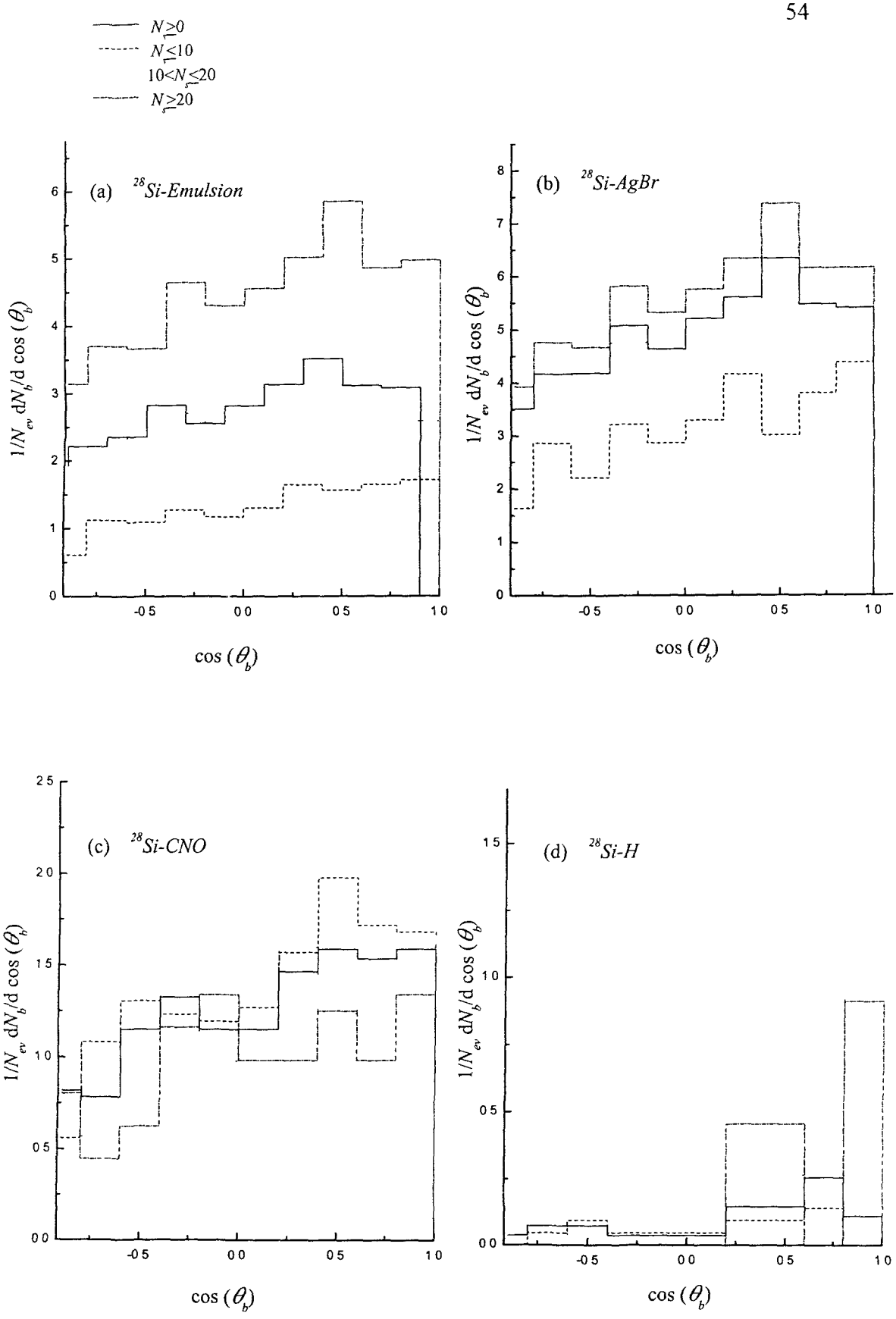

Figure 3.9: (a)-(d) represent angular distributions of black particles in different N_s intervals for ^{28}Si-*Emulsion*, ^{28}Si-*AgBr*, ^{28}Si-*CNO* and ^{28}Si-*H* collisions at 14.6*A GeV* respectively.

Similar results were obtained by N. N. Abd Allah et al. [36] for ^{24}Mg-*Emulsion* collisions at 4.5*A GeV/c*, by M. Tariq et al. [29] for ^{28}Si-*Emulsion* collisions at 4.5*A GeV* and by DGKLMTW collaboration [14] for α-*Emulsion* collisions at 4.5*A GeV*. From the similarity in these results one may conclude that the mechanism of production of shower particles is independent of the mass and energy of the projectile.

The angular distribution of grey and black particles (target fragments) emitted in ^{28}Si-*Emulsion*, ^{28}Si-*AgBr*, ^{28}Si-*CNO* and ^{28}Si-*H* collisions at 14.6*A GeV* for four groups of N_s intervals are shown in Figures 3.8 and 3.9. In these figures no prominent peak is observed.

3.9 Multiplicity Moments

The scaling test of the experimental data could be performed through the study of multiplicity moments. The normalized moments of relativistic charged secondaries are defined as

$$C_q = \langle N_s^q \rangle / \langle N_s \rangle^q \qquad 3.5$$

where q has the values 2, 3, 4, etc. Further the following relation gives the dispersion

$$D(N_s) = (\langle N_s^2 \rangle - \langle N_s \rangle^2)^{1/2} \qquad 3.6$$

Table 3.5, shows the values of multiplicity moments C_2, C_3, C_4, C_5 and $\langle N_s \rangle / D$ along with the value of dispersion for ^{28}Si–*Emulsion*, ^{28}Si–*AgBr* and ^{28}Si–*CNO* collisions at 14.6*A GeV*. The values of above parameters for different projectiles at different energies taken from references [14,22,31,35,37] are also presented in Table 3.5. From the table, we see that the values of the ratio $\langle N_s \rangle / D$ for various projectiles are about the same, which indicates that the mechanism of shower particle production may be similar for different types of collisions. We also observe that the value of dispersion varies linearly with the mean multiplicity and the value of C_q increases with increase in the value of q.

3.10 Multiplicity Distributions

Multiplicity distributions of charged particles produced in relativistic nuclear collisions are useful in testing the predictions of various theoretical models proposed to explain the mechanism of multiparticle production. To study the multiplicity distributions of secondary charged particles produced in collisions of ^{28}Si in emulsion and with nuclei of different target groups, that is, *AgBr*, *CNO* and *H* at 14.6*A GeV*, we have plotted the

Table 3.5: Table for multiplicity moments.

Type of collisions	*Energy AGeV*	$\langle N_s \rangle$	D	$\langle N_s \rangle / D$	C_2	C_3	Ref
P – Emulsion	4.5	1.63±0.02	1.08±0.02	1.51±0.03	1.44±0.02	2.55±0.04	31
α - Emulsion	2.1	3.06±0.28	2.49±0.04	1.23±0.11	1.44±0.04	2.55±0.09	14
^{12}C- Emulsion	4.5	7.77±0.16	5.72±0.09	1.36±0.04	1.52±0.05	2.6±0.08	35
^{14}N- Emulsion	2.1	8.85±0.28	5.59±0.17	1.58±0.07	1.4±0.05	2.58±0.11	22
^{24}Mg- Emulsion	4.5	12.37±0.22	7.02±0.23	---	1.32±0.08	2.11±0.28	37
^{28}Si- Emulsion	14.6	18.72±0.56	15.56±0.39	1.20±0.05	1.69±0.14	3.75±0.46	Present work
^{28}Si-AgBr	14.6	27.08±0.91	17.28±0.64	1.57±0.08	1.41±0.13	2.37±0.32	
^{28}Si-CNO	14.6	13.11±0.54	9.15±0.39	1.43±0.08	1.49±0.17	2.79±0.49	

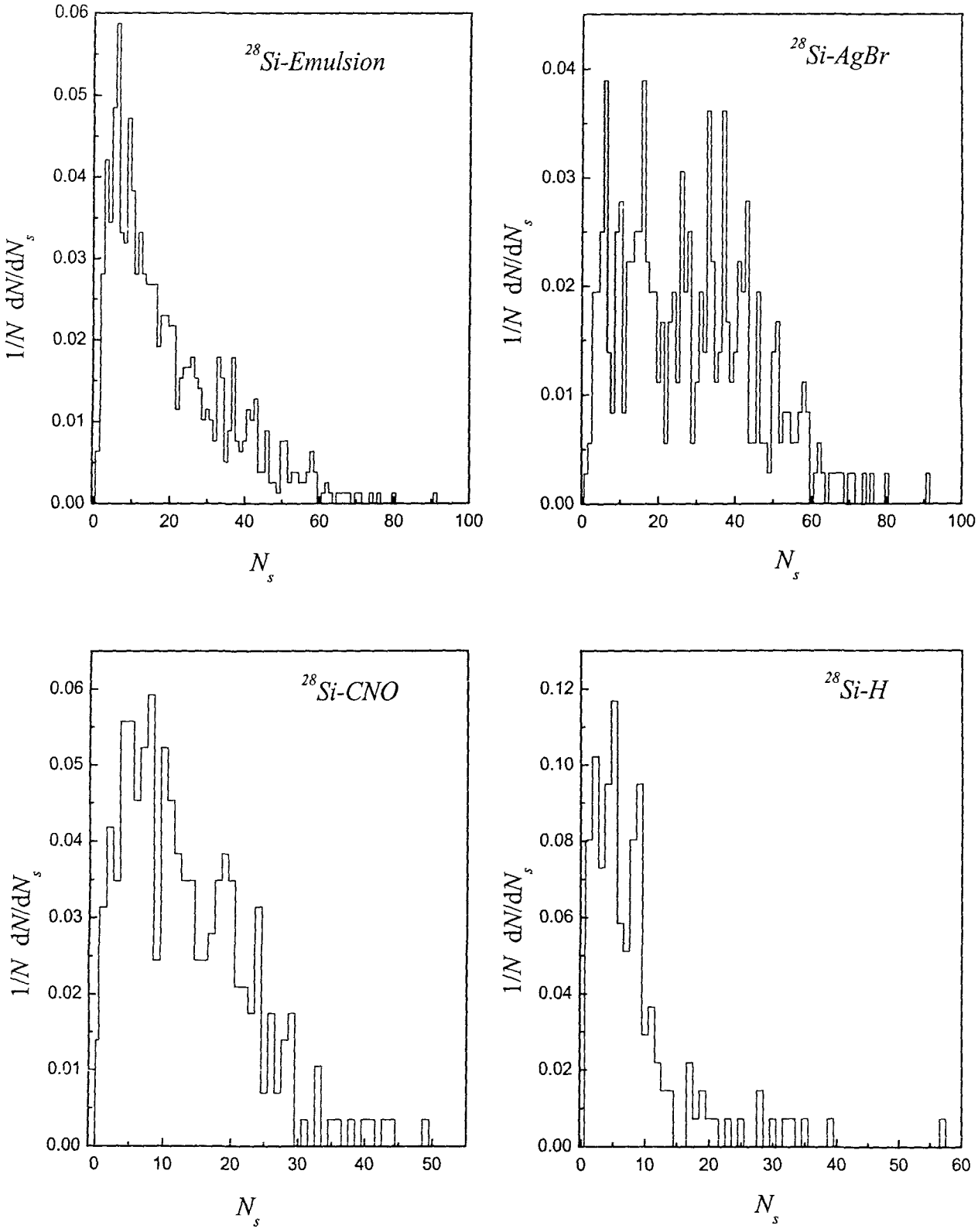

Figure 3.10 : Multiplicity distributions of shower particles for ^{28}*Si-Emulsion*, ^{28}*Si-AgBr*, ^{28}*Si-CNO* and ^{28}*Si-H* collisions at 14.6*A GeV*.

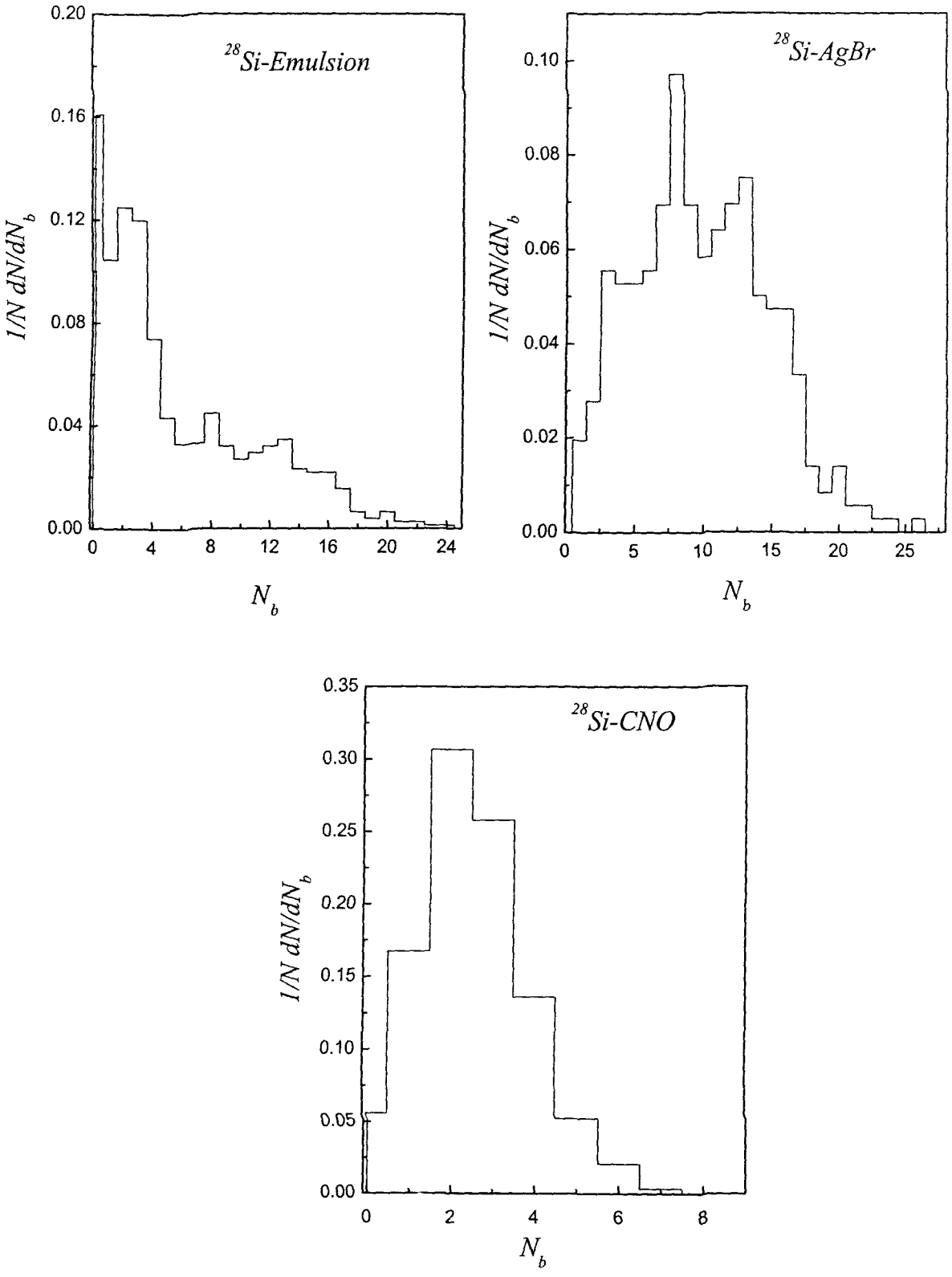

Figure 3.11 : Multiplicity distributions of black particles for ^{28}*Si-Emulsion*, ^{28}*Si-AgBr* and ^{28}*Si-CNO* collisions at 14.6*A GeV*.

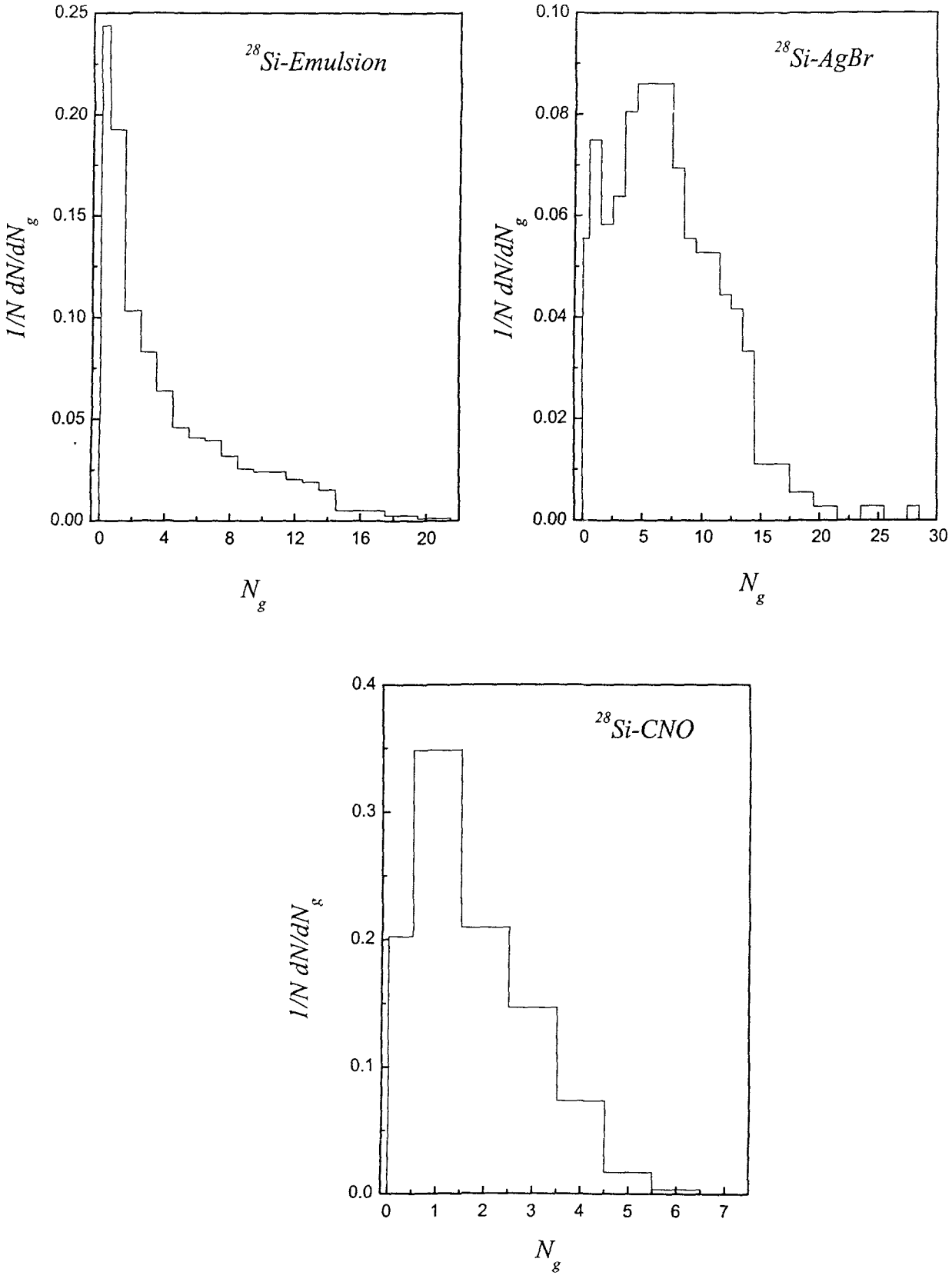

Figure 3.12 : Multiplicity distributions of grey particles for ^{28}*Si-Emulsion*, ^{28}*Si-AgBr* and ^{28}*Si-CNO* collisions at 14.6*A GeV*.

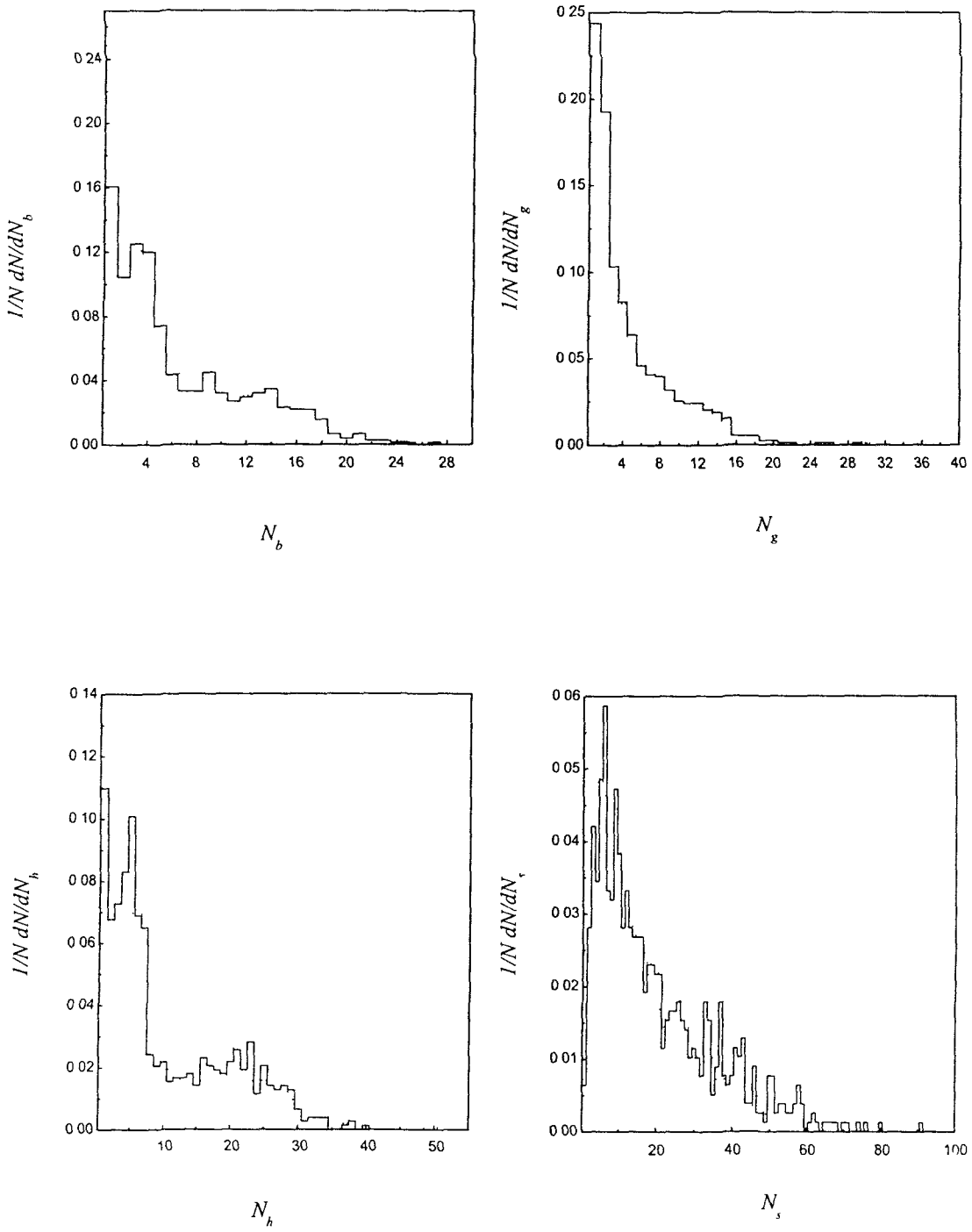

Figure 3.13: Histograms shown by solid and dotted lines represent the multiplicity distributions of black, grey, heavy and shower particles for ^{28}*Si-Emulsion* collisions at 14.6*A GeV* and at 4.5*A GeV* respectively.

graph between $\frac{1}{N}\frac{dN}{dN_i}$ and N_i where i=b, g or s. N is the total number of events in the sample. dN is the number of events in the interval dN_i Figures 3.10-3.12 show the multiplicity distributions of secondary particles produced in collisions of ^{28}Si with different target groups. From the figures it is clear that

(i) the shape of N_s distributions strongly depends on the target mass and

(ii) the multiplicity distributions of grey and black particles show that the distributions for ^{28}Si-$AgBr$ collisions are broader than those for ^{28}Si-CNO collisions. This may be due to the effect of target mass number on the number of collisions of ^{28}Si with the target nuclei.

Figure 3.13 shows the multiplicity distributions of different particles produced in ^{28}Si-$Emulsion$ collisions at 14.6A GeV along with the corresponding results from the collisions of the same projectile at 4.5 $AGeV$ [1]. From these distributions we observe that

(i) the peaks of distributions appear in the lower region of N_s value but it is slightly higher in the case of 14.6A GeV collisions and

(ii) the tail of the distribution extends to much higher values of N_s in the case 14.6A GeV collisions in comparison with the collisions at 4.5A GeV.

Thus we can say that with increasing energy more and more relativistic charged particles are produced that confirms the conversion of energy into mass.

3.10.1 Negative Binomial Distributions

Ever since the UA5 collaboration [38] has shown that the multiplicity distribution of charged particles produced in $p\bar{p}$ interactions at 540 GeV can be described by a negative binomial distribution, this parameterization has been found to be valid in lepton–hadron, hadron–nucleus and nucleus-nucleus collisions with centre of mass energies ranging from 10 to more than 1000 GeV [39-42]. The parameterization of the multiplicity distribution in terms of the negative binomial distribution has been found to hold not only in full phase space but in the limited intervals of phase space also. However, Mukhopadhyay et al [41] reported that the negative binomial distribution matches the multiplicity distributions of shower particles produced in nucleus-nucleus collisions at relativistic energies only if the analysis was restricted within the central pseudorapidity regions. For wider intervals they found that the negative binomial

parameterization was not so good, probably because of the effects of different conservation laws. Several kinematical schemes have been advocated by different investigators to find out the origin of the negative binomial distributions from some general properties [43-46].

The negative binomial distribution is given by the formula

$$P(n,\bar{n},k)=\frac{k(k+1)....(k+n-1)}{n!}\frac{\bar{n}^n k^k}{(\bar{n}+k)^{(n+k)}} \qquad 3.7$$

where $\bar{n}$ is the mean multiplicity $<n>=\bar{n}$ and parameter k is related to $\bar{n}$ and dispersion D by

$$\frac{D^2}{\bar{n}^2}=\frac{1}{\bar{n}}+\frac{1}{k} \qquad 3.8$$

the dispersion D can be calculated using the relation

$$D^2=\overline{n^2}-\bar{n}^2 \quad . \qquad 3.9$$

The distribution 3.7 was originally proposed by Max Planck to describe the radiation emitted by k independent sources, each of them obeying Bose-Einstein statistics. The sources thus emit radiation according to a geometrical distribution

$$P(n)=\left(\frac{\bar{n}}{\bar{n}+1}\right)^n\frac{1}{\bar{n}+1} \qquad 3.10$$

which is a special case of the distribution 3.7 for k = 1. The success of the negative binomial distribution in fitting the shape of the multiplicity distributions has led to a number of theoretical interpretations. The Planck interpretation has been employed by Carruthers and Shih [43] in their stochastic cell model for multiparticle production in pp and $p\bar{p}$ collisions. For this interpretation to be meaningful k should be an integer. However, for the experimental multiplicity distributions observed in different production processes, the value of k is found to vary continuously with energy.

Another interpretation has been suggested by Giovannini and Van Hove [44]. They assumed that particle production takes place in two steps. In the first step clusters or clans are produced. The number of clans obeys a Poisson distribution

$$P_P(n) = \exp(-\overline{N})\frac{\overline{N}^{N}}{N!} \qquad 3.11$$

In the second step these clans decay into observed hadrons. The number of hadrons inside a single clan follows a logarithmic probability distribution

$$P_L(n_c) = \frac{(1-b)\overline{n}_c b^{n_c}}{bn_c} \quad \text{for} \quad n_c \geq 1. \qquad 3.12$$

Since a cluster by definition should contain at least one particle, one gets $P_L(0) = 0$, where b is given by the relation

$$b = \overline{n}/(\overline{n} + k). \qquad 3.13$$

Thus the negative binomial distribution is a mathematical combination of the Poisson and Logarithmic distributions. The average number of particles inside a clan ($\overline{n}_c$) and the average number of clans ($\overline{N}$) can be directly calculated from the relations

$$\overline{n}_c = \frac{\overline{n}}{k\ln(1+\overline{n}/k)} \qquad 3.14$$

$$\overline{N} = \frac{\overline{n}}{\overline{n}_c} \qquad 3.15$$

In this section we study the multiplicity distributions of shower particles produced in ^{28}Si-*Emulsion*, ^{28}Si-*AgBr* and ^{28}Si-*CNO* collisions 14.6*A GeV* in various intervals of the pseudorapidity and the azimuthal angle within the central regions so that the influences of the constraints due to charge, energy and momentum conservations could be minimized.

The pseudorapidity window of width $\Delta\eta$ was selected symmetrically about the peak value of pseudorapidity of the Gaussian fit of the pseudorapidity distribution, that is, $\eta_{peak} - \frac{\Delta\eta}{2} < \eta < \eta_{peak} + \frac{\Delta\eta}{2}$.

In Figures 3.14-3.16 symbols show the multiplicity distributions of shower particles produced in ^{28}Si-*Emulsion*, ^{28}Si-*AgBr* and ^{28}Si-*CNO* collisions respectively for different values of pseudorapidity interval such as $\Delta\eta$ = 4.00, 3.75, 3.50, 3.25, 3.00, 2.75, 2.50, 2.25, 2.00, 1.75, 1.50, 1.25, 1.00, 0.75, 0.50, 0.25 and the solid curves represent the

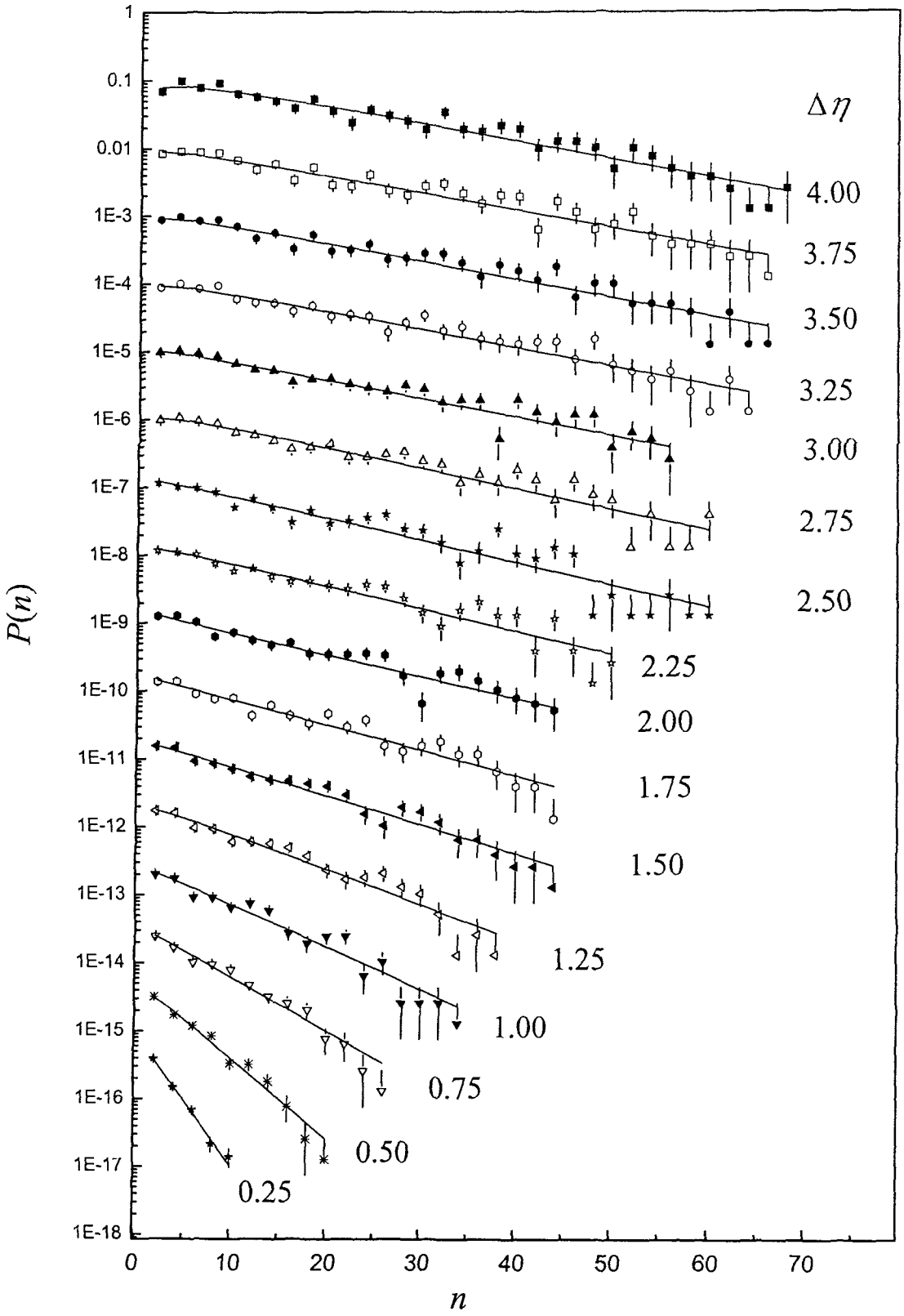

Figure 3.14: Multiplicity distributions in different pseudorapidity intervals $\Delta\eta$ for ^{28}*Si-Emulsion* collisions at 14.6*A GeV*. Symbols represent the experimental values and solid curves represent the best NBD fits. For $\Delta\eta = 4.00$ the distribution is plotted in the normal scale and for all subsequent intervals the probability values are multiplied by 10^{-1},10^{-2},10^{-3}, 10^{-4},...10^{-15} respectively.

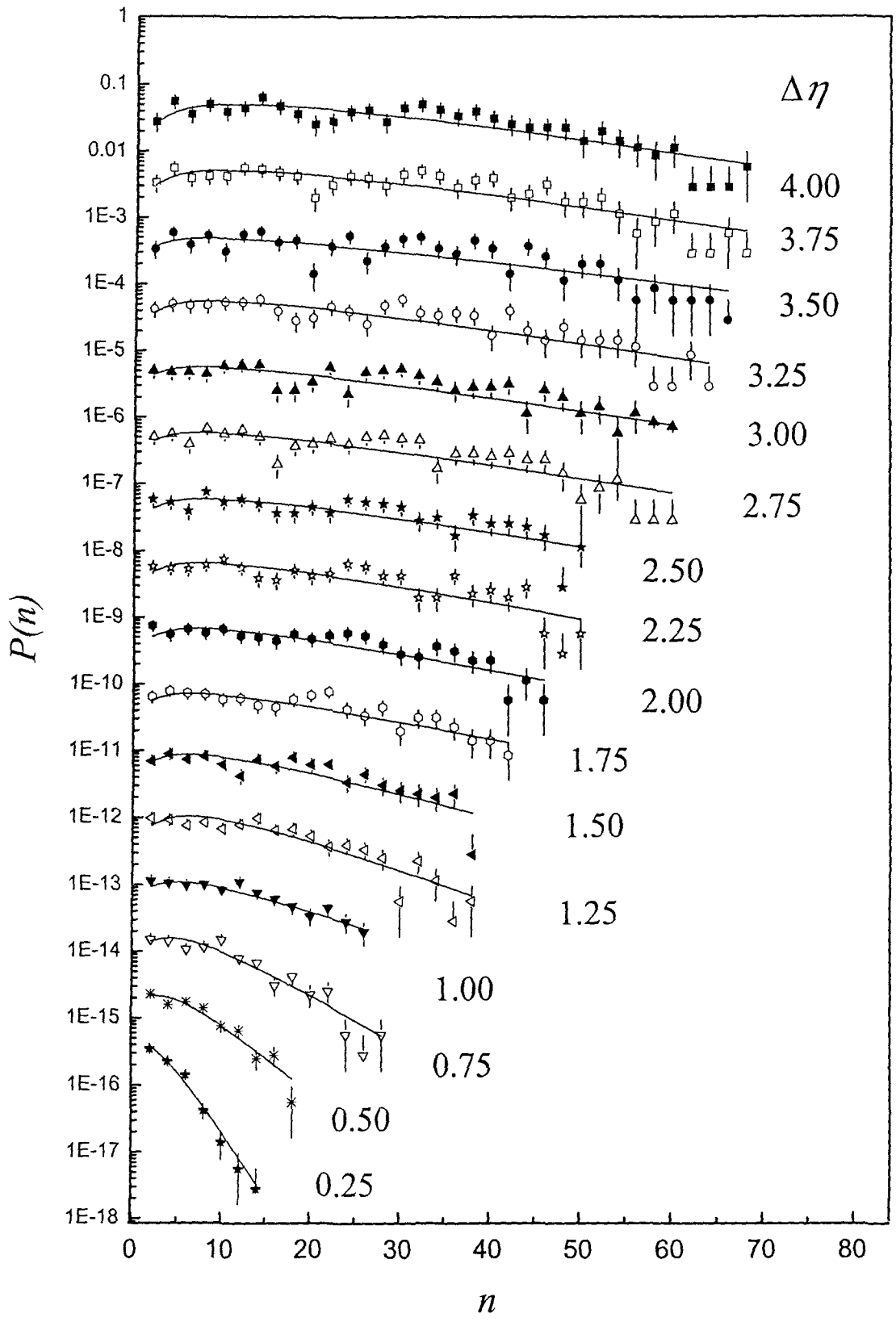

Figure 3.15: Multiplicity distributions in different pseudorapidity intervals $\Delta\eta$ for ^{28}Si- *AgBr* collisions at 14.6*A GeV*. Symbols represent the experimental values and solid curves represent the best NBD fits. For $\Delta\eta = 4.00$ the distribution is plotted in the normal scale and for all subsequent intervals the probability values are multiplied by 10^{-1},10^{-2},10^{-3}, 10^{-4},....10^{-15} respectively.

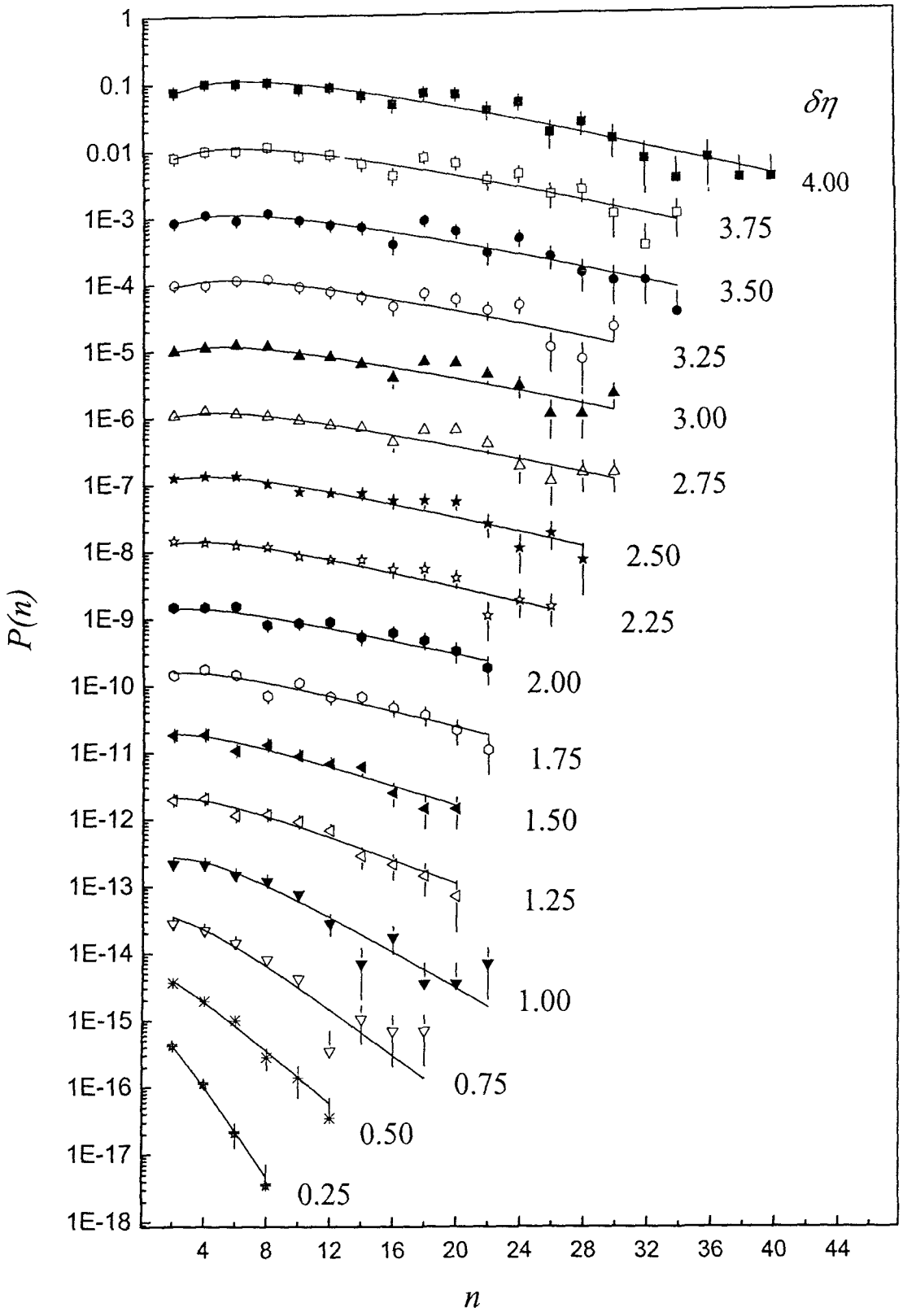

Figure 3.16: Multiplicity distributions in different pseudorapidity intervals $\Delta\eta$ for ^{28}Si- *CNO* collisions at 14.6*A GeV*. Symbols represent the experimental values and solid curves represent the best NBD fits. For $\Delta\eta = 4.00$ the distribution is plotted in the normal scale and for all subsequent intervals the probability values are multiplied by 10^{-1},10^{-2},10^{-3}, 10^{-4},....10^{-15} respectively

fitting with the negative binomial distribution (Equation 3.7) using CERN MINUTE program, keeping $\bar{n}$, k as free parameters. In the figures, the distribution corresponding to widest interval is plotted in normal scale. For all subsequent intervals the probability values are multiplied by factors 10^{-1}, 10^{-2}, 10^{-3}, 10^{-4}, 10^{-5}, 10^{-6}, 10^{-7},..., 10^{-15} respectively. Since values of the probability $P(n)$ are plotted in logarithmic scale, the error bars for a few data points for large multiplicity could not shown properly. We observe from the figures that the negative binomial distribution fits the data well with small values of χ^2/dof. The values of the free parameters $\bar{n}$, k and the χ^2/dof are listed in Tables 3.6-3.8 for ^{28}Si-*Emulsion*, ^{28}Si-*AgBr* and ^{28}Si-*CNO* collisions respectively. From the tables it can be seen that the values of k are small and are almost constant for different window sizes for collisions with all target groups, indicating that the multiplicity distributions differ significantly from the Poisson distribution ($k \rightarrow \infty$). We have also calculated the values of $<N_s>$ and dispersion D using Equation 3.9, for all $\Delta\eta$ values for ^{28}Si-*Emulsion*, ^{28}Si-*AgBr* and ^{28}Si-*CNO* collisions. These values are also listed in Tables 3.6-3.8. We observe that in all the cases values of $<N_s>$ and dispersion D increase with increase in the size of the pseudorapidity window. Further the values of $<N_s>$ and D corresponding to each pseudorapidity interval increases with increase in the target mass. This is an evidence of the production of large number of shower particles with increasing target mass. We also calculated the clan multiplicity $\overline{N}$ and size of the clans $\bar{n}_c$ for each window size $\Delta\eta$ for the three types of collisions and their values are also given in Tables 3.6-3.8. Figures 17-19 show the plots of $\overline{N}$ and $\bar{n}_c$ versus $\Delta\eta$ for ^{28}Si-*Emulsion*, ^{28}Si-*AgBr* and ^{28}Si-*CNO* collisions respectively. In all the cases we observe that the clan multiplicity $\overline{N}$ increases with increase in the window size indicating that more clusters are formed with increasing size of the pseudorapidity interval. Further it can also be observed that clan size $\bar{n}_c$ increases with increase in $\Delta\eta$ but saturate at $\Delta\eta \approx 2.0$ for collisions with all the three target groups. This shows that the size of clusters becomes approximately constant. Since the clan multiplicity do not saturate, the average number of shower particles $<N_s>$ increases with increase in the window size. However, larger values of clan size $\bar{n}_c$ are observed corresponding to each window size $\Delta\eta$ for ^{28}Si-*CNO*, ^{28}Si-*Emulsion* and ^{28}Si-*AgBr* collisions respectively. This is an evidence for the increase in the size of clusters with increase in the target mass.

Table 3.6: Results of NBD fitting for ^{28}Si-*Emulsion* collisions at 14.6*A GeV* in η-space.

$\Delta\eta$	$<N_s>$	D	Fitting results			b	$\overline{n}_c$	$\overline{N}$
			$\overline{n}$	k	χ^2/ d.o.f			
0.25	1.69	2.03	1.66	1.20	1.12	0.58	1.59	1.04
0.50	3.43	3.54	3.39	1.08	1.34	0.76	2.21	1.53
0.75	5.03	4.99	5.13	1.04	1.48	0.83	2.77	1.85
1.00	6.70	6.43	6.65	1.03	2.15	0.87	3.21	2.07
1.25	8.27	7.86	8.19	1.07	1.51	0.88	3.55	2.31
1.50	9.66	9.06	9.83	1.02	0.99	0.91	4.08	2.41
1.75	11.00	10.22	11.19	1.00	1.54	0.92	4.47	2.50
2.00	12.14	11.14	12.90	0.96	1.50	0.93	5.03	2.56
2.25	13.14	11.91	12.90	1.02	1.34	0.93	4.84	2.67
2.50	14.02	12.60	13.10	1.04	1.85	0.93	4.83	2.71
2.75	15.13	13.40	14.77	1.03	1.10	0.93	5.25	2.81
3.00	15.74	13.86	15.96	1.05	1.06	0.94	5.46	2.92
3.25	16.58	14.34	16.60	1.10	0.94	0.94	5.43	3.06
3.50	16.96	14.63	16.86	1.10	1.09	0.94	5.49	3.07
3.75	17.36	14.86	17.46	1.10	1.13	0.94	5.62	3.11
4.00	17.91	15.05	17.96	1.20	1.02	0.94	5.40	3.32

Table 3.7: Results of NBD fitting for ^{28}Si-$AgBr$ collisions at 14.6A GeV in η-space.

$\Delta\eta$	$<N_s>$	D	Fitting results			b	$\overline{n}_c$	$\overline{N}$
			$\overline{n}$	k	χ^2/d.o.f			
0.25	2.60	2.37	2.58	1.70	1.271	0.60	1.64	1.57
0.50	5.26	4.18	5.46	1.79	1.974	0.75	2.18	2.50
0.75	7.80	5.86	7.94	1.82	1.961	0.81	2.60	3.06
1.00	10.22	7.50	12.15	1.54	0.684	0.89	3.61	3.36
1.25	12.44	8.94	12.87	1.80	1.811	0.88	3.41	3.78
1.50	14.70	10.35	15.60	1.60	1.907	0.91	4.11	3.80
1.75	16.49	11.50	19.60	1.43	0.931	0.93	5.10	3.84
2.00	18.12	12.52	20.53	1.47	1.118	0.93	5.16	3.98
2.25	19.66	13.36	21.17	1.50	1.704	0.93	5.20	4.07
2.50	20.93	14.28	23.73	1.47	1.596	0.94	5.68	4.18
2.75	21.93	14.90	24.40	1.47	1.840	0.94	5.79	4.22
3.00	22.98	15.51	24.98	1.48	1.540	0.94	5.85	4.27
3.25	23.96	16.00	25.50	1.50	1.220	0.94	5.88	4.34
3.50	24.96	16.37	25.60	1.57	1.825	0.94	5.72	4.48
3.75	25.38	16.61	27.08	1.58	1.256	0.94	5.91	4.58
4.00	25.70	16.71	28.02	1.67	1.117	0.94	5.83	4.81

Table 3.8: Results of NBD fitting for ^{28}Si-CNO collisions at 14.6A GeV in η-space.

$\Delta\eta$	$<N_s>$	D	Fitting results			b	$\overline{n}_c$	$\overline{N}$
			$\overline{n}$	k	χ^2/d.o.f			
0.25	1.10	1.34	1.07	1.38	0.178	0.44	1.35	0.79
0.50	2.15	2.17	2.16	1.35	0.665	0.62	1.67	1.29
0.75	3.41	3.38	3.06	1.70	2.883	0.64	1.75	1.75
1.00	4.50	4.21	4.40	1.90	1.728	0.70	1.93	2.28
1.25	5.51	5.03	5.79	1.49	0.926	0.80	2.45	2.36
1.50	6.40	5.63	6.63	1.41	1.065	0.82	2.70	2.45
1.75	7.41	6.31	8.14	1.40	1.254	0.85	3.03	2.69
2.00	8.29	6.83	9.28	1.34	0.743	0.87	3.35	2.77
2.25	9.13	7.37	9.35	1.51	0.678	0.86	3.14	2.98
2.50	9.92	7.84	9.74	1.56	0.741	0.86	3.15	3.09
2.75	10.74	8.26	10.84	1.60	0.707	0.87	3.30	3.28
3.00	11.13	8.47	11.25	1.66	0.984	0.87	3.30	3.40
3.25	11.52	8.63	11.31	1.78	1.216	0.86	3.18	3.55
3.50	12.11	8.84	11.87	1.81	1.126	0.87	3.24	3.66
3.75	12.33	8.93	11.95	1.90	1.049	0.86	3.17	3.77
4.00	12.74	9.05	12.16	2.00	0.723	0.86	3.11	3.91

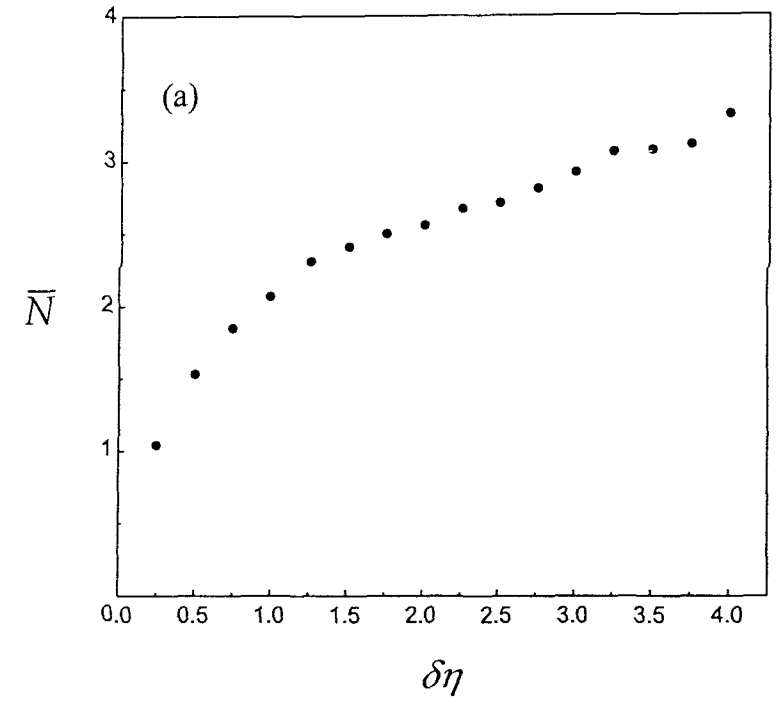

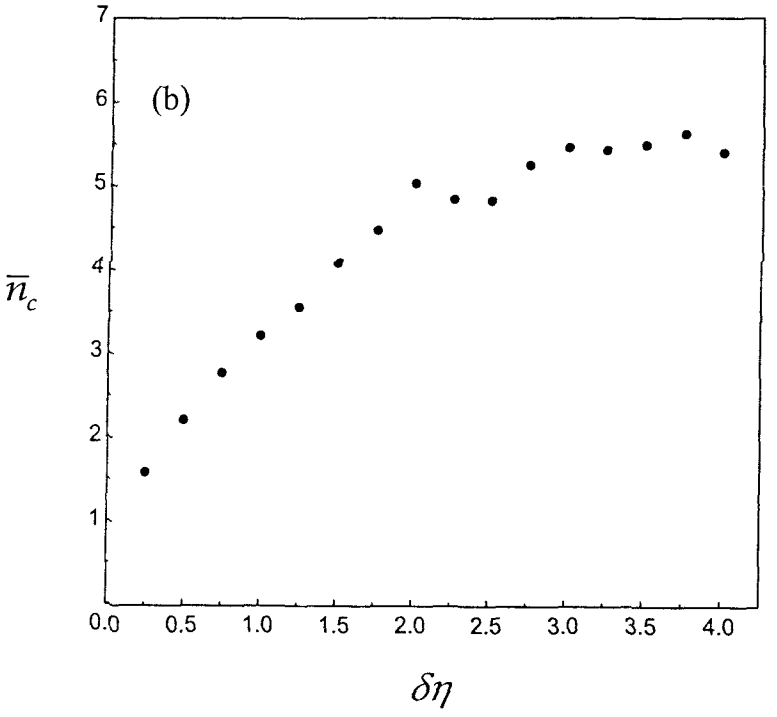

Figure 3.17: (a) $\overline{N}$ versus $\delta\eta$ plot for ^{28}*Si-Emulsion* collisions at 14.6*A GeV*.
(b) $\overline{n}_c$ versus $\delta\eta$ plot for ^{28}*Si-Emulsion* collisions at 14.6*A GeV*.

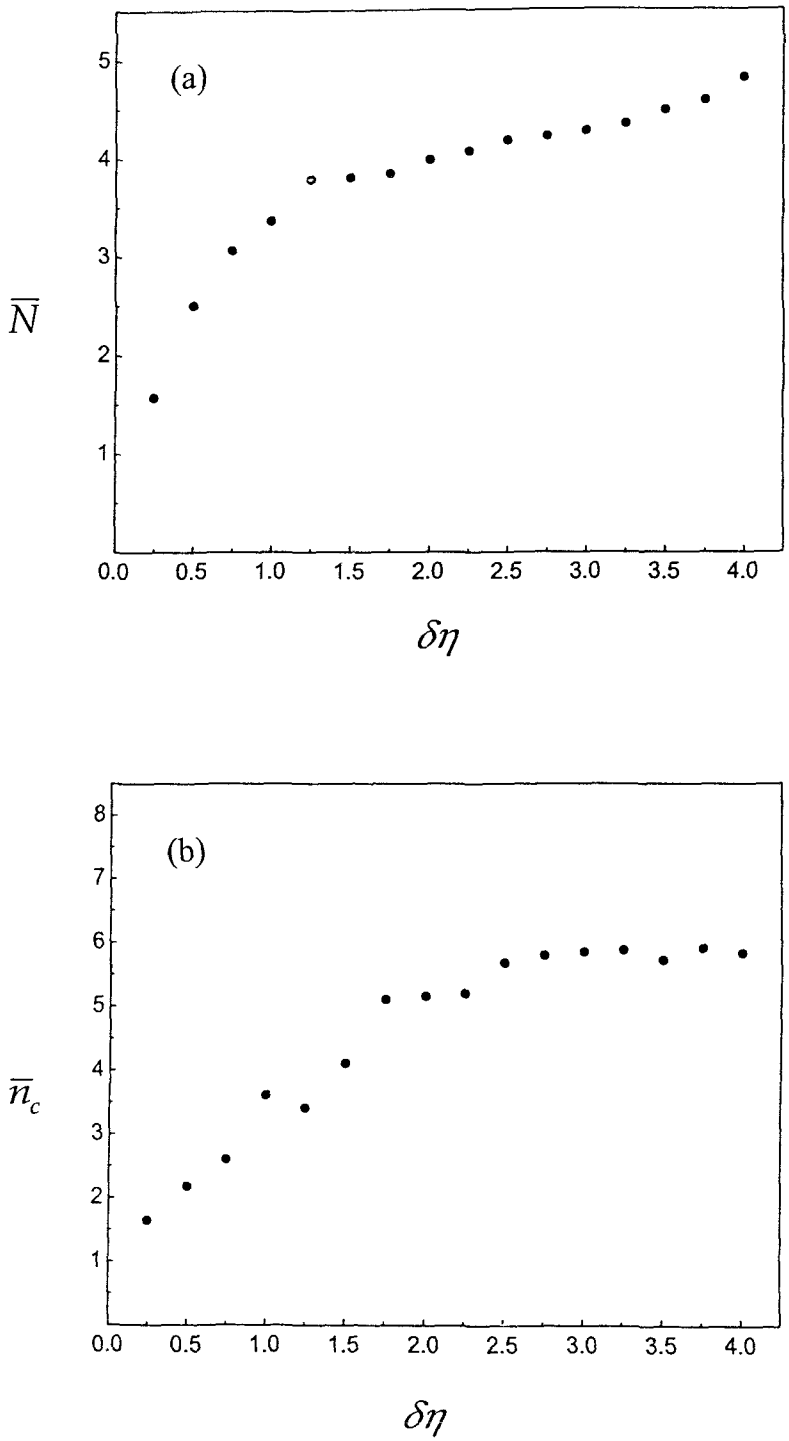

Figure 3.18: (a) $\overline{N}$ versus $\delta\eta$ plot for ^{28}Si-$AgBr$ collisions at 14.6A GeV.
(b) $\overline{n}_c$ versus $\delta\eta$ plot for ^{28}Si-$AgBr$ collisions at 14.6A GeV.

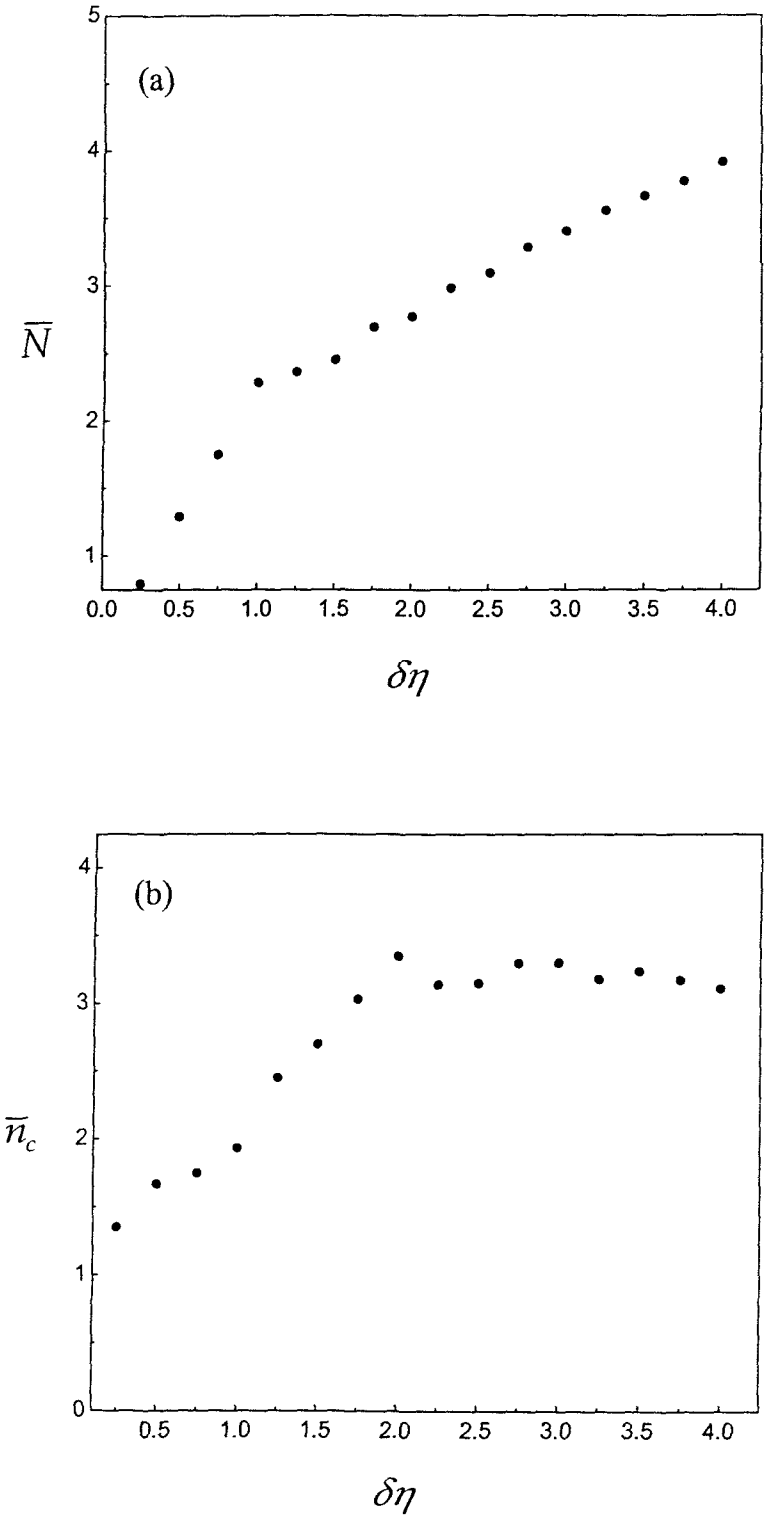

Figure 3.19: (a) $\overline{N}$ versus $\delta\eta$ plot for ^{28}Si-CNO collisions at 14.6A GeV.
(b) $\overline{n}_c$ versus $\delta\eta$ plot for ^{28}Si-CNO collisions at 14.6A GeV.

Now we study the validity of the negative binomial distributions in the azimuthal angle space φ. In the azimuthal plane, shower particles are isotropically distributed with φ values ranging from 0 to 2π and thus we observe a plateau for distributions of shower particles in the azimuthal plane. The centers of all such distributions are considered to be situated at $\varphi = \pi$. Each of the φ windows was selected symmetrically about this value. Thus a window of width $\Delta\varphi$ lies between $\pi-\frac{\Delta\varphi}{2}<\varphi<\pi+\frac{\Delta\varphi}{2}$. In our analysis we have taken $\Delta\varphi$= 360, 315, 270, 225, 180, 135, 90 and 45 degrees.

In Figures 3.20-3.22 symbols show the multiplicity distributions of shower particles produced in ^{28}*Si-Emulsion*, ^{28}*Si-AgBr* and ^{28}*Si-CNO* collisions respectively for different window sizes in φ space and the solid curves represent the fitting of the negative binomial distribution according to Equation 3.7, keeping $\overline{n}$, k as free parameters. In the figures, the distribution corresponding to widest interval is plotted in normal scale. For all subsequent intervals the probability values are multiplied by factors 10^{-1}, 10^{-2}, 10^{-3}, 10^{-4}, 10^{-5}, 10^{-6} and 10^{-7} respectively. We observe from the figures that the negative binomial distribution fits the data well with small values of χ^2/dof. The values of the free parameters $\overline{n}$, k and the χ^2/dof are listed in Tables 3.9-3.11 for ^{28}*Si-Emulsion*, ^{28}*Si-AgBr* and ^{28}*Si-CNO* collisions respectively. From the tables we find that the values of k are small and are almost constant for different window sizes for collisions with all target groups, indicating that the multiplicity distributions differ significantly from the Poisson distribution ($k \to \infty$). We have also calculated the values of $<N_s>$ and dispersion D using Equation 3.9 for all $\Delta\varphi$ values for ^{28}*Si-Emulsion*, ^{28}*Si-AgBr* and ^{28}*Si-CNO* collisions. These values are also listed in Tables 3.9-3.11. From the tables we can see that in all the cases, values of $<N_s>$ and dispersion D increase with increase in the size of the azimuthal window. Also the values of $<N_s>$ and D corresponding to each φ interval increases with increase in the target mass. These results are similar to the corresponding results in η space. Further, the clan multiplicity $\overline{N}$ and size of the clans $\overline{n}_c$ for each window size $\Delta\varphi$ for the three types of collisions are calculated and values obtained are given in Tables 3.9-3.11. Figures 23-25 show the plots of $\overline{N}$ and $\overline{n}_c$ versus $\Delta\varphi$ for ^{28}*Si-Emulsion*, ^{28}*Si-AgBr* and ^{28}*Si-CNO* collisions respectively. As observed in the pseudorapidity space, in all the cases we again observe that the clan multiplicity $\overline{N}$ increases with increase in the window size,

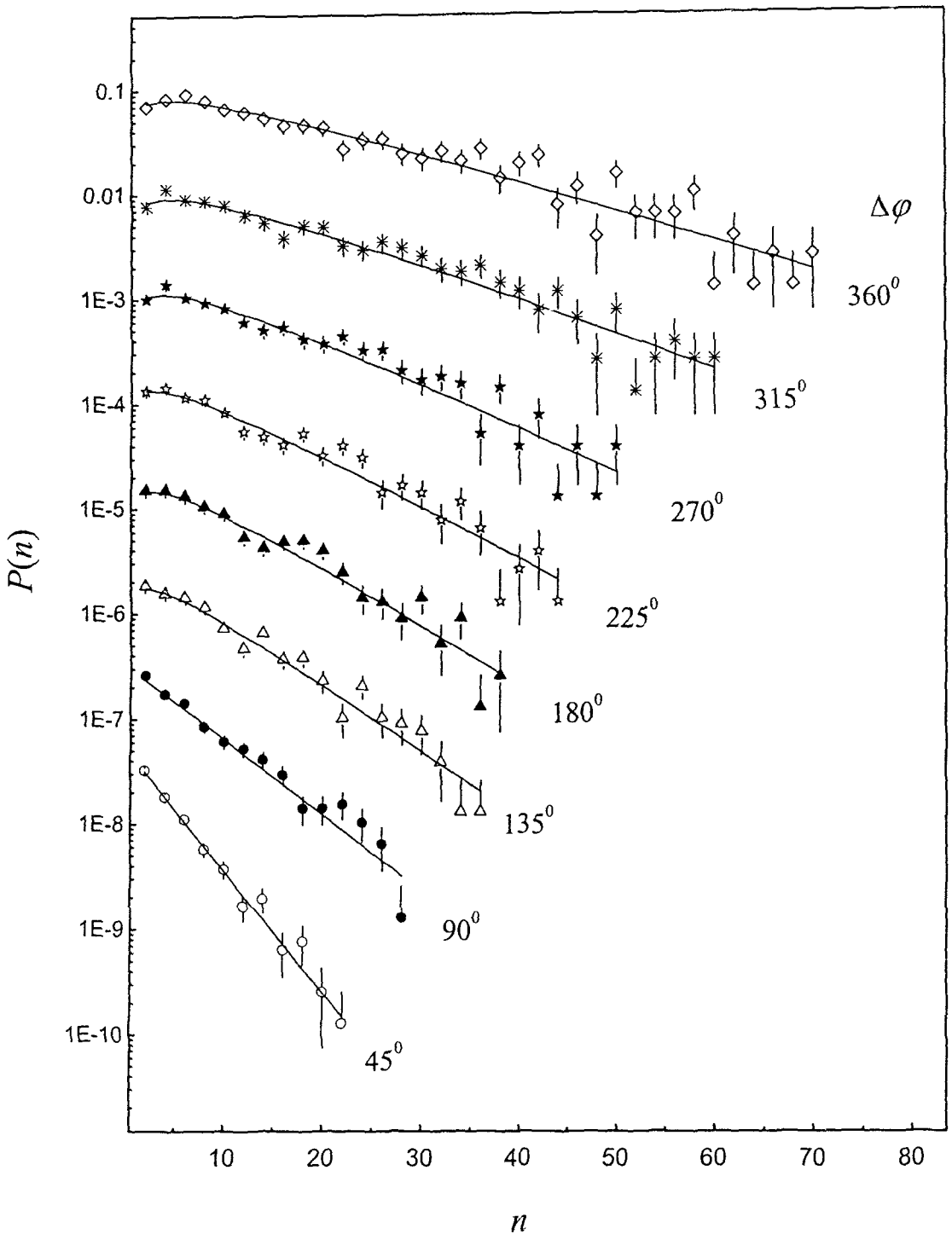

Figure 3.20: Multiplicity distributions in different azimuthal angle intervals $\Delta\varphi$ for ^{28}*Si-Emulsion* collisions at 14.6*A GeV*. Symbols represent the experimental values and solid curves represent the best NBD fits. For $\Delta\varphi \approx 360^{\circ}$ the distribution is plotted in the normal scale and for all subsequent intervals the probability values are multiplied by 10^{-1},10^{-2},10^{-3}, 10^{-4}, 10^{-5}, 10^{-6}, 10^{-7} respectively.

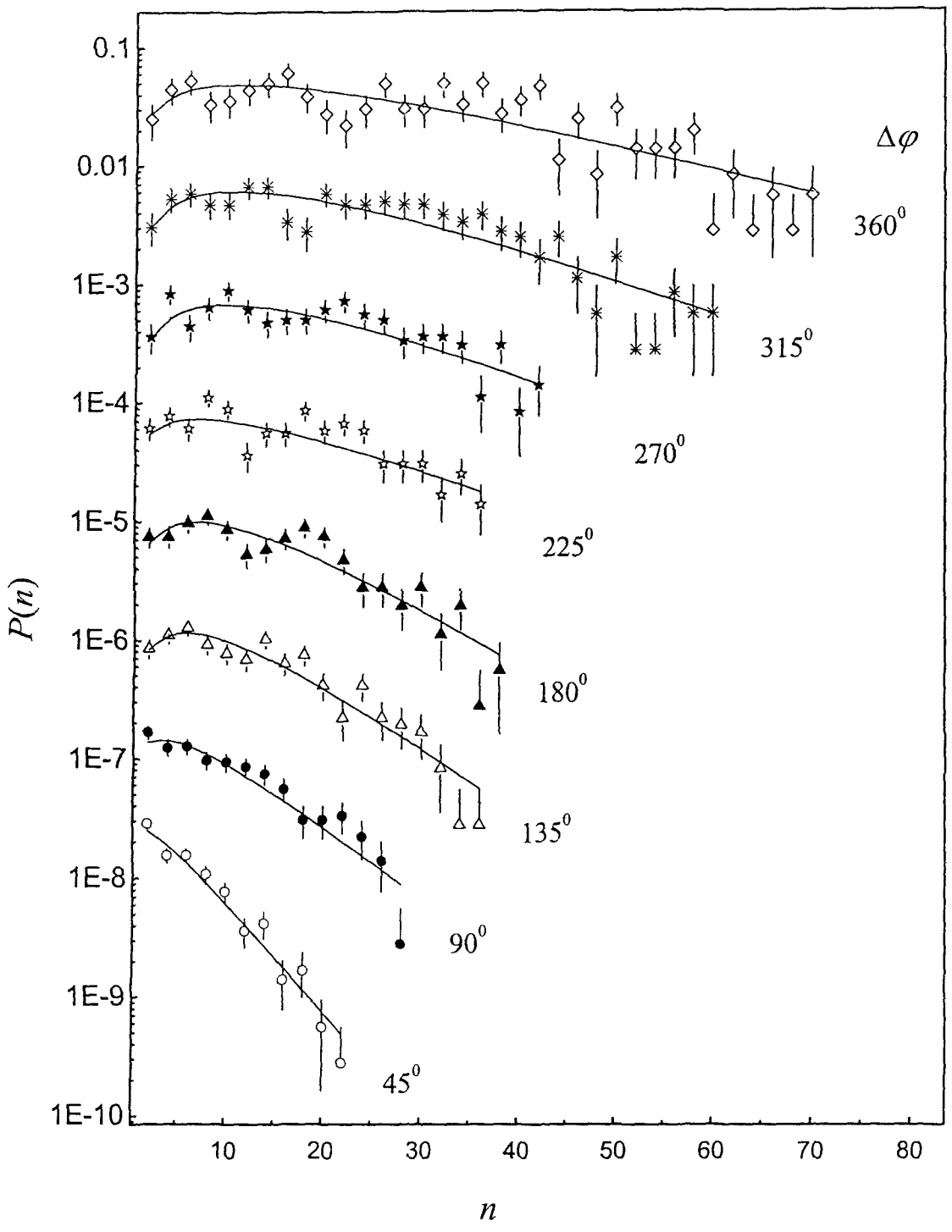

Figure 3.21: Multiplicity distributions in different azimuthal angle intervals $\Delta\varphi$ for ^{28}Si-$AgBr$ collisions at 14.6*A GeV*. Symbols represent the experimental values and solid curves represent the best NBD fits. For $\Delta\varphi = 360^{\circ}$ the distribution is plotted in the normal scale and for all subsequent intervals the probability values are multiplied by 10^{-1}, 10^{-2}, 10^{-3}, 10^{-4}, 10^{-5}, 10^{-6}, 10^{-7} respectively.

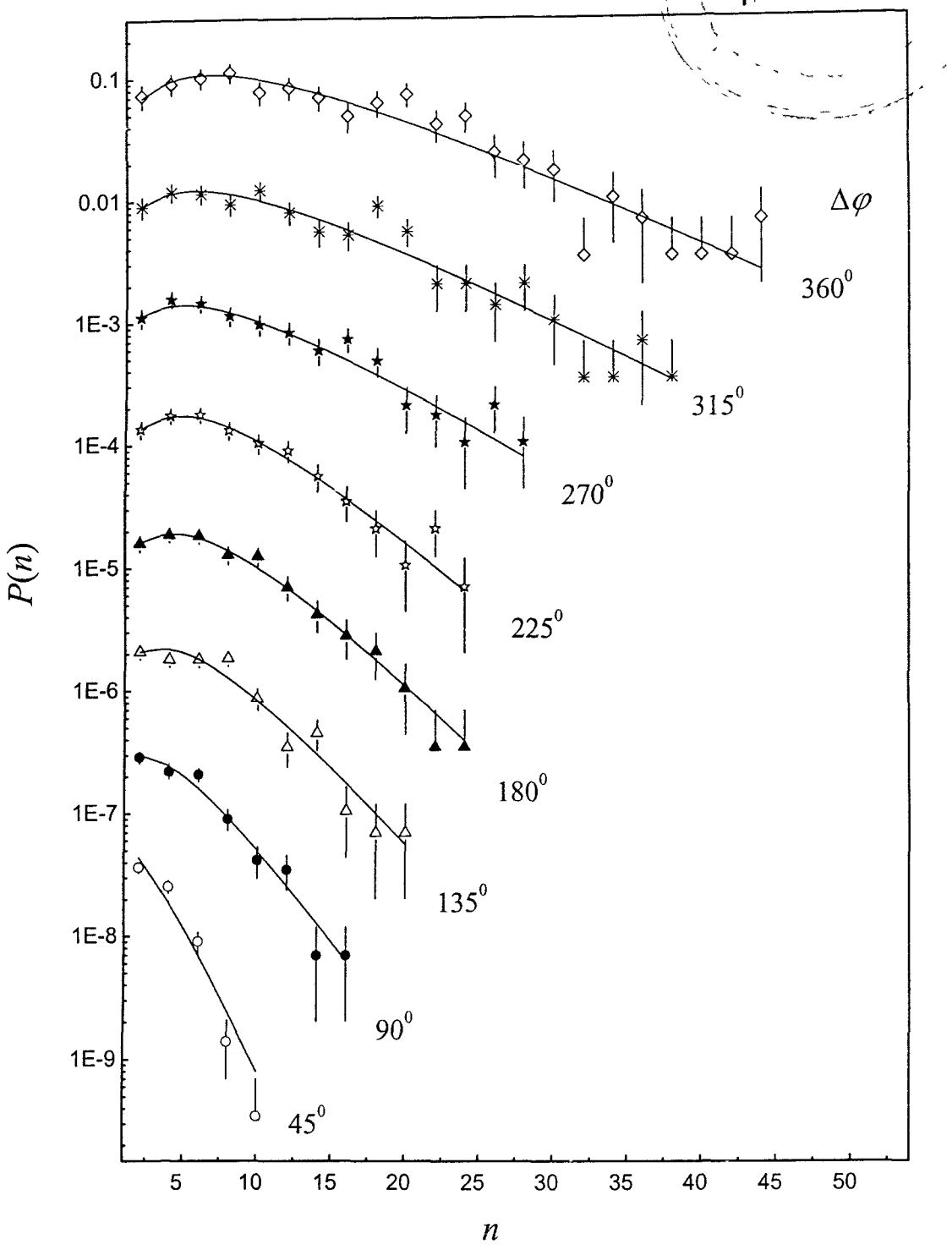

Figure 3.22: Multiplicity distributions in different azimuthal angle intervals $\Delta\varphi$ for ^{28}Si-*CNO* collisions at 14.6*A GeV*. Symbols represent the experimental values and solid curves represent the best NBD fits. For $\Delta\varphi = 360^{\circ}$ the distribution is plotted in the normal scale and for all subsequent intervals the probability values are multiplied by 10^{-1}, 10^{-2}, 10^{-3}, 10^{-4}, 10^{-5}, 10^{-6}, 10^{-7} respectively.

Table 3.9: Results of NBD fitting for ^{28}*Si-Emulsion* collisions at 14.6*A GeV* in φ-space.

$\Delta\varphi$	$\langle N_s \rangle$	D	Fitting results			b	$\overline{n}_c$	$\overline{N}$
			$\overline{n}$	k	χ^2/d.o.f			
45	3.23	3.65	3.16	0.94	0.53	0.77	2.28	1.38
90	5.90	5.68	5.60	1.04	1.10	0.84	2.90	1.93
135	7.90	6.88	7.54	1.26	1.32	0.86	3.08	2.45
180	9.23	7.91	8.83	1.31	1.32	0.87	3.29	2.68
225	10.55	8.99	9.98	1.28	1.31	0.89	3.59	2.78
270	12.71	10.56	12.14	1.34	1.30	0.90	3.92	3.09
315	15.51	12.78	15.17	1.33	0.94	0.92	4.53	3.35
360	18.72	15.56	17.72	1.27	1.02	0.93	5.16	3.44

Table 3.10: Results of NBD fitting for ^{28}Si-$AgBr$ collisions at 14.6A GeV in φ-space.

$\Delta\varphi$	$\langle N_s \rangle$	D	Fitting results			b	$\overline{n}_c$	$\overline{N}$
			$\overline{n}$	k	χ^2/d.o.f			
45	5.03	4.38	4.86	1.24	1.32	0.80	2.46	1.98
90	8.77	6.59	8.80	1.49	1.28	0.86	3.06	2.88
135	11.43	7.78	11.45	1.91	1.27	0.86	3.08	3.72
180	13.36	8.85	13.53	1.92	1.73	0.88	3.38	4.00
225	15.22	9.98	18.72	1.64	1.93	0.92	4.53	4.13
270	18.17	11.62	20.60	1.86	1.42	0.92	4.45	4.63
315	22.18	14.09	22.85	1.85	1.46	0.93	4.77	4.79
360	27.08	17.28	28.44	1.63	1.62	0.95	5.99	4.75

Table 3.11: Results of NBD fitting for ^{28}Si-*CNO* collisions at 14.6*A GeV* in φ-space.

$\Delta\varphi$	$\langle N_s \rangle$	D	Fitting results			b	$\overline{n}_c$	$\overline{N}$
			$\overline{n}$	k	χ^2/d.o.f			
45	2.02	1.86	1.90	1.67	4.47	0.53	1.50	1.27
90	4.00	3.14	3.98	2.14	1.21	0.65	1.77	2.25
135	5.56	3.92	5.51	2.43	1.78	0.69	1.92	2.88
180	6.51	4.57	6.60	2.50	0.30	0.73	2.04	3.23
225	7.45	5.37	7.38	2.47	0.35	0.75	2.16	3.42
270	9.13	6.59	9.08	1.95	0.56	0.82	2.69	3.38
315	11.11	7.90	10.75	1.93	0.96	0.85	2.96	3.63
360	13.11	9.15	12.51	2.02	0.85	0.86	3.14	3.99

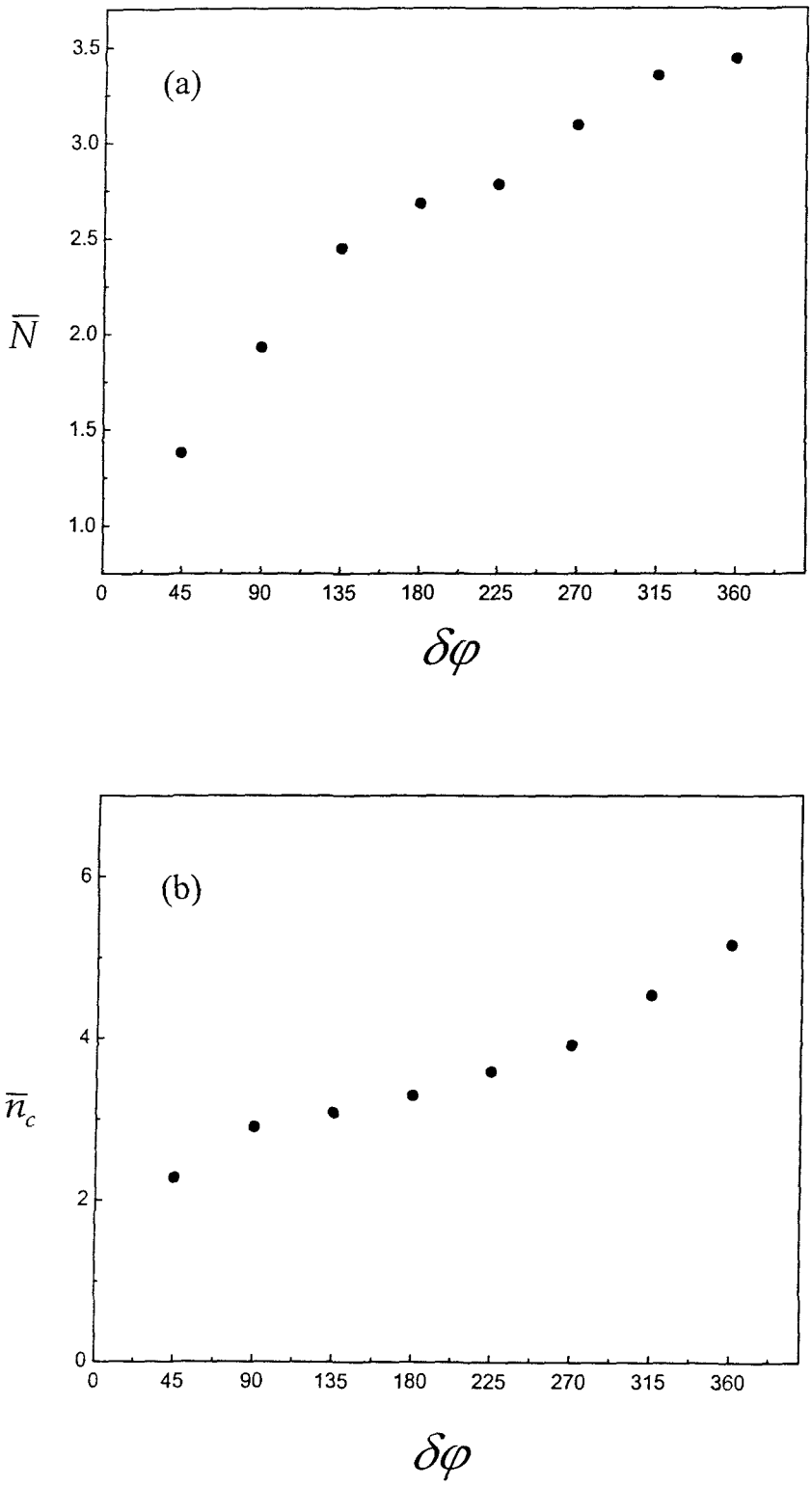

Figure 3.23: (a) $\overline{N}$ versus $\delta\varphi$ plot for ^{28}*Si-Emulsion* collisions at 14.6*A GeV*.
(b) $\overline{n}_c$ versus $\delta\varphi$ plot for ^{28}*Si-Emulsion* collisions at 14.6*A GeV*.

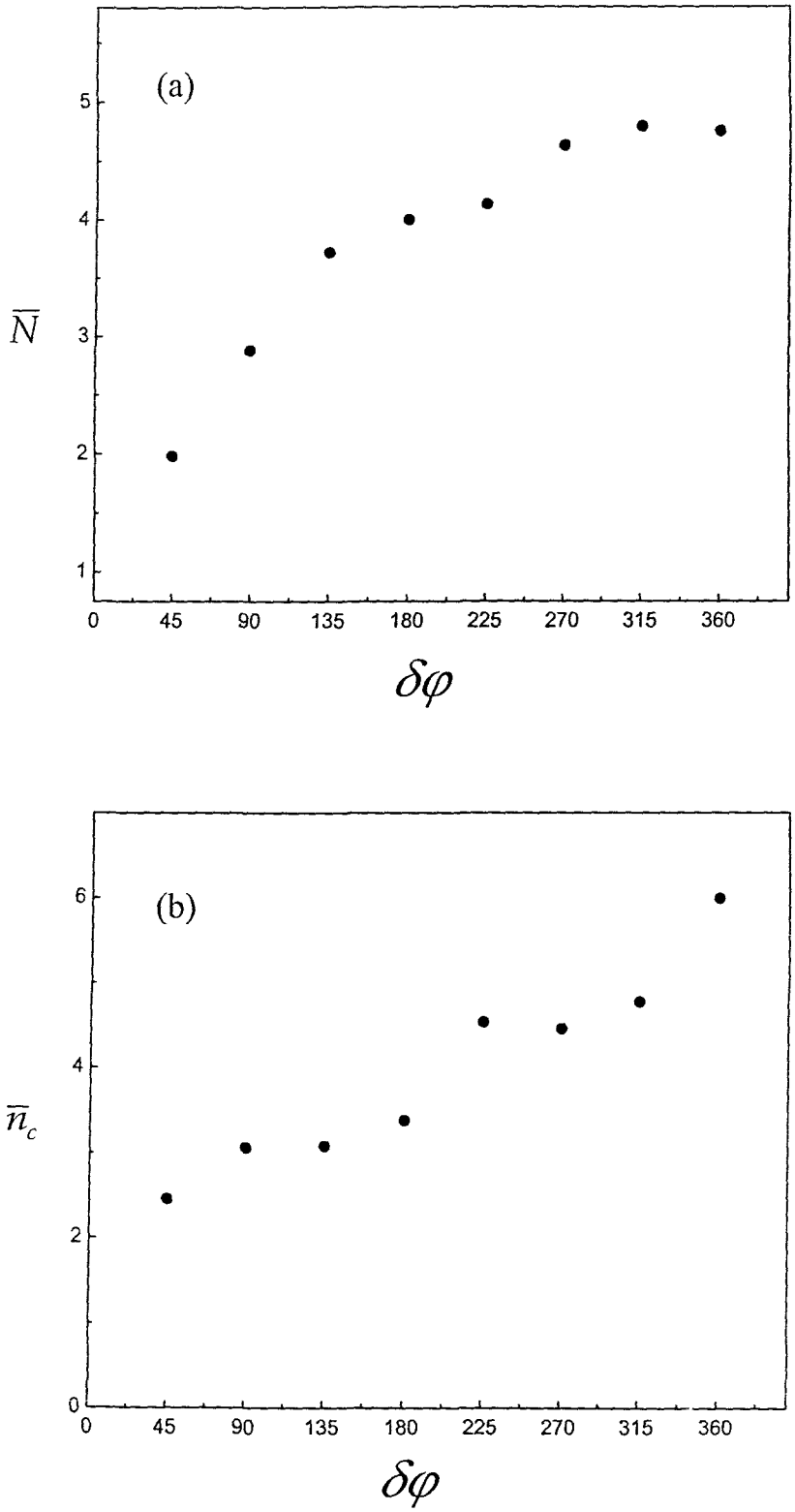

Figure 3.24: (a) $\overline{N}$ versus $\delta\varphi$ plot for ^{28}Si-$AgBr$ collisions at 14.6A GeV.
(b) $\bar{n}_c$ versus $\delta\varphi$ plot for ^{28}Si-$AgBr$ collisions at 14.6A GeV.

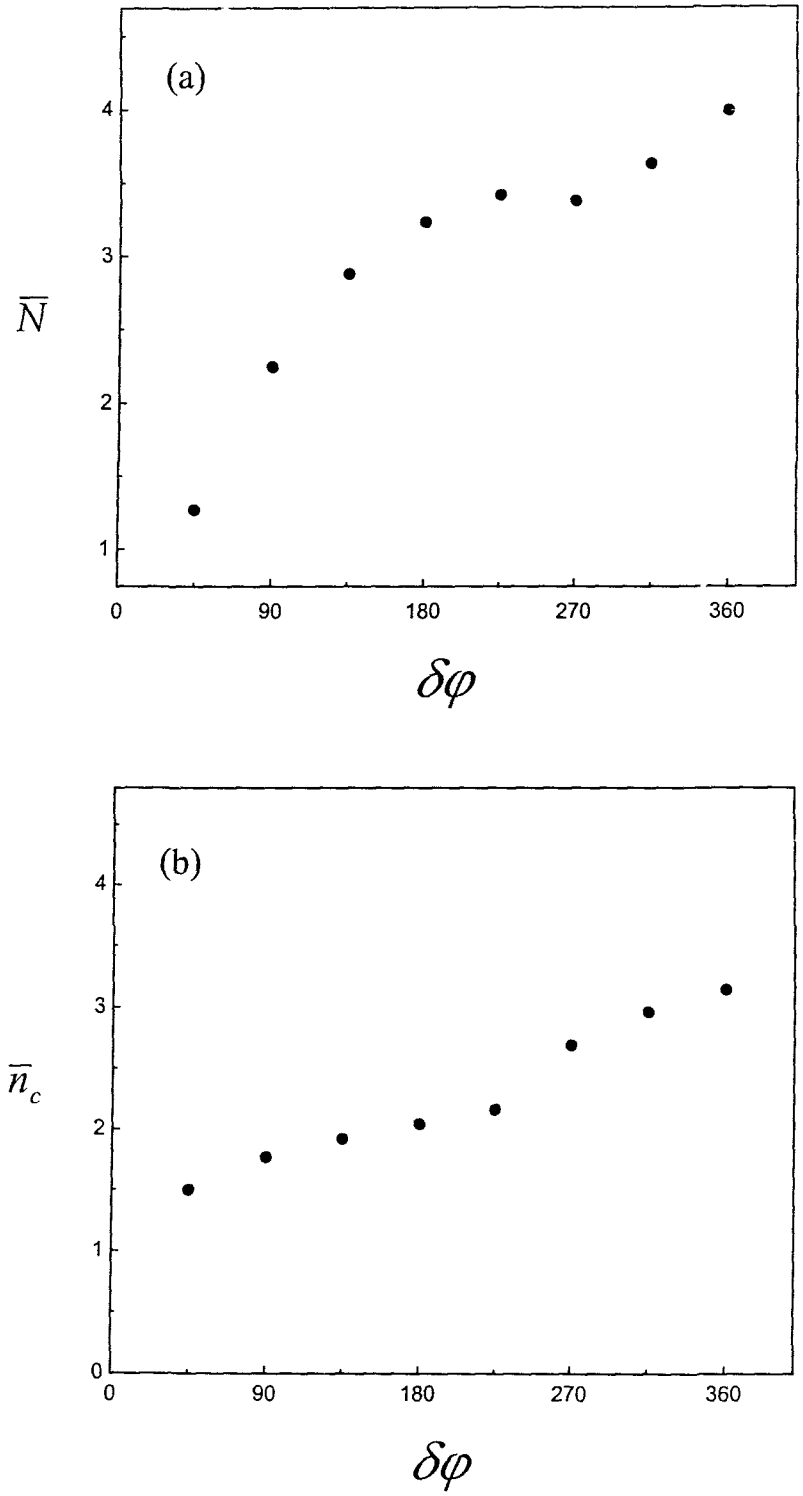

Figure 3.25: (a) $\overline{N}$ versus $\delta\varphi$ plot for ^{28}Si-CNO collisions at 14.6A GeV.
(b) $\overline{n}_c$ versus $\delta\varphi$ plot for ^{28}Si-CNO collisions at 14.6A GeV.

which is another evidence for more clusters being formed with increase in the size of the azimuthal angle interval. Further, it can also be observed that the clan size $\overline{n}_c$ increases with increase in the window size and does not saturate as observed in the pseudorapidity space for collisions with all the three target groups. Since both the clan multiplicity $\overline{N}$ and the clan size $\overline{n}_c$ increase with the increase in the azimuthal angle interval $\Delta\varphi$, the average number of produced shower particles $<N_s>$ increases with increase in the window size. Further, larger values of clan size $\overline{n}_c$ are observed corresponding to each window size $\Delta\varphi$ for $^{28}Si\text{-}CNO$, $^{28}Si\text{-}Emulsion$ and $^{28}Si\text{-}AgBr$ collisions respectively, which is an evidence for the increase in the size of clusters with increase in the target mass.

3.11 Characteristics of Charged Particles in the Forward and Backward Hemispheres

The study of shower and grey particles emitted in the backward ($\theta_{Lab} \geq 90^0$) and forward ($\theta_{Lab} < 90^0$) hemispheres has become a subject of considerable interest. This is due to the fact that the emission of hadrons in the backward hemisphere is kinamatically restricted (limited cascading) as compared with the emission in the forward hemisphere (more branched cascading). Emission of relativistic hadrons in the backward hemisphere beyond the kinematic limit may be an evidence for exotic production mechanism, such as production from clusters [47-51]. Baldin [52] suggested that the dominant mechanism for producing relativistic hadrons was the interaction between the incident nucleons from the projectile and the multinucleon clusters in the target. There are models to understand these phenomena [47,50,53,54], but till now, we do not have a clear understanding of the mechanism of production of relativistic hadrons in the backward hemisphere in relativistic nucleus-nucleus collisions. In the following sections we study the characteristics of charged particles emitted in the forward and backward hemispheres for our data.

3.11.1 Multiplicities of Shower and Grey Particles in the Forward and Backward Hemispheres

The average multiplicities of shower and grey particles emitted in both the forward and backward hemispheres for $^{28}Si\text{-}Emulsion$, $^{28}Si\text{-}AgBr$ and $^{28}Si\text{–}CNO$ collisions

Table 3.12: The values of the average multiplicities of the shower and grey particles in the forward and backward hemispheres.

Projectiles	Energy *A GeV*	Reaction Group	$<N_s^F>$	$<N_s^B>$	$<N_g^F>$	$<N_g^B>$	Ref.
^{6}Li	4.5	*Emulsion*	5.30 ± 0.15	0.41 ± 0.01	2.08 ± 0.08	0.98 ± 0.05	55
^{12}C	4.5	*Emulsion*	7.11 ± 0.02	0.45 ± 0.01	4.52 ± 0.20	1.38 ± 0.07	56
^{22}Ne	4.1	*Emulsion*	9.85 ± 0.04	0.45 ± 0.01	4.80 ± 0.20	1.42 ± 0.08	57
^{22}Ne	4.1	*Emulsion*	9.71 ± 0.23	0.40 ± 0.02	-	-	58
^{28}Si	4.5	*Emulsion*	11.36 ± 0.09	0.44 ± 0.02	4.98 ± 0.18	1.42 ± 0.07	59
^{28}Si	4.5	*Emulsion*	11.43 ± 0.35	0.35 ± 0.02	-	-	58
^{28}Si	14.6	*CNO*	12.97 ± 0.54	0.14 ± 0.02	1.37 ± 0.54	0.24 ± 0.02	Present work
		Emulsion	18.45 ± 0.54	0.28 ± 0.02	2.90 ± 0.54	0.95 ± 0.02	
		AgBr	26.61 ± 0.89	0.48 ± 0.02	5.17 ± 0.89	1.86 ± 0.04	
^{32}S	4.5	*CNO*	8.91 ± 0.41	0.09 ± 0.02	1.11 ± 0.06	0.16 ± 0.02	2
		Emulsion	14.58 ± 0.48	0.46 ± 0.03	3.17 ± 0.14	0.82 ± 0.05	
		AgBr	18.15 ± 0.91	0.69 ± 0.02	4.47 ± 0.22	1.23 ± 0.06	

at 14.6*A GeV* are calculated. These values are presented in Table 3.12 along with the corresponding values taken from references [2,55-59]. We observe from the table that the average multiplicity of shower particles in the forward hemisphere increases with projectile size and energy, whereas in the backward hemisphere it is almost independent of projectile size and energy. Further, it is also observed that the average multiplicity of shower particles in the backward hemisphere increases with target size. These results support the mechanism, which considers the backward particle production as a consequence of the isotropic decay of a highly excited target nucleus in its rest frame after the forward particle production.

We also observe from the table that the average multiplicities of shower and grey particles in both the hemispheres increase with increasing target size. These dependences on the target size can be parameterized by the following power law form

$$\left\langle N_i^k \right\rangle = \beta_i^k \left\langle A_T \right\rangle^{\alpha_i^k} \qquad 3.16$$

where $i = s$ (shower) or g (grey) and $k = F$ (for forward hemisphere) or B (for backward hemisphere).

Figures 3.26 (a) – (d) show the plots of $<N_s^F>$, $<N_s^B>$, $<N_g^F>$ and $<N_g^B>$ versus $<A_T>$ respectively for our data. The smooth curves in the figures are the fits to the data points using Equation 3.16. The values of the fitting parameters β_i^k and α_i^k obtained are given in Table 3.13. It can be seen from the table that the values of the parameters α_s^F and α_g^F for our data are consistent with the corresponding values for ^{32}S-*Emulsion* collisions at 4.5A GeV [2] and with those given in references [60,61]. From the table we also observe that the values of α_s^B and α_g^B are greater than the values of these parameters in the forward hemisphere (α_s^F and α_g^F) for our data. Similar results have also been reported for ^{32}S-*Emulsion* collisions at 4.5*A GeV* [2]. Many investigators [55,57.59,62] have suggested that the dominant mechanism for producing such backward pions is the collision between the incident nucleon and the multinucleon clusters in the target. Therefore, the dependence of the backward emission of pions on target size is expected to be more pronounced than that for the forward emission.

Further, to investigate the effect of mass and energy of the projectile on shower and grey particles emitted in nucleus-nucleus collisions, the forward backward multiplicity ratios for our data have been calculated for these particles for collisions with different target groups. The values of the forward-backward ratios for different N_h intervals

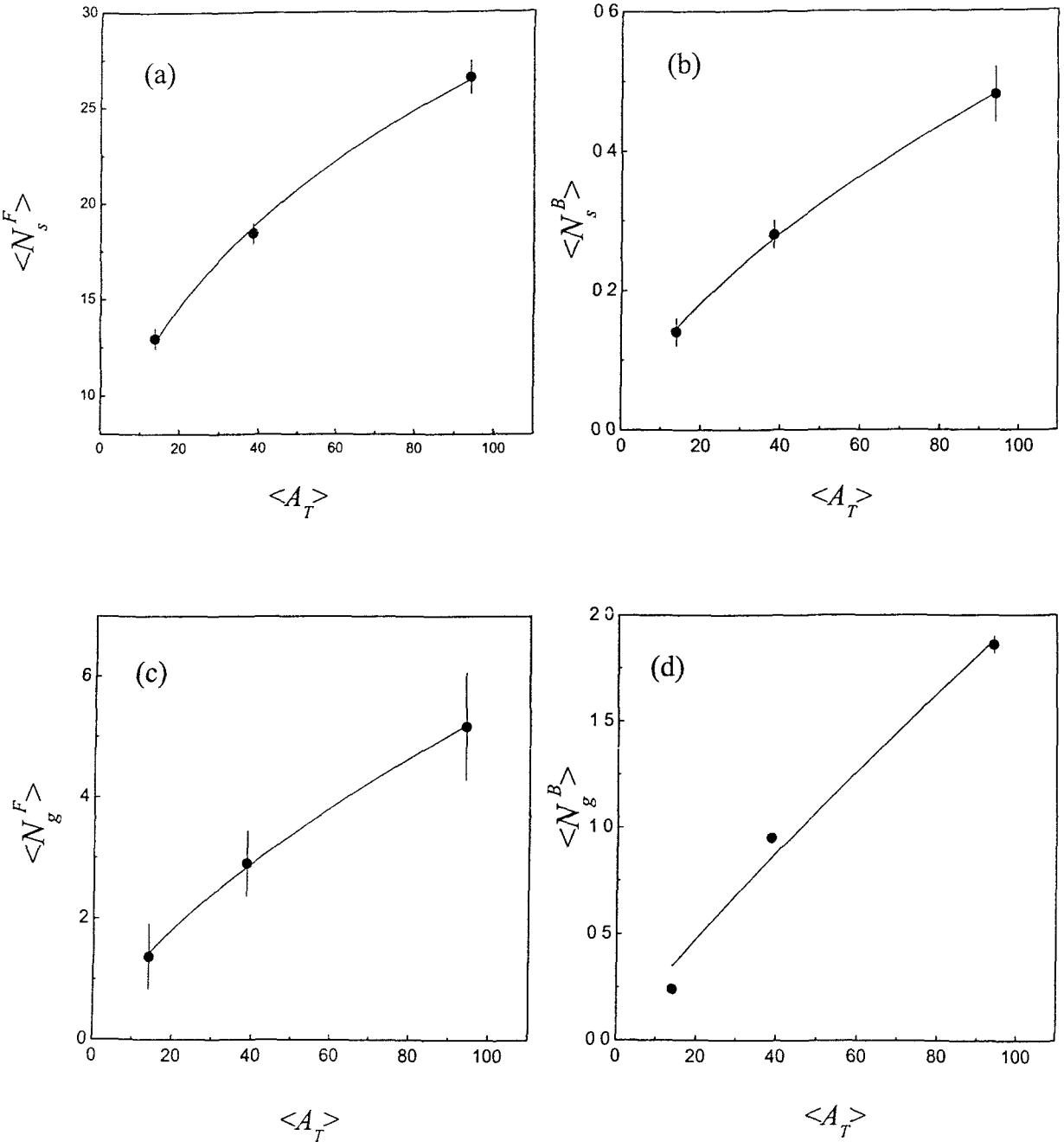

Figure 3.26: (a) $<N_s^F>$ versus $<A_T>$ plot, (b) $<N_s^B>$ versus $<A_T>$ plot, (c) $<N_g^F>$ versus $<A_T>$ plot and (d) $<N_g^B>$ versus $<A_T>$ plot for our data. The smooth curve in each plot represents fit to the data points using Equation 3.2.

Table 3.13: The values of the fitting parameters of Equation 3.16 for ^{28}*Si-Emulsion* collisions at 14.6*A GeV* and ^{32}*S-Emulsion* collisions at 4.5*A GeV* [2]

Parameters	^{28}*Si-Emulsion* at 14.6*A GeV*	^{32}*S-Emulsion* at 4.5*A GeV*
α_s^F	0.38 ± 0.02	0.44 ± 0.03
α_s^B	0.63 ± 0.02	1.06 ± 0.09
β_s^F	4.62 ± 0.35	4.98 ± 0.22
β_s^B	0.03 ± 0.00	-2.27 ± 0.17
α_g^F	0.68 ± 0.03	0.75 ± 0.06
α_g^B	0.88 ± 0.16	1.05 ± 0.08
β_g^F	0.24 ± .03	-0.83 ± .06
β_g^B	0.03 ± .02	-0.21 ± .02

Table 3.14: The forward-backward multiplicity ratios for shower, grey and black particles for different projectiles in different N_h intervals.

Projectiles	Energy *A GeV*		N_h (1-7)	N_h (8-17)	N_h (18-27)	N_h28	Total	Ref.
^{12}C	4.5	$(F/B)_s$	44.20	27.00	22.50	18.50	16.93	56
		$(F/B)_g$	4.08	3.41	3.20	3.30	3.51	
^{22}Ne	4.1	$(F/B)_s$	48.04	27.54	21.21	16.58	21.89	57
		$(F/B)_g$	4.80	3.30	3.10	2.90	3.30	
^{28}Si	4.5	$(F/B)_s$	62.40	44.04	23.64	17.88	25.82	62
		$(F/B)_g$	4.40	3.50	2.90	3.10	3.52	
^{28}Si	14.6	$(F/B)_s$	98.30	66.92	52.18	39.79	66.04	*
		$(F/B)_g$	5.40	3.20	2.62	2.73	3.07	
		$(F/B)_b$	1.49	1.24	1.28	1.19	1.30	
^{32}S	4.5	$(F/B)_s$	95.50	32.53	20.20	21.47	31.76	2
		$(F/B)_g$	6.70	3.51	3.06	4.13	3.91	

* Present work

obtained for our data along with corresponding values for different projectiles [2,56,57,62] are listed in Table 3.14. From the table we observe that the values of the forward-backward ratios for shower particles decrease rapidly with increasing target size (N_h) and increase with increase in projectile size and energy. This shows the increase in the number of produced shower particles with projectile size and energy. The forward-backward ratio for grey particles exhibits almost a limiting behaviour.

3.11.2 Multiplicity Distributions of Particles Emitted in the Backward Hemisphere

We study the multiplicity distributions of shower and grey particles emitted in the backward hemisphere for ^{28}Si-*Emulsion*, ^{28}Si-*AgBr* and ^{28}Si–*CNO* collisions at 14.6*A GeV*. The backward multiplicity distribution of the emitted shower or grey particles can be represented by a decay exponential law formula [2]

$$P\left(N_i^B\right) = P_i \, e^{-\lambda_i^B N_i^B}, \qquad 3.17$$

where i represents the shower or grey particles. The above relation represents the fundamental equation of the decay of an excited system.

Figures 3.27 (a) – (c) and (d) – (f) show the plots of $P(N_g^B)$ versus N_g and $P(N_s^B)$ versus N_s for the collisions of ^{28}Si in *Emulsion* and with *CNO* and *AgBr* target groups at 14.6*A GeV* respectively. In the figures symbols represent the experimental data points and the straight lines represent the fittings according to the decay exponential law (Equation 3.17). The values of λ_s^B and λ_g^B obtained by fitting Equation 3.17 to our data points and the corresponding data points for different projectiles taken from reference [2] are listed in Table 3.15. It can be seen from the table that the value of λ_s^B for ^{28}Si-*Emulsion* at 14.6*A GeV* is greater than the corresponding values obtained for ^{28}Si-*Emulsion* and ^{22}Ne-*Emulsion* collision at 4.5*A GeV* and it decreases as target size increases. From the table we can also see that the value of λ_g^B for grey particles in the backward hemisphere for collisions of different projectiles with the same target (*Emulsion*) remains almost the same within the experimental errors and that the value of λ_g^B decreases as target size increases.

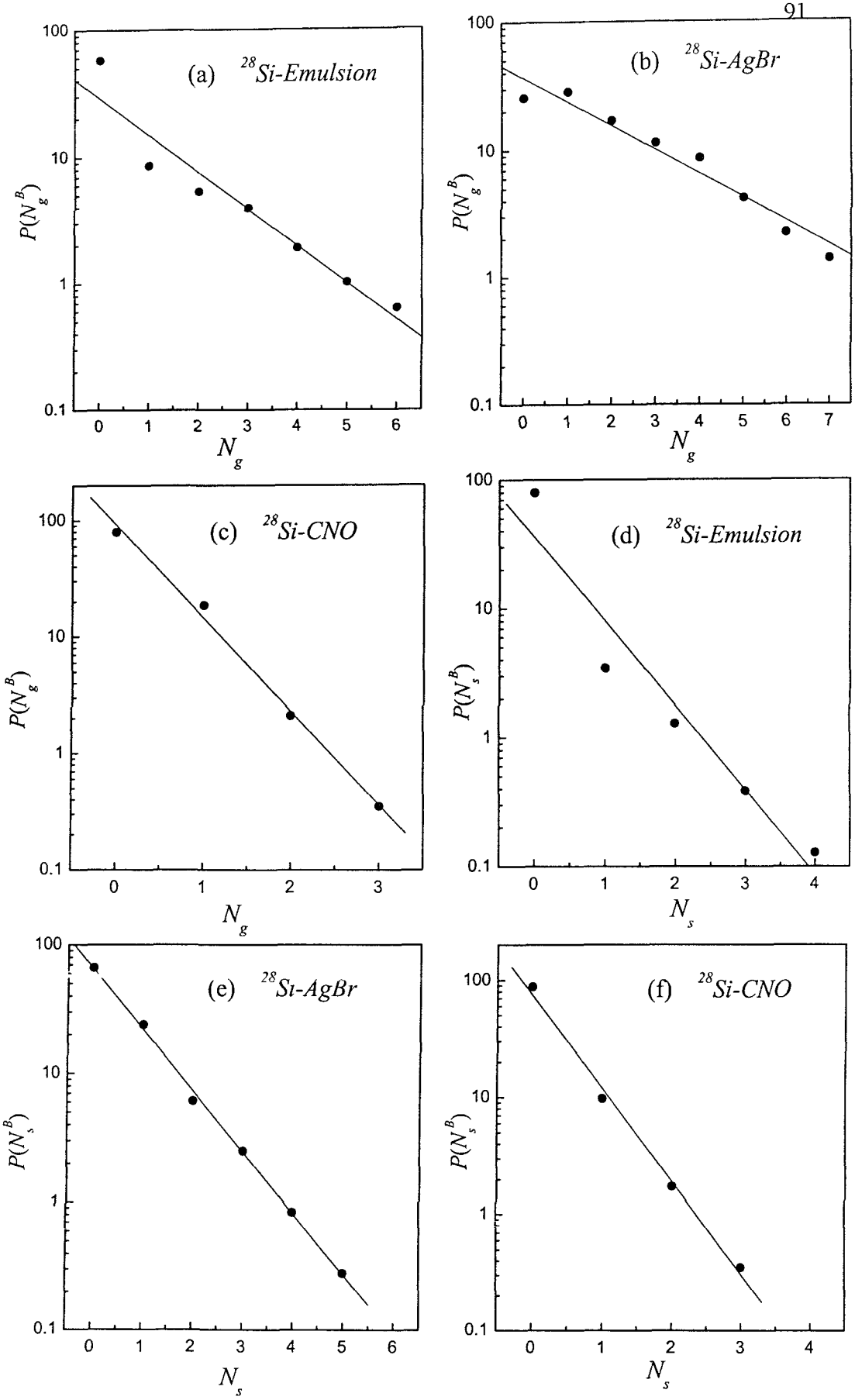

Figure 3.27: (a) - (c) represent normalized multiplicity distributions of grey particles in BHS for ^{28}Si-*Emulsion*, ^{28}Si-*AgBr* and ^{28}Si-*CNO* collisions and (d) - (f) represent normalized multiplicity distributions of shower particles in BHS for ^{28}Si-*Emulsion*, ^{28}Si-*AgBr* and ^{28}Si-*CNO* collisions at 14.6*A GeV* respectively.

Table 3.15: Values of the parameters obtained by fitting the multiplicity distributions of shower and grey particles emitted in the backward hemisphere for ^{28}Si-*Emulsion* collisions at 14.6*A GeV* with Equation 3.17.

Projectile	Target	λ_s^B	p_s	λ_g^B	p_g	Ref.
^{22}Ne	*Emulsion*	1.06±0.04	58.52±6.98	0.66±0.04	40.91±7.58	2
^{28}Si	*Emulsion*	1.02±0.08	54.93±13.14	0.67±0.04	42.11±8.88	2
^{28}Si	*CNO*	1.86±.09	74.13±5.90	1.86±.09	91.20±7.23	Present work
	Emulsion	1.53±.23	36.31±9.08	0.67±.09	28.84±3.75	
	AgBr	1.12±.02	64.54±1.94	0.44±.02	36.31±2.18	
^{32}S	*CNO*	2.38±0.10	86.86±11.22	1.81±0.04	83.07±6.64	2
	Emulsion	1.05±0.05	62.67±7.06	0.76±0.02	50.88±5.23	
	AgBr	0.89±0.05	61.68±6.97	0.67±0.03	52.77±7.68	

3.11.3 Multiplicity Correlations of Particles Emitted in the Forward and Backward Hemispheres

In this section we study the multiplicity correlations of charged particles emitted in the forward and backward hemispheres for ^{28}Si-*Emulsion* collisions at 14.6*A GeV*. In order to investigate the correlation between N_s^F and N_s^B, the correlation coefficient between the multiplicities of shower particles produced in the forward and backward hemispheres is calculated using the relation

$$R = \frac{\left\langle (N_s^F - \langle N_s^F \rangle)(N_s^B - \langle N_s^B \rangle) \right\rangle}{\left[\langle (N_s^F - \langle N_s^F \rangle)^2 \rangle \langle (N_s^B - \langle N_s^B \rangle)^2 \rangle \right]^{1/2}} \qquad 3.18$$

The dependences of $\langle N_s^F \rangle$ on N_s^B and $\langle N_s^B \rangle$ on N_s^F are fitted by the relations

$$\langle N_s^F (N_s^B) \rangle = a_F + b_F N_s^B \qquad 3.19$$

$$\langle N_s^B (N_s^F) \rangle = a_B + b_B N_s^F \qquad 3.20$$

where $\langle N_s^F (N_s^B) \rangle$ and $\langle N_s^B (N_s^F) \rangle$ are the average multiplicities of shower particles emitted in the forward and backward hemispheres at certain values of N_s^B and N_s^F respectively. The slopes b_F and b_B give measures of the correlation strengths The correlation strengths can also be defined as [58]

$$R_F = \frac{\left\langle (N_s^F - \langle N_s^F \rangle)(N_s^B - \langle N_s^B \rangle) \right\rangle}{\langle (N_s^B - \langle N_s^B \rangle)^2 \rangle} \qquad 3.21$$

$$R_B = \frac{\left\langle (N_s^F - \langle N_s^F \rangle)(N_s^B - \langle N_s^B \rangle) \right\rangle}{\langle (N_s^F - \langle N_s^F \rangle)^2 \rangle} \qquad 3.22$$

From Equations 3.18, 3.21 and 3.22 we obtain

$$R^2 = R_F . R_B \qquad 3.23$$

When the dependences of $\langle N_s^F (N_s^B) \rangle$ on N_s^B and $\langle N_s^B (N_s^F) \rangle$ on N_s^F are linear, we get $R_F = b_F$ and $R_B = b_B$

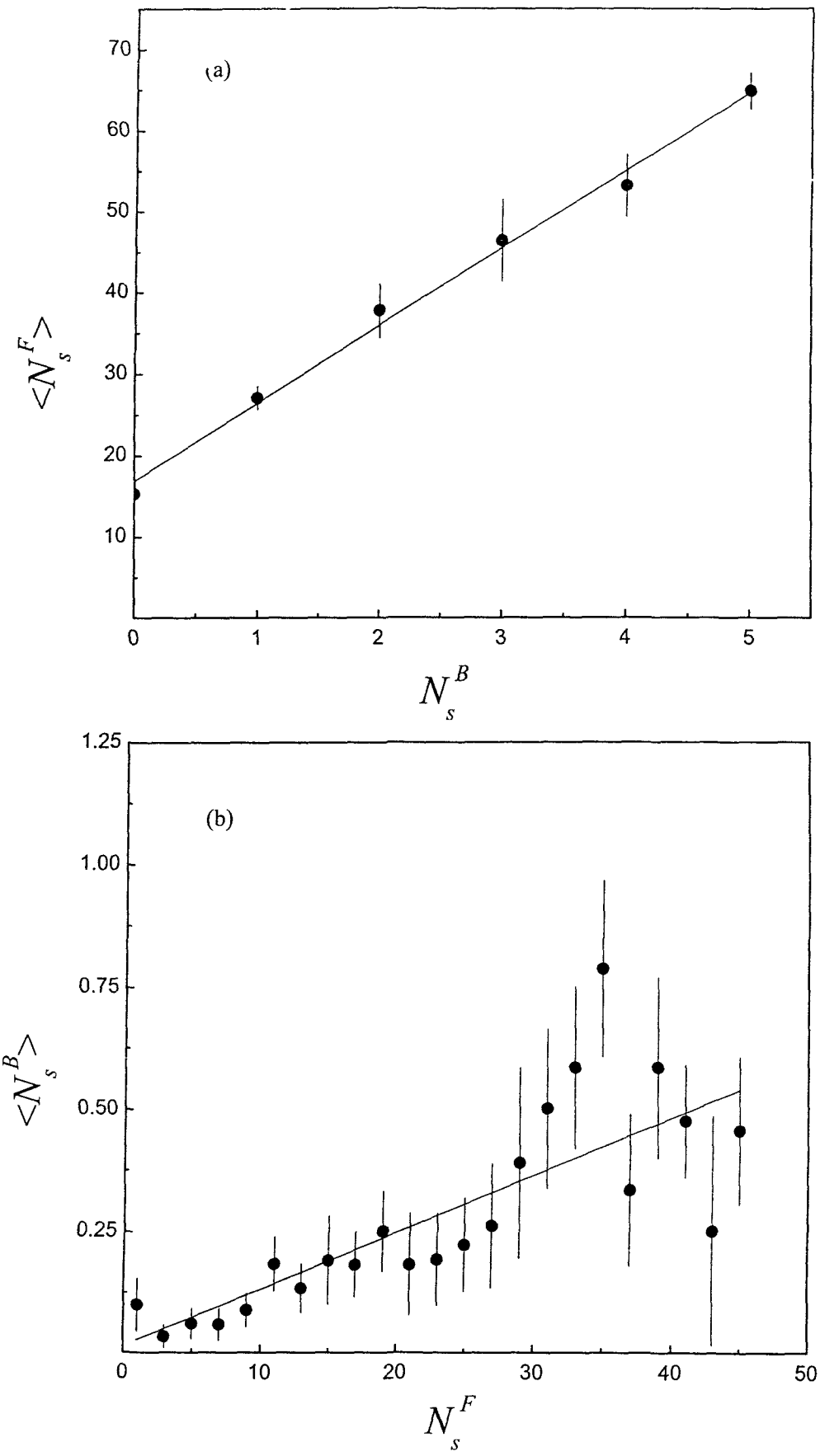

Figure 3.28: (a) $<N_s^F>$ versus N_s^B and (b) $<N_s^B>$ versus N_s^F plots for ^{28}*Si-Emulsion* collisions at 14.6*A GeV*. Straight lines represent the linear fits to the data points.

Table 3.16: The values of the correlation parameters.

Correlation parameters	^{22}*Ne-Emulsion* at 4.1*A GeV* [58]	^{28}*Si-Emulsion* at 4.5*A GeV* [58]	^{28}*Si-Emulsion* at 14.6*A GeV* [*]
R	0.987	0.988	0.460
R_F	24.332	32.573	10.860 ± 0.562
R_B	0.041	0.031	0.019 ± 0.003
b_F	6.426 ± 0.181	8.138 ± 0.408	9.599 ± 0.385
b_B	0.029 ± 0.002	0.017 ± 0.002	0.012 ± 0.002

* Present work

In order to study the forward-backward multiplicity correlations, we have plotted $<N_s^F(N_s^B)>$ versus N_s^B and $<N_s^B(N_s^F)>$ versus N_s^F in Figure 3.28. In Figure 3.28 (a) symbols show the values of $<N_s^F>$ for certain values of N_s^B for *^{28}Si-Emulsion* collisions at 14.6*A GeV* and straight line represents the linear fits using Equation 3.19. The value of the slope b_F (9.599 ± 0.385) is approximately equal to R_F (10.860 ± 0.562) calculated using Equation 3.21. Further, in Figure 3.28 (b) we have plotted $<N_s^B>$ versus N_s^F, where solid circles represent the experimental data and the solid straight line represents the linear fit using Equation 3.20. We again observe that the value of the slope b_B (0.012 ± 0.002) is approximately equal to R_B (0.019 ± 0.003) calculated using Equation 3.22. Thus we find that the dependences of $<N_s^F(N_s^B)>$ on N_s^B and $<N_s^B(N_s^F)>$ on N_s^F are linear. The values of the correlation coefficients R, R_F, b_F, R_B and b_B are listed in Table 3.16 along with the corresponding results obtained by A. El-Naghy et al [58] for *^{22}Ne-Emulsion* collisions at 4.1*A GeV/c* and *^{28}Si-Emulsion* collisions at 4.5*A GeV/c*. We observe from the table that both b_B and R_B slightly decrease with the projectile mass while b_F increases significantly with increase in the projectile size.

The total number of shower and grey particles emitted per event in the backward hemisphere (N_c^B) is an important parameter in the investigation of the production mechanism and the number of heavily ionizing particles N_h emitted per event assists in determining the size of the target nucleus in emulsion. We, therefore, study the correlations between the average number of shower, grey and black particles emitted in the forward and backward hemispheres and N_c^B / N_h for *^{28}Si-Emulsion* collisions at 14.6*A GeV*. The correlations are fitted with the equation

$$<N_i^k> = \xi N_j + \omega \qquad 3.24$$

where $i \neq j$ and $k = F$ (for forward hemisphere) or B (for backward hemisphere).

Figures 3.29 (a) – (c) show the plots of $<N_b^F>$, $<N_g^F>$ and $<N_s^F>$ versus N_c^B respectively. The straight lines in the figures represent linear fits to the data points using Equation 3.24. We observe that $<N_b^F>$ versus N_c^B is fitted well up to $N_c^B = 4$, $<N_g^F>$ versus N_c^B is fitted well up to $N_c^B = 5$ and $<N_s^F>$ versus N_c^B is fitted well up to $N_c^B = 4$. In Figures 3.30 (a) – (c) symbols represent the plots of $<N_b^B>$, $<N_g^B>$ and $<N_s^B>$ versus N_c^B respectively and the straight lines represent linear fits to the data points using Equation 3.24. We find that $<N_b^B>$ versus N_c^B is fitted well up to $N_c^B = 4$, $<N_s^B>$ and $<N_g^B>$ versus N_c^B is fitted well for whole range of N_c^B. The values of the fitting parameters are given in Table 3.17. In Figures 3.31 (a) – (c) symbols represent the plots of $<N_b^F>$, $<N_g^F>$ and $<N_s^F>$ versus N_h and the straight lines represent the linear fits to the

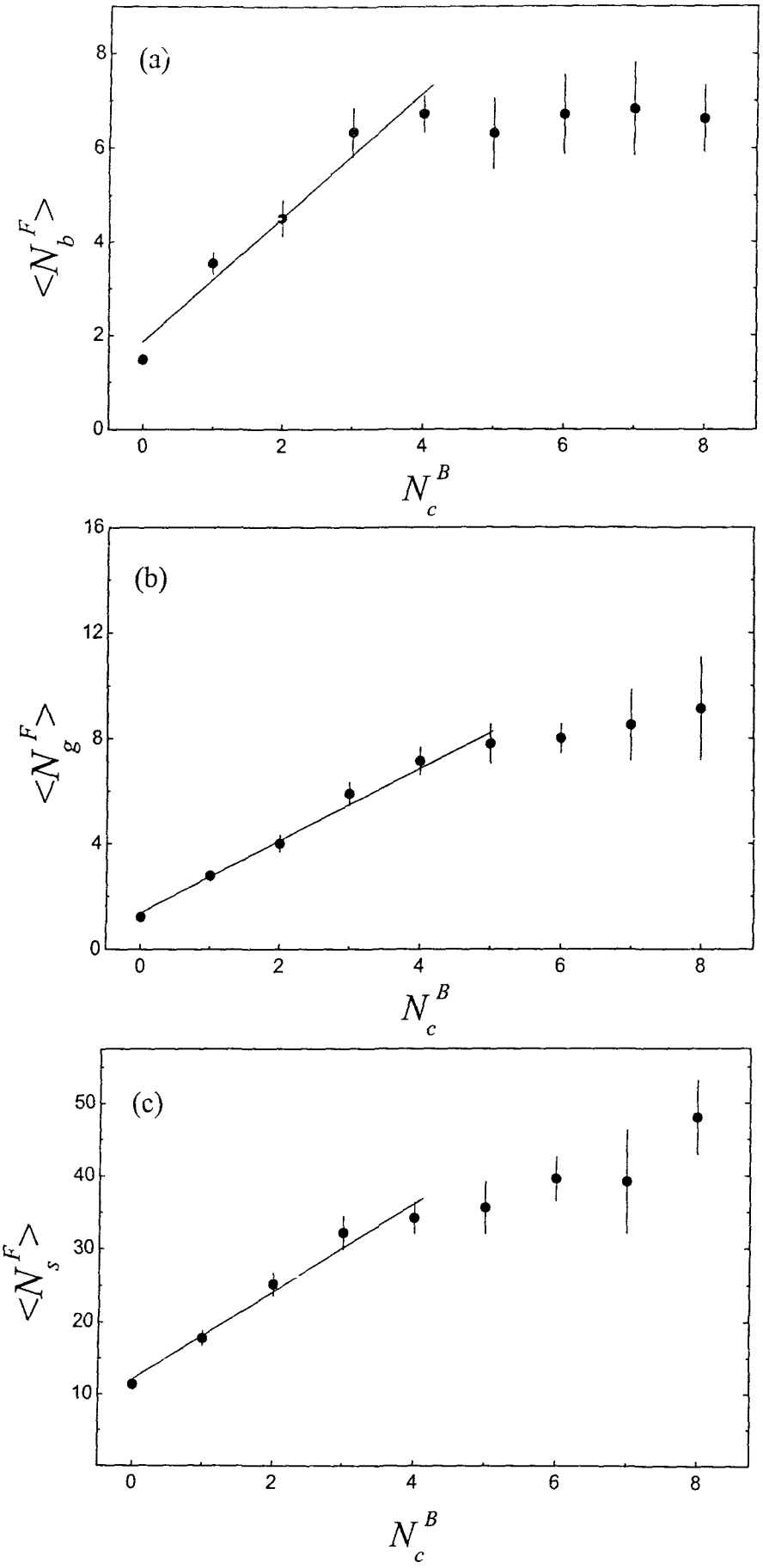

Figure 3.29: (a)-(c) represent $<N_b^F>$, $<N_g^F>$ and $<N_s^F>$ versus N_c^B plots for ^{28}*Si-Emulsion* collisions at 14.6*A GeV*. Straight lines represent the linear fits to the data points.

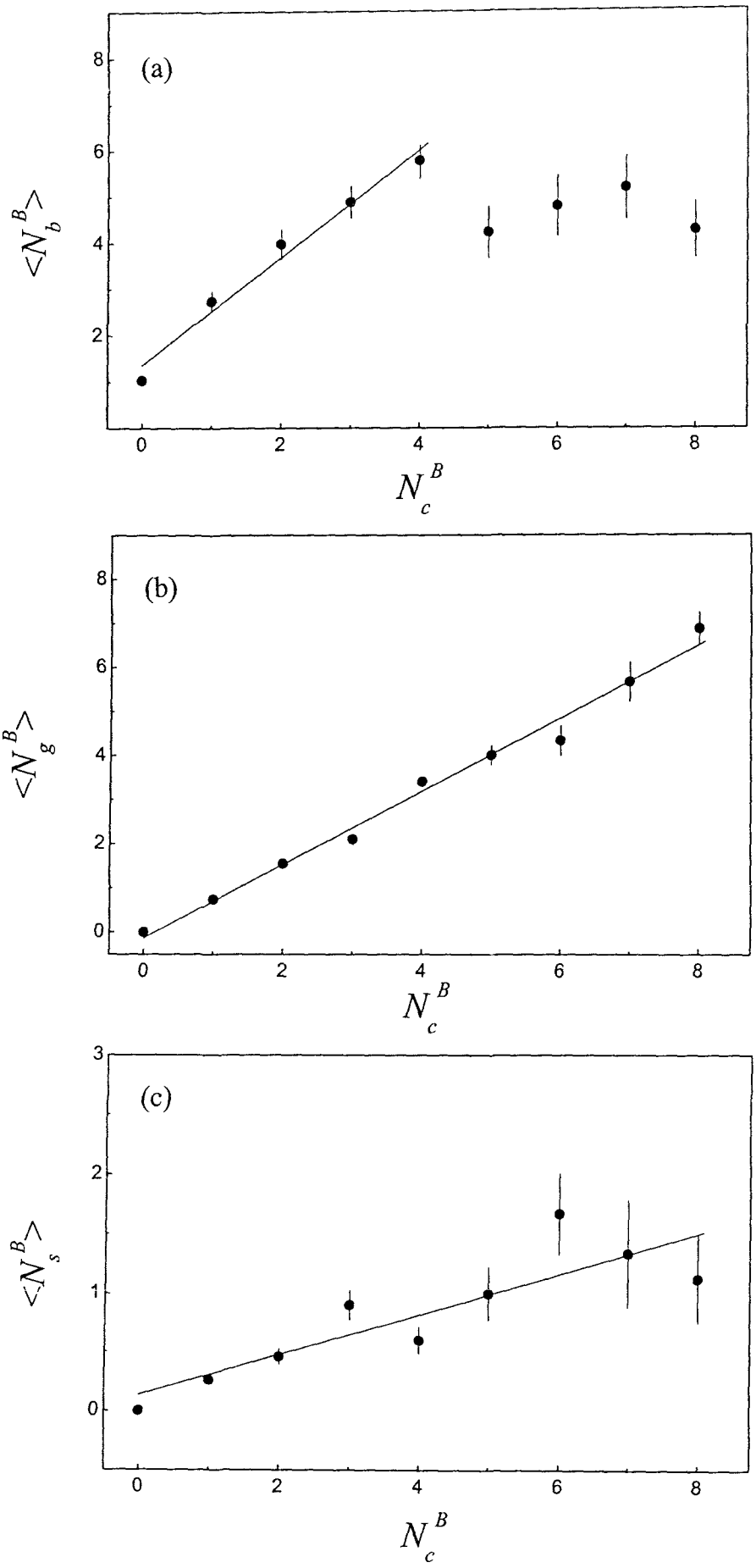

Figure 3.30: (a)-(c) represent $<N_b^B>$, $<N_g^B>$ and $<N_s^B>$ versus N_c^B plots for ^{28}*Si-Emulsion* collisions at 14.6*A GeV*. Straight lines represent the linear fits to the data points.

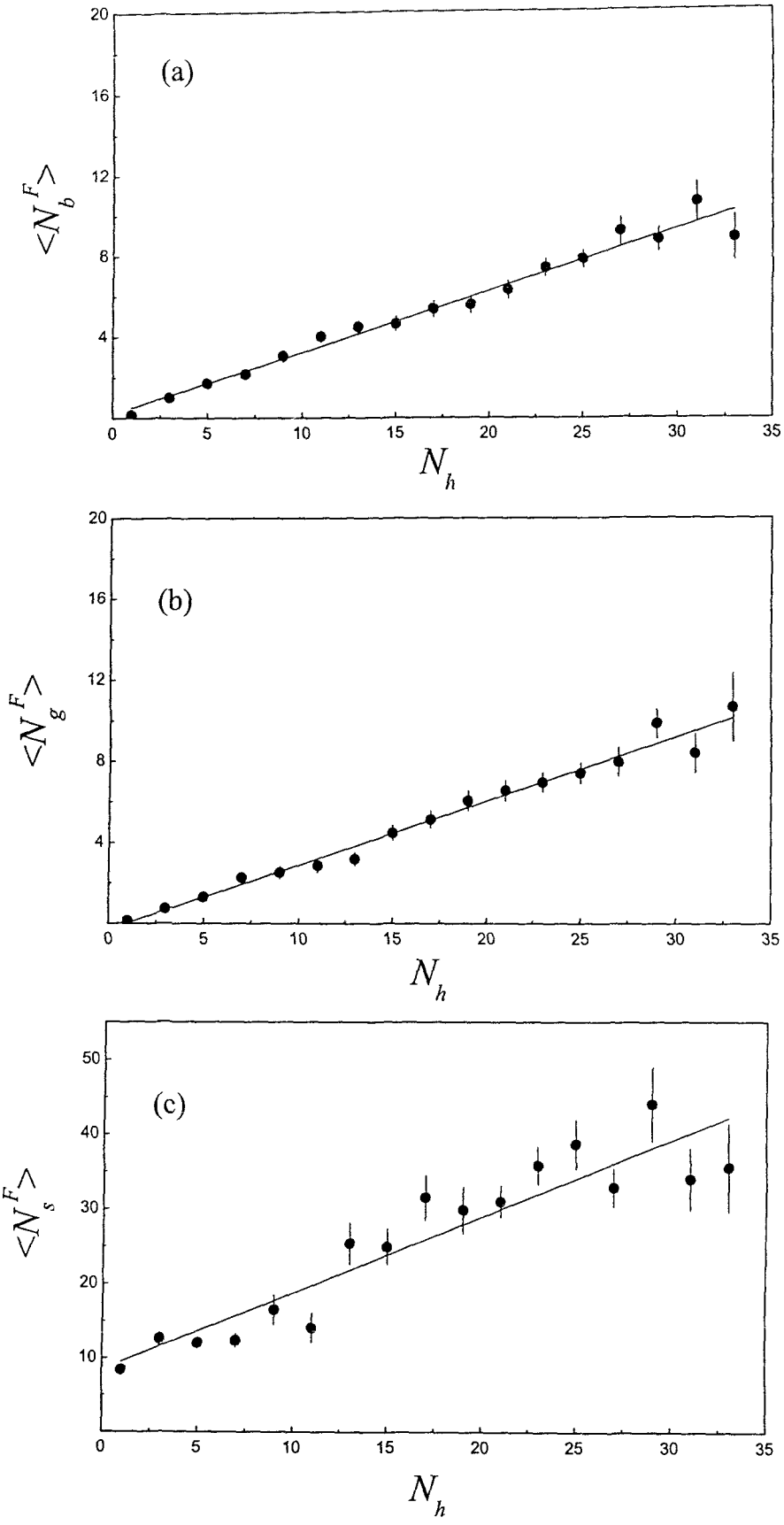

Figure 3.31: (a)-(c) represent $<N_b^F>$, $<N_g^F>$ and $<N_s^F>$ versus N_h plots for ^{28}Si-*Emulsion* collisions at 14.6*A GeV*. Straight lines represent the linear fits to the data points.

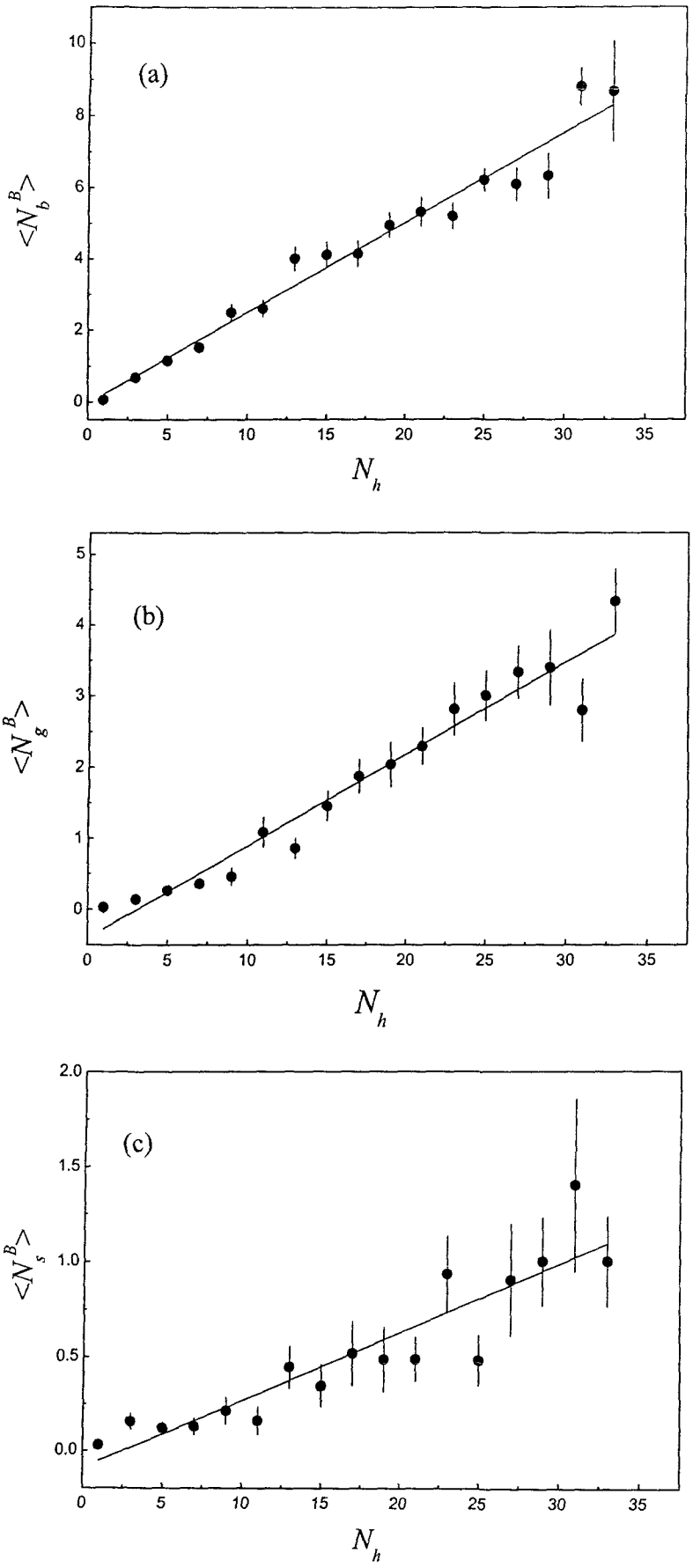

Figure 3.32: (a)-(c) represent $<N_b^B>$, $<N_g^B>$ and $<N_s^B>$ versus N_h plots for ^{28}*Si-Emulsion* collisions at 14.6*A GeV*. Straight lines represent the linear fits to the data points.

Table 3.17: The fitting parameters for the average multiplicities of shower, grey and black particles emitted in the forward and the backward hemispheres for ^{28}*Si-Emulsion* collisions at 14.6*A GeV*.

Correlation	Slope (ξ)	Intercept (ω)
$\langle N_s^F \rangle$ - N_c^B	6.01 ± 0.57	12.11 ± 1.39
$\langle N_g^F \rangle$ - N_c^B	1.37 ± 0.08	1.38 ± 0.24
$\langle N_b^F \rangle$ - N_c^B	1.33 ± 0.15	1.85 ± 0.38
$\langle N_s^B \rangle$ - N_c^B	0.83 ± 0.04	-0.13 ± 0.16
$\langle N_g^B \rangle$ - N_c^B	0.02 ± 0.03	0.13 ± 0.16
$\langle N_b^B \rangle$ - N_c^B	1.16 ± 0.09	1.35 ± 0.24
$\langle N_s^F \rangle$ - N_h	1.02 ± 0.10	8.54 ± 2.03
$\langle N_g^F \rangle$ - N_h	0.32 ± 0.01	-0.30 ± 0.23
$\langle N_b^F \rangle$ - N_h	0.30 ± 0.01	0.19 ± 0.26
$\langle N_s^B \rangle$ - N_h	0.04 ± 0.00	-0.09 ± 0.08
$\langle N_g^B \rangle$ - N_h	0.13 ± 0.01	-0.41 ± 0.15
$\langle N_b^B \rangle$ - N_h	0.25 ± 0.01	-0.04 ± 0.24

data points. Similarly in Figures 3.32 (a) – (c) symbols represent the plots of $<N_b^B>$, $<N_g^B>$ and $<N_s^B>$ versus N_h and the straight lines represent the linear fits to the data points. We observe that in all the cases plots are fitted well for the whole range of N_h. The values of ξ and ω obtained by fitting the data points are listed in Table 3.17. From the table we observe that there is a strong correlation between $<N_s^F>$ and N_c^B. Significant correlations are observed between $<N_g^F>$ and N_c^B, $<N_b^F>$ and N_c^B, $<N_b^B>$ and N_c^B and also between $<N_s^F>$ and N_h. We, therefore, conclude that the average number of shower and grey particles in the forward hemisphere depend strongly on the total number of shower and grey particles emitted in the backward hemisphere (N_c^B), whereas the average number of grey and shower particles in the backward hemisphere depends weakly on N_c^B. This shows that pions and protons emitted in the backward hemisphere are somewhat different from those emitted in the forward hemisphere.

References

1. B.K. Singh et al., *Nucl. Phys.* **A 570** (1994) 819.
2. A Abdelsalam , *J. Phys. G: Nucl. Part.Phys.* **28** (2002) 1375.
3. H. L. Bradt and B. Peters, *Phys. Rev.* **77** (1950) 54.
4. H. H. Heckman et al., *Phys. Rev.* **C 17** (1978) 1735.
5. M. Q. R. Khan et al., *Nuvo Cim.* **A 99** (1988) 417.
6. M. M. Aggarwal and P. L. Jain, *Physical Rev.* **C 31** No.4 (1985) 1233
7. R. R. Joseph et al., J. Phys. G: *Nucl. & Part. Phys.* **G 18** (1992) 1817.
8. EMU-01Coll. *Z. Phys.* **A 358** (1997) 337.
9. G. Baroni et al., *Nucl. Phys.* **A 437** (1985) 729.
10. L. K. Mangotra et al., *Nuvo Cim.* **A 87** (1985) 279.
11. E. M. Friedlander et al., *Phys. Rev. Lett.* **45** (1980) 1084.
12. B. Jakobsson & R. Kullberg; *Phys. Scripta* **13** (1976) 327.
13. M. Bogdanski et al., *Helv. Phys. Acta.* **42** (1969) 485.
14. DGKLMTW Coll. *JINR Dubna Communication*, PL-8313 (1974).
15. N.N. Abd-Allah et al., *Phys. Scrp.* **54** (1996) 436.
16. R. Bhanja et al., *Nucl. Phys.* **A 411** (1983) 507.
17. C. Bjarle et al., *Nucl. Phys.* **A 381** (1982) 544.
18. N.N. ABD Allah et al., *J. Phys. Soc. Jap.* **69** No.4 (2000) 1068.
19. M. Mohery & N.N. ABD Allah, *IJMP* **E 11** No.2 (2002) 161.
20. G. M. Chernov et al., *Nucl. Phys.* **A 412** (1984) 534.
21. Alma-Ata Collaboration, *Z. Phys.* **A 302** (1981) 133.
22. G. M. Chernov et al., *Nucl. Phys.* **A 280** (1977) 478.
23. V. A. Antonchik et al., *Sov. J. Nucl. Phys.* **39** (1984) 774.
24. D. Ghosh et al., *Nucl. Phys.* **A 499** (1989) 815.
25. S. A. Azimov et al., *Nucl. Phys.* **A 470** (1987) 653.
26. A-ABDDKLMTU-B Collaboration, *Z. Phys.* **A 302** (1981) 133.
27. I. Otterlund et al., *Nucl. Phys.* **B 142** (1978) 445.
28. M. K. Hegab and J. Hufner, *Nucl. Phys.* **A 384** (1982) 353.
29. M. Tariq et al., *Nuvo Cim.* **A 107** (1994) 2687.
30. E. S. Basova et al., *Dokl. Uzbek acad. Sc.* **8** (1980) 28.
31. B. P. Bannik et al.; Czech. J. Phys. **B 31** (1981) 490.
32. E. Stenlund and I. Otterlund et al., *Nucl. Phys.* **B 198** (1982) 407.
33. Tauseef Ahmad and M. Irfan, *IL Nuovo Cim.* **A 106** (1993) 171.

34. A. Dabrowska et al., *Cracow report NR.* (1992) 1595/PH.
35. M. S. Ahmad M. Q. R. Khan, K. A. Siddique and R. Hasan; *IJMP* **A 10** No.6 (1995) 845.
36. N.N. ABD Allah et al., *IJMP* **E 10** No.1 (2001) 55-68.
37. D. Ghosh et al., *Nucl. Phys.* **A 499** (1989) 850.
38. UA5 Collaboration (G. J. Alner et al.), *Phys. Lett.* **B 160** (1985) 193, 199. ; M. Derrick et al., *Phys. Lett.* **B 168** (1986) 299.
39. M. Arendo et al., *Z. Phys* **C** *Particles & Fields* **35** (1987) 335.
40. D. Ghosh et al., *J. Phys.* **G 16** (1990) 1505.
41. A. Mukhopadhyay et al., *IL Nuovo Cim.* **A 106** (1993) 967.
42. EHS-NA22 Collaboration I. V. Ajinenko et al., *Z. Phys.* **C 46** (1990) 569.
43. P. Carruthers and C. C. Shih: *Phys. Lett.* **B 127** (1983) 242.
44. A. Giovannini and L. Van Hove, *Z. Phys* **C 30** (1986) 391.
45. K. Fialkowski , *Phys. Lett.* **B 169** (1986) 436.
46. M. Kutschera and K. Werner, *Z. Phys.* **C 45** (1989) 91.
47. Frankfurt L. L. and Strikman M. J., *Phys. Lett.* **B 83** (1979) 497.
48. Burov V. V., Lukyanov V. K. and Titov A. I., *Phys. Lett.* **B 67** (1977) 46.
49. Gorentein M. I. and Zinovjev G. M., *Phys. Lett.* **B 67** (1977) 100.
50. Methis H. B. and Meng Ta-Chung, *Phys. Rev.* **C 18** (1978) 952.
51. Baldin A. M., *Preprint JINR-P1-11302 Dubna* (1978).
52. Baldin A. M., *Proceedings of the International Conference of Extreme State in Nuclear System, Dresden* (1980).
53. Schmidt I. A. and Blankenbecler R., *Phys. Rev.* **D 15** (1977) 3321.
54. Harris J. W., *Proceedings of the Workshop on Nuclear Dynamics, California,* March 1980.
55. El-Nadi M et al., *Nuovo Cimento.* **A 111** (1998) 1243.
56. El-Nadi M et al., *Nuvo Cim.* **A 110** (1998) 1255.
57. El-Nadi M et al., *IJMP* **E 3** (1994) 811.
58. A. El-Naghy, N. M. Sadek and M. Mohery., *Il Nuovo Cimento.* **A 110** (1997) 125.
59. El-Nadi M et al., *Radiat. Phys.Chem.* **47** (1996) 681.
60. El-Sharkawy S. et al., *Phys. Scr.* **47** (1993) 512.
61. Otterlund I. et al., *Nucl. Phys.* **A 384** (1982) 353.
62. El-Nadi M et al., *Eur. Phys. J.* **A 3** (1998) 183.

CHAPTER IV

Multifractal Analysis of Multiplicity Fluctuations in ^{28}Si-$AgBr$ Collisions at 14.6A GeV

4.1 Introduction

The study of non-statistical fluctuations in the density of charged particles produced in high-energy collisions is considered an important tool in the understanding of the dynamics of multiparticle production. Among various methods of studying the non-statistical fluctuations, the most commonly used one is the method of studying the behaviour of the scaled factorial moments F_q as a function of the size of phase space interval $\delta\eta$. Bialas and Peschanski [1] first suggested this method. This method removes statistical fluctuations due to the finite number of charged particles in an event. A power law growth of the scaled factorial moments with decreasing size of phase space interval $\delta\eta$ ($F_q \propto \delta\eta^{-\phi_q}$) signals the presence of dynamical fluctuations in the data. Being similar in nature to the power law variation of moments due to the intermittent structure that appears in a turbulent fluid hydro-dynamics, the phenomenon of power law variation of the scaled F_q-moments is termed as intermittency. ϕ_q are called intermittency indices. Evidence of intermittency has been found in $e^+ e^-$ annihilation [2-4], hadron-nucleus [5,6] and nucleus-nucleus collisions [7-9].

The power law behaviour of the scaled factorial moments indicates the existence of self-similarity. The concept of self-similarity is closely related to multifractality, which is a consequence of cascade mechanism prevailing in the multiparticle production. Therefore, the necessity of using the multifractal technique to study the multiplicity fluctuations has arisen. In the multifractal technique, the nuclear interactions can be treated as geometrical objects with non-integer dimensions. The technique has been successfully used to study the intermittent behavior of turbulent fluids and other chaotic systems [10-12]. Chiu and Hwa [13] developed formalism for investigating the fractal structure in multiparticle production. According to this formalism, the empty bins in the pseudorapidity distribution are treated as holes and the set of non-empty bins at any stage of binning constitutes one of the fractal sets of multifractal structure in multiparticle production. Using this concept of multifractality, Chiu and Hwa [13] defined G_q-moments and evaluated the parameters that characterize the fractal properties. The G_q-moments share with the scaled factorial moments the property that the self-similar density fluctuations lead to the power law behavior: $G_q \propto \delta\eta^{\tau_q}$ as $\delta\eta 0$, where τ_q are known as fractal indices. This method has been used to study multifractality in e^+e^- annihilation

[13] and in hadron-nucleus [14] and nucleus-nucleus collisions [15,16] at relativistic energies.

The G_q-moments have the advantage that not only peaks of the rapidity distribution are included in the analysis but also the non-empty valleys ($q<0$). The disadvantages are that the G_q-moments saturate as $\delta\eta 0$. Further it has been found that for low multiplicity events the G_q-moments are dominated by statistical fluctuations [15]. In order to suppress the statistical contribution to the observed fluctuations, Hwa and Pan [17] suggested a modified form of G_q-moments with the help of a step function.

Although many attempts have been made to study the fractal properties of $\mu p, p\bar{p}$ and $e^{+}e^{-}$ data [18,19] using the modified G_q-moments, there have been only a few attempts to study the fractal behavior of relativistic nucleus-nucleus collisions using this method [20,21]. In this chapter, we therefore investigate the fractal behavior of multiplicity fluctuations in $^{28}Si\text{-}AgBr$ collisions at $14.6A\ GeV$ using the modified G_q-moments in both the pseudorapidity (η) and azimuthal angle (φ) spaces. The dynamical component of $<G_q>$ has been determined using the method suggested by Hwa and Pan [17].

As already mentioned above, the power law behaviour of F_q-moment indicates the existence of self-similarity, which is closely related to multifractality. We have therefore studied the connection between F_q-moments and G_q-moments. Using a relation between the intermittency indices ϕ_q and fractal indices τ_q, multifractality in our data has also been studied through F_q-moment method in both the pseudorapidity (η) and azimuthal angle (φ) spaces. And we have calculated the values of the generalized fractal dimensions D_q^{dyn} and the multifractal specific heat (c) for our data.

Apart from the modified G_q-moment and F_q-moment methods, Takagi method [22] has also been used to study multifractality in multiparticle production. This method has been successfully applied to study multifractality in UA5 data on $p\bar{p}$ collisions [23] and TASSO and DELPHI data on $e^{+}e^{-}$ annihilations [24,25]. This method has also been used to study the multifractal behaviour of shower particles produced in hadron-nucleus [26,27] and nucleus-nucleus collisions [27-29] at relativistic energies. Ghosh et al. [28,29] have used Takagi method to study multifractal behaviour of target evaporated slow particles (black particles) and medium energy target fragmented protons (grey particles) emitted in $^{32}S\text{-}AgBr$ collisions at $200A\ GeV$ and $^{16}O\text{-}AgBr$ collisions at

60A GeV. We have also used Takagi method to study the multifractal behavior of shower particles produced in ^{28}*Si-AgBr* collisions at 14.6*A GeV* in the pseudorapidity (η) and azimuthal angle (φ) spaces. In both the spaces the multiplicity moments are found to have a power law dependence on the mean multiplicity with decreasing bin size.

Several models of multiparticle production in relativistic nucleus-nucleus collisions have been developed. A comparison of our results with the corresponding results for events generated using these models would provide valuable inputs to these models. We have therefore simulated ^{28}*Si-AgBr* collisions using the string hadronic model *UrQMD* and found that our results deviate significantly from the corresponding results for *UrQMD* events.

4.2 Results and Discussion

Various methods have been proposed to investigate multifractality in multiparticle production. We have studied the multifractality in our data using the following three methods: (i) modified G_q-moment method [17], (ii) F_q-moment method [1] and (iii) Takagi method [22]. The analysis has been done for ^{28}*Si-AgBr* collisions only. Out of the total 784 inelastic collisions collected in the present experiment, 360 were ^{28}*Si-AgBr* collisions. To minimize the contribution of statistical fluctuations due to low multiplicity, only collisions with $N_s \geq 8$ were considered for the analysis. Thus 297 events representing ^{28}*Si-AgBr* collisions were selected for the present analysis. Further the analysis was restricted to shower particles lying in the central region of pseudorapidity with $\eta_{peak} - 2 \leq \eta \leq \eta_{peak} + 2$. This range of pseudorapidity covers almost all produced particles.

The single particle density distribution in the pseudorapidity space is not flat due to the energy and momentum constraints [30]. Although some models [31] predict a flat central region in the density distribution in the pseudorapidity space at ultrarelativistic energies, the experimental distributions are found to have some shape even in the central region [30]. To avoid the effect of non-flat particle density distribution $\rho(\eta)$ on the investigation of the dynamical fluctuations, Bialas and Gazdzicki [32] have introduced a new scaled cumulative variable X related to the single particle density distribution $\rho(\eta)$ as

$$X(\eta) = \frac{\int_{\eta_1}^{\eta} \rho(\eta)\, d\eta}{\int_{\eta_1}^{\eta_2} \rho(\eta)\, d\eta}, \qquad 4.1$$

where η_1 and η_2 are the minimum and maximum values of the pseudorapidity in the interval $\Delta\eta$. In X space, the single particle density distribution is uniformly distributed from 0 to 1. Pseudorapidity values of shower particles emitted in all ^{28}Si-$AgBr$ collisions were converted to the corresponding X-values using Equation 4.1.

4.2.1 Modified G_q-Moment Method

In order to suppress the contribution of statistical fluctuations, Pan and Hwa [17] defined a modified form of G_q-moment as

$$G_q = \sum_{m=1}^{M} \left(\frac{n_m}{N}\right)^q \theta(n_m - q), \qquad 4.2$$

where q is a positive integer, M is the total number of bins in which the X-interval (0-1) has been divided, n_m is the multiplicity of particles in the mth bin, $N = \sum_{m=1}^{M} n_m$ denotes the total multiplicity in the interval X = 0-1 and θ is the step function. . It is equal to 1 for n_m q and 0 otherwise. This definition of G_q-moments differs from the earlier definition [13] only by the θ function. When the multiplicity N is very large so that $N/M >> q$, the two definitions of G_q give the same result. However, for low multiplicity events, the step function exerts a crucial influence on the values of G_q-moments. For an ensemble of events, the vertical average of G_q-moments can be calculated from the following relation.

$$\langle G_q \rangle = \frac{1}{N_{ev}} \sum_{1}^{N_{ev}} G_q\,, \qquad 4.3$$

where N_{ev} is the total number of events in the ensemble. Values of $< G_q >$ for our data were calculated using Equations 4.2 and 4.3 for q = 2-6. M was varied from 2 to 35. The $\ln < G_q >$ versus $\ln M$ graphs for ^{28}Si-$AgBr$ collisions with $N_s \geq 8$ are shown in Figure 4.1(a). $\ln < G_q >$ exhibits a linear dependence on $\ln M$, indicating that G_q-moments have a power law dependence on M of the form

$$\langle G_q \rangle \propto M^{-\tau_q} \qquad 4.4$$

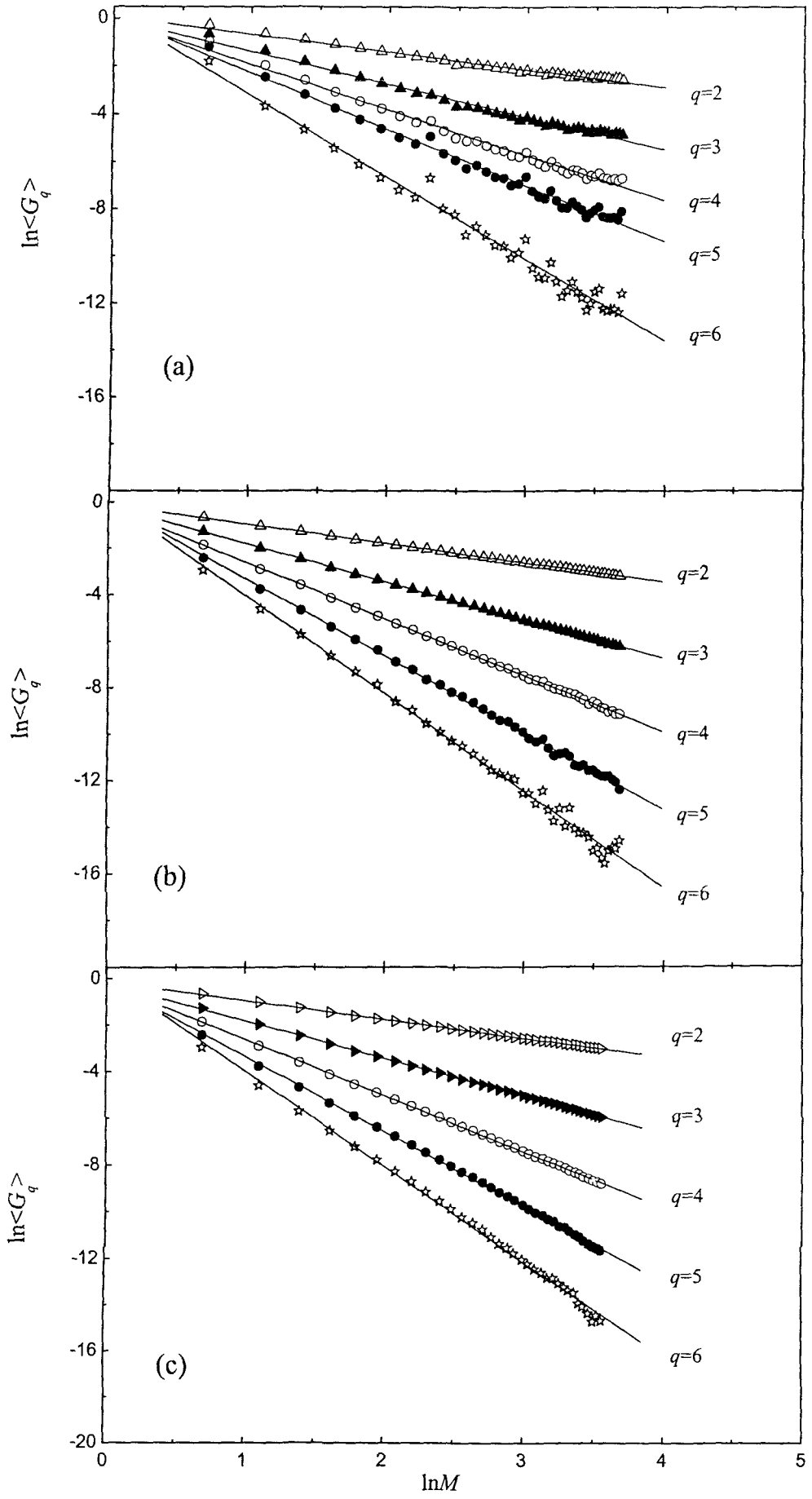

Figure 4.1: (a) ln<G_q> versus ln$M$ plots for ^{28}*Si-AgBr* collisions at 14.6*A GeV* in η-space.
(b) ln<G_q> versus ln$M$ plots for *randomly generated* events in η-space.
(c) ln<G_q> versus ln$M$ plots for *UrQMD* events in η-space.

This is an evidence of self-similarity in the multiparticle production in our data. Straight lines in Figure 4.1(a) show the linear fits to the data points. Slopes of the lines τ_q for different values of q are given in Table 4.1.

To calculate the statistical contribution to G_q, random events were generated in X-space according to the following criteria:

(i) N particles in each event are distributed randomly in X- space from 0-1.

(ii) The randomly generated events have the same multiplicity distribution as that of the experimental events.

$\ln < G_q >^{stat}$ versus $\ln M$ graphs for the randomly generated events for q = 2-6 are shown in Figure 4.1(b). As can be seen from the figure, $< G_q >^{stat}$ exhibits a linear dependence on $\ln M$ indicating that $< G_q >^{stat}$, like $< G_q >$, also exhibits power law dependence on M as

$$\left\langle G_q \right\rangle^{stat} \propto M^{-\tau_q^{stat}} \tag{4.5}$$

Values of τ_q^{stat}, obtained from straight line fits to the plots, shown in Figure 4.1(b), are listed in Table 4.1. The dynamical component of $< G_q >$ can now be determined from the following relation

$$\left\langle G_q \right\rangle^{dyn} = \frac{\left\langle G_q \right\rangle}{\left\langle G_q \right\rangle^{stat}} M^{1-q} \tag{4.6}$$

It is clear from Figures 4.1 (a) and (b) that both $< G_q >$ and $< G_q >^{stat}$ exhibit a power law dependence on M. If $< G_q >^{dyn}$ also exhibits a power law dependence on M as $\left\langle G_q \right\rangle^{dyn} \propto M^{-\tau_q^{dyn}}$, then we would have

$$\tau_q^{dyn} = \tau_q - \tau_q^{stat} + q - 1 \tag{4.7}$$

If $< G_q >$ is purely statistical, that is, $\tau_q = \tau_q^{stat}$ then according to Equation 4.7, $\tau_q^{dyn} = (q\text{-}1)$. Therefore, any deviation of τ_q^{dyn} from $(q\text{-}1)$ would signal the presence of dynamical fluctuations. Values of τ_q^{dyn} for our data for q = 2-6 calculated from Equation 4.7 are also

Table 4.1: Values of the slopes τ_q along with the statistical and dynamical components for ^{28}Si-$AgBr$ collisions at 14.6A GeV for different values of q in η-space.

q	τ_q	τ_q^{stat}	τ_q^{dyn}	$(q\text{-}1)$- τ_q^{dyn}
2	0.753 ± 0.017	0.833 ± 0.002	0.920 ± 0.017	0.080 ± 0.017
3	1.380 ± 0.028	1.641 ± 0.004	1.739 ± 0.028	0.261 ± 0.028
4	1.912 ± 0.035	2.424 ± 0.008	2.488 ± 0.036	0.512 ± 0.036
5	2.374 ± 0.045	3.289 ± 0.026	3.085 ± 0.052	0.915 ± 0.052
6	2.791 ± 0.067	4.196 ± 0.059	3.595 ± 0.089	1.605 ± 0.089

Table 4.2: Values of slopes τ_q along with the statistical and dynamical components for the events generated using *UrQMD* model for different values of q in η-space.

q	τ_q	τ_q^{stat}	τ_q^{dyn}	$(q\text{-}1) - \tau_q^{dyn}$
2	0.824 ± 0.003	0.833 ± 0.002	0.991 ± 0.004	0.009 ± 0.004
3	1.617 ± 0.004	1.641 ± 0.004	1.976 ± 0.006	0.024 ± 0.006
4	2.408 ± 0.007	2.424 ± 0.008	2.984 ± 0.011	0.016 ± 0.011
5	3.215 ± 0.016	3.289 ± 0.026	3.926 ± 0.031	0.074 ± 0.031
6	4.084 ± 0.043	4.196 ± 0.059	4.888 ± 0.073	0.112 ± 0.073

listed in Table 4.1. As can be seen from the table, these values of τ_q^{dyn} deviate significantly from (q-1). Thus fluctuations of dynamical origin are present in our data.

We have also carried out G_q-moment analysis of our data in the azimuthal angle (φ) space. Like the pseudorapidity distribution, the azimuthal angle distribution of all shower particles lying in the central region of pseudorapidity $\eta_{peak}-2\leq\eta\leq\eta_{peak}+2$ has also been converted into the corresponding X-distribution using the relation

$$X(\varphi) = \frac{\int_0^{\varphi} \rho(\varphi)\, d\varphi}{\int_0^{2\pi} \rho(\varphi)\, \varphi} . \qquad 4.8$$

We divided the interval ΔX (=1.0) into M bins each of size δX= 1.0/M and values of modified $< G_q >$ moments were calculated using Equations 4.1 and 4.2 for q=2-6 for ^{28}Si-$AgBr$ collisions with $N_s \geq 8$. M was varied from 2-35. Figure 4.2(a) represents the plots of ln$< G_q >$ versus ln$M$ in φ-space. It is clear from the figure that ln$<G_q>$ exhibits a linear dependence on ln$M$. Thus in azimuthal angle (φ) space also G_q-moments for our data have a power law dependence on M, which again indicates self-similarity in particle production process. Straight lines in Figure 4.2(a) show linear fits to the data points. Slopes of the lines τ_q for different values of q are given in Table 4.3.

To calculate the statistical contribution to G_q, random events were generated in the azimuthal angle space according to the following criteria:

(i) N particles in each event are distributed randomly in X- space from X=0 to X=1.

(ii) The randomly generated events have the same multiplicity distribution as that of the experimental events.

Again we divided the interval ΔX (=1.0) into M bins each of size δX = 1.0/M and values of the modified $<G_q>^{stat}$ moments were calculated using Equations 4.1 and 4.2 for q=2-6 for ^{28}Si-$AgBr$ collisions with $N_s \geq 8$. M was varied from 2-35. Figure 4.2 (b) shows plots of ln$<G_q>^{stat}$ versus ln$M$ for different values of q in φ-space for the generated events. The straight lines shown in the graph are the linear fits to the plots. The slopes of the fitted lines give the values of τ_q^{stat} in φ-space. Values of τ_q^{dyn} were calculated using

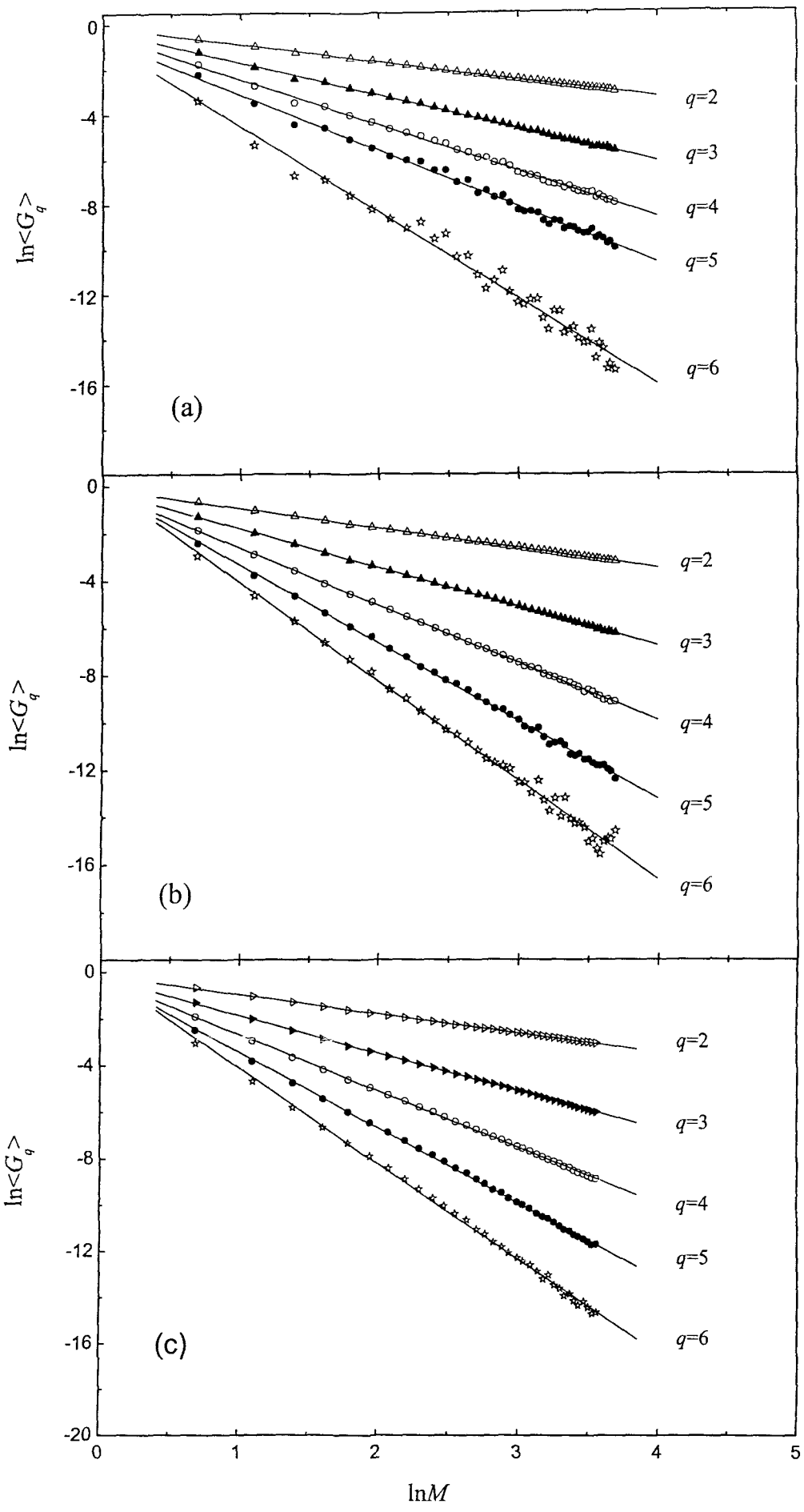

Figure 4.2: (a) ln<G_q> versus ln$M$ plots for ^{28}*Si-AgBr* collisions at 14.6*A GeV* in φ-space.
(b) ln<G_q> versus ln$M$ plots for *randomly generated* events in φ-space.
(c) ln<G_q> versus ln$M$ plots for *UrQMD* events in φ-space.

Table 4.3: Values of slopes τ_q along with the statistical and dynamical components for $^{28}Si\text{-}AgBr$ collisions at 14.6A GeV for different values of q in φ-space.

q	τ_q	τ_q^{stat}	τ_q^{dyn}	$(q\text{-}1)$ - τ_q^{dyn}
2	0.770 ± 0.003	0.834 ± 0.002	0.936 ± 0.004	0.064 ± 0.004
3	1.434 ± 0.009	1.643 ± 0.004	1.791 ± 0.010	0.209 ± 0.010
4	2.018 ± 0.017	2.427 ± 0.009	2.591 ± 0.019	0.409 ± 0.019
5	2.473 ± 0.033	3.299 ± 0.022	3.174 ± 0.040	0.826 ± 0.040
6	3.075 ± 0.071	4.182 ± 0.062	3.893 ± 0.094	1.107 ± 0.094

Table 4.4: Values of slopes τ_q along with the statistical and dynamical components for $^{28}Si\text{-}AgBr$ collisions generated using *UrQMD* model for different values of q in φ-space.

q	τ_q	τ_q^{stat}	τ_q^{dyn}	$(q\text{-}1)$ - τ_q^{dyn}
2	0.825 ± 0.003	0.834 ± 0.002	0.991 ± 0.004	0.009 ± 0.004
3	1.621 ± 0.004	1.643 ± 0.004	1.978 ± 0.006	0.022 ± 0.006
4	2.423 ± 0.008	2.427 ± 0.009	2.996 ± 0.012	0.004 ± 0.012
5	3.241 ± 0.014	3.299 ± 0.022	3.942 ± 0.026	0.058 ± 0.026
6	4.116 ± 0.031	4.182 ± 0.062	4.934 ± 0.069	0.066 ± 0.069

Equation 4.7. Values of τ_q, τ_q^{stat} and τ_q^{dyn} for q =2-6 in φ-space are listed in Table 4.3. As can be seen from the table, τ_q^{dyn} values in φ-space also differ significantly from (q-1), thus giving another evidence of the dynamical origin of multiplicity fluctuations in our data.

In order to study whether the multifractality observed in our data could be explained by the standard models of particle production, we simulated 14000 ^{28}Si-$AgBr$ events using the string hadronic model *UrQMD*. A similar G_q-moment analysis was done for *UrQMD* events also in both the pseudorapidity (η) and azimuthal (φ) angle spaces. Figures 4.1 (c) and 4.2 (c) show ln$\langle G_q \rangle$ versus ln$M$ plots for *UrQMD* events for q=2-6 in η and φ spaces respectively. M was again varied from 2 to 35. As can be seen from Figures 4.1 (c) and 4.2 (c), ln$\langle G_q \rangle$ for *UrQMD* events also exhibits a linear dependence on ln$M$ in both the spaces. Table 4.2 shows the slopes τ_q of ln$\langle G_q \rangle$ versus ln$M$ plots for q=2-6 for *UrQMD* events in η-space. τ_q^{stat} are the slopes of the corresponding plots for random events generated as mentioned earlier and are listed in Table 4.2. Values of τ_q^{dyn} have been calculated using Equation 4.7 and are also listed in the Table 4.2. From Table 4.2 we notice that the slopes of ln$\langle G_q \rangle$ versus ln$M$ plots τ_q for *UrQMD* events are greater than the slopes of the corresponding plots for experimental events (Table 4.1). In fact these slopes τ_q are about the same as τ_q^{stat}, the slopes of the corresponding plots for random events We also notice from Table 4.2 that for *UrQMD* events values of (q-1) - τ_q^{dyn}, which quantifies the amount of dynamical fluctuations are negligible as compared to the corresponding values for experimental events given in Table 4.1. Therefore, *UrQMD* model fails to explain the observed dynamical fluctuations and multifractality in our data. A similar result is observed for φ-space also (Table 4.4).

4.2.2 F_q-Moment Method

The scaled factorial moments F_q that have been studied in emulsion experiments are defined as

$$\langle F_q \rangle = M^{q-1} \sum_{m=1}^{M} \frac{\langle n_m (n_m - 1).....(n_m - q + 1) \rangle}{\langle N \rangle^q} \qquad 4.9$$

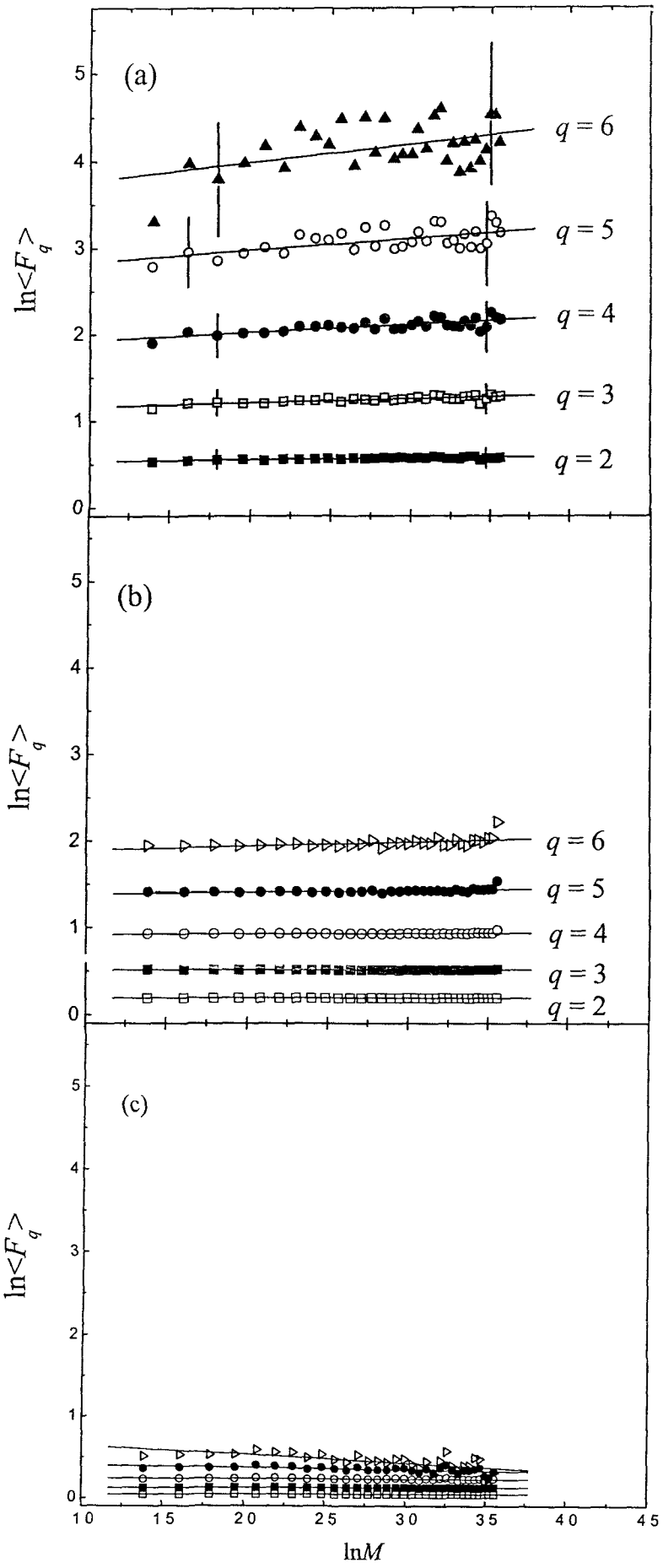

Figure 4.3: (a) $\ln\langle F_q \rangle$ versus $\ln M$ plots for ^{28}Si-$AgBr$ collisions at 14.6A GeV in η-space.
(b) $\ln\langle F_q \rangle$ versus $\ln M$ plots for *randomly generated* events in η-space.
(c) $\ln\langle F_q \rangle$ versus $\ln M$ plots for *UrQMD* events in η-space.

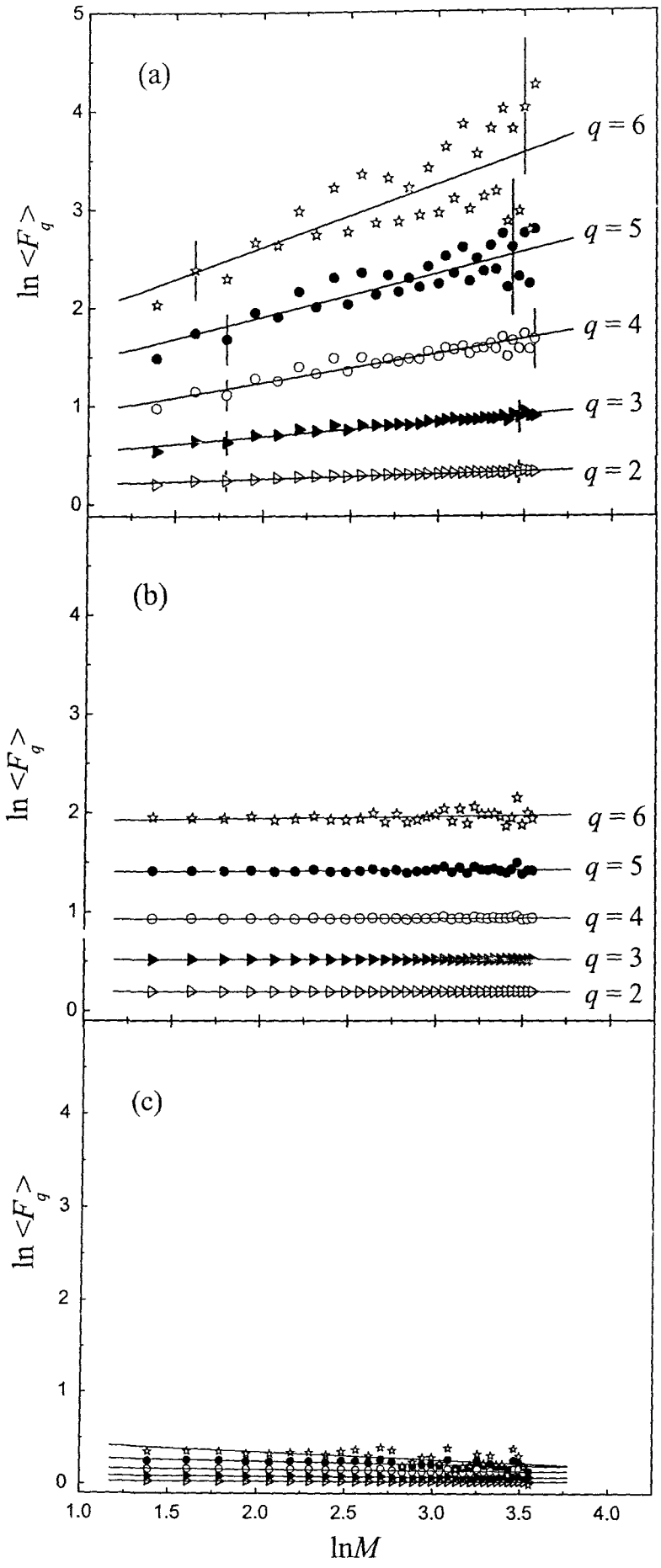

Figure 4.4: (a) $\ln\langle F_q \rangle$ versus $\ln M$ plots for ^{28}Si-$AgBr$ collisions at 14.6A GeV in φ-space.
(b) $\ln\langle F_q \rangle$ versus $\ln M$ plots for *randomly generated* events in φ-space.
(c) $\ln\langle F_q \rangle$ versus $\ln M$ plots for *UrQMD* events in φ-space.

Table 4.5: Values of the slopes ϕ_q of $\ln\langle F_q \rangle$ versus $\ln M$ plots for $^{28}Si\text{-}AgBr$ collisions at 14.6*A GeV* along with those for the randomly generated and *UrQMD* events in η-space.

q	slopes ϕ_q		
	Experimental Events	*Randomly Generated Events*	*UrQMD Events*
2	0.020 ± 0.002	0.0000 ± 0.0002	0.0007 ± 0.0002
3	0.060 ± 0.007	0.0005 ± 0.0006	0.0007 ± 0.0008
4	0.124 ± 0.017	0.0059 ± 0.0021	-0.0034 ± 0.0025
5	0.195 ± 0.044	0.0231 ± 0.0059	-0.0202 ± 0.0074
6	0.290 ± 0.096	0.0543 ± 0.0142	-0.0761 ± 0.0019

Table 4.6: Values of the slopes ϕ_q of $\ln\langle F_q \rangle$ versus $\ln M$ plots for $^{28}Si\text{-}AgBr$ collisions at 14.6*A GeV* along with those for the randomly generated and *UrQMD* events in φ-space.

q	slopes ϕ_q		
	Experimental Events	*Randomly Generated Events*	*UrQMD Events*
2	0.069 ± 0.003	-0.0001 ± 0.0002	-0.0020 ± 0.0004
3	0.194 ± 0.010	0.0008 ± 0.0007	-0.0059 ± 0.0012
4	0.362 ± 0.024	0.0030 ± 0.0022	-0.0127 ± 0.0029
5	0.580 ± 0.056	0.0077 ± 0.0065	-0.0317 ± 0.0085
6	0.842 ± 0.125	0.0188 ± 0.0168	-0.0831 ± 0.0233

where < > denotes the average over the number of events analysed. M is the total number of bins in which the X-interval (0-1) has been divided, n_m is the multiplicity of particles in mth bin, $<N>$ denotes the average multiplicity of particles in the pseudorapidity interval $\eta_{peak} - 2 \leq \eta \leq \eta_{peak} + 2$. Figures 4.3 (a) and 4.4(a) show $\ln<F_q>$ versus $\ln M$ plots for our data in η and φ spaces. The values of $<F_q>$ were calculated from Equation 4.9. A linear dependence of $\ln<F_q>$ on $\ln M$, indicating the power law dependence of F_q on M, is observed. The values of the slopes ϕ_q in both the η and φ spaces, determined from the least square fitting of the data points, are listed in Tables 4.5 and 4.6 respectively. Deviation of ϕ_q from 0 is a measure of the non-statistical or dynamical fluctuations in our data and points to a self-similar mechanism of multiparticle production.

Figures 4.3 (b and c) and 4.4 (b and c) show $\ln<F_q>$ versus $\ln M$ plots for random and *UrQMD* events in η and φ spaces respectively. Values of the slopes of these plots are given in Tables 4.5 and 4.6 respectively. We observe from these tables that the slopes ϕ_q for *UrQMD* and random events are negligible as compared to the ϕ_q values for the experimental events. In fact in the absence of dynamical fluctuations ϕ_q values should all be zero. Therefore, *UrQMD* model fails to explain the observed power law growth of the scaled factorial moments with decreasing bin size also.

4.2.3 Connection Between F_q and G_q

The normalized factorial moments F_q are used to investigate the self-similar properties of multiparticle production whereas G_q-moments are defined as a mean of studying the multifractal properties of a self-similar process. Hwa and Pan [17] have investigated the relation between F_q and G_q by expanding both in terms of basic functions $B_{q,k}(M)$ and have been able to establish a relationship between the fractal behavior of F_q and G_q. In the following, we use their method to investigate the relationship between F_q and G_q for our data.

The normalized factorial moments F_q are defined for integer values of q (≥ 1) whereas G_q are defined for all real values of q. However, to establish a connection between them q should be restricted to positive integer values ($q \geq 1$) for G_q-moments also. Let us define a function $B_{q,k}(M)$ as

$$B_{q,k}(M) = \left\langle \frac{Q_{q+k}(M,N)}{N^q} \right\rangle, \qquad 4.10$$

where $Q_{q+k}(M,N)$ are the number of bins containing $(q+k)$ particles in an event of multiplicity N in the pseudorapidity range $\Delta\eta$. $k = 0,1,2\ldots$ The angular brackets indicate the average over all events. The functions $B_{q,k}(M)$ express the basic fractal structure of the data. In terms of these functions G_q-moments can be expressed as

$$\langle G_q(M) \rangle = \sum_{k=0}^{\infty} B_{q,k}(M)(q+k)^q \qquad 4.11$$

Writing the first few terms of the above expression

$$\langle G_q(M) \rangle = B_{q,0}(M) q^q \left[1 + \frac{B_{q,1}(M)}{B_{q,0}(M)} \left(\frac{q+1}{q} \right)^q + \ldots\ldots \right] . \qquad 4.12$$

In the above expression, only the first few terms make significant contribution at large M and the sum of these terms determines τ_q .

However, to express F_q in terms of $B_{q,k}(M)$, $\langle N \rangle$ in Equation 4.9 has to be replaced by N. In terms of $B_{q,k}(M)$, $\langle F_q \rangle$ can be written as

$$\langle F_q \rangle = M^{q-1} \sum_{k=0}^{\infty} B_{q,k}(M) \frac{(q+k)!}{k!} \qquad 4.13$$

The first few terms of the above expression are

$$\langle F_q \rangle = M^{q-1} B_{q,0}(M) q! \left[1 + \frac{B_{q,1}(M)}{B_{q,0}(M)} (q+1) + \ldots\ldots \right] \qquad 4.14$$

It is clear from Equations 4.12 and 4.14 that $\langle F_q \rangle$ and $\langle G_q \rangle$ do not have identical M dependences. However, considering only the leading terms, we would have

$$\phi_q \cong q - 1 - \tau_q \qquad 4.15$$

If we use the modified G_q-moments, the above relation changes to

$$\phi_q \cong q - 1 - \tau_q^{dyn} \qquad 4.16$$

To compare ϕ_q with the deviations of τ_q^{dyn} from $(q\text{-}1)$, a plot of ϕ_q and $q\text{-}1\text{-}\tau_q^{dyn}$ as a function of q is shown in Figure 4.5. As can be seen from the figure, for $q>3$ the values of

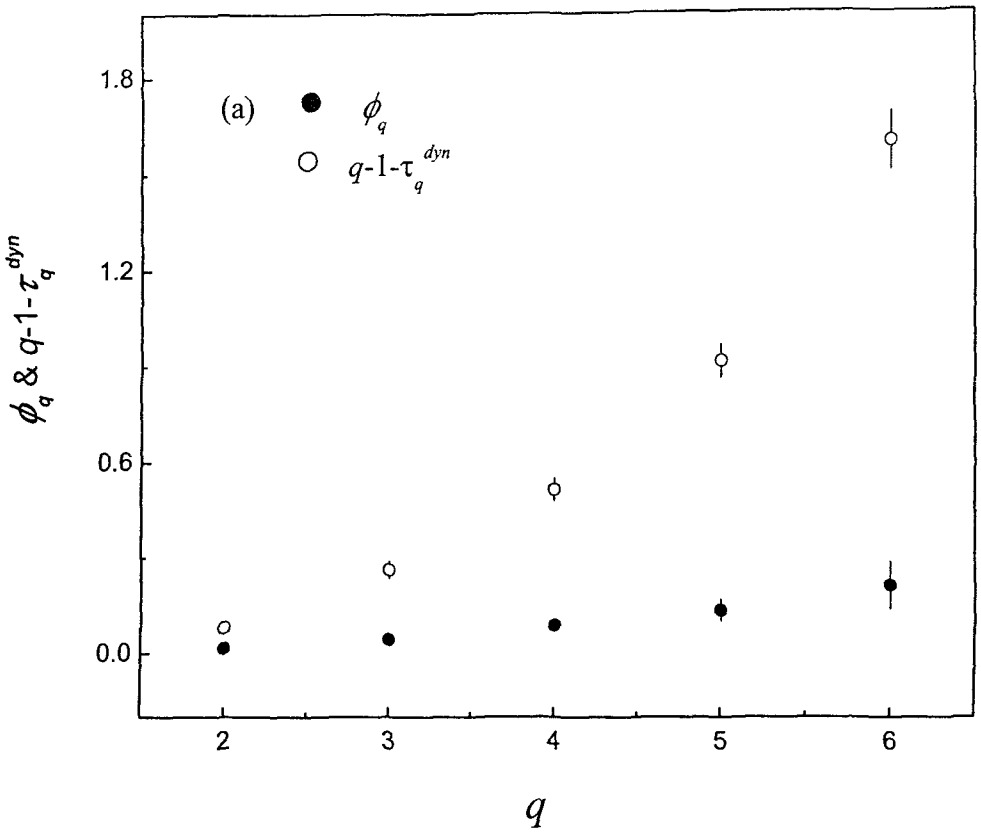

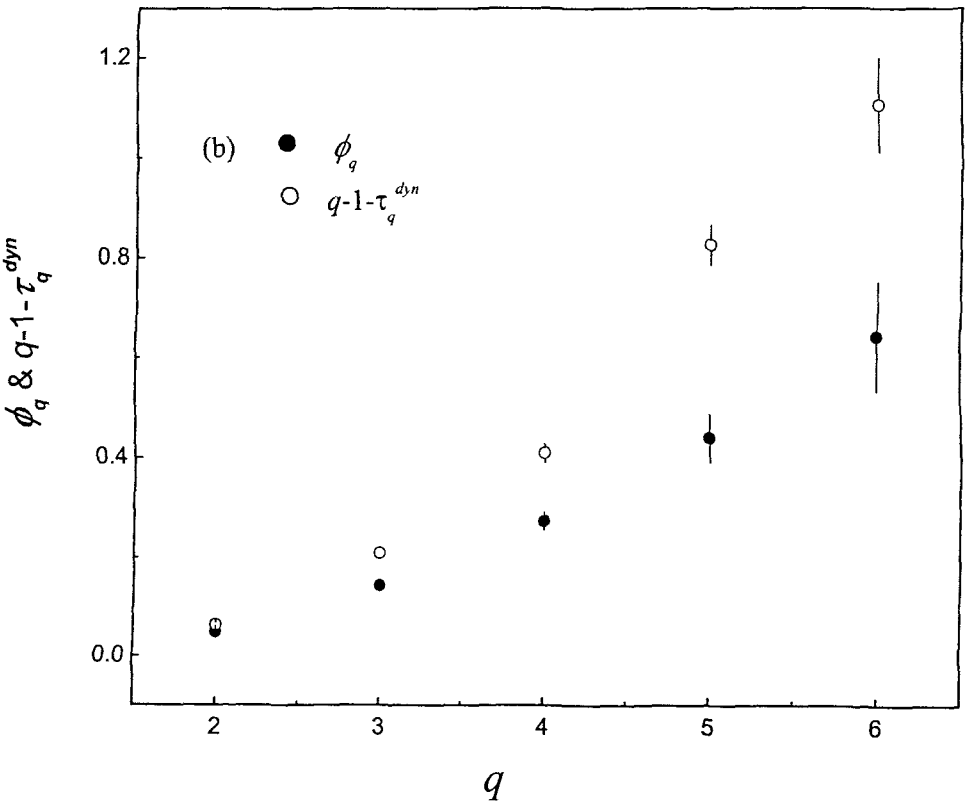

Figure 4.5: (a) Plots of ϕ_q and q-1- τ_q^{dyn} versus q for ^{28}Si-$AgBr$ collisions at 14.6A GeV in η-space.

(b) Plots of ϕ_q and q-1- τ_q^{dyn} versus q for ^{28}Si-$AgBr$ collisions at 14.6A GeV in φ-space.

ϕ_q and $q\text{-}1\text{-}\tau_q^{dyn}$ differ significantly for our data. A similar result was observed by Shivpuri et al. for *p-Emulsion* collisions at 800 *GeV/c* [33], by Jain et al. for nucleus-nucleus collisions at different energies [20] and by Derado et al in EMC data on μp and μd collisions [18]. ϕ_q values obtained in these investigations and also in the present one are smaller than the corresponding values $q\text{-}1\text{-}\tau_q^{dyn}$. Recently Ghosh et al. [21] have studied intermittency and multifractality in ^{16}O-*Emulsion* collisions at 60*A GeV*. The values of the intermittency indices ϕ_q obtained by them are also very different from the corresponding values of $q\text{-}1\text{-}\tau_q^{dyn}$. But unlike ours, ϕ_q values obtained by Ghosh et al. are larger than the corresponding values of $q\text{-}1\text{-}\tau_q^{dyn}$. The reason for the deviation of ϕ_q from $q\text{-}1\text{-}\tau_q^{dyn}$ in our data could be the fact that Equations 4.12 and 4.14 have different M dependences and that the relation $\phi_q \approx q\text{-}1\text{-}\tau_q^{dyn}$ was obtained by considering only the leading terms of Equations 4.12 and 4.14. Another reason for the deviation could be the fact that the modified G_q-moments, although defined to suppress statistical fluctuations, are not able to eliminate them completely.

4.2.4 Takagi Method

Apart from G_q-moment and F_q-moment methods, Takagi method [22] is also used to study the multifractality in multiparticle production. In the following we discuss Takagi method briefly. A single event contains n shower particles distributed in the interval $\Delta\eta (= \eta_{max} - \eta_{min})$ in the pseudorapidity space. The multiplicity of shower particles changes from event to event according to the distribution $P_n(\Delta\eta)$. The interval $\Delta\eta$ is divided into M bins having size of each bin $\delta\eta = \Delta\eta/M$.

Let $P_n(\delta\eta)$ denotes the multiplicity distribution for a single bin. It is assumed that the inclusive rapidity distribution $dn/d\eta$ is constant and $P_n(\delta\eta)$ is independent of the location of the bin. For particles produced in Ω independent events, there are $\Omega \times M$ bins and thus produced particles are distributed in these bins, each of size $\delta\eta$. Let K be the total number of particles produced in Ω events and n_{ji} the multiplicity of particles in the ith bin of the jth event. The theory of multifractal motivates us to consider the normalized density P_{ji} defined by

$$P_{ji} = \frac{n_{ji}}{K} \tag{4.17}$$

and to consider if the quantity

$$T_q(\delta\eta) = \ln \sum_{j=1}^{\Omega} \sum_{i=1}^{M} P_{ji}^q \quad \text{for q} > 0 \tag{4.18}$$

behaves like a linear function of logarithm of the resolution $R(\delta\eta)$

$$T_q(\delta\eta) = A_q + B_q \ln R(\delta\eta)\,, \tag{4.19}$$

where A_q and B_q are constants independent of $\delta\eta$. If the linear behavior is observed over a large range of $R(\delta\eta)$, a generalized dimension may be defined as

$$D_q = B_q / (q\text{-}1) \tag{4.20}$$

Now we evaluate the double sum of P_{ji}^q when the number of events is very large.

$$\sum_{j=1}^{\Omega} \sum_{i=1}^{M} P_{ji}^q = \sum_{n=0}^{\infty} \Omega M P_n(\delta\eta) \left[\frac{n}{K}\right]^q = \frac{\langle n^q \rangle}{K^{q-1} \langle n \rangle} \tag{4.21}$$

where a generic notation

$$\langle f(n) \rangle = \sum_{n=0}^{\infty} f(n) P_n(\delta\eta) \tag{4.22}$$

and the relation $<n>=K/\Omega M$ have been used. Here, $<f(n)>$ is a function of $\delta\eta$ in general but the $\delta\eta$ dependence is suppressed for brevity. Since we have

$$\delta\eta = \frac{\Delta\eta}{M}$$

i.e. $M=\Delta\eta/\delta\eta$,

we can write

$$<n>=K/\Omega M=K.\ \delta\eta/\Omega.\Delta\eta. \tag{4.23}$$

Using Equations 4.18, 4.19 and 4.21, for the simplest choice $R(\delta\eta)=\delta\eta$, we can obtain the relation

$$\ln \langle n^q \rangle = A_q + \{B_q + 1\} \ln \delta\eta \tag{4.24}$$

By using Equation 4.20, the above equation can be written as

$$\ln\langle n^q\rangle = A_q + \{(q\text{-}1)\, D_q + 1\} \ln\delta\eta \qquad 4.25$$

To check the validity of the above relation, Takagi [22] plotted $\ln\langle n^q\rangle$ versus $\ln\eta_c$ for UA5 data on $p\bar{p}$ collisions at $\sqrt{s}$ =200GeV. Deviation from the linear behaviour was observed in large η_c region. It is reasonable to expect that this deviation may be due to the non-flat behaviour of $dn/d\eta$ in projectile and target fragmentation regions where η is large. Therefore, $<n>$ is considered a better choice of $R(\delta\eta)$ because $dn/d<n>$ is flat by definition. Thus Equation 4.25 can be written as

$$\ln\langle n^q\rangle = A_q + K_q \ln\langle n\rangle \quad ,$$

where

$$K_q=(q\text{-}1)\, D_q + 1 \qquad 4.26$$

A linear behavior over a considerable range of $\langle n\rangle$ points towards the fractal structure in multiparticle production. The generalized dimensions D_q for $q \geq 2$ can then be easily obtained from the slopes of $\ln\langle n^q\rangle$ versus $\ln\langle n\rangle$ plots.

We now use the Takagi methodology to study multifractality in the multiplicity distribution of shower particles produced in $^{28}Si\text{-}AgBr$ collisions at 14.6 *A GeV* in both η and φ spaces. The analysis was performed on the same data sample as was used for the G_q-moment analysis. As done earlier, the analysis was restricted to the central region of pseudorapidity with $\eta_{peak} - 2 \leq \eta \leq \eta_{peak} + 2$. As mentioned in the beginning of this section, the single particle density distribution is assumed constant in the Takagi method. Therefore, to avoid the effect of non-flat density distribution, the observed pseudorapidity and azimuthal angle distributions have been converted into the corresponding X-distributions using Equations 4.1 and 4.8. As mentioned earlier, in X-space single particle density distribution is flat and X values are uniformly distributed between X=0.0 and X=1.0.

Values of η and φ converted into the corresponding cumulative X-variables (X_η and X_φ) were used for the analysis. The initial cumulative X variable interval ΔX becomes 1.0 corresponding to the initial rapidity interval $\Delta\eta$ = 4.0. The ΔX was subsequently decreased in steps of 0.025 and the values of $\ln\langle n^q\rangle$ and $\ln<n>$ were

computed for each interval. Here n is the multiplicity of shower particles in an event in the given interval ΔX. Figure 4.6 (a) shows the plots of $\ln\langle n^q \rangle$ versus $\ln\langle n \rangle$ for q=2-6 in η space. From the figure it is clear that the behavior of $\ln\langle n^q \rangle$ versus $\ln\langle n \rangle$ plots is linear. Further, in the case of azimuthal angle space, the initial cumulative X variable interval ΔX becomes 1.0 corresponding to the azimuthal interval $\Delta\varphi = 360.0$. The ΔX was subsequently decreased in steps of 0.025 and $\ln\langle n^q \rangle$ and $\ln\langle n \rangle$ were computed for each interval. Here n is the multiplicity of shower particles in an event in the given interval ΔX. Figure 4.7 (a) shows the plots of $\ln\langle n^q \rangle$ versus $\ln\langle n \rangle$ for q=2-6 in φ-space. From the figure we observe that the dependence of $\ln\langle n^q \rangle$ on $\ln\langle n \rangle$ is linear in φ-space also.

In order to find whether the observed dependence of $\ln\langle n^q \rangle$ on $\ln\langle n \rangle$ could be explained by the string hadronic model *UrQMD* a similar analysis was performed for the random and *UrQMD* events in both the η and φ spaces. Figures 4.6 (b) and 4.6 (c) show the $\ln\langle n^q \rangle$ versus $\ln\langle n \rangle$ plots for the random and *UrQMD* events respectively in η-space. We observe from Table 4.7 that the slopes of the plots for the random and *UrQMD* events are about the same as those for the corresponding plots for the experimental events in η-space. Similarly in φ-space Figures 4.7 (b) and 4.7 (c) show the $\ln\langle n^q \rangle$ versus $\ln\langle n \rangle$ plots for the random and *UrQMD* events respectively. We again observe from Table 4.8 that the slopes of the plots for the random and *UrQMD* events are about the same as those for the corresponding plots for the experimental events in φ-space. Whereas the statistical fluctuations are completely eliminated in F_q-moment method [1] and are suppressed in the modified G_q-moment method [17], no attempt is made in the Takagi method to eliminate or suppress the statistical fluctuations. This is the reason as to why we get about the same values of the slopes of $\ln\langle n^q \rangle$ versus $\ln\langle n \rangle$ plots for the experimental, random and *UrQMD* events. Thus no meaningful conclusion regarding multifractality in the data could be drawn from the Takagi method. We therefore suggest that only F_q-moment or G_q-moment method should be used for the study of multifractality in multiparticle production as the multiplicity moments calculated in the Takagi method are dominated by statistical fluctuations.

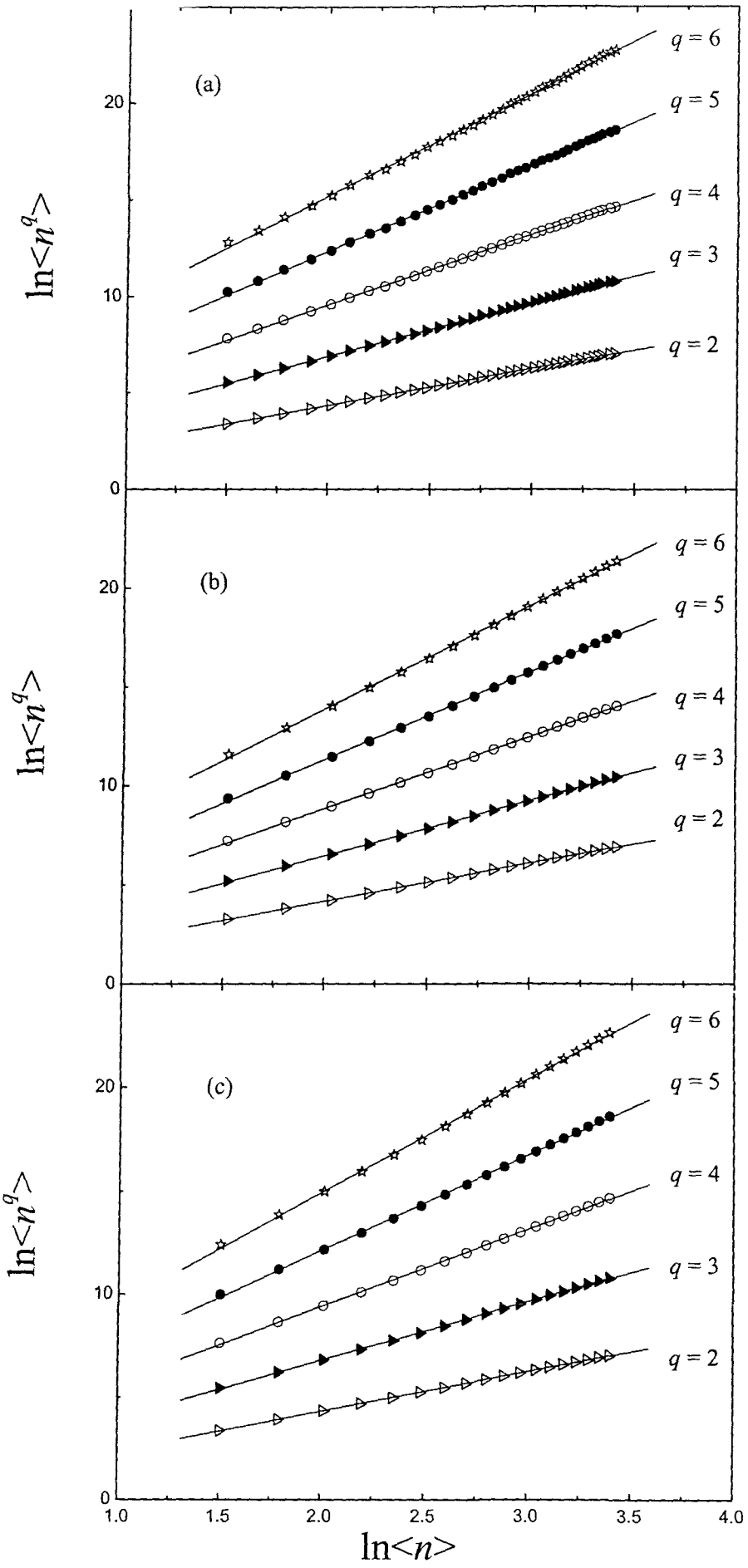

Figure 4.6: (a) $\ln\langle n^q\rangle$ versus $\ln\langle n\rangle$ plots for ^{28}Si-$AgBr$ collisions at 14.6A GeV in η-space.
(b) $\ln\langle n^q\rangle$ versus $\ln\langle n\rangle$ plots for *randomly generated* events in η-space.
(c) $\ln\langle n^q\rangle$ versus $\ln\langle n\rangle$ plots for *UrQMD* events in η-space.

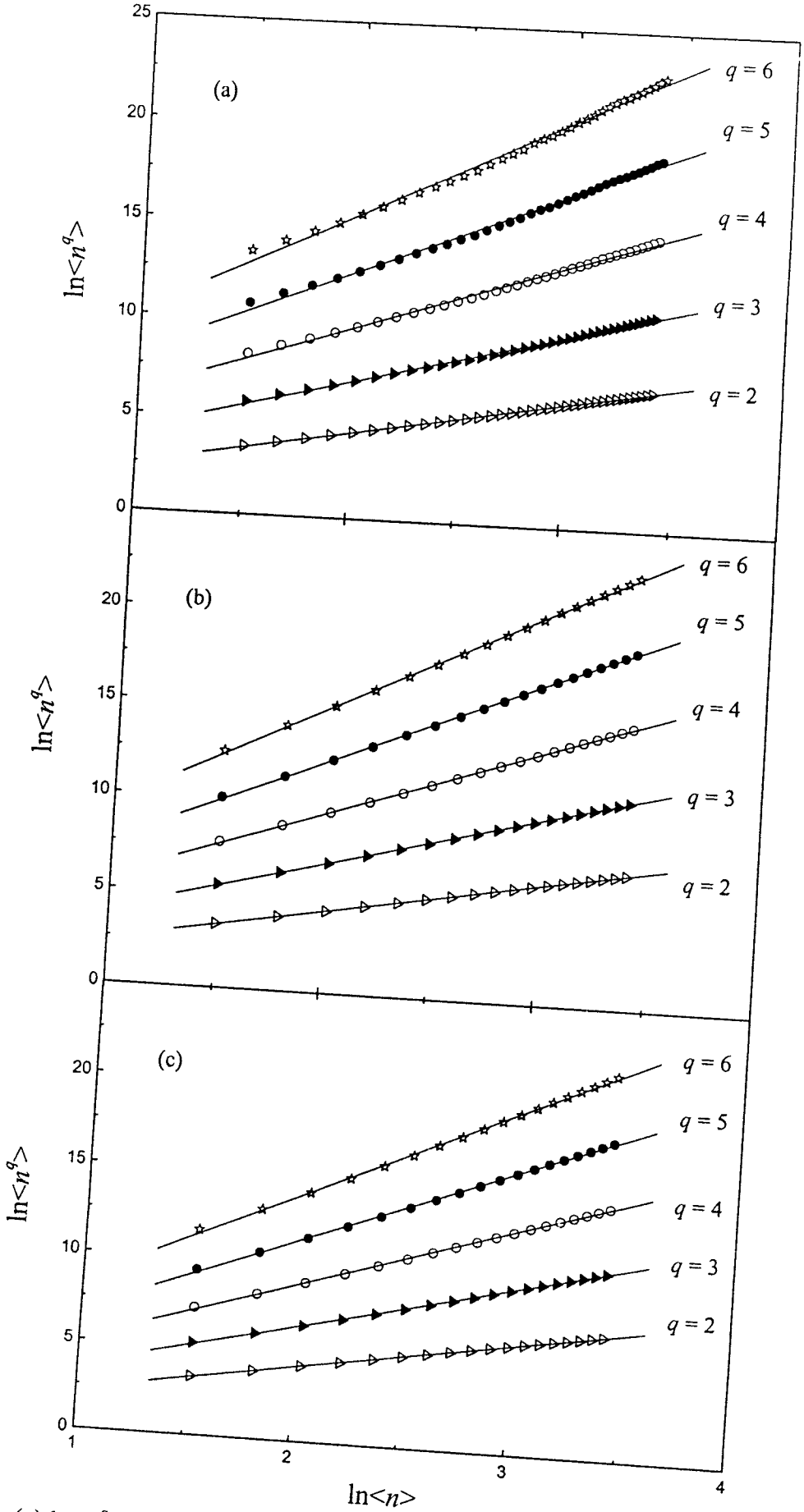

Figure 4.7: (a) $\ln\langle n^q\rangle$ versus $\ln\langle n\rangle$ plots for ^{28}Si-$AgBr$ collisions at 14.6A GeV in φ-space.
(b) $\ln\langle n^q\rangle$ versus $\ln\langle n\rangle$ plots for *randomly generated* events in φ-space.
(c) $\ln\langle n^q\rangle$ versus $\ln\langle n\rangle$ plots for *UrQMD* events in φ-space.

Table 4.7: Values of the slopes of $\ln\langle n^q\rangle$ versus $\ln\langle n\rangle$ plots for ^{28}Si-*AgBr* collisions at 14.6*A GeV* along with those for the randomly generated and *UrQMD* events for different values of q in η-space.

q	values of the slopes		
	Experimental Events	*Randomly Generated Events*	*UrQMD Events*
2	1.920 ± 0.002	1.934 ± 0.004	1.919 ± 0.004
3	2.810 ± 0.005	2.838 ± 0.009	2.790 ± 0.010
4	3.677 ± 0.010	3.720 ± 0.016	3.624 ± 0.016
5	4.527 ± 0.016	4.586 ± 0.023	4.428 ± 0.022
6	5.366 ± 0.025	5.437 ± 0.030	5.207 ± 0.029

Table 4.8: Values of the slopes of $\ln\langle n^q\rangle$ versus $\ln\langle n\rangle$ plots for ^{28}Si-*AgBr* collisions at 14.6*A GeV* along with those for the randomly generated and *UrQMD* events for different values of q in φ-space.

q	values of the slopes		
	Experimental Events	*Randomly Generated Events*	*UrQMD Events*
2	1.873 ± 0.007	1.934 ± 0.004	1.925 ± 0.004
3	2.698 ± 0.017	2.836 ± 0.009	2.803 ± 0.011
4	3.505 ± 0.029	3.713 ± 0.014	3.648 ± 0.018
5	4.308 ± 0.043	4.570 ± 0.020	4.465 ± 0.026
6	5.113 ± 0.060	5.410 ± 0.026	5.259 ± 0.034

4.3 Generalized Dimensions

Power law behavior is a characteristic of fractals, that is, self-similar objects. According the theory of fractals, self-similar systems are characterized by infinite spectrum of non-integer generalized dimensions D_q. It has been observed in sections 4.2.1 and 4.2.2 that both $<F_q>$and $<G_q>$ exhibit power law dependences on M, thereby indicating the self-similar nature of the multiparticle production process. Therefore, the generalized dimensions that characterize the multiparticle production process can be obtained from both the F_q-moment and G_q-moment analyses, using the following relations

$$D_q = \frac{\tau_q^{dyn}}{(q-1)} \qquad 4.27$$

Substitution of τ_q^{dyn} from Equation 4.16 gives D_q in terms of intermittency indices ϕ_q

$$D_q = 1 - \frac{\phi_q}{(q-1)} \quad . \qquad 4.28$$

D_q values for experimental and *UrQMD* events in both the η and φ spaces were calculated using Equation 4.27 from τ_q^{dyn} values obtained from the G_q-moment analysis and are listed in Table 4.9. D_q values for experimental and *UrQMD* events in both the η and φ spaces were also calculated using Equation 4.28 from ϕ_q values obtained from the F_q-moment analysis and are listed in Tables 4.10. It is clear from Tables 4.9 and 4.10 that for experimental events D_q values obtained from the F_q-moment method in η-space are greater than the corresponding values in φ-space. However, values of D_q obtained from the G_q-moment method in η-space are smaller than the corresponding values in φ space. This is a well-known result. D_q values not only depend on the space in which the analysis in done but also on the method of analysis. The reason is the difference between the definitions of the two moments. Whereas F_q-moments eliminate statistical fluctuations completely, G_q-moments, as pointed out in section 4.2.3 are not able to eliminate them completely. However, as can be seen from Tables 4.9 and 4.10, D_q values in each case for our experimental events decrease with increasing q. This is an evidence of the presence of multifractality in our data. It can be observed from Tables 4.9 and 4.10 that values of the generalized dimensions D_q for *UrQMD* events calculated from the F_q-moment and G_q-moment methods are almost independent of q. D_q values for q=2-6 are all equal to one

Table 4.9: Values of the generalized dimensions D_q for $^{28}Si\text{-}AgBr$ collisions at 14.6 $AGeV$ determined from the G_q-moment method in η and φ spaces.

q	*Generalized Dimensions* (D_q)			
	η-space		φ-space	
	Experimental Events	*UrQMD Events*	*Experimental Events*	*UrQMD Events*
2	0.920 ± 0.017	0.991 ± 0.017	0.936 ± 0.004	0.991 ± 0.004
3	0.869 ± 0.014	0.988 ± 0.014	0.895 ± 0.005	0.989 ± 0.005
4	0.829 ± 0.012	0.994 ± 0.012	0.864 ± 0.006	0.999 ± 0.006
5	0.771 ± 0.013	0.982 ± 0.013	0.794 ± 0.010	0.985 ± 0.010
6	0.719 ± 0.018	0.977 ± 0.018	0.779 ± 0.019	0.987 ± 0.019

Table 4.10: Values of the generalized dimensions D_q for $^{28}Si\text{-}AgBr$ collisions at 14.6A GeV determined from the F_q-moment method in η and φ spaces.

q	*Generalized Dimensions* (D_q)			
	η-space		φ-space	
	Experimental Events	*UrQMD Events*	*Experimental Events*	*UrQMD Events*
2	0.980 ± 0.002	0.9993 ± 0.0002	0.931 ± 0.003	1.002 ± 0.000
3	0.970 ± 0.003	0.9996 ± 0.0004	0.903 ± 0.005	1.003 ± 0.001
4	0.960 ± 0.005	1.0011 ± 0.0008	0.879 ± 0.006	1.004 ± 0.001
5	0.951 ± 0.011	1.0050 ± 0.0018	0.855 ± 0.014	1.008 ± 0.003
6	0.942 ± 0.019	1.0152 ± 0.0004	0.832 ± 0.025	1.016 ± 0.004

another within errors This points to the absence of dynamical fluctuation and multifractality in *UrQMD* events This again establishes that the hadronic string model *UrQMD* fails to explain the observed dynamical fluctuations and multifractality in our data.

4.4 Multifractal Specific Heat

Bershadskii [34] showed that Bernoulli distribution appears in a natural way when transition from mono-fractality to multifractality is studied. Starting from the definition of G_q-moment, he derived the following relation

$$D_q = D_\alpha + c\frac{\ln q}{(q-1)} \qquad 4.29$$

for the multifractal Bernoulli fluctuations. In the above relation, D_q are the generalized dimensions. If we use the thermodynamic interpretation of multifractality [35], then the constant c can be interpretated as multifractal specific heat of the system. Bershadskii analyzed the data on nucleus-nucleus collisions at various energies and found good agreement between the data and the multifractal Bernoulli representation (Equation 4.29) We also determine the multifractal specific heat for our data using different sets of D_q values given in Tables 4.9 and 4.10. Figures 4.8 (c) and (d) show the plots of D_q obtained from the F_q-moment method as a function of ln $q/(q\text{-}1)$ for $^{28}Si\text{-}AgBr$ collisions at 14.6 $AGeV$ in both the η and φ phase spaces Straight lines are the linear fits to the data, indicating good agreement between our data and the multifractal Bernoulli representation. The slopes of the fitted lines, which give the values of the multifractal specific heat c for our data, are 0.11 ± 0.01 and 0.29 ± 0.03 for η-space and φ-space respectively.

Figures 4.8 (a) and (b) show the plots of D_q, obtained from the G_q-moment method, as a function of ln $q/(q\text{-}1)$ for $^{28}Si\text{-}AgBr$ collisions at 14.6 $AGeV$ in both the η and φ phase spaces. The values of c, the slopes of the fitted lines, in η and φ phase spaces in this case are 0.57 ± 0.09 and 0.48 ± 0.08 respectively.

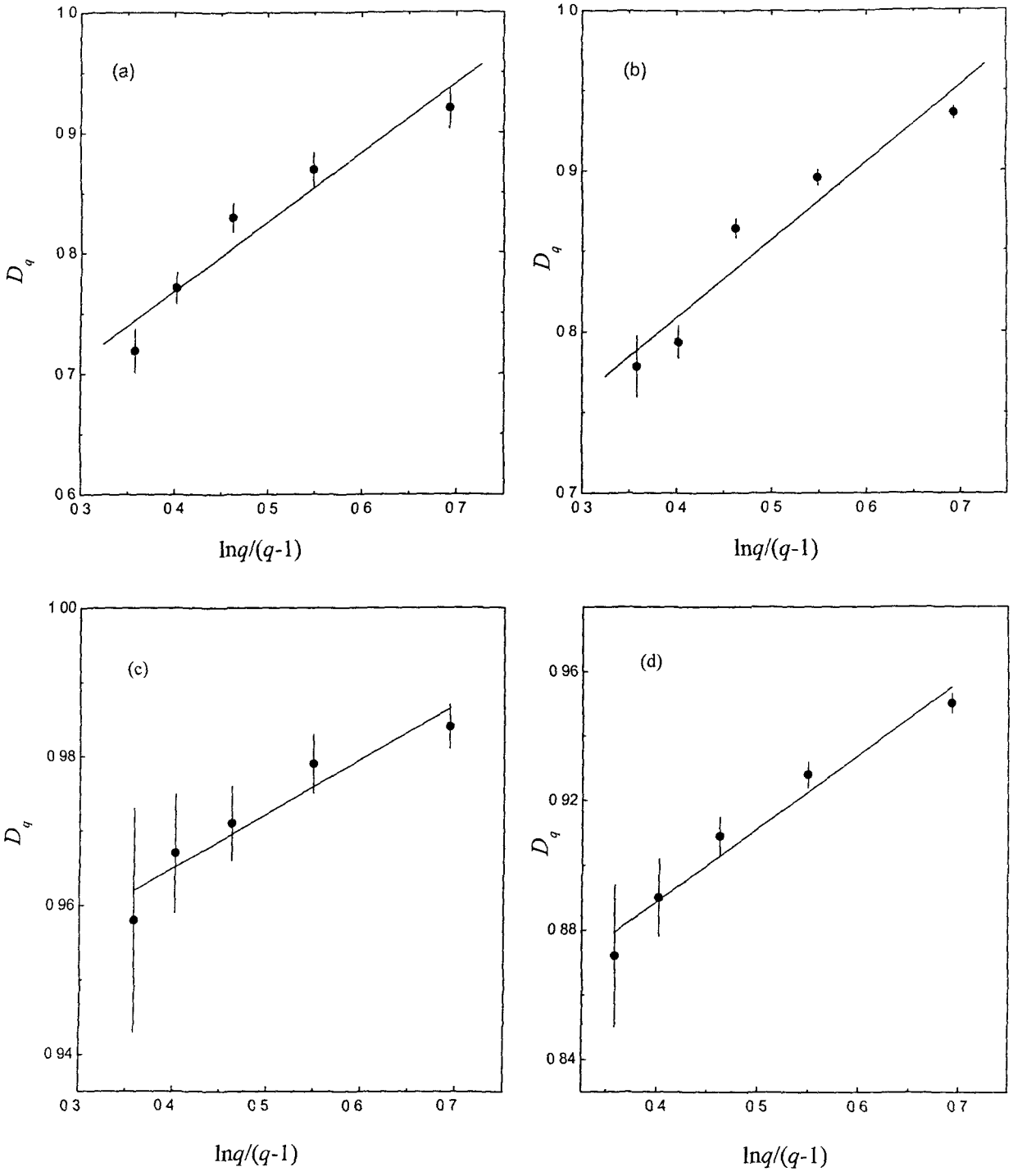

Figure 4.8: The generalized dimensions D_q versus ln$q$/(q-1) plots for ^{28}Si-$AgBr$ collisions at 14.6A GeV (a) in η-space, D_q obtained from G_q-moment method, (b) in φ-space, D_q obtained from G_q-moment method, (c) in η-space, D_q obtained from F_q-moment method and (d) in φ-space, D_q obtained from F_q-moment method.

References

1. A. Bialas and R. Peschanski, *Nucl. Phys.* **B 273** (1986) 703.
2. DELPHI Collaboration, *Phys. Lett.* **B 247** (1990) 137.
3. TASSO Collaboration, *Phys. Lett.* **B 231** (1989) 548.
4. I. Derado, G. Jansco, N. Schnitz and P. Stopa, *Z. Phys.* **C 47** (1990) 235.
5. W. Shaoshun, Z. Jie, Y. Yunxiu, X. Chinguo and Z. Yu, *Phys. Rev.* **D 49** (1994) 5785.
6. UA1 Collaboration, *Nucl. Phys.* **B 345** (1990) 1.
7. KLM Collaboration, *Phys. Rev.* **C 40** (1989) R2449.
8. D. Ghosh et al., *Phys. Rev.* **D 49** (1994) 3113.
9. R. K. Shivpuri and V. K. Verma, *Phys. Rev.* **D 47** (1993) 123.
10. G. Paladin and A. Vulpiani, *Phys. Rep.* **156** (1987) 147.
11. H. Hiramoto and M. Kohmoto, *Int. J. Mod. Phys.* **B 6** (1992) 281.
12. Janssen, *Int. J. Mod. Phys.* **B 8** (1994) 943.
13. C. B. Chiu and R. C. Hwa, *Phys. Rev.* **D 45** (1992) 2276.
14. R. K. Shivpuri and V. K. Verma, *Phys. Rev.* **D47** (1993) 123.
15. EMU-01 Collaboration, *Europhys. Lett.* **44** (1998) 571.
16. P. L. Jain, G. Singh, and A. Mukhopadhyay, *Phys. Rev.* **C 46** (1992) 721.
17. R. C. Hwa and J. Pan, *Phys. Rev.* **D45**, (1992) 1476.
18. I. Derado, R. C. Hwa, G. Jancso and N. Schmitz, *Phys. Lett.* **B 283** (1992) 151.
19. C. Albajar et al., (UA1), *Z. Phys.* **C 56** (1992) 37.
20. P. L. Jain, G. Singh and A. Mukhopadhyay, *Phys. Rev.* **C 48** (1993) R517.
21. D. Ghosh et al., *Nucl. Phys.* **A 707** (2002) 213.
22. Fujio Takagi, *Phys. Rev. Lett.* **72** (1994) 32.
23. R. E. Ansorge *et al.* (UA5 Collaboration), *Z. Phys.* **C 43** (1989) 357.
24. W. Braunschweig *et al.* (TASSO Collaboration), *Z. Phys.* **C 41** (1988) 159.
25. P. Abreu et al. (DELPHI Collaboration), *Z. Phys.* **C 52** (1991) 271.
26. Neeti Prashar, R. K. Shivpuri, Sudhir Malik and S. K. Soni, *J. Phys.* **G 21** (1995) 173.
27. R. Hasan, M. Mohibul-Haq and Saiful Islam, *Int. J. Mod. Phys.* **E 9** (2000) 417-429.
28. D. Ghosh et al., *Phys. Rev.* **C 58** (1998) 3553.

29. D. Ghosh et al., *Int. J. Mod. Phys.* **A 14** No. 13 (1999) 2091-2101.
30. D. H. Skelding, *Ph. D. Thesis*, *Univ. of Washington* (1996)
31. J. D. Bjorken, *Phys. Rev.* **D 27** (1983) 140.
32. A. Bialas and M. Gazdzicki, *Phys. Lett.* **B 252** (1990) 483.
33. R. K. Shivpure and V. Anand, *Phys. Rev.* **D 50** (1994) 287.
34. A. Bershadskii, *Phys. Rev.* **C 59** (1999) 364.
35. E. Stanely and P. Meakin, *Nature* **335** (1988) 405.

CHAPTER V

Scaled Factorial Cumulant Moments and Factorial Correlators for ^{28}Si-$AgBr$ Collisions at 14.6A GeV

5.1 Introduction

In the last chapter, we studied the fluctuations in the pseudorapidity and azimuthal angle distributions of shower particles produced in $^{28}Si\text{-}AgBr$ collisions at $14.6A\ GeV$, using F_q-moment and modified G_q-moment methods. The fluctuations present in the distributions are the results of dynamical correlations among the produced particles. Various processes would lead to correlations in different number of particles. Binary decays would generate two particle correlations, decay chain would introduce correlations in a few particles and jet structures could correlate a few tens of particles. Collective flow, chaotic hydrodynamic processes and self similar cascades would generate correlations in varying numbers of particles, depending on the details of the dynamics of particle production.

In the scaled factorial moments F_q, the order q is a measure of the number of particles involved in the correlations. Thus F_2 is sensitive to two particle correlations. The higher order factorial moments of order $q > 2$ depend on the multiparticle correlations of all orders $\leq q$. Therefore, F_3 is sensitive to two as well as three particle correlations.

There are enough indications that correlations of order greater than two are present in the multiparticle production data [1]. In order to study different orders of correlations independently, the method of scaled factorial cumulant moments has been developed [2]. These moments are defined in such a way so as to remove the effects of the lower order correlations. Thus the scaled factorial cumulant moments offer a way of studying correlations of a given order.

In this chapter we study the fluctuations in the pseudorapidity distributions of shower particles produced in $^{28}Si\text{-}AgBr$ collisions at $14.6A\ GeV$ using the cumulant moment method. We compare our results with the corresponding results obtained for $^{28}Si\text{-}AgBr$ collisions simulated using the string hadronic model *UrQMD* and the independent source model.

Additional information about local non-statistical fluctuations in different domains of phase space could be obtained by studying correlations between different pseudorapidity bins through the study of factorial correlators. Very scanty experimental data exist on the study of factorial correlators. Only a few investigations have reported results on factorial correlators in nucleus-nucleus collisions [3, 4]. Therefore we study in this chapter bin-bin correlations of shower particles produced in $^{28}Si\text{-}AgBr$ collisions at

14.6*A GeV* also through the study of factorial correlators and compare our results with the corresponding results obtained by analyzing ^{28}*Si-AgBr* events simulated using the string hadronic model *UrQMD*. Finally we confront our results with the predictions of the α-model [5].

5.2 Scaled Factorial Cumulant Moments

The second order factorial cumulant moment of mth bin is defined as [2]

$$f_2^{\,m} = \langle n_m(n_m - 1)\rangle - \langle n_m\rangle^2 \qquad 5.1$$

where n_m denotes the number of particles in the mth bin for a particular event. The sign $< >$ denotes the average taken over the whole sample of events. We can see that the equation is obtained by subtracting the first order contribution, $[f_1^m]^2 = \langle n_m\rangle^2$, from the second order factorial moment $\langle n_m(n_m\text{-}1)\rangle$.

Similarly by subtracting the three possible pair correlation contributions, $f_2^m\langle n_m\rangle$ and the single particle contribution $\langle n_m\rangle^3$ from the third order factorial moment, the third order factorial cumulant moment is obtained as

$$f_3^{\,m} = \langle n_m(n_m - 1)(n_m - 2)\rangle - 3f_2^{\,m}\langle n_m\rangle - \langle n_m\rangle^3 \qquad 5.2$$

Using Equation 5.1, the above equation can be written as

$$f_3^{\,m} = \langle n_m(n_m - 1)(n_m - 2)\rangle - 3\langle n_m(n_m - 1)\rangle\langle n_m\rangle + 2\langle n_m\rangle^3. \qquad 5.3$$

The scaled factorial cumulant moment of order q is then defined as

$$K_q = \frac{1}{M}\sum_{m=1}^{M}\frac{f_q^m}{\langle n_m\rangle^q} \qquad 5.4$$

where f_q^m is the factorial cumulant moment of order q for mth bin. Further we can easily get the relation between the scaled factorial cumulants moments and the scaled factorial moments as

$$K_2 = F_2\text{-}1 \qquad 5.5$$

$$K_3 = F_3 - 3F_2 + 2 \qquad 5.6$$

Where F_2 and F_3 represent the scaled factorial moments of order 2 and 3. We can see from Equation 5.5 that the behaviour of the second order scaled factorial cumulant moment is the same as that of the second order scaled factorial moment. But the higher order scaled factorial moments reveal little new information because of their strong dependence on two particle correlations. Further, for a Poisson distribution of particles

the scaled factorial cumulant moments of all orders except the first are identically equal to zero [6]. Thus they automatically remove any contribution due to Poissonian fluctuations and any deviation from zero of a scaled cumulant moment of a given order indicates the presence of non-statistical correlations of that order. The cumulant indices are defined as the slopes of K_q versus - $\ln\delta\eta$ plots

$$\pi_q = -\delta K_q/\delta(\ln\delta\eta) \qquad 5.7$$

where bin width $\delta\eta = \Delta\eta/M$

i.e. $\delta\eta \propto M^{-1}$.

Thus Equation 5.7 can be written as

$$\pi_q = \delta K_q/\delta(\ln M) \qquad 5.8$$

Using Equation 5.4 the scaled factorial cumulant moments are calculated for q =2 and 3 for our data in η space. In Figure 5.1 (a) we plot K_q versus $\ln M$ for q =2 and 3 in η space. It should be noted that we plot K_q on a linear scale rather than a logarithmic scale as is done for the scaled factorial moments. The reason is that the scaled cumulant moment of a given order is calculated by subtracting the effects of lower order correlations. Thus the scaled cumulant moments are not positive-definite like the scaled factorial moments and may have negative values. So it is not practical to plot them on a logarithmic scale.

From Figure 5.1(a) we observe that both the second and third order scaled cumulant moments K_2 and K_3 have non-zero values, which indicates that the multiplicity distribution of shower particles produced in ^{28}Si-$AgBr$ collisions at 14.6A GeV is not Poissonian. Further significant deviation of the values of the second and third order cumulant moments (K_2 and K_3) from zero is an evidence of the presence of dynamical two particle and three particle correlations. However, in order to extract more information from the cumulant moment analysis and to compare our results with the corresponding results of independent source model, we have to investigate the slopes of K_q versus $\ln M$ plots. The slopes of the linear fits of these plots give the values of cumulant indices, which are $\pi_2 = 0.018 \pm 0.004$, $\pi_3 = 0.012 \pm 0.003$.

In order to find whether our results on the cumulant moments could be explained by the standard generators of particle production in nucleus-nucleus collisions at relativistic energies, we simulated 14000 ^{28}Si-$AgBr$ collisions at 14.6A GeV using the string hadronic model $UrQMD$. K_q versus $\ln M$ plots for $UrQMD$ events are shown in Figure 5.1 (b). From the figure we observe that K_3 values for different M are almost zero,

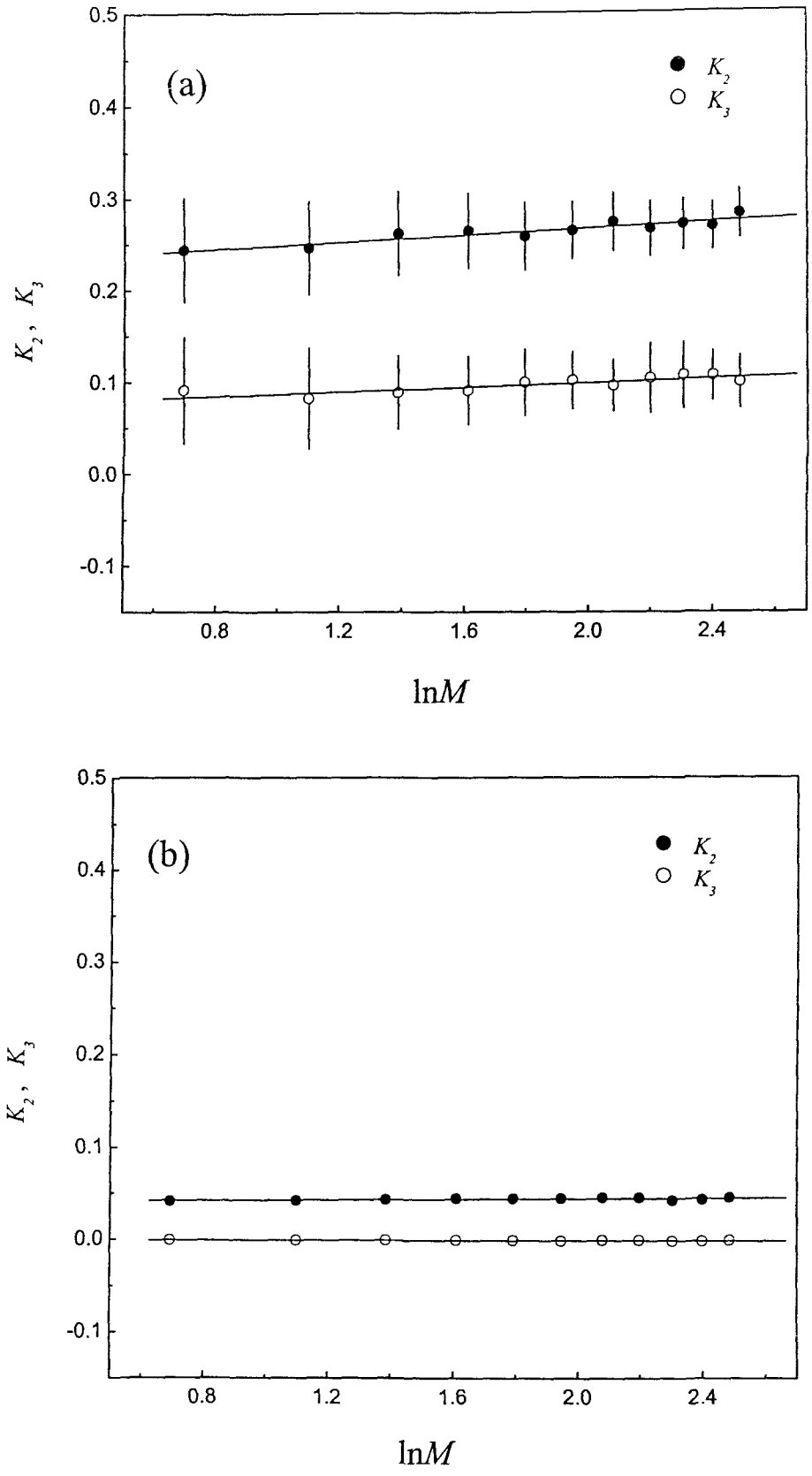

Figure 5.1: Plots of scaled factorial cumulant moments K_2 and K_3 versus ln$M$ for shower particles in η-space for (a) ^{28}Si-$AgBr$ collisions at 14.6A GeV and (b) $UrQMD$ events.

indicating the absence of three particle correlations in *UrQMD* events. However, K_2 values for different M deviate significantly from zero, indicating that significant two particle correlations are present in *UrQMD* events. The slopes of K_q versus ln$M$ plots (cumulant indices) for simulated events for q = 2 and 3 are π_2 = 0.002 ± 0.001, π_3 = -0.000 ± 0.000 which are consistent with being zero. However, not only two particle correlations but also significant three particle correlations are present in our data. Further, the values of cumulant indices for our data are also not zero. Thus the string hadronic model *UrQMD* fails to explain the observed correlations in our data.

If we assume that the multiparticle production in nucleus-nucleus collisions could be thought of as a superposition of N independent sources, which are identical for different types of colliding systems, we can derive a relation between the cumulant moments and the average pseudorapidity density of particles produced. Such independent sources could be fireballs, QGP bubbles, clusters or independent hadron-hadron collisions. In this model, the cumulant moments for a given type of collision, the cumulant moments for an individual source and the average number of sources per collision are related as [7]

$$K_2{}^T = K_2 + \frac{K_2^s + 1}{\overline{N}} \tag{5.9}$$

and

$$K_3{}^T = K_3 + 3\frac{(K_2^s + 1)K_2}{\overline{N}} + \frac{K_3^s + 3K_2^s + 1}{\overline{N}^2} \tag{5.10}$$

where $K_2{}^T$ and $K_3{}^T$ are the second and third order factorial cumulant moments for the total collisions, K_2 and K_3 are normalized scaled factorial cumulant moments which are independent of partition scale. Thus we can write

$$\pi_q{}^S = -\partial K_q{}^S / \partial \ln \eta \tag{5.11}$$

using Equations 5.9 and 5.10 we get

$$\pi_2{}^T = \frac{\pi_2{}^S}{\overline{N}} \tag{5.12}$$

$$\pi_3{}^T = 3\frac{(\pi_2{}^S)K_2}{\overline{N}} + \frac{\pi_3{}^S}{\overline{N}^2} + \frac{3\pi_2{}^S}{\overline{N}^2} \tag{5.13}$$

From Equation 5.12 we see that the cumulative index π_2^T is inversely proportional to the average number of sources and thus inversely proportional to the average particle densities $<\rho>$ that means

$$\pi_2^T \propto \frac{1}{\overline{N}}$$

$$\pi_2^T \propto \frac{1}{\langle\rho\rangle} \tag{5.14}$$

Now if we assume that the distribution of source number is Poissonian than K_20 so that

$$\pi_3^T = \frac{\pi_3^S}{\overline{N}^2} + \frac{3\pi_2^S}{\overline{N}^2} \tag{5.15}$$

$$\pi_3^T = \frac{\pi_3^S + 3\pi_2^S}{\overline{N}^2} \tag{5.16}$$

$$\pi_3^T \propto \frac{1}{\overline{N}^2}$$

$$\pi_3^T \propto \frac{1}{\langle\rho\rangle^2} \tag{5.17}$$

Further, if we assume that the three particle correlations of individual sources are small compared to the two particle correlations that is $\pi_3^S << \pi_2^S$ then Equation 5.15 reduces to

$$\pi_3^T = \frac{3\pi_2^S}{\overline{N}^2}$$

$$= \frac{3}{\overline{N}} \times \frac{\pi_2^S}{\overline{N}}$$

$$\pi_3^T = \frac{3}{\overline{N}}\pi_2^T \tag{5.18}$$

Relations 5.14 and 5.17 can be written as

$$\pi_2^T = \frac{a}{\langle\rho\rangle} \tag{5.19}$$

$$\pi_3^T = \frac{b}{\langle\rho\rangle^2} \tag{5.20}$$

where the coefficient a and b are obtained from the slopes of the plots of π_2^T versus $1/\langle\rho\rangle$ and π_3^T versus $1/\langle\rho\rangle^2$ respectively.

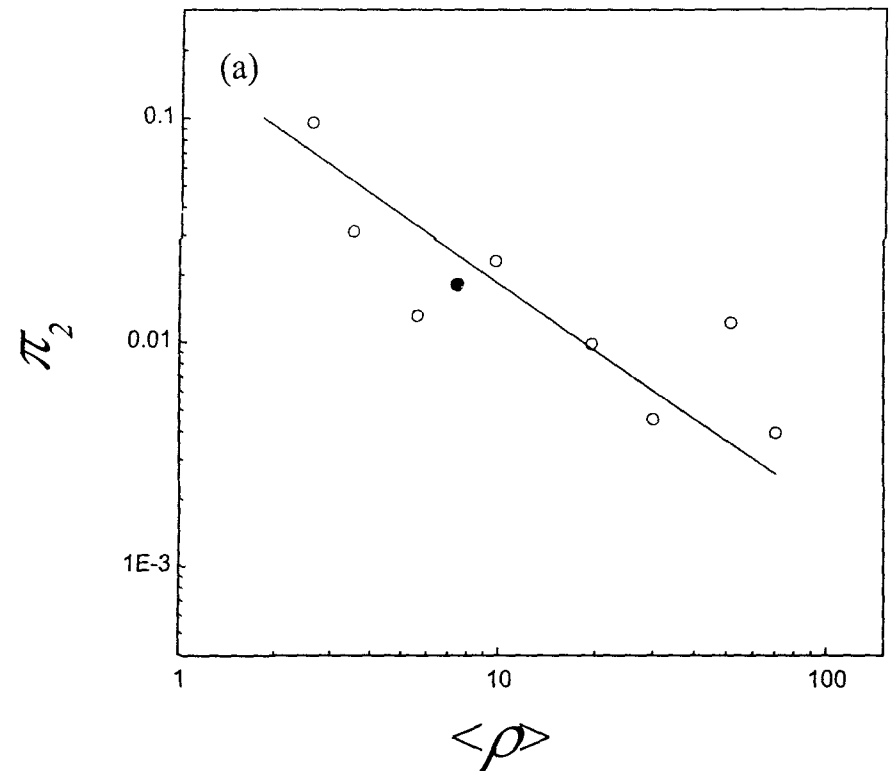

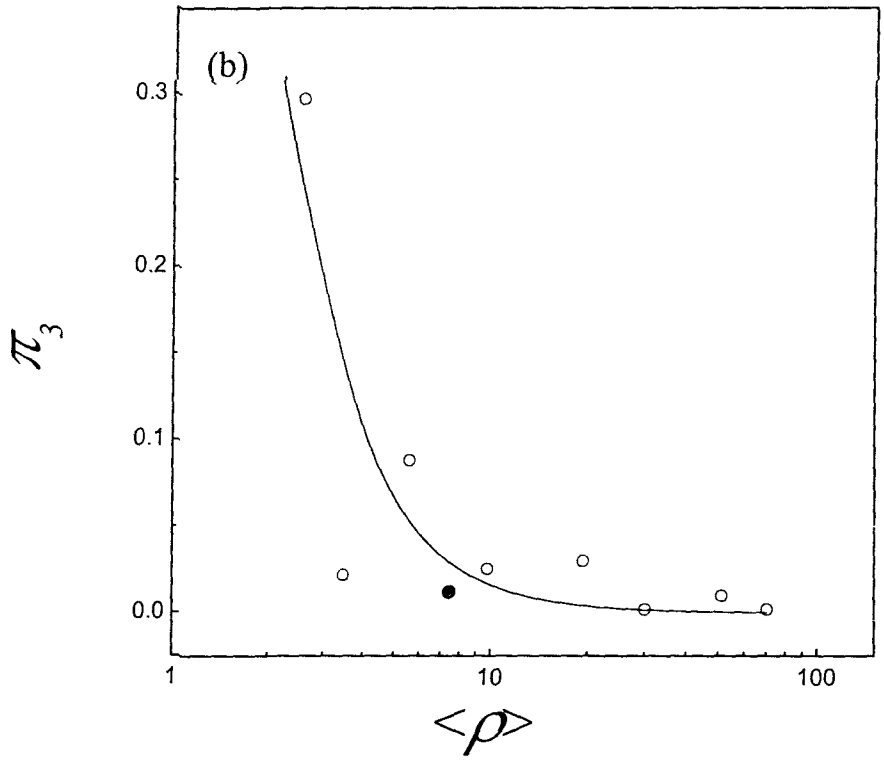

Figure 5.2: (a) π_2 versus $\langle\rho\rangle$ plot. Straight line represents the fitting using equation $\pi_2 = a/\langle\rho\rangle$.

(b) π_3 versus $\langle\rho\rangle$ plot. The smooth curve represents the fitting using equation $\pi_3 = b/\langle\rho\rangle^2$.

In each plot the symbol • represents our data point.

Using Equations 5.18, 5.19 and 5.20 we get

$$\overline{N} = \frac{3a\langle\rho\rangle}{b} \qquad 5.21$$

Therefore, if the particle production mechanisms were the same for various energies and projectiles then we would expect the cumulant indices to be inversely proportional to pseudorapidity density [8]. In Figure 5.2 we plot second order factorial cumulant indices as a function of pseudorapidity density for our data along with various event samples as *π-Emulsion* at 200 GeV, *p-Emulsion* at 200 *GeV*, *O-Emulsion* at 14.6, 60 and 200*A GeV* and *S-Emulsion* at 200*A GeV* [1]. We observe that the cumulant indices show an inverse dependence upon pseudorapidity density, indicating that all types of interactions involve similar physics in terms of the types of particle sources created. The curve in the figure represents the fitting of the data points using Equation 5.19. Further π_3 versus $<\rho>$ plot is shown in Figure 5.2 (b) and fitted using Equation 5.20. The values of the fitting parameters a and b are found to be 0.181 ± 0.025 and 1.615 ± 0.268 respectively.

Using Equation 5.21 we now can calculate the number of sources $\overline{N}$ for ^{28}*Si-AgBr* collisions at 14.6*A GeV*. The value of $\overline{N}$ is found to be 2.52. It should be pointed out here that the value of $\overline{N}$ obtained from NBD fitting of rapidity distribution of shower particles in the same rapidity interval is 4.81 (section 3.10.1). One of the reasons for different values of $\overline{N}$ obtained from two methods could be the assumptions used in arriving at Equation 5.21 that is used to find $\overline{N}$. It has been assumed that the second order factorial cumulant of the number of sources is zero. This assumption is not valid because the multiplicity distribution is not Poissonian as $K_2 \neq 0$. The other assumption that three particle correlations are negligible compared to two particle correlations is also not valid as significant three particle correlations are present in our data (Figure 5.1)

5.3 Factorial Correlators

So for we have concentrated our efforts on different types of moments estimated for a single bin. Additional information about the dynamics of multiparticle production could be obtained by investigating bin-bin correlations through the study of factorial correlators. The correlators measure not only the non-statistical local density fluctuations

but also give important information about the correlations between the local density fluctuations in different regions of phase space. The factorial correlators are computed using the following relations [9].

$$F_{ij}^{kl}(\delta X)=\frac{\langle n_k(n_k-1).....(n_k-i+1)\times n_l(n_l-1).....(n_l-j+1)\rangle}{\langle n_k(n_k-1).....(n_k-i+1)\rangle\langle n_l(n_l-1).....(n_l-j+1)\rangle} \qquad 5.22$$

where X is cumulative variable (see section 5.2), n_k and n_l are the multiplicity in kth and lth bins respectively. The factorial correlators are computed for each combination of i and j for a particular δX and average is taken for all possible bin-bin combinations with a given separation $D = d \times \delta X$, where $d = |k - l|$ of the kth and lth bins. The average factorial correlators for all bin combinations with a given distance D are given as

$$C_{ij}(D,\delta X)=\frac{1}{2(M-d)}\left[\sum_{k=1}^{M-d}F_{ij}^{k,k+d}(\delta X)+\sum_{l=1}^{M-d}F_{ij}^{l+d,l}(\delta X)\right]$$

$$=\frac{1}{2(M-d)}\sum_{k=1}^{M-d}\left[F_{ij}^{k,k+d}(\delta X)+F_{ji}^{k,k+d}(\delta X)\right] \qquad 5.23$$

According to the α-model [5] the intermittent behaviour of pionization implies that C_{ij} would depend on the bin-bin separation D, following a power law

$$C_{ij} \propto D^{-\phi_{ij}} \qquad 5.24$$

And that it should be independent of δX. However, this δX independence of factorial correlators is a common feature of any model dealing with short-range correlation function.

The factorial correlators C_{ij} are calculated using Equation 5.23 for six different values of bin size ($\delta X = \Delta X/M$ = 0.125, 0.083, 0.062, 0.050, 0.042 and 0.036) by choosing M = 8, 12, 16, 20, 24 and 28 respectively for different sets of i and j. In Figures 5.3 (a and c), 5.4 (a and c) and 5.5 (a and c) symbols represents the plots of $\ln C_{ij}$ versus $-\ln D$ for different sets of i and j for M = 8, 12, 16, 20, 24 and 28 respectively. It can be observed from the figures that $\ln C_{ij}$ increases with $-\ln D$ but the rise is not linear in the full range of D. However in the region of small D (D < 0.5), the rise is linear and that C_{ij} exhibits power law dependence on D. The data points of the plots of $\ln C_{ij}$ versus $-\ln D$ in the region D < 0.5 are fitted to the straight line. The slopes (ϕ_{ij}) obtained are listed in Table 5.1.

Further to compare our results with the string hadronic *UrQMD* model we have calculated C_{ij} for *UrQMD* events. Again we selected six different values of bin size

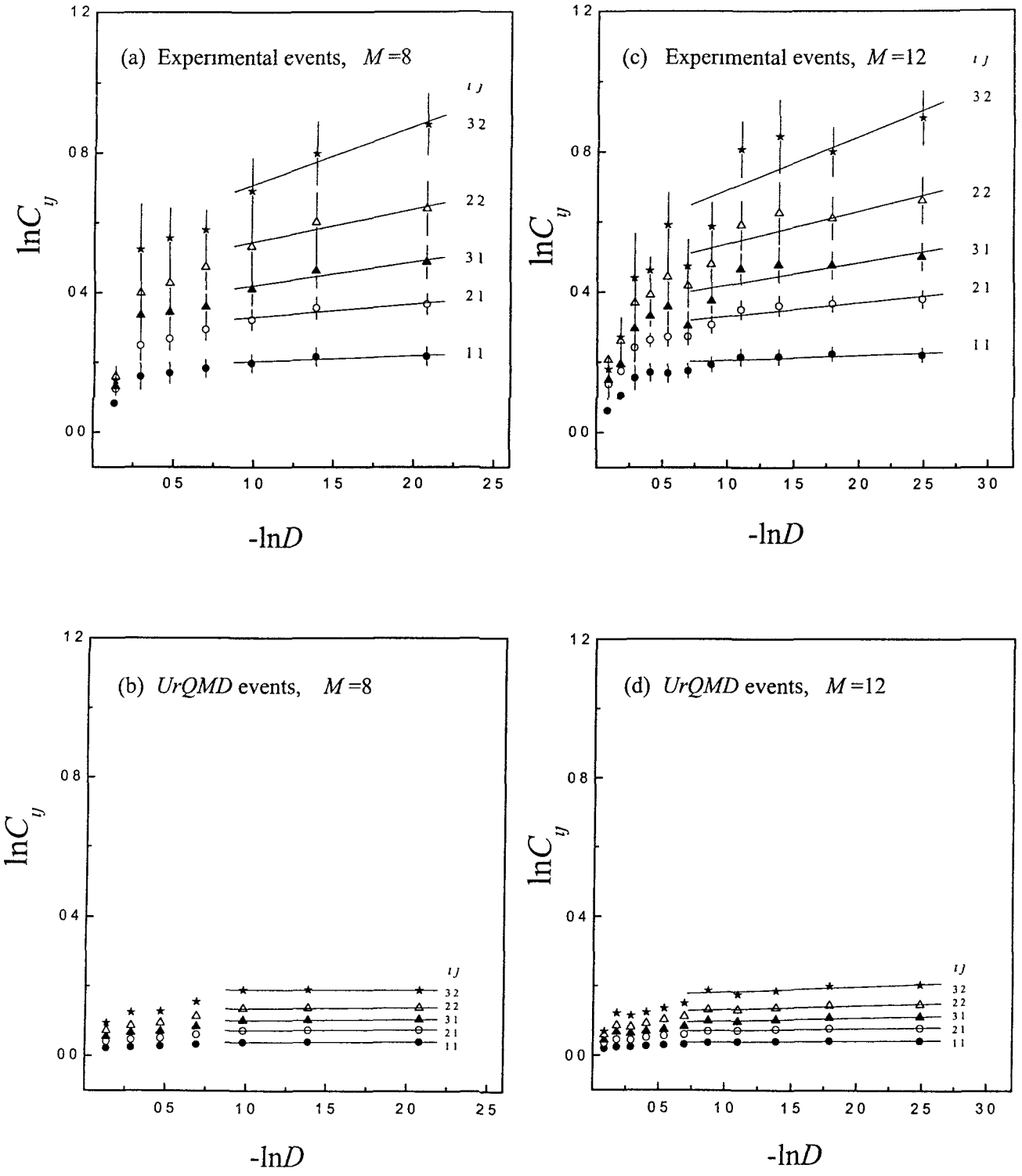

Figure 5.3: $\ln C_{ij}$ versus -ln$D$ plots for different sets of i and j for (a) ^{28}Si *-AgBr* collisions at 14.6*A GeV* for M=8, (b) *UrQMD* events for M=8, (c) ^{28}Si *-AgBr* collisions at 14.6*A GeV* for M=12 and (d) *UrQMD* events for M=12.

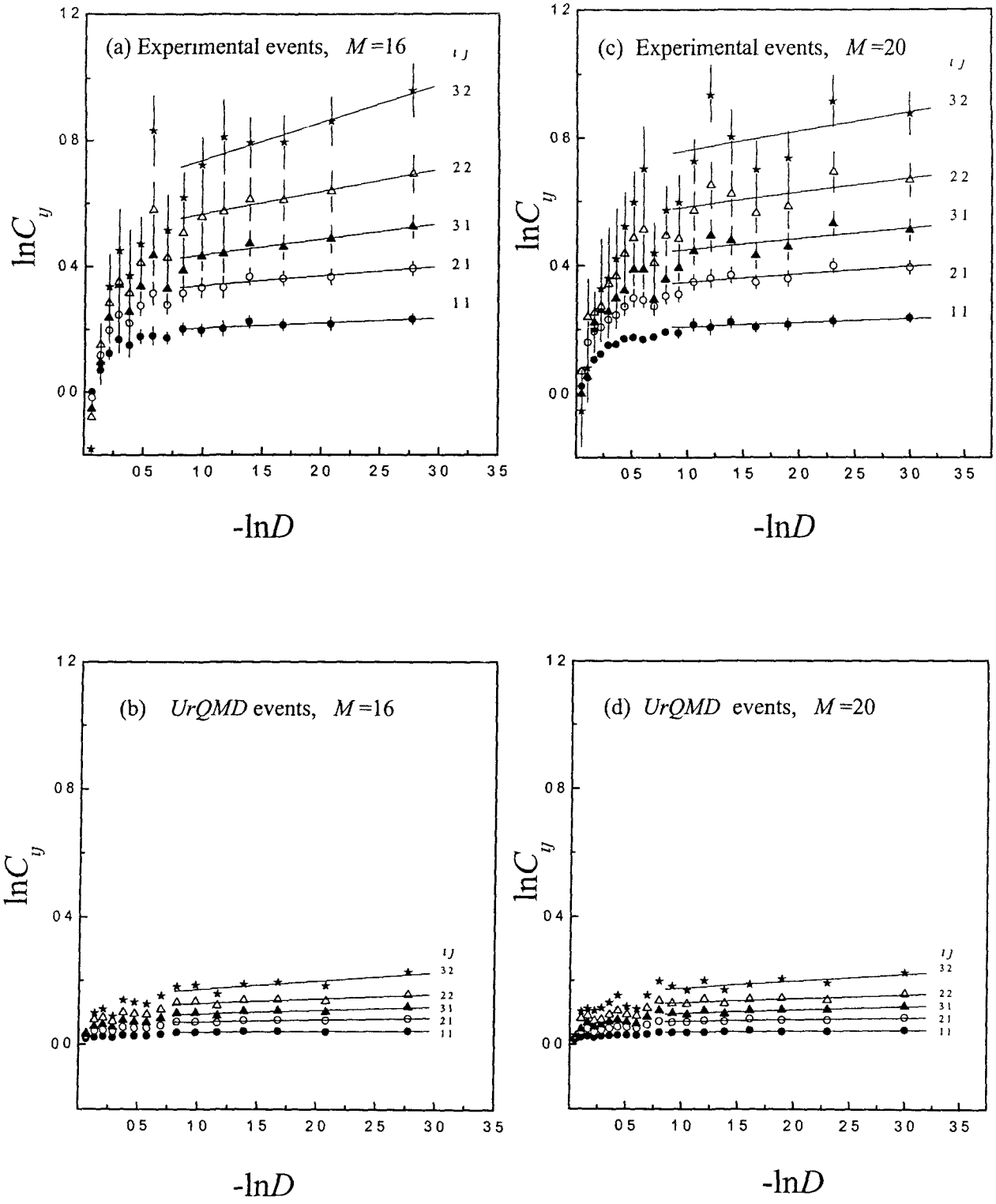

Figure 5.4: $\ln C_{ij}$ versus -ln$D$ plots for different sets of i and j for (a)^{28}Si *-AgBr* collisions at 14.6*A GeV* for M=16, (b) *UrQMD* events for M=16, (c)^{28}Si *-AgBr* collisions at 14.6*A GeV* for M=20 and (d) *UrQMD* events for M=20.

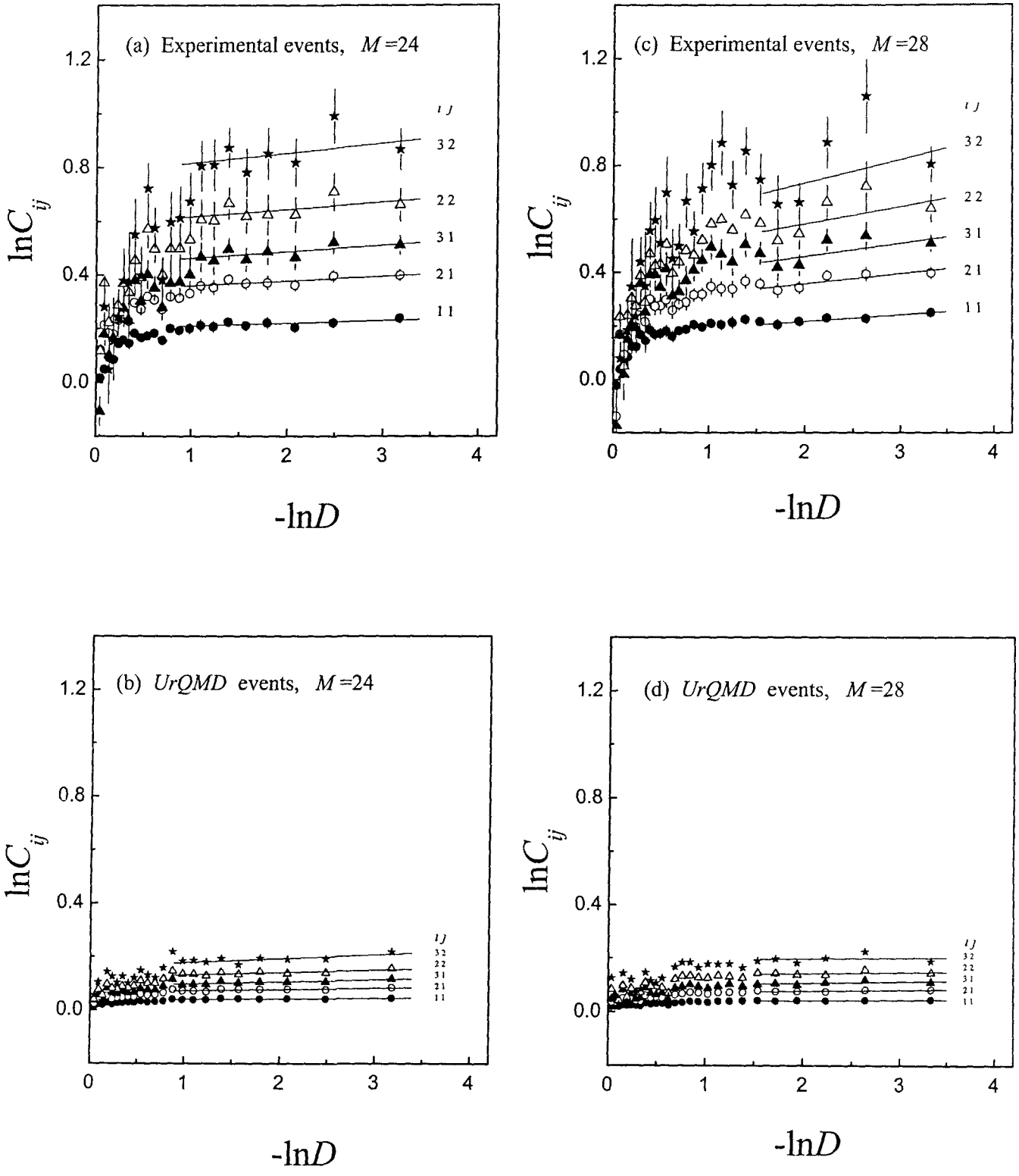

Figure 5.5: $\ln C_y$ versus -ln$D$ plots for different sets of i and j for (a)^{28}*Si -AgBr* collisions at 14.6*A GeV* for M=24, (b) *UrQMD* events for M=24, (c)^{28}*Si -AgBr* collisions at 14.6*A GeV* for M=28 and (d) *UrQMD* events for M=28.

Table 5.1: Values of slopes ϕ_{ij} of $\ln C_{ij}$ versus $-\ln D$ plots for different sets of i and j for ^{28}Si-$AgBr$ collisions at 14.6A GeV and the values shown within brackets are for *UrQMD* events.

ij	δX= 0.125 (0.01 ≤ D ≤ 0.37)	δX= 0.083 (0.08 ≤ D ≤ 0.41)	δX= 0.062 (0.06 ≤ D ≤ 0.37)	δX= 0.050 (0.05 ≤ D ≤ 0.40)	δX= 0.042 (0.04 ≤ D ≤ 0.37)	δX= 0.036 (0.04 ≤ D ≤ 0.18)
11	0.016±0.011 (0.0020±0.0003)	0.013±0.007 (0.0035±0.0008)	0.015±0.005 (0.0025±0.0010)	0.012±0.004 (0.0028±0.0010)	0.010±0.005 (0.0020±0.0009)	0.024±0.004 (0.0023± 0.0002)
21	0.037±0.017 (0.0027±0.0001)	0.037±0.013 (0.0059±0.0013)	0.029±0.006 (0.0064±0.0018)	0.024±0.008 (0.0056±0.0016)	0.017±0.006 (0.0049±0.0016)	0.038±0.015 (0.0040±0.0012)
31	0.066±0.025 (0.0035±0.0005)	0.063±0.027 (0.0093±0.0023)	0.048±0.006 (0.0116±0.0037)	0.033±0.017 (0.0110±0.0029)	0.024±0.010 (0.0078±0.0018)	0.049±0.031 (0.0059±0.0046)
22	0.093±0.029 (0.0035±0.0005)	0.093±0.034 (0.0114±0.0021)	0.070±0.007 (0.0144±0.0050)	0.045±0.024 (0.0124±0.0043)	0.027±0.017 (0.0091±0.0028)	0.066±0.048 (0.0043±0.0058)
32	0.165±0.038 (-0.0002±0.0010)	0.153±0.068 (0.0154±0.0056)	0.119±0.048 (0.0267±0.0105)	0.062±0.048 (0.0221±0.0081)	0.036±0.029 (0.0146±0.0053)	0.089±0.093 (0.0031±0.0147)

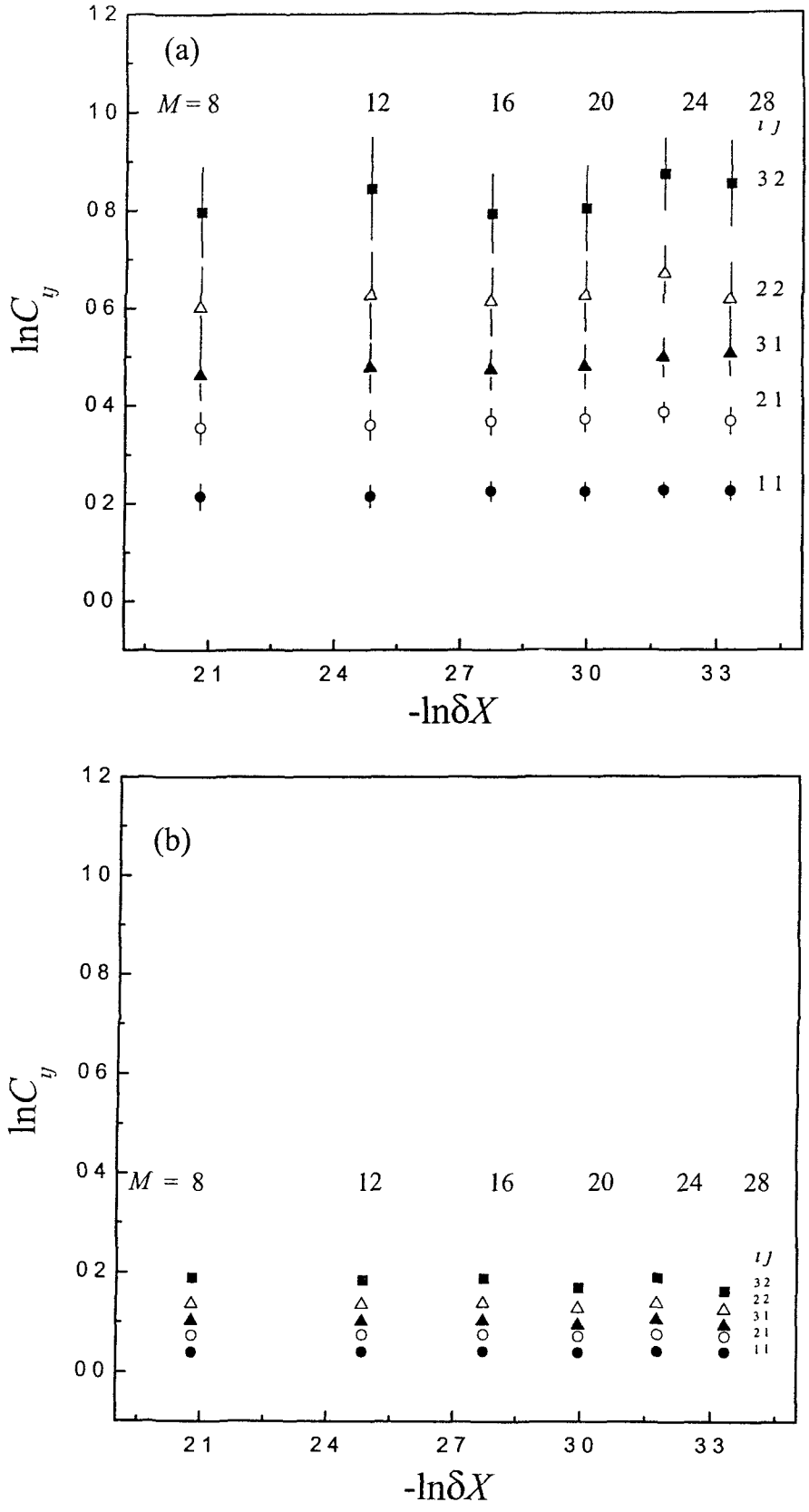

Figure 5.6: (a) $\ln C_{ij}$ versus $-\ln \delta X$ plots for different sets of i and j for D=0.25 for ^{28}Si-$AgBr$ collsions at 14.6A GeV.
(b) $\ln C_{ij}$ versus $-\ln \delta X$ plots for different sets of i and j for D=0.25 for $UrQMD$ events.

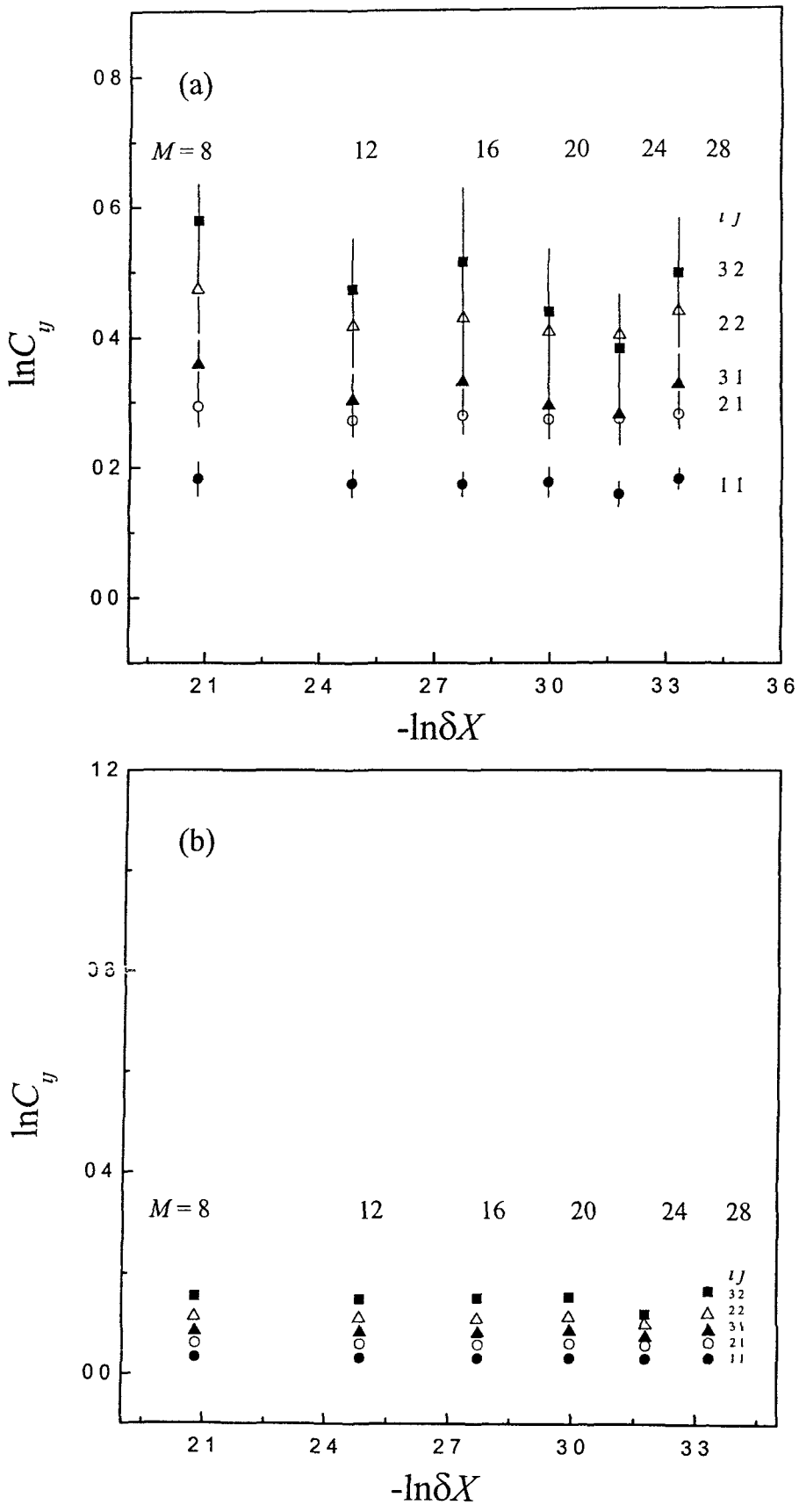

Figure 5.7: (a) lnC_{ij} versus -lnδX plots for different sets of i and j for D=0.50 for ^{28}Si-$AgBr$ collsions at 14.6A GeV.
(b) lnC_{ij} versus -lnδX plots for different sets of i and j for D=0.50 for $UrQMD$ events.

($\delta X = \Delta X/M$ = 0.125, 0.083, 0.062, 0.050, 0.042 and 0.036) by choosing M = 8, 12, 16, 20, 24 and 28 respectively and for each set of δX, the values of C_{ij} were calculated using Equation 5.23 for *UrQMD* events for different sets of i and j. In Figures 5.3 (a and c), 5.4 (a and c) and 5.5 (a and c) symbols represents $\ln C_{ij}$ versus $-\ln D$ plots for different orders of i and j for M = 8, 12, 16, 20, 24 and 28 respectively.

It is clear from Figures 5.3, 5.4 and 5.5 that for *UrQMD* events, $\ln C_{ij}$ increases slowly with $-\ln D$ but the rise is not linear in the full range of D. However, in the region of small D ($D < 0.5$), the rise is linear but the values of $\ln C_{ij}$ are very nearly equal to zero. The data points of $\ln C_{ij}$ versus $-\ln D$ plots in the region $D < 0.5$ are fitted to the straight line. The slopes (ϕ_{ij}) obtained are also listed in Table 5.1 within brackets. We can see from the table that the values of ϕ_{ij} are very nearly equal to zero. In the experimental events we observe that the slopes of $\ln C_{ij}$ versus $-\ln D$ plots increases with increase in the order of correlations but for *UrQMD* events for δX = 0.125 and 0.036, we observe no such pattern. Thus *UrQMD* model again fails to explain our experimental results on factorial correlators.

Figures 5.6 (a) and (b) represent $\ln C_{ij}$ versus $-\ln \delta X$ plots for different sets of i and j at D = 0.25 for experimental and *UrQMD* events respectively. The figures show in favour of δX independence of C_{ij} for D = 0.25. We also observed that the data points of *UrQMD* events are much below the data points of experimental events. Figures 5.7 (a) and (b) represent $\ln C_{ij}$ versus $-\ln \delta X$ plots for different sets of i and j of δX at D = 0.50 for experimental and *UrQMD* events respectively. Again we observe that the data points of *UrQMD* events are much below the data points of the experimental events. In this case we observe that the δX independence of C_{ij} for D = 0.50 is not as good as we observe for D = 0.25. Thus we observe in favour of δX independence of C_{ij} for small values of D, but the scaling seems to fail at large values of D ($D > 0.5$). These results are in agreement with the α-model, which predicts that factorial correlators have a power law increase with decreasing distance between intervals and have no dependence on the size of the intervals (δX). But this does not guarantee the success of α-model, as other models with short-range order have similar predictions. The scaling behaviour has also been reported for NA22 collaboration data on $\pi^+ p$ and $k^+ p$ collisions at 250 *GeV/c* [10] and muon-nucleon scattering at 280 *GeV* [11].

References

1. M. I. Adamovich et al., *Phys. Rev.* **D 47** No. 9 (1993) 3726.
2. P. Carruthers et al., *Phys. Lett.* **B 254** (1991) 258.
3. EMU01 Collaboration (Adamovich M. I. et al.), University of Lund preprint, LUIP (1992) 9202.
4. G. Singh and P. L. Jain, *Il Nuovo Cimento* **A 110** No. 3 (1997) 239.
5. A. Bialas and R. Peschanski, *Nucl. Phys.* **B 308** (1988) 857.
6. M. Kendall et al., *Kendall's Advanced Theory of Statistics* (Oxford University Press, New York 1987), Vol **1**, page 87.
7. H. C. Eggers, *Ph. D. Thesis*, University of Arizona (1991) 49.
8. D. Seibert, *Phys. Lett.* **B 240** (1990) 215; **254** (1991) 253.
9. A. Bialas and R. Peschanski, *Nucl. Phys.* **B 273** (1986) 703; *Phys. Lett.* **B 207** (1988) 59.
10. NA22 Collaboration, V. V. Aivazyan et al., *Phys. Lett.* **B 258** (1991) 487.
11. I. Derado et al., *Z. Phys.* **C 54** (1992) 357.

CHAPTER VI

Levy Stable Law of Intermittency and Multifractal Spectrum for ^{28}Si-$AgBr$ Collisions at 14.6A GeV

6.1 Introduction

In chapter IV we studied the dependence of the scaled factorial moments (F_q) on the size of phase space partition. A power law dependence was observed. The power law dependence is known as intermittency and is an evidence of the presence of dynamical fluctuations in multiparticle production. Evidence of intermittency has been observed in all types of processes and it now seems to be a general property of multiparticle production. However, a single mechanism that could explain intermittency has not been observed.

The observed intermittency points towards a self-similar cascade process of multiparticle production. The self-similarity is closely related to the fractal geometry. According to the fractal geometry, the multiparticle production can be treated as a fractal system, characterized by non-integer fractal dimensions. In the last chapter we studied the fractal properties of the multiparticle production through modified G_q-moments and F_q-moments and found evidence of multifractality in our data. Once the multifractal properties of produced particles in nucleus-nucleus collisions is established, the next logical step is to study this fractal system (multiparticle production) in detail. As a fractal system, the multiparticle production can be characterized in terms of a very important parameter called Levy stability index μ, which tells us about the behaviour of fluctuations in the tail of multiplicity distributions.

In this chapter, we study the generalized power law behaviour of the scaled factorial moments for $^{28}Si\text{-}AgBr$ collisions at $14.6A\ GeV$. Levy stability indices μ have been determined in both η and φ spaces for our data and found that these values lie in the range (0–2), consistent with the levy stability. Further, using the theory of multifractals we have calculated multifractal spectrum $f(\alpha_q)$, where α_q is the Lipschitz-Holder exponent. The right wing of the spectrum, corresponding to negative q values, has been obtained through an analytical continuation of Brax and Peschanski formula for intermittency indices [1].

6.2 Results and Discussion

6.2.1 Generalized Power Law

In section 4.2.2 values of the scaled factorial moments $\langle F_q \rangle$ were calculated for q=2-6 for our data in η and φ spaces. M was varied from 2-36. We observed that the

scaled factorial moment $<F_q>$ exhibits power law behaviour on M, indicating the presence of dynamical fluctuations and multifractality in our data. The values of the intermittency indices ϕ_q were obtained by linear fits to the data points of $\ln<F_q>$ versus $\ln M$ plots for different q in η and φ spaces.

In multiplicative random cascade models [2] the one-dimensional scaled factorial moments also follow a generalized power law of the type

$$< F_q(M) > \propto [g(M)]^{\phi_q} \qquad 6.1$$

where $g(M)$ is a generalized function of M. Writing g in terms of $<F_2>$, we get the following linear relation.

$$\ln < F_q > = C_q + \frac{\phi_q}{\phi_2} \ln < F_2 > \qquad 6.2$$

From Equation 6.2, ϕ_q/ϕ_2 can be directly obtained by plotting $\ln<F_q>$ as a function of $\ln<F_2>$ in η and φ spaces. In Figures 6.1 (a) and (b), we plot $\ln<F_q>$ as a function of $\ln<F_2>$ for q = 3-6 in η and φ spaces respectively for our data. The linear behaviour of the plots indicates the validity of Equations 6.2 for our data. Values of ϕ_q/ϕ_2 for different q values are obtained by fitting Equations 6.2 to the graphs plotted in Figures 6.1 (a) and (b). In multiplicative random cascade models q dependence of ϕ_q/ϕ_2 is claimed to be indicative of the mechanism causing intermittency in the multiparticle production. In the gaussian lognormal approximation, the use of the central limit theorem leads to the relation [3]

$$\frac{\phi_q}{\phi_2} = \frac{q(q-1)}{2} \qquad 6.3$$

However, it has been pointed out that the lognormal approximation is inaccurate, particularly in the tail of the distribution i.e. for moments of the higher order. As argued by Brax and Peschanski [4], a better description of the random cascade models might be obtained if instead of lognormal approximation, the density probability distribution is assumed to be a log-Levy stable distribution, characterized by Levy index μ. In that case Equation 6.3 generalizes to

$$\frac{\phi_q}{\phi_2} = \frac{q^{\mu} - q}{2^{\mu} - 2} \qquad 6.4$$

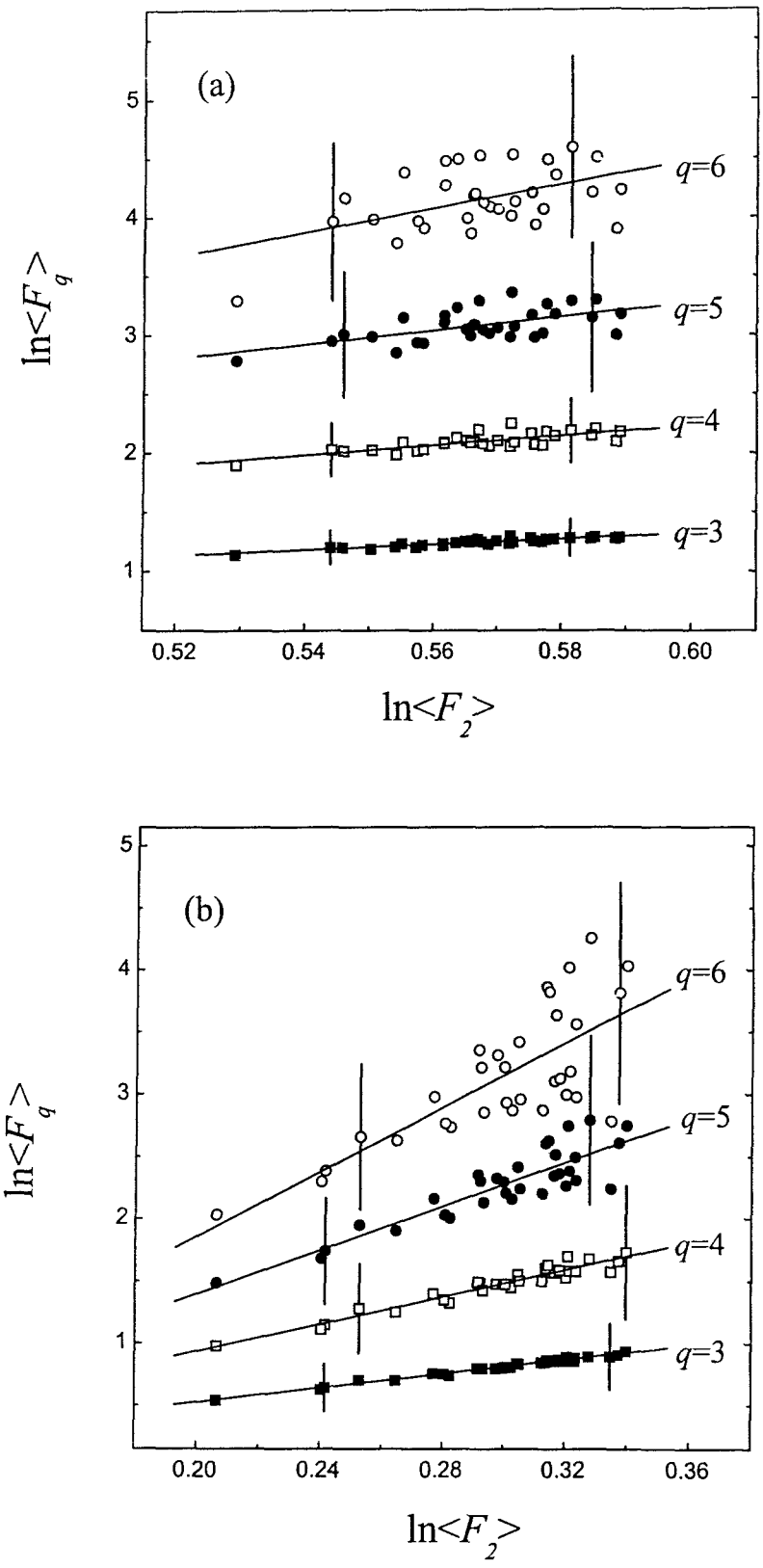

Figure 6.1: (a) $\ln\langle F_q \rangle$ versus $\ln\langle F_2 \rangle$ plots for $^{28}Si\text{-}AgBr$ collisions at 14.6A GeV in η-space. (b) $\ln\langle F_q \rangle$ versus $\ln\langle F_2 \rangle$ plots for $^{28}Si\text{-}AgBr$ collisions at 14.6A GeV in φ-space. Solid lines represent the linear fits to the data points.

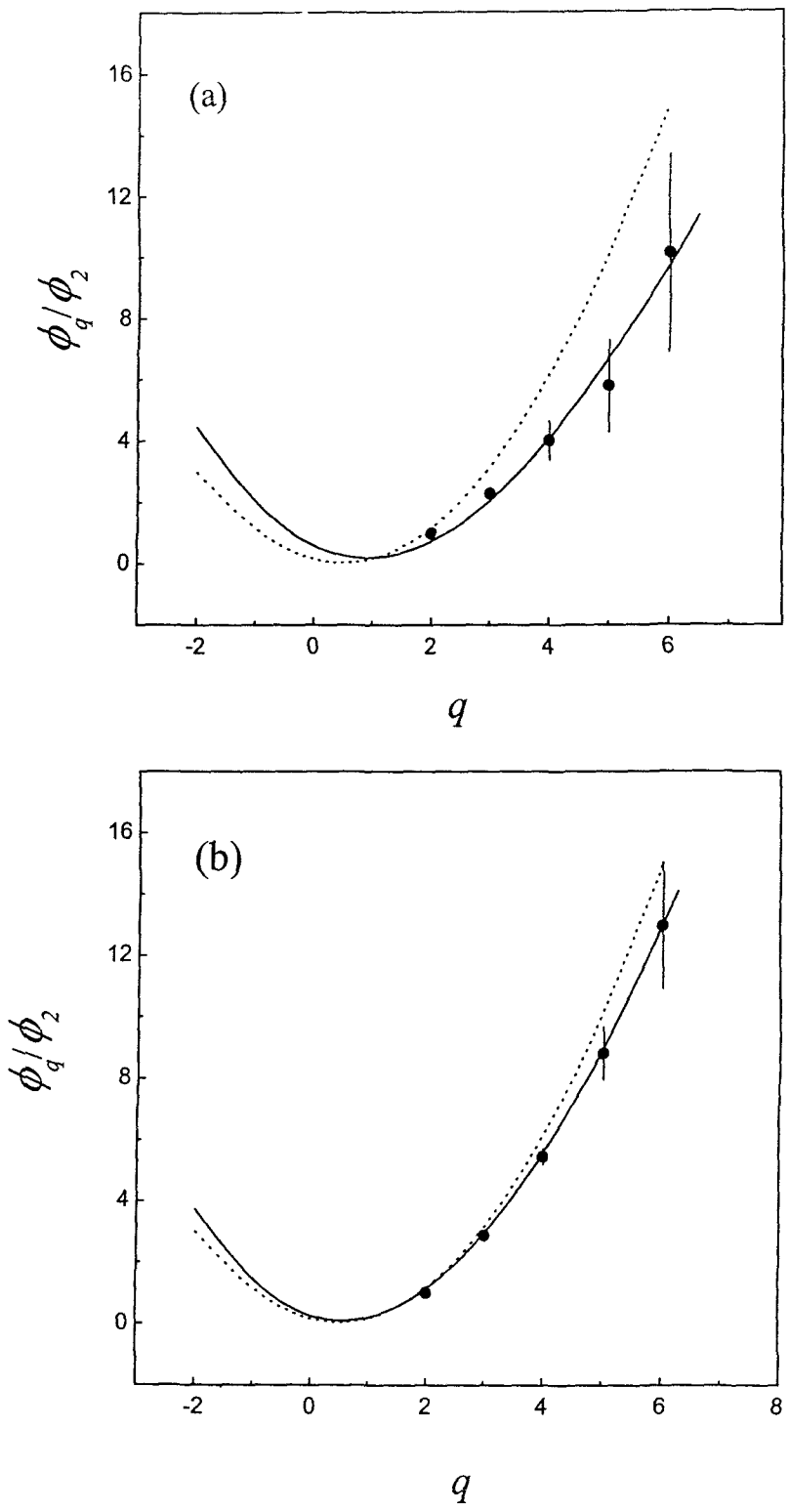

Figure 6.2: (a) ϕ_q/ϕ_2 versus q plot for ^{28}Si-$AgBr$ collisions at 14.6A GeV in η-space. (b) ϕ_q/ϕ_2 versus q plot for ^{28}Si-$AgBr$ collisions at 14.6A GeV in φ-space. In each plot solid curve represents Equation 6.7 fitted to the data points and dashed curve represents Equation 6.5.

For μ=2, the gaussian case, Equation 6.4 reduces to Equation 6.3 According to Levy stable theory, the Levy index μ is confined to $0 \leq \mu \leq 2$ and the central limit theorem corresponds to $\mu \to 2$. In this limit Equation 6.4 passes to Equation 6.3.

In Figures 6.2 (a) and (b), we plot ϕ_q / ϕ_2, obtained from the linear fits of the graphs shown in Figures 6.1 (a) and (b), as a function of q in η and φ spaces respectively. The solid curves represent Equation 6.4, fitted to ϕ_q / ϕ_2 versus q plots. The dashed curves in Figures 6.2 (a) and (b) represent Equation 6.3. It can be noted that Equation 6.3 is valid for any real value of q including $q \leq 0$, whereas Equation 6.4 in its present form cannot be applied to $q \leq 0$. An analytical continuation of Equation 6.4, which is applicable to $q \leq 0$ also and in the limit $\mu \to 2$ passes to Equation 6.3 in the whole range of q is [1]

$$\frac{\phi_q}{\phi_2} = \frac{(q^2)^{\mu/2} - q}{2^{\mu} - 2} \quad . \tag{6.5}$$

The values of the Levy index in η and φ spaces, obtained from the fits of Equation 6.5 to the data points in Figures 6.2 (a) and (b), are $\mu = 1.635 \pm 0.012$ and $\mu = 1.801 \pm 0.003$ respectively. Both these values lie in the range (0-2) consistent with the Levy stability.

It can be seen from Figure 6.2 (a) that in η space the dashed curve, which represents Equation 6.3, deviates significantly from the data points for $q \geq 4$. However, for ϕ space (Figure 6.2 (b)) this deviation is not very significant but the Brax and Peschanski formula (Equations 6.4 and 6.5) gives a better fit to the data points. This indicates that the lognormal approximation is not valid for higher order moments, that is, in the tail of the density distribution but the log levy stable distribution is valid for higher order moments also.

6.2.2 Generalized Dimensions and Multifractal Spectrum

Once ϕ_q and μ are determined for the data, we can make use of the theory of multifractals to calculate multifractal spectrum $f(\alpha_q)$ of the multi-hadron final states in $^{28}Si\text{-}AgBr$ collisions at 14.6*A GeV*. From the Legendre transform

$$\alpha_q = \frac{\partial \tau_q}{\partial q} \tag{6.6}$$

and $$f(\alpha_q) = q\alpha_q - \tau_q \qquad 6.7$$

where α_q is the Lipschitz-Holder exponent and τ_q is the mass exponent. The spectral function $f(\alpha_q)$ is a smooth function, concave downward with its maximum at $q = 0$. It gives a qualitative description of the density fluctuations in the peaks as well as in the valleys of the distribution. The Renyi generalized dimensions D_q can be obtained from the relation

$$D_q = 1 - \frac{\phi_q}{q-1} \qquad . \qquad 6.8$$

Mono-fractals are characterized by constant D_q values and are associated with second order phase transitions e.g. the quark-gluon plasma while multi-fractals are characterized by decreasing values of D_q with increasing q and are associated with the self-similar cascade process.

Values of the exponent τ_q can be determined from the G_q-moment analysis of the data. But as already mentioned G_q-moments are dominated by statistical fluctuations. Hence the values of τ_q obtained from G_q-moment analysis are also not free from statistical content. In F_q-moment analysis, the statistical fluctuations are completely eliminated. The values of the intermittency indices ϕ_q are therefore free from statistical content. Due to this reason, we have used the following relation to calculate τ_q [5].

$$\tau_q = q - 1 - \phi_q . \qquad 6.9$$

The generalized dimensions D_q and the multifractal spectrum $f(\alpha_q)$ are calculated for η and φ spaces using Equations 6.7 and 6.8 with $q = -1$ to 6.4 in steps of 0.2. D_q versus q graphs are shown in Figures 6.3 (a) and (b) in η and φ spaces respectively. From Figure 6.3 (a), it can be seen that in η-space, D_q decreases from 1.016 ± 0.006 to 0.959 ± 0.005 as q increases from -1 to 6.8. In φ-space, (Figure 6.3 (b)), it decreases from 1.034 ± 0.001 to 0.874 ± 0.019 for the same range of q. The decrease in D_q with increasing q in both the spaces is an indication of the multifractality in the multiparticle production in $^{28}Si\text{-}AgBr$ collisions at $14.6A\ GeV$.

In Figures 6.4 (a) and (b), we show $f(\alpha_q)$ spectra in η and φ spaces for our data. In each case $f(\alpha_q)$ spectrum is a continuous curve concave downwards with its maximum at $q = 0$, thus characterizing the qualitative manifestation of multiplicity fluctuations in η

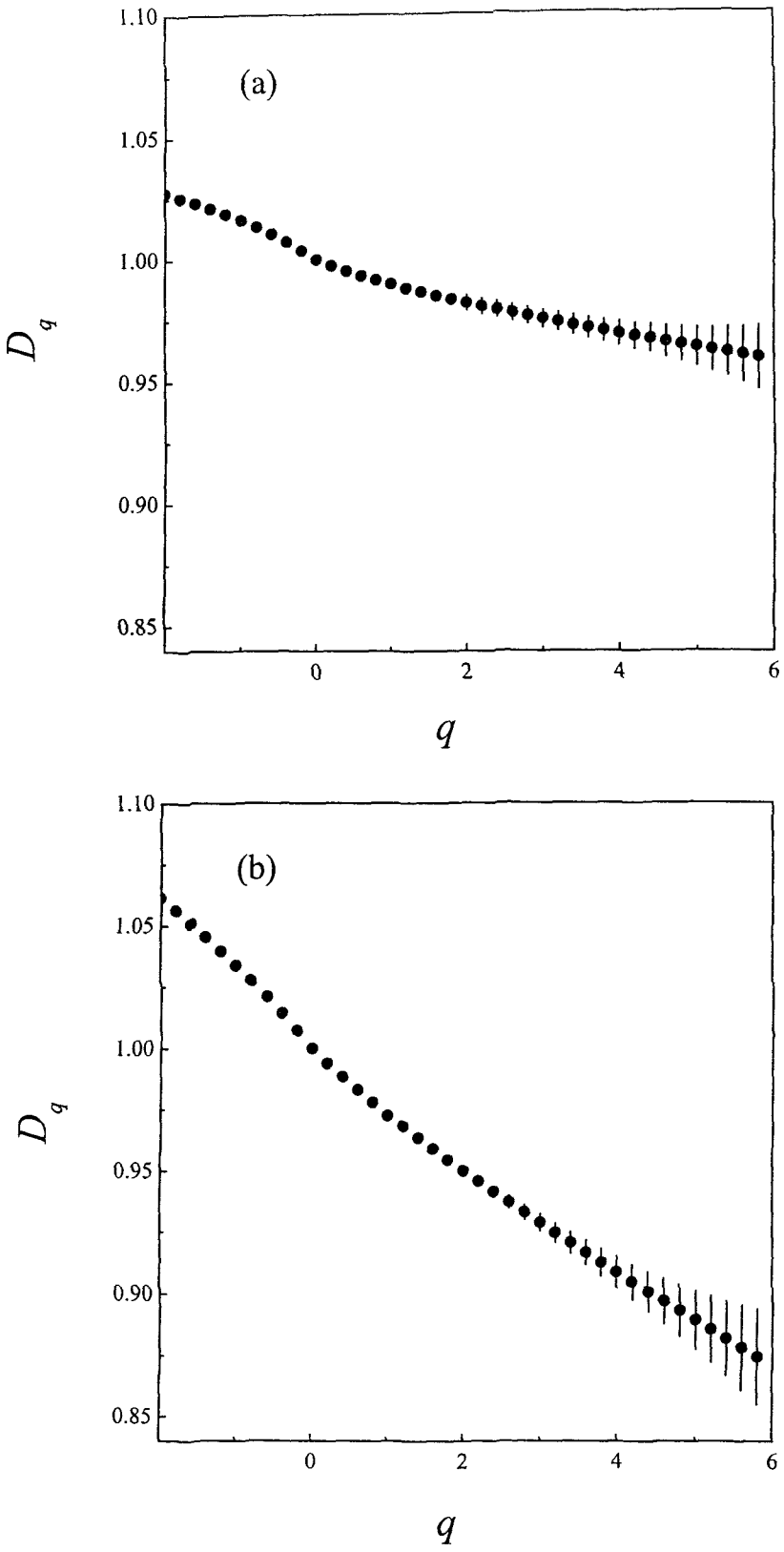

Figure 6.3: (a) D_q versus q plot for ^{28}Si-$AgBr$ collisions at 14.6A GeV in η-space.
(b) D_q versus q plot for ^{28}Si-$AgBr$ collisions at 14.6A GeV in φ-space.

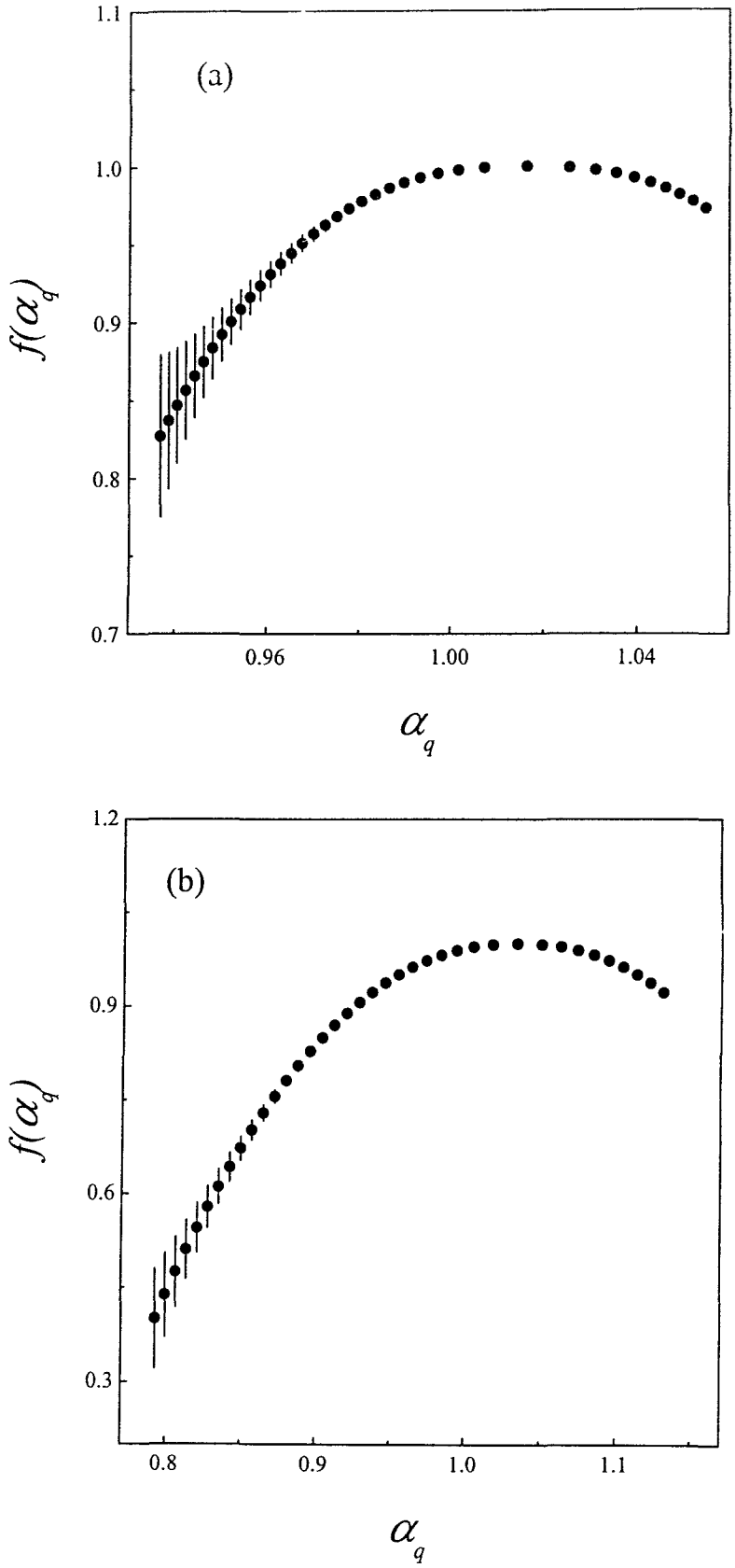

Figure 6.4: (a) $f(\alpha_q)$ versus α_q plot for ^{28}Si-$AgBr$ collisions at 14.6A GeV in η-space.
(b) $f(\alpha_q)$ versus α_q plot for ^{28}Si-$AgBr$ collisions at 14.6A GeV in φ-space.

and φ spaces. The tangents to $f(\alpha_q)$ spectrum with slopes 1 and 2 determine the points $[\alpha_1, f(\alpha_1)]$ and $[\alpha_2, f(\alpha_2)]$. The values of the information dimension $D_1 = f(\alpha_1) = \alpha_1$ and the correlation dimension $D_2 = 2\alpha_2 - f(\alpha_2)$ in η space are 0.989 ± 0.003 and 0.982 ± 0.003 respectively for $^{28}Si\text{-}AgBr$ collisions at $14.6A$ *GeV*. The corresponding values of these dimensions in φ-space are 0.962 ± 0.001 and 0.954 ± 0.002 . Our values of D_1 and D_2 are slightly greater than those obtained by Jain et al [6] from a similar analysis for $^{28}Si\text{-}AgBr$ collisions at $14.6A$ *GeV* in both η and φ spaces. This is due to different methods employed to determine the values of the multifractal dimensions. Jain et al [6] obtained τ_q values from the G_q-moment method, which fails to filter out statistical fluctuations. However, in the present analysis τ_q values have been obtained from the F_q-moment method, which eliminates statistical fluctuations completely.

References

1. Chen Gang and Liu Lian-shou, *Chin. Phys. Lett.* **19** (2002) 1271.
2. W.Ochs and J.Wosiek, *Phys. Lett.* **B 214** (1988) 617.
3. A. Bialas and R. Peschanski, *Nucl. Phys.* **B 308** (1988) 857.
4. Ph. Brax and R.Peschanski, *Phys. Lett.* **B 253** (1991) 226.
5. E.A.De Wolf, I.M.Dremin and W.Kittel, *Phys. Rep.* **270** (1996) 1.
6. P. L. Jain, G. Singh, and A. Mukhopadhyay, *Phys. Rev.* **C 46** (1992) 721.

CHAPTER VII

Conclusions

A sample of 784 inelastic collisions of 14.6*A GeV* Silicon nuclei with emulsion has been used to study the general characteristics and dynamical fluctuations in the pseudorapidity distributions of particles produced in these collisions. We observed that the percentage of collisions with nuclei of different target groups depends weakly on the mass of the projectile. The mean multiplicity of all the secondary charged particles depends on the mass of the target nucleus whereas the average multiplicity of shower particles depends on the energy of the projectile also. These dependences are well described by the relation $\langle N_i \rangle = a_i \langle A_T \rangle^{bi}$.

The Gaussian distribution is found to fit well the pseudorapidity distribution of shower particles produced in ^{28}*Si-Emulsion* collisions at 14.6*A GeV*. It is observed that with increase in the energy of the projectiles, the peak of the pseudorapidity distribution shifts towards the higher value of η, which corresponds to small angle of emission. The Gaussian distribution fits well the pseudorapidity distributions of shower particles also for ^{28}*Si-AgBr*, ^{28}*Si-CNO* and ^{28}*Si-H* collisions and the distributions are almost the same at higher values of pseudorapidity and the centroids of the distribution grow and shift towards smaller values of pseudorapidity as the target mass increases from *H* to *AgBr* group.

We observe that the pseudorapidity space could be divided into three regions: (i) target fragmentation region, (ii) central region and (iii) projectile fragmentation region. The target fragmentation region corresponds to the lower η values, that is, larger values of emission angle, which is characterized by the target nuclei. The projectile fragmentation region is assumed to be populated by fragments of projectile nucleus corresponding to larger values of η, that is, small angles of emission. The central region is believed to be enriched by the particles produced in collisions of the participants of colliding nuclei and is independent of either of the fragmentation regions.

The charged particle multiplicity correlations in ^{28}*Si-Emulsion* collisions at 14.6*A GeV* can be approximated by a linear dependence with positive slope. The strongest correlation is observed between $\langle N_s \rangle$ and N_g with a slope 2.67±0.13. Thus N_g can be considered a measure of the number of interacting projectile nucleons The angular distributions of relativistic charged particles is independent of target mass and prominent peaks are observed at smaller angles. The angular distributions of grey and black particles

(target fragments) show no significant peaks, which could be attributed to the shock-wave phenomenon.

The study of multiplicity moments shows that the values of the ratio $<N_s>/D$ for various projectiles are almost the same that indicates a similar mechanism of shower particle production. The values of dispersion increase linearly with increase in the mean multiplicity of shower particles and the values of multiplicity moments C_q increase with increasing value of q. The same trend is followed by the data on different projectiles as well. The shape of the multiplicity distribution of shower particles strongly depends on target mass. The multiplicity distributions of grey and black particles show that the distributions for ^{28}Si-$AgBr$ collisions are broader than those for ^{28}Si-CNO. This may be due to the effect of target mass on the number of collisions of ^{28}Si with the target nuclei. The tail of the multiplicity distribution of shower particles extends to much higher values of N_s with the increase in projectile energy. This is due to the production of more relativistic charged particles with increasing energy.

The negative binomial distribution is found to describe well the shower particle multiplicity distributions for ^{28}Si-$Emulsion$, ^{28}Si-$AgBr$ and ^{28}Si-CNO collisions for windows of different sizes in both the pseudorapidity (η) and azimuthal angle (φ) phase spaces. In both the phase spaces, increasing values of clan size $\bar{n}_c$ are observed corresponding to each window size for ^{28}Si-CNO, ^{28}Si-$Emulsion$ and ^{28}Si-$AgBr$ collisions. This is an evidence of the increase in the size of clusters with increase in the target mass.

From the results obtained from the analysis of the charged particles in the forward and backward hemispheres, we conclude that the backward particle production may be a consequence of the isotropic decay of a highly excited target nucleus in its rest frame after the forward particle production. The average multiplicities of shower and grey particles in both the hemispheres increase with increasing target size. These dependences on the target size are well parameterized by the power law of the form $\left\langle N_i^k \right\rangle = \beta_i^k \left\langle A_T \right\rangle^{\alpha_i^k}$. A mild dependence of the forward backward ratio on the size of the projectile is observed for target fragments, whereas in the case of relativistic charged particles, a strong dependence is observed. The results obtained from the analysis of multiplicity distributions of the shower and grey particles emitted in the backward hemisphere confirm the limiting fragmentation hypothesis. Further, the results of the forward-backward multiplicity correlations show that the dependences of $<N_s^F(N_s^B)>$ on N_s^B and

$<N_s^B(N_s^F)>$ on N_s^F are linear. The average number of shower and grey particles in the forward hemisphere depend strongly on the total number of shower and grey particles emitted in the backward hemisphere, whereas the average number of grey and shower particles in the backward hemisphere depends weakly on the total number of shower and grey particles emitted in the backward hemisphere. This shows that pions and protons emitted in the backward hemisphere are somewhat different from those emitted in the forward hemisphere.

In our systematic study of multifractality in $^{28}Si\text{-}AgBr$ collisions at $14.6A\ GeV$, the following results are obtained: By using the modified multifractal moments G_q and the scaled factorial moments F_q, fractal structures and dynamical fluctuations are observed in our data in both η and φ spaces. Further, we have compared our results with the string hadronic *UrQMD* model. It is observed that *UrQMD* model fails to explain the observed dynamical fluctuations and multifractality in our data in both η and φ spaces. It also fails to explain the observed power law growth of the scaled factorial moments with decreasing bin size in both the spaces.

We have also used Takagi method to study multifractality in our data and observed that the results for the random and *UrQMD* events are about the same as those obtained for the experimental events in both the spaces. Thus no meaningful conclusion regarding multifractality in the data could be drawn from the analysis done using the Takagi method. We therefore suggest that only F_q-moment or G_q-moment method should be used for the study of multifractality in multiparticle production as the multiplicity moments calculated using the Takagi method are dominated by statistical fluctuations.

The generalized dimension D_q are determined from G_q-moment and F_q-moment analyses for experimental and *UrQMD* events in η and φ spaces. D_q values for our experimental events are found to decrease with increasing q. This shows the presence of multifractality in our data. However, for *UrQMD* events, D_q values for different q values are equal within the errors. Thus, the model again fails to explain the observed dynamical fluctuations and multifractality in our data. Therefore, we conclude that the string hadronic *UrQMD* model could not explain the experimental results on the generalized dimension. The multifractal specific heat c is also determined from G_q-moment and F_q-moment analyses. Differences in the values of D_q and c obtained from the two

methods are mainly due to the difference in the definitions of G_q-moments and F_q-moments.

From the analysis of the scaled factorial cumulant moments for shower particles produced in ^{28}Si-$AgBr$ collisions at 14.6A GeV, we observe that both the second and third order scaled factorial cumulant moments K_2 and K_3 have non-zero values, which indicates that the multiplicity distributions of shower particles is not Poissonian. Further, significant deviation of the values of the second and third order scaled factorial cumulant moments from zero is an evidence of the presence of dynamical two particle and three particle correlations. On comparing our results with the results obtained for events simulated using the string hadronic model *UrQMD,* we observe that K_3 values for different M are almost zero, indicating the absence of three particle correlations in *UrQMD* events. However, K_2 values for different M deviate significantly from zero, indicating that significant two particle correlations are present in *UrQMD* events. Further, to extract more information from the scaled factorial cumulant moment analysis we have investigated the slopes of K_q versus ln$M$ plots (cumulant indices). The cumulant indices for experimental events are $\pi_2 = 0.018 \pm 0.004$, $\pi_3 = 0.012 \pm 0.003$, whereas for *UrQMD* events they are $\pi_2 = 0.002 \pm 0.001$, $\pi_3 = -0.000 \pm 0.000$. The cumulant indices for *UrQMD* events are consistent with being zero. However, not only two particle correlations but also significant three particle correlations are present in our data. Moreover, the values of cumulant indices for our data are also not zero. Thus the string hadronic model *UrQMD* fails to explain the observed correlations in our data.

We observe that the cumulant indices show an inverse dependence upon the pseudorapidity density. This indicates that all types of collisions involve similar physics in terms of the types of particle sources created. We have calculated the number of independent sources for ^{28}Si-$AgBr$ collisions at 14.6A GeV. The value of the average number of independent sources ($\overline{N}$) obtained using independent source model deviates significantly from the value obtained from the negative binomial distribution fitting of the pseudorapidity distribution. One of the reasons for different values of $\overline{N}$ obtained from two methods could be the assumption used in arriving at $\overline{N} = \frac{3a\langle\rho\rangle}{b}$ (Equation 4.21) that is used to find $\overline{N}$. It has been assumed that the second order scaled factorial cumulant of the number of sources is zero. This assumption is not valid because the multiplicity

distribution is not Poissonian as $K_2 \neq 0$. The other assumption that three particle correlations are negligible compared to two particle correlations is also not valid as significant three particle correlations are present in our data.

Additional information about the dynamics of multiparticle production by investigating bin-bin correlations was obtained through the study of factorial correlators. The correlators measure not only the non-statistical local density fluctuations but also give important information about the correlations between the local density fluctuations in different regions of phase space. We have studied factorial correlators for ^{28}Si-$AgBr$ collisions at 14.6A GeV and $UrQMD$ events in the full range of correlation length (D) and observe power law behaviour in the region $D < 0.5$. The slopes (ϕ_{ij}) obtained for $UrQMD$ events are very nearly equal to zero. For the experimental events we observe that the slopes (ϕ_{ij}) increase with increase in the order of correlations but for $UrQMD$ events for $\delta X = 0.125$ and 0.036, we observe no such pattern. Thus $UrQMD$ model fails to explain our experimental results on factorial correlators also. Further, we have observed results in favour of δX independence of C_{ij} for small values of D, but the scaling seems to fail at large values of D ($D > 0.5$). The results obtained for our data are in agreement with the α-model, which predicts that the factorial correlators have a power law increase with decreasing distance between intervals and have no dependence on the size of the intervals (δX). But this does not guarantee the success of α-model, as other models with short-range order have similar predictions.

Further, the scaled factorial moments F_q are studied for ^{28}Si-$AgBr$ collisions at 14.6A GeV. These moments follow the generalized power law $\langle F_q(M)\rangle \propto [g(M)]^{\phi_q}$. The values of ϕ_q/ϕ_2 obtained from the linear fits of $\ln\langle F_q\rangle$ versus $\ln\langle F_2\rangle$ graphs are found to obey the Brax-Peschanski formula for intermittency indices with Levy index $\mu = 1.635 \pm 0.012$ for η space and $\mu = 1.801 \pm 0.003$ for φ space. These values lie within the Levy stable region 0 μ 2. It is observed that the generalized dimensions D_q decreases with increasing q, which indicates that the multiparticle production in ^{28}Si-$AgBr$ collisions at 14.6A GeV is a self-similar cascade process. The multifractal spectra $f(\alpha_q)$ in η and φ spaces are obtained. $f(\alpha_q)$ spectra are smooth and concave downward, indicating the presence of dynamical fluctuations in our data.

We have collected very useful information about the dynamics of multiparticle production in nucleus-nucleus collisions at relativistic energy. Significant dynamical

fluctuations are observed in our data. It is believed that the fluctuations could be due to the formation of quark-gluon plasma (Q.G.P.) in these collisions. But evidence of dynamical fluctuations has also been obtained in low energy nucleus-nucleus collisions where the formation of Q.G.P. is not expected. Even in target fragmentation process, where the Q.G.P. phase transition is most unlikely, evidence of dynamical fluctuations has been reported by some investigators. So Q.G.P. phase transition cannot be the only reason for the fluctuations observed in our data. It may be possible that the observed fluctuations may have a more conventional explanation. The presence of random cascade mechanism or short-range correlations or some collective phenomena may be responsible for the observed dynamical correlations in relativistic nucleus-nucleus collisions.